Advanced Diffusion-weighted Imaging of the pancreas:

Pre-clinical and clinical developments

CARLOS JOSÉ DOS REMÉDIOS BILREIRO

A thesis submitted in fulfilment of the requirements for the Doctoral Degree in Health Sciences in the speciality of Medicine at Faculdade de Ciências Médicas | NOVA Medical School of NOVA University Lisbon

March, 2025

nms.unl.pt

ADVANCED DIFFUSION-WEIGHTED IMAGING OF THE PANCREAS:

PRE-CLINICAL AND CLINICAL DEVELOPMENTS

Carlos José dos Remédios Bilreiro

Supervisors:
Celso Matos, MD, Director of Research and Radiology Department,
Champalimaud Foundation
Noam Shemesh, PhD, Principal Investigator of Pre-Clinical MRI Lab,
Champalimaud Foundation
Rui Mateus Marques, MD PhD, Invited Assistant Professor,
NOVA Medical School

A thesis submitted in fulfilment of the requirements for the Doctoral Degree in Health Sciences in the speciality of Medicine

March, 2025

Statements of originality and ethical commitment

I certify that the content of this Thesis is original and that I was responsible for data collection and analysis, and writing of all publications.

The studies performed with humans or human data included in this Thesis have been approved by the Ethics Research Committee of Champalimaud Foundation and Ethics Research Committee of NOVA Medical School. The studies performed in animals included in this Thesis have been approved by the Animal Welfare Body of Champalimaud Foundation (ORBEA), Direção Geral de Alimentação e Veterinária (DGAV) and Ethics Research Committee of NOVA Medical School.

Carlos José dos Remédios Bilreiro



The works presented in this Thesis were conducted in the Pre-clinical MRI Laboratory and Radiology Department of Champalimaud Foundation

Publications

1. Bilreiro C, Matos C (2021) Diffusion-Weighted Imaging of the Pancreas. In: Matos C, Papanikolaou N (eds) Diffusion Weighted Imaging of the Hepatobiliary System. Springer, Cham.
2. Bilreiro C, Fernandes FF, Andrade L, Chavarrías C, Simões RV, Matos C, Shemesh N. Effective bowel motion reduction in mouse abdominal MRI using hyoscine butylbromide. Magn Reson Med. 2021; 86(4):2146-2155. doi: 10.1002/mrm.28824.
3. Bilreiro C, Andrade L, Marques RM, Matos C. Diffusion-weighted imaging for determining response to neoadjuvant therapy in pancreatic cancer: a systematic review and meta-analysis. Eur Radiol. 2024; 34(5):3238-3248. doi: 10.1007/s00330-023-10381-0.
4. Bilreiro C, Andrade L, Santiago I, Marques RM, Matos C. Imaging of pancreatic ductal adenocarcinoma – An update for all stages of patient management. Eur J Radiol Open. 2024; 12:100553. doi: 10.1016/j.ejro.2024.100553.
5. Bilreiro C, Fernandes FF, Simões RV, Henriques R, Chavarrías C, Ianus A, Castillo-Martin M, Carvalho T, Matos C, Shemesh N. Pancreatic Intraepithelial Neoplasia Revealed by Diffusion-Tensor MRI. Invest Radiol. 2024. doi: 10.1097/RLI.0000000000001142.
6. Bilreiro C, Andrade L, Henriques R, Loução N, Shemesh N, Matos C. Diffusion Tensor Imaging and Diffusion Kurtosis Imaging of the Pancreas - Feasibility, Robustness and Protocol comparison in a Healthy population. Accepted for publication in Abdominal Radiology on 10/03/2025.

Acknowledgements

At the end of this journey, marked by many projects, challenges and achievements, I must acknowledge the people who helped me along the way and made it all possible.

I must thank Dr. Celso Matos, who invited me to work at Champalimaud Foundation in 2019, and challenged me to pursue a research project on pancreatic cancer. Over the course of these years, his contributions were invaluable, both for my research and clinical career. The research projects developed in the Radiology Department of our Institution would not have been possible without his continued support and push for providing researchers with the necessary conditions for developing their work, especially having time reserved for research in weekly work schedules.

I am grateful to Dr. Noam Shemesh, who guided my pre-clinical research. His enthusiasm about the research carried out in the Lab and his constant encouragement towards me and Lab colleagues were empowering, motivating conjoined efforts in driving all the different research projects forward. I cherish the classes in MRI he gave me at the beginning of this journey, and the many insightful and stimulating discussions we had during the years. I will also take with me the valuable lessons he taught me in overcoming technical and organizational challenges of scientific projects, as well as managing expectations, establishing effective communication and creating conditions for thriving in a team environment.

I thank Prof. Rui Mateus Marques, who accepted to co-Tutor me as a PhD student. He helped me with my clinical projects and provided significant contributions to the overall structuring of my Thesis. His insights on clinical Radiology and his accumulated experience have been of great value for the quality of this work.

I also want to thank Dr. Jorge Brito, Prof. Filipe Caseiro Alves and Prof. Carmen Ayuso. They have impacted on my professional choices, by motivating me to continuously grow as a radiologist and dedicate most of my time to the field of Abdominal and Gastrointestinal Radiology. They have also provided me with key opportunities, that ultimately led me to pursue research projects and complete this PhD.

I want to thank all my co-authors, who have individually contributed to the works composing this Thesis. First, I must acknowledge my own wife, Dr. Luísa Andrade, one the best radiologists I have ever known. She has contributed as an active investigator on most of my research projects, and was the driving force for continuing this journey, behind many tough periods over the years. In the Pre-clinical MRI Lab, I must especially thank a few brilliant researchers: Francisca Fernandes, Dr. Rui Simões, Dr. Rafael Henriques, Dr. Cristina Chavarrías and Dr. Andrada Ianus. Each one of them contributed directly to these projects as researchers, and indirectly by teaching me much of what I learned during this time. Additionally, I am obviously thankful to Dr. Mireia Castillo-Martin and Dr. Tânia Carvalho, our amazing clinical and veterinary pathologists. They played a central role in our pre-clinical research and provided invaluable data and insights. I also thank Eng. Nuno Loução, who collaborated with me in my clinical research projects, and Dr. Inês Santiago who collaborated with me in a clinical review. In the end, it was the combined efforts and expertise of all these people that made everything possible.

I am grateful to the Champalimaud Foundation Administration Board, its president Dr. Leonor Beleza and vice-president Dr. João Silveira Botelho. They have provided me with the opportunity to conduct my research in this Institution, and it was the Champalimaud Foundation who provided many of the necessary resources and funding for our research.

I am also thankful to all the staff members in the Radiology Department of Champalimaud Foundation, many of whom have contributed as volunteers on one of our research projects. It has been a pleasure working with them during these years.

Finally, I am the most thankful to my Family. First, my extraordinary wife Luísa, who has been by my side for all the best and worst life may give us. Besides contributing directly as a researcher on most of my projects, it was her love and support what motivated me and enabled me to press onwards during difficult periods. I thank my sons, Luís and José, the brightest lights in my life who make me the proudest father every day. I thank my loving mother, Teresa, for always being there for me and making me the person that I am. I thank my amazing sisters, Mariana and Leonor, for their unconditional friendship; I am proud to be your brother.

Abstract

Pancreatic cancer is one of the most lethal cancers worldwide, with a higher burden in the western world. The overall survival rate at 5 years is estimated at 13%. This dismal scenario is attributed to its common late diagnosis at advanced stages, precluding surgical resection, which remains the only potentially curative option. Thus, early diagnosis is key for improving patient prognosis. Recent data established that pancreatic cancer carcinogenesis follows a progressive development of pre-malignant lesions, the most relevant being pancreatic intraepithelial neoplasia (PanIN). This process entails potential opportunities for early diagnosis and intervention, which could effectively reduce the burden of pancreatic cancer. Current imaging methods, namely computerized tomography (CT) and magnetic resonance imaging (MRI), are well established for the diagnosis and characterization of pancreatic cancer. These methods are, nevertheless, ineffective for diagnosing pre-malignant lesions, i.e., PanIN. Current imaging is also lacking when assessing response to neoadjuvant therapy for pancreatic cancer, a crucial point for patient management.

Diffusion-weighted imaging (DWI) has become a staple of MRI for a great number of clinical applications, due to its microstructure probing ability, with its robust metric - apparent diffusion coefficient (ADC) being widely accepted. However, the full complexity of diffusion is not captured by conventional DWI. More advanced diffusion-based methods include diffusion tensor imaging (DTI) and diffusion kurtosis imaging (DKI). DTI provides a rotationally invariant representation of the diffusion process, allowing characterization of anisotropy and diffusivities across major axes. This technique is routinely used for neuroimaging, namely for tractography, but not for pancreatic imaging. DKI explores the non-Gaussianity of diffusion, which has been associated with microstructural complexity, therefore presenting potential for characterizing pancreatic changes at the microscopic level.

The works presented in this Thesis were aimed at developing tools with potential for improving the dismal reality of pancreatic cancer, through the detection of the major pre-malignant lesions – PanIN, and better characterization of response to neoadjuvant therapy. First, since DWI's role on evaluating response to neoadjuvant therapy is not yet clear, a systematic review and meta-analysis was performed for he published literature

on this matter. Then, a pre-clinical study was conducted, using genetically engineered mouse models (GEMM) which develop PanIN and pancreatic cancer. In the first part of this pre-clinical study, we developed a new method for bowel motion reduction using hyoscine butylbromide with different dosages, allowing for high-quality MRI of the mouse abdomen. Secondly, the GEMM were imaged periodically with anatomical T2-weighted pulse sequence, to determine age of onset of detectable pancreatic changes. The third part of this study consisted of developing a DTI application for *in vivo* GEMM, searching for PanIN and PDAC. Following *in vivo* DTI, we performed *ex vivo* MR Microscopy through ultrahigh resolution DTI, which allowed a direct correlation with histology and determination of underlying histological features responsible for MRI contrasts. As a final part of the pre-clinical study, human pancreatic samples were imaged, to evaluate the technique's translational potential. The final study included in this Thesis was aimed at providing an adaptation of DTI and DKI of the healthy pancreas in a clinical setting, exploring its feasibility, repeatability, quality and inter-reader agreement.

In the matter of DWI's role for evaluating response to neoadjuvant therapy, our systematic review and meta-analysis revealed that, although DWI is reported as useful for this purpose, further studies with robust data are needed to provide specific recommendations for clinical practice. This conclusion was motivated by high heterogeneity and risk for bias between studies. Also, ADC values overlapped for responders and non-responders between studies, underlining the need for standardization in image acquisition and evaluation.

Our first pre-clinical study demonstrated the efficacy of hyoscine butylbromide at high dosage for reducing bowel motion artifacts in abdominal MRI of the mouse. The bowel motion reduction window was observed 8.5 min after injection and lasted up to 45 min. Its use allowed the acquisition of high-quality images of the mouse abdomen, including DWI.

We found that DTI can be used to detect and characterize PanIN *in vivo* in GEMM, with high diagnostic performance (up to AUC = 1). Using MR Microscopy, we observed specific microstructural features of PanIN and PDAC with direct histological correlation: anisotropy in peripheral areas of fibrosis, high diffusivities in cystic areas and high axial diffusivity and T2* in stromal components. These same contrasts were present in the

human pancreas allowing the identification of PanIN, determining its potential for clinical translation.

Finally, we developed a clinically feasible DTI and DKI acquisition for pancreatic imaging. Both techniques were acquired in a single session, with excellent inter-observer agreement. Although DTI provided optimal image quality and repeatability, MK inaccuracies were observed, prompting further research into artifacts correction. A shorter protocol with 6 diffusion directions may be preferred.

In conclusion, the works presented in this Thesis have contributed to furthering knowledge on pancreatic cancer imaging. The most relevant findings for clinical practice include the clarification of DWI's role in evaluating response to neoadjuvant therapy, and the development of clinically feasible DTI and DKI acquisition of the pancreas, with high-quality DTI. The development of DTI for the detection and characterization of PanIN offers new possibilities for researching pancreatic cancer carcinogenesis, both in pre-clinical and clinical contexts. Simultaneously, our findings represent a first step towards early and noninvasive detection of PanIN, which could ultimately provide more effective avenues for treating, or even preventing, pancreatic cancer.

Resumo

O cancro do pâncreas é um dos cancros mais letais no mundo, com maior peso no mundo ocidental. A taxa de sobrevivência global aos 5 anos é estimada atualmente em 13%. Este cenário sombrio é atribuído ao habitual diagnóstico tardio em fases avançadas, impossibilitando a ressecção cirúrgica, que continua a ser a única opção potencialmente curativa. Assim, o diagnóstico precoce é fundamental para melhorar o prognóstico do doente com cancro de pâncreas. Dados recentes estabeleceram que a carcinogénese do cancro do pâncreas segue um desenvolvimento progressivo de lesões pré-malignas, sendo a mais relevante neste contexto a neoplasia intraepitelial pancreática (PanIN). Este processo fornece oportunidades potenciais de diagnóstico e intervenção precoces, o que poderia melhorar o cenário clínico do cancro do pâncreas. Os métodos de imagem atuais, nomeadamente a tomografia computorizada (TC) e a ressonância magnética (RM), estão bem estabelecidos para o diagnóstico e caracterização do cancro do pâncreas. Estes métodos são, no entanto, ineficazes para o diagnóstico de lesões pré-malignas, nomeadamente PanIN. Os estudos de imagem atuais são também insuficientes para a avaliação à resposta à terapêutica neoadjuvante para o cancro do pâncreas, um ponto crucial para a gestão do doente.

A imagem ponderada em difusão (DWI) tornou-se um componente básico da RM para um grande número de aplicações clínicas devido à sua capacidade de sondar a microestrutura de tecidos biológicos, sendo o seu coeficiente de difusão aparente (ADC) uma métrica amplamente aceite. No entanto, a complexidade do processo de difusão nos tecidos não é inteiramente captada pela DWI convencional. Métodos mais avançados baseados em difusão incluem tensor de difusão (DTI) e curtose de difusão (DKI). O DTI fornece uma representação rotacionalmente invariante do processo de difusão, permitindo a caracterização da anisotropia e das difusividades nos eixos espaciais principais. Esta técnica é utilizada por rotina em neurorradiologia, principalmente para tractografia, mas não para imagiologia pancreática. O DKI explora a não-Gaussianidade da difusão, que está associada à complexidade microestrutural nos tecidos, apresentando, por isso, potencial para caracterizar alterações pancreáticas a nível microscópico.

Os trabalhos apresentados nesta Tese tiveram como objectivo desenvolver ferramentas com potencial para melhorar a realidade do tratamento do cancro do pâncreas, através da deteção das principais lesões pré-malignas – PanIN, e da melhor caracterização da resposta à terapêutica neoadjuvante. Em primeiro lugar, como o papel da DWI na avaliação da resposta à terapêutica neoadjuvante ainda não é claro, foi realizada uma revisão sistemática e meta-análise da literatura publicada sobre o tema. De seguida, foi realizado um estudo pré-clínico, utilizando modelos de ratinhos geneticamente modificados (GEMM) que desenvolvem PanIN e cancro do pâncreas. Na primeira parte deste estudo pré-clínico, desenvolvemos um novo método para a redução do movimento intestinal utilizando butilbrometo de hioscina com diferentes dosagens, permitindo realizar RM de alta qualidade do abdómen do ratinho. Depois, os GEMM foram analisados periodicamente por RM com uma sequência de pulso anatómica ponderada em T2, para determinar a idade de início das alterações pancreáticas detetáveis por RM. A terceira parte deste estudo consistiu no desenvolvimento de uma aplicação de DTI para GEMM *in vivo*, procurando lesões de PanIN e cancro de pâncreas. Após esta fase, realizámos microscopia por RM *ex vivo* através de DTI de resolução ultra-alta, o que permitiu uma correlação direta com a histologia e a determinação das características histológicas subjacentes responsáveis pelos contrastes de RM. Como parte final do estudo pré-clínico, foram obtidas amostras pancreáticas humanas para avaliar o potencial de translação clínica da técnica. O último estudo incluído nesta Tese teve como objetivo proporcionar uma adaptação da DTI e DKI do pâncreas saudável em ambiente clínico, explorando a sua viabilidade, repetibilidade, qualidade e concordância interobservador.

Relativamente ao papel da DWI na avaliação da resposta à terapêutica neoadjuvante, a nossa revisão sistemática e meta-análise revelaram que, embora a DWI seja reportada como útil para este propósito, são necessários estudos adicionais com dados robustos para fornecer recomendações específicas para a prática clínica. Esta conclusão foi motivada pela elevada heterogeneidade e risco de viés entre os estudos. Além disso, os valores de ADC sobrepuseram-se para os doentes respondedores e não respondedores entre os diferentes estudos, realçando a necessidade de padronização na aquisição e avaliação de imagens.

O nosso primeiro estudo pré-clínico demonstrou a eficácia do butilbrometo de hioscina em doses elevadas para reduzir os artefactos de movimento em RM abdominal de ratinhos. A janela de redução do movimento intestinal foi observada 8.5 minutos após a

injeção e durou até 45 minutos. A sua utilização permitiu a aquisição de imagens de alta qualidade do abdómen do ratinho, incluindo DWI.

Verificámos que o DTI pode ser utilizado para detetar e caracterizar PanIN *in vivo* em GEMM, com um elevado desempenho diagnóstico (até AUC = 1). Através da microscopia por RM, observámos características microestruturais específicas de PanIN e cancro de pâncreas com correlação histológica direta: anisotropia em áreas periféricas de fibrose, elevadas difusividades em áreas quísticas e elevada difusividade axial e T2* em componentes estromais. Estes mesmos contrastes estavam presentes no pâncreas humano, permitindo a identificação de PanIN, determinando o seu potencial para a translação clínica.

Por fim, desenvolvemos uma aquisição de DTI e DKI clinicamente viável para imagiologia pancreática. Ambas as técnicas foram adquiridas numa única sessão, com excelente concordância interobservador. Embora o DTI tenha proporcionado uma qualidade de imagem e repetibilidade ótimas, foram observadas imprecisões nas estimativas de DKI, apontando para a necessidade de investigação adicional para correção de artefactos. Um protocolo mais curto com 6 direções de difusão pode ser neste caso preferível.

Em conclusão, os trabalhos apresentados nesta Tese contribuíram para aprofundar o conhecimento sobre a imagiologia do cancro do pâncreas. Os achados mais relevantes para a prática clínica incluem o esclarecimento do papel da DWI na avaliação da resposta à terapêutica neoadjuvante e o desenvolvimento de uma aquisição clinicamente viável de DTI e DKI do pâncreas, com DTI de alta qualidade. O desenvolvimento de DTI para a deteção e caracterização de PanIN oferece novas possibilidades para a investigação da carcinogénese do cancro do pâncreas, tanto em contextos pré-clínico como clínico. Simultaneamente, as nossas descobertas representam um primeiro passo em direção à deteção precoce e não invasiva de PanIN, o que poderá, em última análise, permitir caminhos mais eficazes para tratar, ou mesmo prevenir, o cancro do pâncreas.

Abbreviations

AD, axial diffusivity

ADC, apparent diffusion coefficient

ADM, acinar-to-ductal metaplasia

AK, axial kurtosis

AUC, area under the ROC curve

BUSC, Buscopan®

CA 19-9, carbohydrate antigen 19-9

CDKN2A, cyclin-dependent kinase inhibitor 2A

CHA, common hepatic artery

CT, computerized tomography

DKI, diffusion kurtosis imaging

DPC4, deleted in pancreatic cancer-4

DTI, diffusion tensor imaging

DWI, diffusion weighted imaging

EUS, endoscopic ultrasound

FA, fractional anisotropy

GEMM, genetically engineered mouse models

H&E, hematoxylin and eosin

HA, hepatic artery

ICC, intraclass correlation coefficient

INK4a, inhibitors of CDK4 subset a

IOPN, intraductal oncocytic papillary neoplasm

IPMN, intraductal papillary mucinous neoplasia

ITPN, intraductal tubulopapillary neoplasm

KRAS, Kirsten rat sarcoma virus

MCN, mucinous cystic neoplasm

MD, mean diffusivity

MD-IPMN, main duct intraductal papillary mucinous neoplasia

MGE, multi-gradient echo

MK, mean kurtosis

MP-PCA, Marchenko-Pastur principal component analysis

MRCP, magnetic resonance cholangiopancreatography

MRI, magnetic resonance imaging

MT-IPMN, mixed type intraductal papillary mucinous neoplasia

NAT, neoadjuvant therapy

NCCN, national comprehensive cancer network

PanIN, pancreatic intraepithelial neoplasia

PDAC, pancreatic ductal adenocarcinoma

PDX1, pancreatic and duodenal homeobox 1

PTF1a, pancreas associated transcription factor 1 subunit alpha

PV, portal vein

RD, radial diffusivity

RECIST, response evaluation criteria in solid tumors

RK, radial kurtosis

ROC, receiver operating characteristics

ROI, region of interest

SA, splenic artery

SB-IPMN, side-branch intraductal papillary mucinous neoplasia

SE-EPI, spin-echo echo planar imaging

SMA, superior mesenteric artery

SMAD4, mothers against decapentaplegic homolog 4

SMV, superior mesenteric vein

SNR, signal-to-noise ratio

TE, echo time

TR, repetition time

TSE, turbo spin-echo

US, United States of America

Table of contents

STATEMENTS OF ORIGINALITY AND ETHICAL COMMITMENT V

PUBLICATIONS VII

ACKNOWLEDGEMENTS VIII

ABSTRACT X

RESUMO XIII

ABBREVIATIONS XVI

TABLE OF CONTENTS XVIII

CHAPTER I. INTRODUCTION 1

1.1. PANCREATIC CANCER: EPIDEMIOLOGY AND IMPORTANCE OF EARLY DIAGNOSIS 1

1.1.1. Epidemiology of pancreatic cancer 1

1.1.2. Risk factors for developing PDAC and evidence for surveillance 3

1.2. PRECURSOR LESIONS FOR PANCREATIC DUCTAL ADENOCARCINOMA 5

1.2.1. Current clinical practice 5

1.2.2. Pancreatic intraepithelial neoplasia – histological concepts and clinical relevance 8

1.2.3. Pancreatic intraepithelial neoplasia – genetically engineered mouse models and progression model to PDAC 11

1.3. IMAGING OF PANCREATIC CANCER: RECENT ADVANCEMENTS AND PERSPECTIVES 14

1.3.1. Imaging of pancreatic ductal adenocarcinoma 14

1.3.2. Diffusion-weighted imaging of the pancreas 28

1.4. ADVANCED DIFFUSION-WEIGHTED MRI TECHNIQUES 52

1.4.1. Conventional Diffusion-weighted imaging 52

1.4.2. Diffusion tensor imaging 55

1.4.3. Diffusion kurtosis imaging 59

CHAPTER II. RATIONALE AND AIMS 62

2.1. RESPONSE ASSESSMENT TO NEOADJUVANT THERAPY IN PANCREATIC CANCER 62

2.2. Imaging of the most relevant precursor lesions for pancreatic cancer – PanIN 62
2.2.1. Development of a bowel motion reduction protocol for mouse abdominal MRI 63
2.2.2. Longitudinal assessment of PanIN and PDAC development onset 63
2.2.3. In vivo DTI of the pancreas 64
2.2.4. Magnetic Resonance Microscopy of GEMM pancreatic specimens 64
2.2.5. Human pancreatic specimens 64
2.3. Diffusion tensor imaging and Diffusion kurtosis imaging of the pancreas in the clinical setting 65
CHAPTER III. RESULTS 66
3.1. Diffusion-weighted imaging for determining response to neoadjuvant therapy in pancreatic cancer: a systematic review and meta-analysis. 66
3.2. Effective bowel motion reduction in mouse abdominal MRI using hyoscine butylbromide. 78
3.3. Pancreatic Intraepithelial Neoplasia Revealed by Diffusion-Tensor MRI. 105
3.4. Diffusion Tensor Imaging and Diffusion Kurtosis Imaging of the Pancreas - Feasibility, Robustness and Protocol comparison in a Healthy population. 125
CHAPTER IV. DISCUSSION 156
4.1. The role of DWI in assessing response to neoadjuvant therapy in pancreatic cancer 156
4.2. A bowel motion reduction protocol enabling high-quality MRI of the mouse abdomen 157
4.3. Detecting pancreatic intraepithelial neoplasia with DTI 158
4.4. DTI and DKI of the pancreas: feasibility, repeatability and inter-reader agreement in a clinical context 159
CHAPTER V. CONCLUSIONS 160
REFERENCES 161

Chapter I.

Introduction

1.1. Pancreatic cancer: epidemiology and importance of early diagnosis

1.1.1. Epidemiology of pancreatic cancer

Pancreatic cancer is one of the leading causes of cancer related death, ranking sixth in the entire world [1]. Its incidence is approximately 4 times higher in developed countries, being highest in Europe, North America and Australia/New Zealand [1]. Recent data from the US place it as the third leading cause of cancer related death, with an estimated survival rate of 13% at 5 years [2]. This 5-year survival rate is noticeably far from the average 69% of all cancers during 2013-2019, and from the closest cancers by lethality - liver and esophagus, which have a 5-year survival rate of 22% [2].

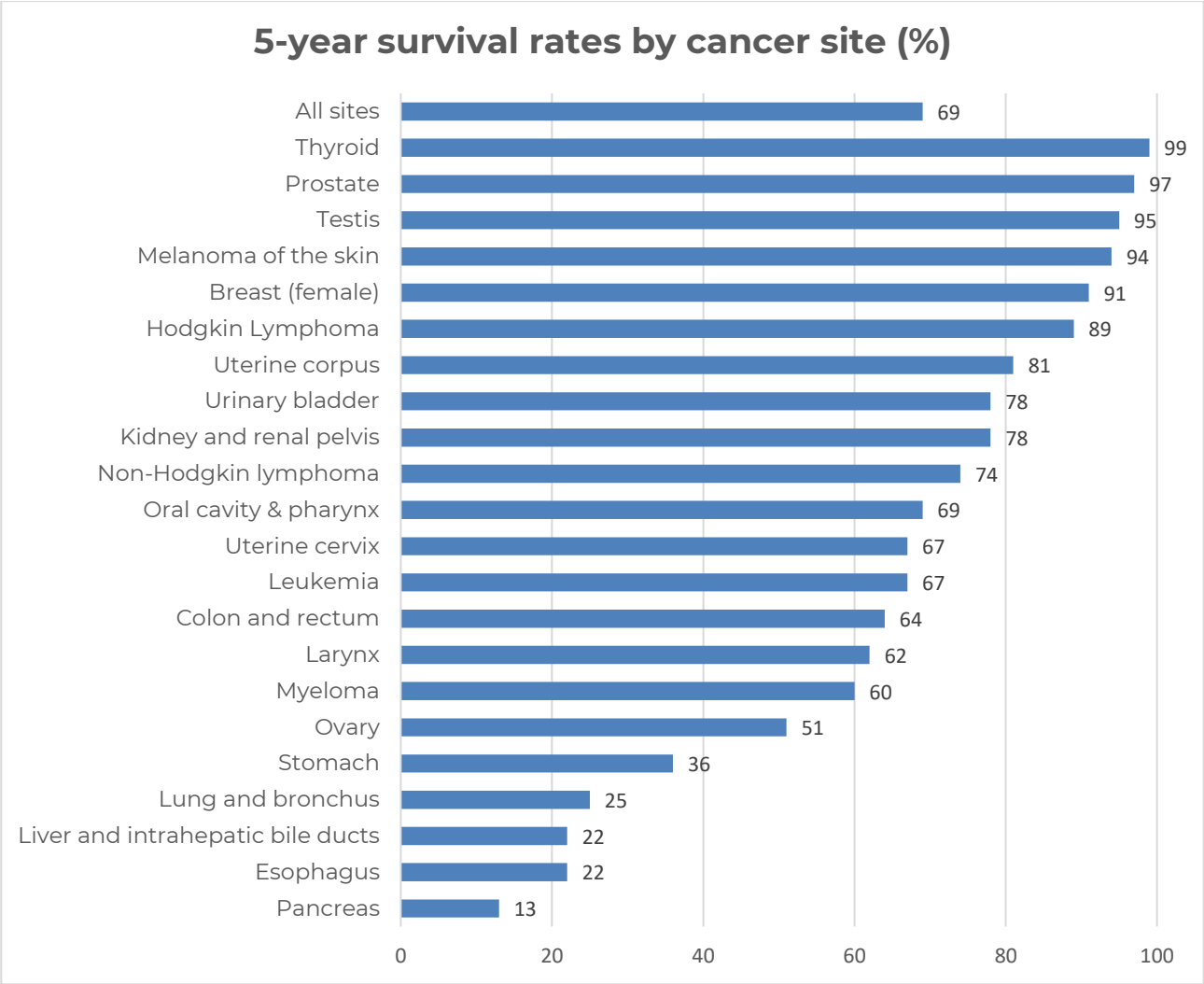


Figure 1. 5-year survival rates of most common cancers in the US, for 2013-2019. Graph built using data from [2].

Pancreatic ductal adenocarcinoma (PDAC) is the most prevalent type of pancreatic cancer, representing approximately 80-90% of pancreatic cancers [3, 4]. The dismal prognosis of PDAC is mainly attributable to a late diagnosis, a consequence of patients only becoming symptomatic and seeking medical care in late stages of the disease, when adjacent organs or vasculature are invaded, or metastases have developed. Common symptoms include weight loss, epigastric and back pain, jaundice, pruritus, light-colored stools and nausea. At these advanced stages (III and IV), 5-year survival rates are estimated at only 0.5-1.9% [5]. Fewer than 20% of patients present with resectable disease, and for these patients who are able to undergo surgery and adjuvant chemotherapy, 5-year survival rates are significantly improved, ranging from 25% to 50% [4, 6, 7]. Thus, early diagnosis is key to improving prognosis of pancreatic cancer.

1.1.2. Risk factors for developing PDAC and evidence for surveillance

There are several modifiable risk factors associated with PDAC development, including tobacco use, alcohol intake, chronic pancreatitis, diabetes and obesity. Smoking and smoke exposure have long been recognized as important risk factors, increasing risk up to double of non-smokers, depending on tobacco use patterns and type of tobacco consumed [8]. The risk associated with alcohol intake is also thought to be dependent on consumption pattern, with the highest risk associated with liquor beverages [9]. Chronic pancreatitis, often associated with alcohol intake and tobacco use, is also thought to further increase the risk for PDAC development [10, 11]. Diabetes is another recognized risk factor, with the risk decreasing with the increasing duration of Diabetes, but with an excess risk of 30% persisting for more than two decades after diagnosis [12]. Obesity, often associated with insulin resistance or Diabetes, is currently thought to be another synergistic risk factor for PDAC [13]. These lifestyle-associated risk factors may contribute to the higher incidence of PDAC in the developed world.

Genetic (non-modifiable) factors also play a role in the risk of developing PDAC. In a large series of case-control studies, 10% of patients with PDAC had a family history of pancreatic cancer [14]. Several hereditary syndromes have a known increased risk for PDAC development, including Peutz-Jeghers, Lynch, breast and ovarian cancer, hereditary pancreatitis, familial pancreatic cancer, familial atypical multiple mole melanoma, cystic fibrosis [4].

These individuals at high-risk for developing pancreatic cancer are obvious candidates for surveillance programs. The current consensus is that individuals with a >5% lifetime risk of developing pancreatic cancer should undergo surveillance [15, 16]. A recent study found that annual surveillance of high-risk individuals leads to the detection of smaller pancreatic tumors, at earlier stage than matched control patients, and to improved survival [17]. In this study, surveillance included a questionnaire, endoscopic ultrasound (EUS), and abdominal contrast-enhanced CT or 1.5T/3T contrast-enhanced MRI with magnetic resonance cholangiopancreatography (MRCP). Another study reported similar outcomes of a surveillance program implemented for high-risk individuals with a germline CDKN2A/p16 PV mutation [18]. Patients under surveillance who developed PDAC had a fourfold increase in surgical resection rates and improved survival. Surveillance was performed with annual MRCP and EUS alternating every 6 months with

MRI (6-months interval for alternating screening tests). Other studies reported similar findings, with earlier detection and improved survival justifying the implementation of surveillance programs for high-risk individuals [19–21].

Despite surveillance programs proving valuable, the best conventional imaging tests (MRI/MRCP and EUS) have provided suboptimal diagnostic yields, with timely diagnosis proving challenging, and underscoring the need for more sensitive diagnostic tests or biomarkers [20, 22].

1.2. Precursor lesions for pancreatic ductal adenocarcinoma

1.2.1. Current clinical practice

Precursor lesions for PDAC have long been recognized as potential targets for surveillance and early intervention [23]. With a first established nomenclature in the late 1990s and early 2000s, pancreatic intraepithelial neoplasia (PanIN) is considered the major precursor lesion for PDAC [24, 25]. Due to its microscopic size, PanIN is not currently diagnosed by conventional imaging modalities, with a single study reporting that pancreatic microcysts seen in MRCP can sometimes represent PanIN [26]. Other well-known precursor lesions include intraductal papillary mucinous neoplasia (IPMN) and mucinous cystic neoplasm (MCN). Contrary to PanIN, both IPMN and MCN have well-established imaging diagnostic criteria and management recommendations.

IPMN are macroscopic (>5 mm) mucin-producing cystic lesions arising in the pancreatic ducts, which can be histologically classified as low-grade and high-grade according to the presence of dysplastic features [27]. IPMN are most commonly found in patients older than 50 years, with a reported prevalence of 10.9% in a large series [28]. On imaging, these cystic lesions can be classified according to their macroscopic appearance as side-branch (SB-IPMN; sometimes also referred to as branch-duct IPMN), main duct (MD-IPMN) or mixed-type (MT-IPMN, with features of both main duct and side branch IPMN). SB-IPMN (Figure 2A) are the most frequent type of IPMN, reportedly more than 80% of IPMNs [28]. MD-IPMNs (Figure 2B) pose the highest risk for malignancy, with a reported malignancy rate of 60% [29]. IPMNs are thought to be responsible for originating approximately 10% of PDAC [28, 30].

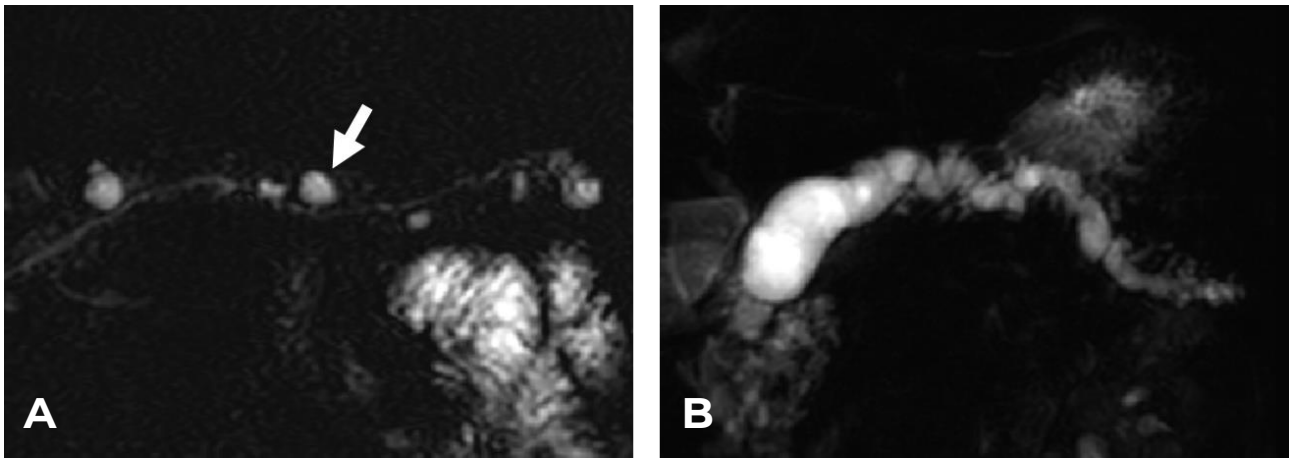


Figure 2. Examples of SB-IPMN and MD-IPMN, as diagnosed by MRCP. In A, typical SB-IPMNs are depicted, one of them with an obvious connection to the main pancreatic duct (arrow). In B, typical findings of a MD-IPMN are shown, with a diffusely dilated main pancreatic duct and slight dilation of secondary ducts.

Being a prevalent lesion with malignant potential, international consensus recommendations for management of IPMN have been published and updated since 2006, the latest in 2024 [31, 32]. In these guidelines, pancreatic cysts are stratified according to the presence of high-risk stigmata (solid component >5 mm, main pancreatic duct ≥10 mm, obstructive jaundice) and worrisome features (≥3 cm, thickened wall, solid component <5 mm, main pancreatic duct with 5-9 mm, lymphadenopathy, abrupt change in caliber of the pancreatic duct with distal pancreatic atrophy, growth rate ≥2.5 mm per year, elevated CA 19-9, clinical symptoms). According to these recommendations, all MD-IPMN (and MT-IPMN), as well as SB-IPMN with high-risk stigmata should be resected. Cysts with worrisome features should be evaluated by EUS, warranting resection if signs suggestive of malignancy are then found, or if clinically adequate in a patient fit for surgery. Other cysts are recommended to undergo surveillance by MRI/MRCP.

MCN (Figure 3) is an uncommon cystic and mucin-producing pancreatic neoplasm with distinctive ovarian-type subepithelial stroma [27]. These tumors comprised 23% of resected pancreatic cysts in a large surgical series [33]. Malignant potential of MCN is clearly recognized, and a systematic review and meta-analysis reported MCN with malignant transformation in 16% of resections [34]. European recommendations take into account lesion size (≥4 cm), presence of mural nodules or associated symptoms for

recommending MCN resection [35]. According to the same guidelines, lesions without these risk factors may undergo surveillance with MRI or EUS. Although the malignant potential of MCN has long been acknowledged, its relative contribution as a precursor lesion to the entirety of PDAC diagnoses is not clear.



Figure 3. Example of typical MCN diagnosed by MRI. A 3 cm pancreatic cyst is incidentally found in a 48-year-old woman, with thick and enhancing internal septa (arrows), as seen in MRCP (A), T2-weighted images (B) and contrast-enhanced T1-weighted images (C).

Other rare pancreatic lesions with recognized malignant potential are intraductal tubulopapillary neoplasm (ITPN) and intraductal oncocytic papillary neoplasm (IOPN)[27]. Patients with these rare lesions and associated invasive carcinoma have a much better prognosis than patients with conventional PDAC, with 5-year survival rates of 71% for ITPN and 100% for IOPN [27].

1.2.2. Pancreatic intraepithelial neoplasia – histological concepts and clinical relevance

Although PanIN is considered the most important precursor lesion for PDAC, much of its biology remains unknown, due to the lack of non-invasive diagnostic tools.

PanIN is defined as a noninvasive epithelial neoplasm in the small pancreatic ducts, smaller than 5 mm in size, and was initially classified into four categories (PanIN-1A, PanIN-1B, PanIN-2, PanIN-3) according to the degree of architectural and nuclear atypia [36, 37]. Often, lobulocentric atrophy and acinar-to-ductal metaplasia (ADM) are found in association with PanIN [38, 39]. In 2015, the Baltimore consensus for neoplastic precursor lesions of the pancreas shortened its classification, due to the fact that PanIN-1 and PanIN-2 are common findings without immediate clinical consequences, while PanIN-3 is associated with the development of PDAC [40]. From this point onwards, a two-tiered classification system has been in use for PanIN: low-grade (PanIN-1A, PanIN-1B, PanIN-2) and high-grade (PanIN-3). The histological characteristics of both the older and more recent classifications of PanIN are presented in Table 1.

Histological features	**Former classification**[36]	**Two-tiered classification**[40]
Flat epithelial lesions composed of tall columnar cells. Basally located small nuclei, round to oval in shape, and abundant supranuclear mucin. No cytologic atypia.	PanIN-1A	Low-grade PanIN
Papillary, micropapillary or basally pseudostratified architecture. Other features similar to PanIN-1A.	PanIN-1B	
Mucinous epithelium may be flat but mostly papillary. Nuclear abnormalities: loss of polarity, nuclear crowding, enlarged nuclei, pseudostratification, hyperchromatism. Rare mitoses, not atypical.	PanIN-2	
Predominantly papillary or micropapillary architecture (rarely flat). Cribriform architecture. Loss of polarity, dystrophic mucinous cells, enlarged irregular nuclei and prominent nucleoli. Increased mitoses, atypical forms may be seen. Features of carcinoma *in situ* (not invading through the basement membrane).	PanIN-3	High-grade PanIN

Table 1. Histological classification systems for PanIN.

Several clinical data associate PanIN, and especially high-grade PanIN, with PDAC. A study on resected pancreatic specimens found PanIN to be present in 82% of patients, and high-grade PanIN in 40% of patients with PDAC [41]. The same study found some association with chronic pancreatitis and PanIN, with 63% of patients presenting PanIN lesions of all grades and 5% of patients presenting high-grade PanIN. Another study on resected pancreatic specimens found PanIN in the vicinity of PDAC in 59% of patients, and 64% of these were high-grade lesions [42]. Another study found PanIN in 26% of the

pancreatic specimens after resection for pancreatic lesions other than PDAC, mostly low-grade PanIN [43]. This latter study did not report apparent prognostic value of the surgically removed PanIN, when considering the development of PDAC in the remaining pancreas. The presence of PanIN at resection margins for PDAC resections also does not appear to affect prognosis, with studies reporting no differences in survival in patients with and without PanIN at this site [42, 44]. However, if high-grade PanIN is found at the resection margin in a patient without documented PDAC, a recommendation for additional surgery may be justified, as the development of PDAC in the remaining pancreas has been reported in these cases [24, 40, 45].

A recent study performed on human pancreatic samples using 3D mapping with genetic analysis correlation, revealed that the normal pancreas often contains multifocal lesions of mainly low-grade PanIN with varying KRAS mutations, indicating polyclonal origins [46]. These findings reinforce the importance of KRAS mutations in initiating PanIN, while also pointing to the necessity of developing biomarkers for noninvasive PanIN identification, especially high-risk lesions.

1.2.3. Pancreatic *intraepithelial neoplasia – genetically engineered mouse models and progression model to PDAC*

Clinical data on PanIN have determined an association with PDAC, but most current knowledge on these lesions was obtained with studies performed on genetically engineered mouse models (GEMM), since being first developed in 2003 [47]. The first mouse model that successfully replicated human PanIN and PDAC, explored the most prevalent genetic mutation in PDAC and PanIN – activated oncogene KRAS ($KRAS^{G12D}$ knock-in allele in the model silenced by a flox STOP transcriptional cassette), and obtained pancreatic specificity using the PDX1 and PTF1α promoters for the bacterial Cre recombinase [47, 48]. This mouse model, later called KC, was found to develop PanIN lesions which progressed to PDAC over the course of several months. These findings helped validate the progression model of PanIN to PDAC. Other GEMM were then developed, which included additional prevalent mutations in tumor suppressor genes TP53 (KPC model) and SMAD4/DPC4, and also p16 (INK4a) [49–53]. These mouse models presented more locally aggressive and metastatic phenotypes, revealing the importance of accumulating genetic mutations additional to KRAS during the development of PDAC [54]. According to these data, and similarly to colon cancer, a stepwise progression model starting with low-grade PanIN (PanIN-1 and -2), then high-grade PanIN and finally PDAC has been established [55, 56]. This stepwise progression model is represented in Figure 4.

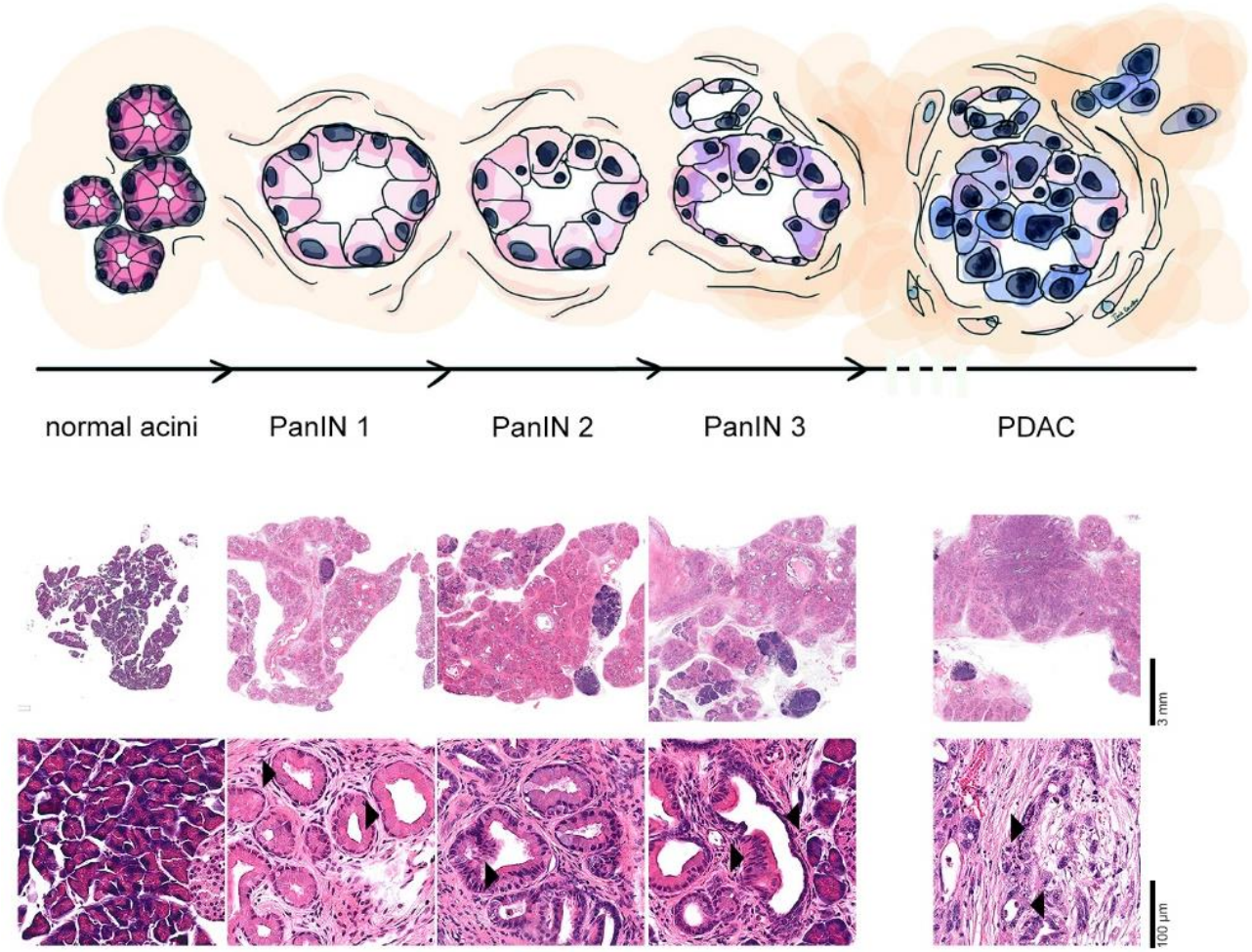


Figure 4. Stepwise progression of PanIN to PDAC. The progressive accumulation of dysplastic changes in each step pf PanIN development is represented with the corresponding histology (H&E), obtained from genetically engineered mouse models (KC and KPC). Figure courtesy of Tânia Carvalho, DVM PhD, Champalimaud Foundation.

GEMM also provided insights into the cell of origin of PDAC, a long-debated issue [57, 58]. Recent studies confirmed that both ductal cells and acinar cells may originate PDAC, although with different progression rates and genetic features [59, 60]. Mouse models with ductal cells-activated $Kras^{G12D}$ and TP53 loss, progressed faster to PDAC while associated with high-grade PanIN, contrasting with similarly mutated acinar cells, which progressed slower to PDAC and associated with ADM and PanIN of both low- and high-grades [60]. Furthermore, ductal cell-derived and acinar cell-derived tumor genetic signatures are enriched in basal-like and classical subtypes of PDAC, respectively [59]. In this latter study, ADM and PanIN were consistently found in the vicinity of acinar cell-

derived tumors, whereas duct cell-derived tumors were surrounded by uninvolved pancreas. These recent findings demonstrate that the cell of origin affects PDAC carcinogenesis, influencing tumor genetic subtypes and the development of associated ADM and PanIN, which may pose diagnostic and prognostic implications, should noninvasive diagnostic biomarkers for PanIN become available in the future.

1.3. Imaging of pancreatic cancer: recent advancements and perspectives

1.3.1. Imaging of pancreatic ductal adenocarcinoma

This section discusses the most up-to-date imaging recommendations, typical and atypical findings, and issues related to each step of patient management for PDAC. Example cases for each relevant condition are presented, and a structured report for disease staging is suggested [61]. The following publication is presented, comprising relevant discussions in this topic: “Bilreiro C, Andrade L, Santiago I, Marques RM, Matos C. Imaging of pancreatic ductal adenocarcinoma - An update for all stages of patient management. Eur J Radiol Open. 2024 doi: 10.1016/j.ejro.2024.100553”.

European Journal of Radiology Open 12 (2024) 100553

Contents lists available at ScienceDirect

European Journal of Radiology Open

journal homepage: www.elsevier.com/locate/ejro

Imaging of pancreatic ductal adenocarcinoma – An update for all stages of patient management

Carlos Bilreiro [a,b,c,*], Luísa Andrade [a], Inês Santiago [a], Rui Mateus Marques [c,d], Celso Matos [a,b]

[a] Radiology Department, Champalimaud Foundation, Lisbon, Portugal
[b] Champalimaud Research, Champalimaud Foundation, Lisbon, Portugal
[c] Nova Medical School, Lisbon, Portugal
[d] Radiology Department, Hospital de S. José, Lisbon, Portugal

HIGHLIGHTS

- Imaging is crucial for patient management in pancreatic ductal adenocarcinoma.
- Contrast-enhanced CT is preferred for diagnosis and staging; MRI for hepatic staging.
- Imaging performs poorly for lymph node staging and response to neoadjuvant therapy.
- Anatomic findings and disease biology should both be considered for patient staging.
- A multidisciplinary team is essential for obtaining the best patient outcomes.

ARTICLE INFO

Keywords:
Pancreatic carcinoma
Neoplasm staging
Neoadjuvant therapy
Patient care team
Neoplasm recurrence, Local

ABSTRACT

Background: Pancreatic ductal adenocarcinoma (PDAC) is a common and lethal cancer. From diagnosis to disease staging, response to neoadjuvant therapy assessment and patient surveillance after resection, imaging plays a central role, guiding the multidisciplinary team in decision-planning.
Review aims and findings: This review discusses the most up-to-date imaging recommendations, typical and atypical findings, and issues related to each step of patient management. Example cases for each relevant condition are presented, and a structured report for disease staging is suggested.
Conclusion: Despite current issues in PDAC imaging at different stages of patient management, the radiologist is essential in the multidisciplinary team, as the conveyor of relevant imaging findings crucial for patient care.

1. Introduction

Pancreatic ductal adenocarcinoma (PDAC) is one of the leading causes of cancer-related death in the modern world, with dismal survival rates [1]. Resection remains the only potentially curative option and, combined with systemic chemotherapy, provides the best therapeutic intervention for improving survival [2–4]. However, tumor resectability relies on an early diagnosis, which is often not possible, due to patients presenting with advanced disease and also diagnostic imaging challenges to detect subclinical disease [5]. Furthermore, defining which patients are best suited for surgery, and which patients should be offered neoadjuvant or palliative therapy is not a simple task. Several staging systems have been developed, with different resectability criteria, and are used in different institutions; the National Cancer Comprehensive Network (NCCN) is the most widely used classification [6–8]. Lastly, there are unresolved issues and difficulties when evaluating patients in the post-neoadjuvant therapy, and post-surgical follow-up periods [9–12]. Imaging plays a central role in all stages of patient management, and the radiologist's assessment is the cornerstone of surgical and medical decision-planning. This review aims to present and discuss the

Abbreviations: ADC, apparent diffusion coefficient; CT, celiac trunk; DWI, diffusion-weighted imaging; EUS, endoscopic ultrasound; HA, hepatic artery; LGA, left gastric artery; MIP, maximum-intensity projection; MPR, multiplanar reformation; MRCP, magnetic resonance cholangiopancreatography; NCCN, National Comprehensive Cancer Network; PDAC, pancreatic ductal adenocarcinoma; PET, positron emission tomography; PV, portal vein; SA, splenic artery; SMA, superior mesenteric artery; SMV, superior mesenteric vein; SV, splenic vein.

* Corresponding author at: Radiology Department, Champalimaud Foundation, Lisbon, Portugal.
E-mail address: carlos.bilreiro@fundacaochampalimaud.pt (C. Bilreiro).

https://doi.org/10.1016/j.ejro.2024.100553
Received 15 October 2023; Received in revised form 2 February 2024; Accepted 3 February 2024
2352-0477/© 2024 Published by Elsevier Ltd. This is an open access article under the CC BY-NC-ND license (http://creativecommons.org/licenses/by-nc-nd/4.0/).

Table 1
CT protocol used in our Institution for pancreatic ductal adenocarcinoma diagnosis and staging.

Oral contrast	Neutral (water, 500 mL ingested over 10 min)	
Intravenous contrast	300 mg/mL; 1.5 mL/kg @ 3-5 mL/s; followed by 20 mL saline flush	
Acquisition phases	Without contrast	Useful for detection of calcifications
	Pancreatic	35-50 s Pancreatic tumor detection; Arterial staging
	Portal venous	70-80 s Metastases detection; Venous staging
	Delayed	3-5 min Isoattenuating tumor detection
Acquisition	Volumetric (isotropic)	Thin slices (≤ 1 mm) Monoenergetic (40 keV)* MPR (tumor-organ relations) MIP (tumor-vascular relations)

* CT equipment with new-generation spectral / dual-energy / photon-counting technology for improved image contrast is recommended. MPR: multiplanar reformation; MIP: maximum intensity projection.

most up-to-date imaging issues on pancreatic cancer diagnosis, staging, response to neoadjuvant therapy and patient follow-up.

2. Diagnosis of pancreatic ductal adenocarcinoma

2.1. Imaging technique and typical findings

CT is the preferred technique for PDAC diagnosis, due to its wide availability and high diagnostic accuracy, with a reported 89–97% sensitivity [9,13]. CT equipments with dual-energy / spectral technology further improve lesion conspicuity and detection, and the newer photon-counting CT equipments have also been reported to do so [14–16]. Lower energy-level (usually 40–50 keV) monoenergetic images provide greater attenuation by iodine contrast material, leading to improved image contrast between the hypovascular PDAC and highly vascularized pancreatic parenchyma. Transabdominal ultrasound maintains some relevancy, as it is the most accessible and least expensive imaging technique, and many pancreatic tumors are first identified on abdominal ultrasound scans [17]. However, due to its low sensitivity and operator dependence, CT should still be performed as a first-line imaging test when PDAC is suspected, or for diagnostic confirmation and tumor staging when a tumor has been identified in ultrasound. MRI is currently a second-line diagnostic technique due to its higher cost and lower availability, with a similar sensitivity to CT for diagnosing PDAC: 83–93.5% [18]. Its use is mainly reserved for diagnostic problem-solving. PET-CT has an estimated 90% sensitivity in detecting pancreatic cancer, but it does not offer clear benefits over CT or MRI for this purpose [19]. Finally, endoscopic ultrasound (EUS) has a reported 91–100% sensitivity for PDAC detection, while also allowing the collection of pancreatic tissue with fine-needle biopsy for histological diagnosis [20,21]. Due to its lower accessibility when compared with other imaging alternatives, EUS is usually reserved for tissue collection for histological analysis.

For PDAC diagnosis, an adequate CT protocol is of paramount importance, including pancreatic, portal venous and delayed phases (Table 1, Fig. 1). Sufficient iodine contrast dose and rate of injection, as well as a saline flush, are necessary to provide adequate lesion conspicuity in dedicated pancreatic multi-phase acquisitions [22,23]. The use of bolus-tracking technique allows acquisition timing to be individualised to each patient circulatory dynamics, ensuring optimal post-contrast phases, and is therefore recommended [22]. When using MRI, an adequate protocol is equally important (Table 2). Typical PDAC diagnostic findings include: (1) pancreatic hypovascular mass with dilation of the upstream main pancreatic duct; (2) simultaneous dilation of the common bile duct and main pancreatic duct if the tumor is located

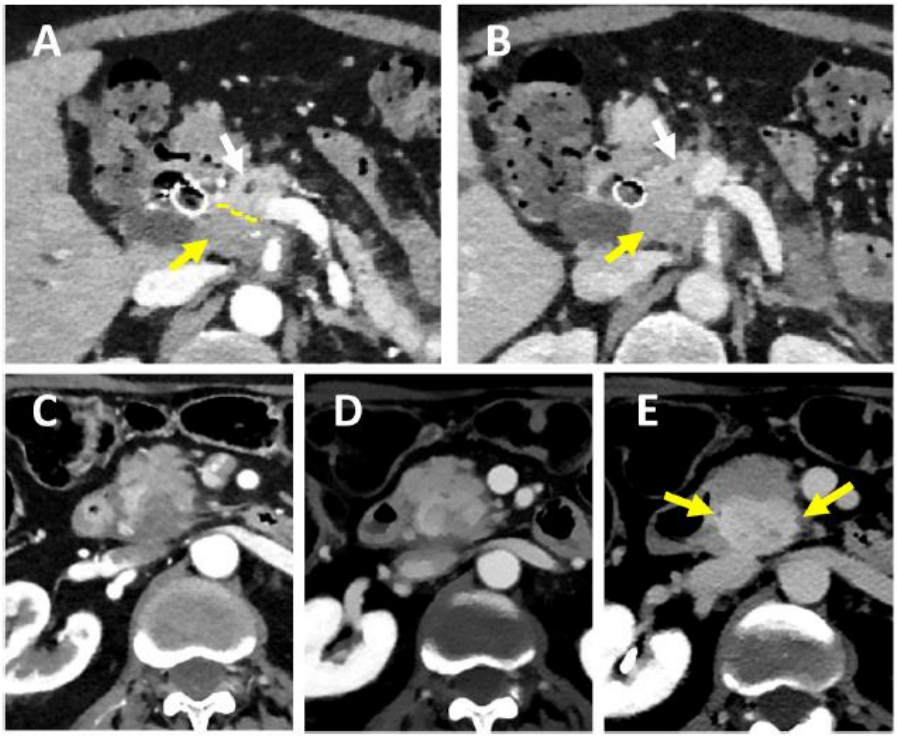


Fig. 1. Importance of the pancreatic and delayed phases for tumor detection. In the pancreatic phase (A), there is a clear distinction (dashed line) between tumoral tissue (yellow arrow) and pancreatic parenchyma (white arrow). In the portal venous phase (B), the distinction between tumor and normal pancreas is not clear. (C - E) depicts another case, where a pancreatic tumor is ill-defined on the pancreatic (C) and portal venous (D) phases, but well-defined on the delayed phase (E, arrows).

Table 2
MRI protocol used in our Institution for pancreatic ductal adenocarcinoma diagnosis and staging.

Acquisitions		T2 TSE	Axial and coronal
		T1 GRE	In- and opposed-phase
		DWI*	b = 10 s/mm^2
		DWI	b ≥ 800 s/mm^2; ADC map
		MRCP	3D or 2D thick slab
Intravenous contrast	THRIVE (fat-saturated T1 GRE)	Without contrast	-
		Pancreatic	35-50 s
		Portal venous	70-80 s
		Delayed	3-5 min

* Fat-suppressed T2 TSE can be acquired as an alternative depending on local preference and MR equipment perfomance. ADC: apparent diffusion coefficient; DWI: diffusion-weighted imaging; GRE: gradient recalled echo; MRCP: magnetic resonance cholangiopancreatography; THRIVE: T1-weighted High Resolution Isotropic Volume Examination; TSE: turbo spin-echo.

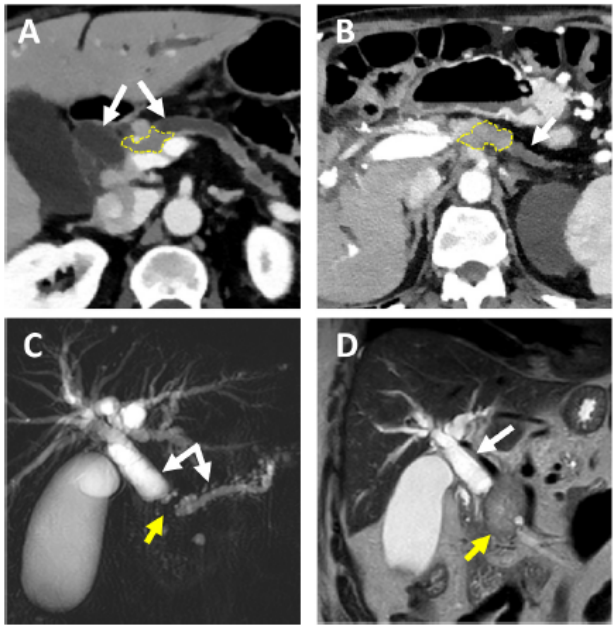


Fig. 2. Typical findings of PDAC. (A) depicts a double duct sign, where both the main pancreatic duct and the biliary tree are dilated (arrows) due to an obstructing tumor in the pancreatic head (dashed line). In (B) there is parenchymal atrophy of the pancreatic tail (arrow), due to an obstructing tumor in the pancreatic body (dashed line). (C) shows a double duct sign in MRCP (white arrows), caused by a presumed obstructing lesion (yellow arrow). (D) reveals an obstructing (white arrow) pancreatic head tumor in a T2-weighted image (yellow arrow).

in the head – also known as "double duct sign"; (3) main pancreatic duct stenosis with signs of chronic pancreatitis in the upstream pancreas (Fig. 2). Imaging staging should be performed before a biliary stent is placed, so ductal anatomy is clearly defined and inflammatory changes do not overlap with tumoral tissue.

Notably, new developments in artificial intelligence applications may provide new opportunities for PDAC diagnosis, such as risk assessment using clinical records and accurate detection using only non-contrast-enhanced CT, as demonstrated in a large multicentric study [24,25].

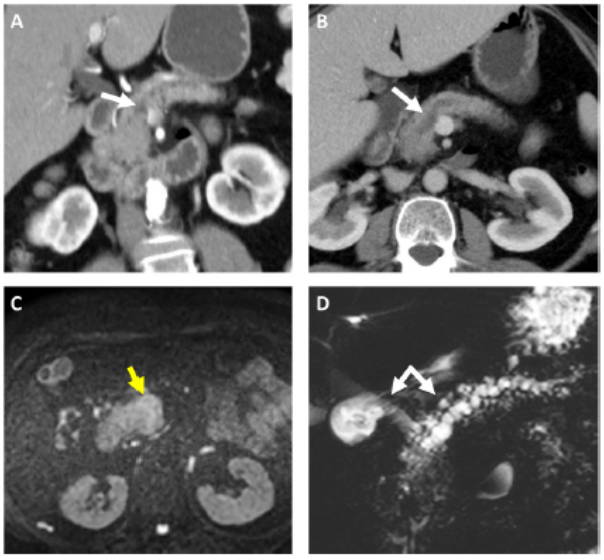


Fig. 3. Isodense PDAC. This patient presented with dilated main pancreatic duct (A and B, white arrows) and slightly dilated biliary tree, but a pancreatic tumor was not clearly seen on CT on both pancreatic (A) and portal venous (B) phases. MRI clearly identifies the obstructing tumor in the pancreatic head, as observed on DWI (C, yellow arrow) and a double duct sign on MRCP (D, white arrows).

2.2. Small and isoattenuating tumors

In 5.4–11% of cases, and most commonly with < 20 mm tumors, PDAC is isoattenuating: it does not stand out from the pancreatic parenchyma in the pancreatic or portal venous phases [26–29]. These tumors have been reported as a frequent cause of missed diagnosis for early PDAC, especially when found incidentally in imaging studies [5]. Indirect signs such as main pancreatic duct dilation upstream of an abrupt stenosis, a double duct sign, segmental pancreatic atrophy or faint enhancement are key to the diagnosis and should prompt further investigation [5,30]. This is also where a delayed acquisition can be very useful, as it has been shown to improve sensitivity for these lesions, which often enhance in delayed scans [29]. MRI is also helpful for detecting small and isoattenuating tumors (Fig. 3), with a reported sensitivity of 79.2% [28]. A reduced field-of-view DWI acquisition and MR perfusion techniques have been reported to improve image quality and pancreatic focal lesion characterization, and could therefore be useful in this context [31,32]. Another useful imaging technique for characterizing small and indeterminate tumors on CT is EUS, with a reported sensitivity of 87.3%, which can be improved with the use of contrast enhancement [20,33,34].

2.3. Diffuse tumoral infiltration and mass-forming pancreatitis

An uncommon diagnostic challenge is the diffuse neoplastic infiltration, mainly in the tail of the pancreas, without dilation of the main pancreatic duct [35]. The main differential diagnosis is autoimmune pancreatitis, which presents similar imaging findings. Likewise, mass-forming pancreatitis can mimic a neoplastic lesion and be impossible to differentiate from PDAC on CT. In both cases, magnetic resonance cholangiopancreatography (MRCP) may be useful, showing the "duct penetrating sign" - characteristic of benign lesions and enhanced with secretin administration [36,37]. Also, MRI can show multi-organ involvement in cases of autoimmune pancreatitis, often in the kidneys in the context of IgG4-related disease, facilitating this diagnosis (Fig. 4) [38,39]. Additional useful findings favoring auto-immune pancreatitis instead of PDAC include the typical diffuse enlargement with loss of

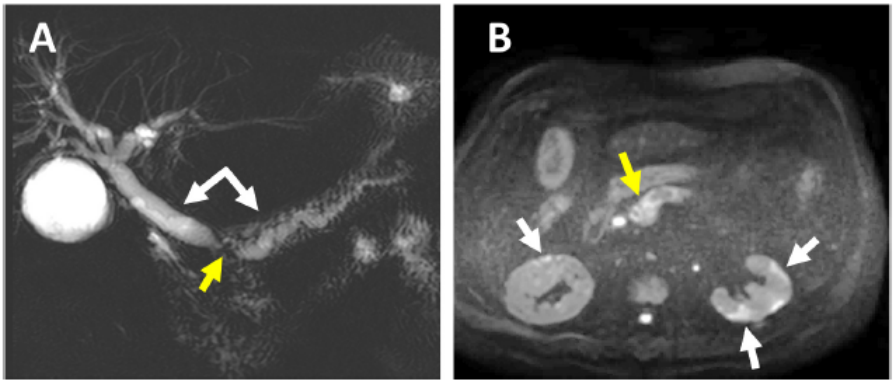


Fig. 4. Diagnostic problem-solving with MRI. This patient presented with dilated main pancreatic duct and biliary tree (A, white arrows), highly suspicious for a pancreatic head tumor (yellow arrow). However, DWI revealed not only a restricting pancreatic head (B, yellow arrow), but also areas of restriction in both kidneys (B, white arrows). These findings prompted the diagnosis of auto-immune pancreatitis, which was confirmed after a 2-week steroid trial.

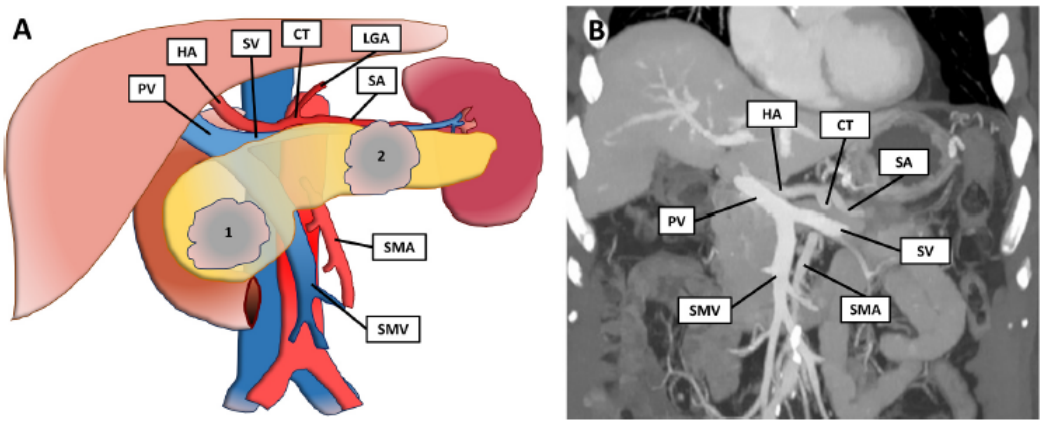


Fig. 5. (A) is a schematic representation of relevant anatomical structures for PDAC staging. If a tumor is located on the pancreatic head (1), a cephalic duodenopancreatectomy is performed, and if the tumor is located on the pancreatic body and/or tail (2), then a distal pancreatectomy is performed. More extensive tumors might require a total pancreatectomy. (B) is a coronal MIP displaying the relevant blood vessels for PDAC staging, an extremely useful tool for showcasing findings in multidisciplinary team meetings. CT: celiac trunk; HA: hepatic artery (comprises both common hepatic and hepatic proper); LGA: left gastric artery; PV: portal vein; SA: splenic artery; SMA: superior mesenteric artery; SMV: superior mesenteric vein; SV: splenic vein.

lobulation of pancreatic parenchyma (sausage-shape), homogeneous enhancement, absence of upstream main pancreatic duct dilatation, capsulelike rim and absence of vascular invasion[39,40].

3. Staging of PDAC

When deciding what treatment to offer a patient with PDAC, either resection, neoadjuvant therapy or palliative care, imaging plays the most central role. Patients' disease is initially staged as resectable, borderline resectable, locally advanced, or metastatic. This review will focus on the latest NCCN PDAC staging criteria, as it is the most widely used classification [6]. The goal is to obtain an R0 resection, which provides the best chance for patient survival, and the surgical procedure is dependent on tumor location, vascular and adjacent organ involvement.

3.1. Local and vascular staging

Vascular involvement is the major resectability determinant in PDAC and is best assessed with contrast-enhanced CT (Fig. 5). Multiplanar reformations (MPR) and maximum intensity projections (MIP) are extremely useful, both for diagnosis and for showcasing findings to the surgeon. The terms "abutment" and "encasement" refer to $\leq 180°$ and $> 180°$ tumoral contact with a blood vessel, respectively, the latter predicting the presence of vascular invasion [41–43]. Blood vessel deformity and the "teardrop sign", as well as occlusion, are also highly predictive of vascular invasion (Figs. 6 and 7) [44].

As summarized in Table 3, resectable tumors have no arterial contact, and no / limited venous contact (abutment). Patients in this category can be proposed for upfront surgery. Borderline resectable tumors include tumors with limited vascular involvement, or vascular involvement that can be surgically repaired. Patients with borderline resectable disease are offered neoadjuvant therapy; surgical resection can be later performed, depending on response to neoadjuvant therapy and local surgical expertise. Patients with locally advanced disease have extensive vascular involvement. These patients are offered systemic chemotherapy, chemoradiation, or inclusion in clinical trials. Depending on response assessment and performance status, resection surgery can still be performed after neoadjuvant therapy [3,6]. If disease progression is evident with vascular involvement precluding surgery or metastatic disease, then the best palliative care or inclusion in clinical trials are the remaining options.

Since being first introduced in 1997, the criteria for borderline resectable staging category have been updated over the years, reflecting accumulating evidence and international consensus [8,45]. These patients have limited vascular involvement and surgical resection is

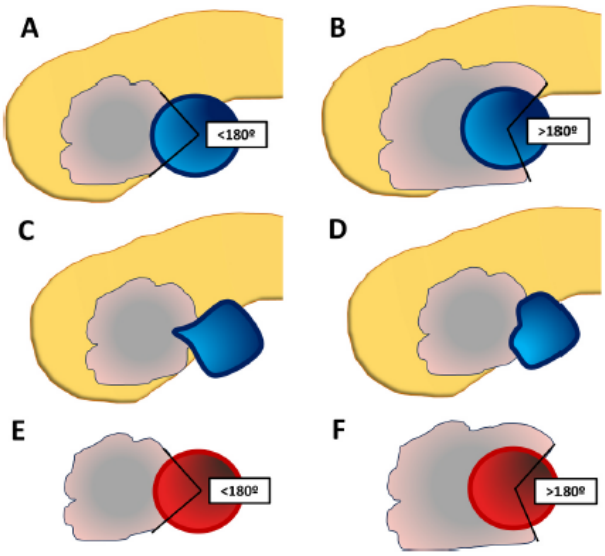


Fig. 6. Schematic representation of blood vessel involvement in PDAC staging. (A) tumor-vein contact ≤ 180° (abutment); (B) tumor-vein contact > 180° (encasement); (C) teardrop sign; (D) vessel contour deformity; (E) and (F) arterial abutment and encasement (≤ and > 180°), respectively.

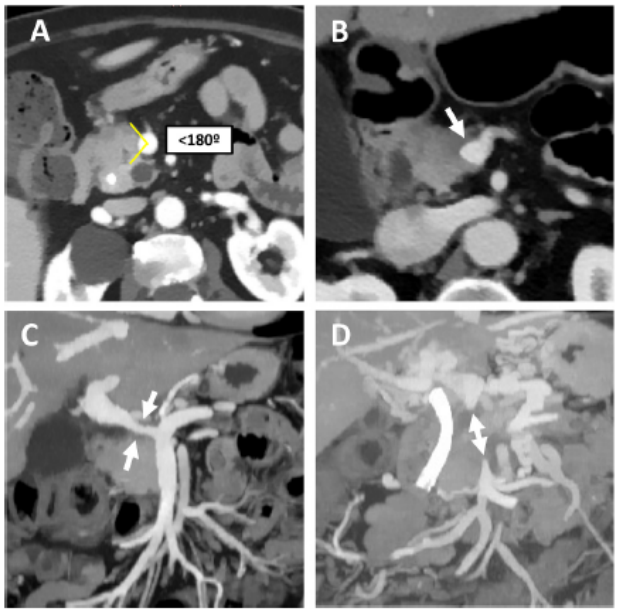


Fig. 7. Venous involvement in PDAC. (A) Tumor-superior mesenteric vein contact < 180° (abutment). (B) Teardrop sign of the superior mesenteric vein (arrow). (D) Portal vein stenosis and deformity (arrows). (D) Superior mesenteric vein occlusion (arrows).

possible, but a margin-free resection is unlikely, therefore benefiting clearly from neoadjuvant therapy. The definition of vascular involvement with objective criteria (vessel circumference involvement and contour irregularity) has contributed to a more standardized classification. More recently, the involvement of proximal jejunal branches was categorized as unresectable disease in 2017, but this involvement is not included in the latest versions [6,46]. This led to a reported improved accuracy in disease staging and better patient stratification [47]. It is important to be aware of the evolving nature of these staging criteria,

Table 3
NCCN V2.2023 resectability criteria adapted from [6].

Resectable	Arteries	No tumoral contact
	Veins	No tumoral contact / ≤ 180° PV or SMV contact without deformity
Borderline	Arteries	≤ 180° SMA or CT contact Limited CHA contact (not extending to its bifurcation nor the CT) Anatomical variant with arterial involvement allowing for surgical management
	Veins	≤ 180° PV or SMV contact with deformity > 180° PV or SMV contact but surgically repairable Tumoral contact with IVC
Unresectable	Arteries	> 180° SMA or CT contact; extensive HA involvement
	Veins	> 180° PV or SMV contact non-surgically repairable

CHA: common hepatic artery; CT: celiac trunk; IVC: inferior vena cava; HA: hepatic artery; NCCN: National Comprehensive Cancer Network; PV: portal vein; SMA: superior mesenteric artery; SMV: superior mesenteric vein. Abutment and encasement are considered synonyms with < 180° and > 180° tumoral contact, respectively.

with consequences both for clinical practice over time and for the validity of reported data, when comparing with current guidelines.

Vascular anatomical variants are common and can have surgical implications for PDAC [43,48–50]. Not only should replaced or accessory hepatic arteries be identified to avoid surgical complications, these variants can also provide surgical opportunities, when providing an alternative hepatic arterial supply without tumoral involvement (Fig. 8). Anatomical variants can also preclude surgery or determine a hepatic resection, especially if a replaced hepatic artery is involved by tumor and there is no collateral arterial inflow.

Celiac trunk stenosis, either due to atherosclerosis or arcuate ligament syndrome, can predispose patients to hepatic ischemia, as the collateral arterial flow to the liver is disrupted during surgery (Fig. 9) [51–53]. CT is the preferred method for diagnosing this condition, allowing preventive surgical procedures, such as arcuate ligament release and celiac artery stenting [43,54].

Besides the vascular staging, involvement of adjacent organs should be identified, most often the duodenum, stomach, left adrenal, left kidney, spleen and colon, as these will have to be resected during surgery if involved by the tumor [55]. Also, tumoral extension to the mesocolon, most often the transverse mesocolon, should be identified at this stage for surgical planning, possibly determining a colon resection.

Of mention, EUS has been reported to improve staging accuracy, especially when compared with older CT technology, identifying 14% unresectable patients previously staged as resectable on CT [56–58]. However, newer CT technology has improved diagnostic and staging accuracy, and comparative studies with EUS are not yet available.

3.2. Hepatic, peritoneal, and pulmonary staging

Liver metastases can be detected by CT, however with a relatively low sensitivity: 69% [59,60]. MRI is superior for this purpose, especially when performed with gadoxetic acid, with a reported sensitivity of 85% [60]. Furthermore, DWI has been reported to detect undiagnosed liver metastases on CT in 10–12.9% of patients and prevent futile surgeries in metastatic patients [61–63]. As such, it is recommended that liver staging is performed using MRI (Fig. 10). PET-CT has a reported 93% sensitivity in the detection of liver metastases for lesions > 1 cm, which is reduced to 70% when considering all lesion sizes [64].

There is no evidence determining the best timing for liver staging MRI (with or without gadoxetic acid) in the case of biliary obstruction, if before or after stent placement. Performing MRI before stent placement, will avoid artifacts in the case of metallic stents and allow better biliary anatomy depiction. Also, biliary stent placement may be associated with cholangitis, which may cause liver perfusion changes and course with small hepatic abscesses [65,66]. For these reasons, we perform hepatic

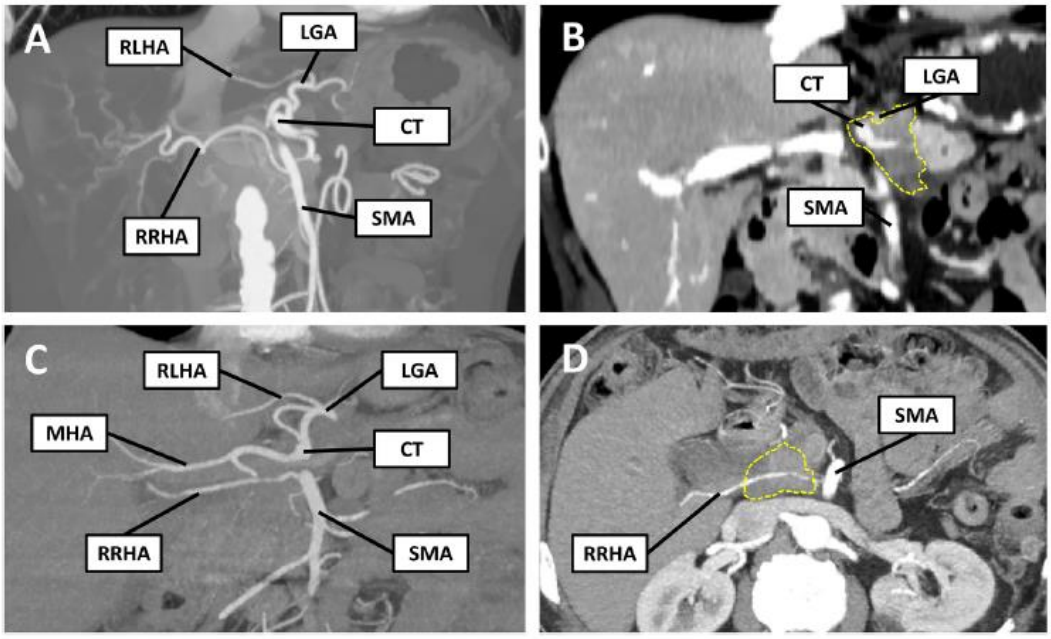


Fig. 8. Arterial variants with surgical implications. (A) depicts the anatomy of a patient with a replaced right hepatic artery (RRHA) originating from the superior mesenteric artery (SMA) and a replaced left hepatic artery (RLHA) originating from the left gastric artery (LGA). The celiac trunk (CT) was encased by the tumor, as represented in (B, dashed line). As arterial collaterals were present between both replaced hepatic arteries, a celiac trunk resection along with tumor resection were performed, and the patient maintained a preserved liver vascularization. (C) represents another patient with the following anatomy: RLHA from LGA, middle hepatic artery (MHA) from CT, and RRHA from SMA. The RRHA was encased by tumor, as shown in (D, dashed line). This allowed tumor resection along with the RRHA, after an embolization procedure for facilitating the development of collaterals.

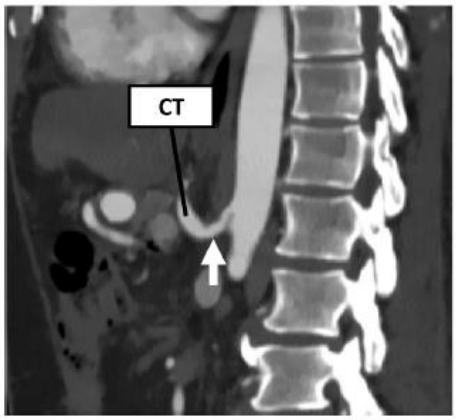


Fig. 9. Arcuate ligament syndrome. Proximal celiac trunk (CT) stenosis with a hooked appearance (arrow), with pos-stenotic dilatation.

staging MRI as soon as possible.

Finally, differentiating small hepatic abscesses from metastases can be a difficult task. Contrast-enhanced CT findings have been reported to help in this regard, favoring the diagnosis of abscesses: patchy parenchymal enhancement, perilesional hyperemia and, especially, arterial rim enhancement persistent through portal venous phase [67]. Dual-energy CT may improve on the technique's ability to distinguish both lesions [68]. DWI may also be helpful, as hepatic metastases tend to present lower ADC values at their periphery, when compared with abscesses [69].

Peritoneal metastases usually manifest as nodular lesions, detectable by both CT and MRI (Fig. 11). However, early peritoneal disease can be hard to identify, and evidence is lacking into imaging effectiveness for its diagnosis [70,71]. Staging laparoscopy can be performed for this purpose, and has been shown to be more sensitive than CT, but its usefulness has been debated due to poor cost-effectiveness when staging MRI is performed [72,73]. Nevertheless, recent data reporting high rates of positive staging laparoscopies has prompted some authors to advocate its use in the majority of patients prior to resection [74].

PDAC can also metastasize to the lung, but the usefulness of including chest CT in tumoral staging and follow-up has been debated [75,76]. Nevertheless, we include a chest CT in our staging protocol, which may serve as a baseline for comparison in future studies, should indeterminate or suspicious lung nodules be identified.

3.3. Lymph node staging

Lymph node staging is still poorly performed by imaging. CT has a reported sensitivity of only 14–44% for diagnosing nodal tumor infiltration when 10 mm short-axis is used as diagnostic criterion [77,78]. Combining size criteria with contour irregularity, heterogeneous signal intensity and/or density and increased number of visible nodes has been reported to improve sensitivity [78]. EUS has been reported to be superior in identifying suspicious lymph nodes in loco-regional and para-aortic locations, and is currently regarded as the most sensitive imaging technique for this purpose [57,58]. Nevertheless, it is not routinely included in lymph node staging recommendations [6]. Gallium-68-labeled fibroblast activation protein inhibitor PET-CT was reported to improve detection of pathologic lymph nodes in a preliminary study, but more data is needed before recommending its use [79]. A promising artificial intelligence model outperformed radiologists in lymph node staging using CT, while also providing prognostic information for patients [80]. Enlarged lymph nodes should be mentioned in the radiological CT or MRI report, especially when outside of loco-regional location, but this low diagnostic performance with current imaging methods must be kept in mind [81].

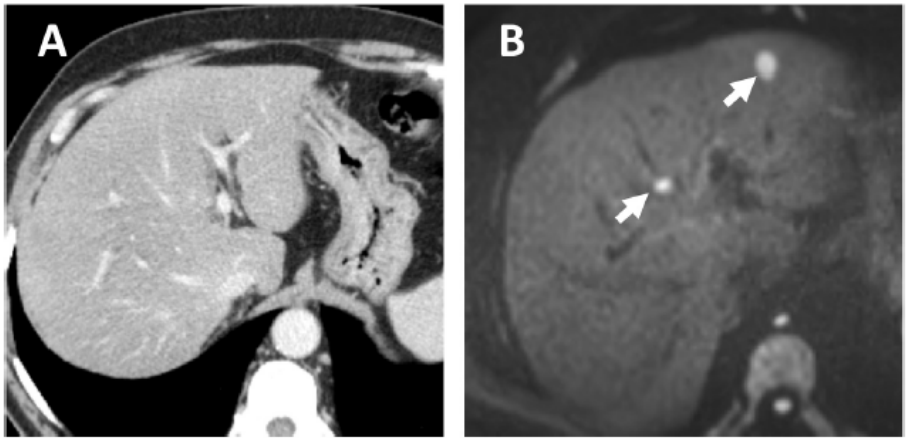


Fig. 10. Importance of MRI for hepatic staging. In a contrast-enhanced CT for PDAC staging (A), no liver lesions were found. The staging MRI clearly revealed hepatic metastases (arrows) with restricted diffusion on DWI (B).

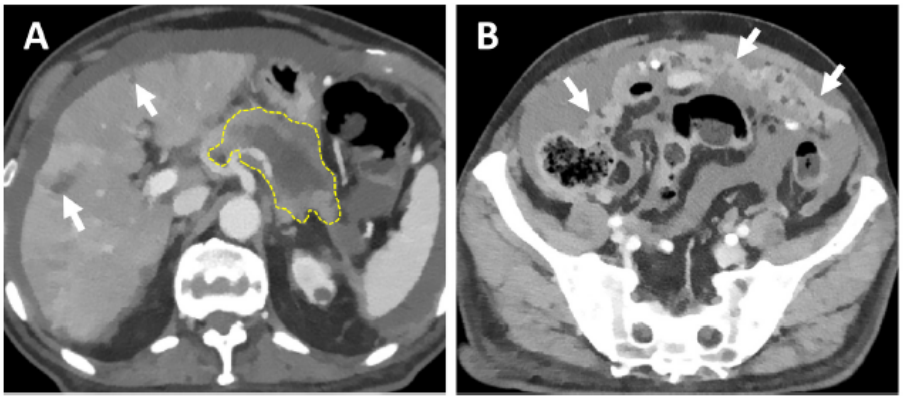


Fig. 11. Metastatic PDAC with peritoneal metastases. (A) reveals a bulky PDAC of the body and tail (dashed line), with hepatic metastases (arrows). There are also peritoneal metastases, as observed with an "omental cake" appearance in the pelvis (B, arrows).

3.4. Radiological structured report

The use of a radiological structured report is recommended, to provide a clear and standardized communication of imaging findings to surgeons and oncologists [6,55]. This also ensures that no relevant structures for tumor staging are forgotten or overlooked in the report. An example structured reporting template is suggested in Table 4, adapted from [55]. The reporting template should be tailored in each center to provide the multidisciplinary team with the information needed in an easily accessible way. Note that extensive descriptions of vascular involvement in patients with metastatic disease are usually not necessary, unless there is a specific motive for it, such as inclusion in a clinical trial.

3.5. Current issues with PDAC staging

Some aspects of the current widely used NCCN staging classification for PDAC have been debated [82]. Mainly, the dependence on strict anatomic criteria for defining treatment strategies for patients with PDAC, directed at surgical feasibility, often fails to consider disease biology.

Starting with anatomic staging issues, the 180° threshold can be insufficient for vascular staging, as the longitudinal extension of vessel involvement also determines surgical technique and has been shown to predict survival: patients with more than 20 mm of vascular involvement have a worse prognosis and may be candidates for neoadjuvant therapy [83]. Another issue is the involvement of the splenic artery which may fit in the resectable category, while the involvement of the celiac trunk, hepatic artery or superior mesenteric artery determine borderline resectable or locally advanced disease [82]. Patients may therefore be proposed for upfront surgery with a resectable although aggressive disease, missing potential survival benefits from neoadjuvant therapy. Finally, large tumor size, which is not category-defining for resectability, has also been associated with poor prognosis, and should be considered when deciding which treatment to offer a patient [84,85].

The presence of para-aortic lymph node metastases, which may easily be missed on imaging as previously discussed, is another predictor of poor prognosis [82,86–88]. Despite these diagnostic difficulties and the fact that they are not routinely removed on surgery, these nodes are considered metastatic disease, and adjuvant chemotherapy has been recommended for improving outcomes in these patients [89,90].

Surgical resection is not recommended for metastatic patients according to current guidelines; however, it is performed after neoadjuvant therapy in some institutions, for selected patients with oligometastatic disease. This has been reported to improve survival, but more evidence is needed before widespread acceptance [91–93].

Recurrence risk is also not sufficiently addressed in the anatomic classification. In a large series evaluating early recurrence, pre-operative risk factors were identified, including: CA 19–9 $>$ 210 U/mL, Charlson age-comorbidity index $\geq$ 4, tumor size $>$ 3 cm; post-operative risk

Table 4
Structured reporting template.

Pancreatic tumor	Location	*Head / Neck / Body / Tail*
	Size	*Largest axis; approximate measurement if ill-defined*
	MPD and biliary tree	*Dilated / Not dilated*
	Adjacent organ involvement	*NA / Describe involvement (stomach, adrenal, colon, etc.)*
Arteries	CT	*Free ≤ 180° / > 180° / Deformity / Occlusion (extension in mm) Mention stenosis or atherosclerosis*
	CHA	*Free ≤ 180° / > 180° / Deformity / Occlusion (extension in mm) Extension to CT or bifurcation*
	SA	*Free ≤ 180° / > 180° / Deformity / Occlusion (extension in mm)*
	SMA	*Free ≤ 180° / > 180° / Deformity / Occlusion (extension in mm)*
	SMA branches	*Free Mention involved branches (extension in mm)*
	Variant anatomy	*NA / Replaced CHA / Accessory RHA / Replaced RHA / Accessory LHA / Replaced LHA / Other**
	Variant involvement	*NA / Free / ≤ 180° / > 180° / Deformity / Occlusion**
Veins	PV	*Free ≤ 180° / > 180° / Deformity / Occlusion (extension in mm)*
	SMV	*Free ≤ 180° / > 180° / Deformity / Occlusion (extension in mm)*
	Collaterals	*NA / pancreatic head / hepatic hilum / mesenteric / LUQ*
Metastases	Liver	*Absent / Present / Indeterminate*
	Peritoneum	*Absent / Present / Indeterminate Ascites Absent / Present*
	Lung	*Absent / Present / Indeterminate*
Lymph nodes	If suspicious, mention location(s)	*NA / Peri-pancreatic / Hepatic hilum / Celiac / Aortocaval / Para-aortic / Splenic*
Other findings		*Free writing*

One or more options presented in *italics* should be chosen in each field according to imaging findings, and longitudinal extension of vessel involvement provided in millimeters. *Further description can be added at the end of the report, when variant anatomy or involvement cannot be adequately described in the template. CHA: common hepatic artery; CT: celiac trunk; LHA: left hepatic artery; LUQ: left upper quadrant; MPD: main pancreatic duct; NA: non-applicable; PV: portal vein; RHA: right hepatic artery; SA: splenic artery; SMA: superior mesenteric artery; SMV: superior mesenteric vein.

factors were also identified, including: poor tumor differentiation, microscopic lymphovascular invasion, lymph node ratio > 0.2, and CA 19–9 > 37 U/mL [94]. None of these are considered in the anatomic resection criteria. Furthermore, the inclusion of neoadjuvant therapy based on risk factors for early recurrence was shown to improve survival [95]. Local recurrence has additionally been associated with high rates of post-venous reconstruction thrombosis, rather than anatomic or technical factors, further demonstrating the relevance of disease biology in determining patient outcomes [96].

Management of patients with PDAC with resectable disease is also currently being discussed. Neoadjuvant therapy has been proposed in purely resectable patients, showing some improvement in disease-free survival in a small number of trials [97]. However, conflicting evidence showed no clear improvement in survival, and more data on this issue is needed before issuing favorable recommendations for clinical practice [98,99]. More recently, a randomised clinical trial found no survival benefit from the use of neoadjuvant therapy in resectable patients with PDAC, when compared to upfront resection, further disfavoring its use [100].

In summary, accumulating data tend to consider PDAC as a systemic disease and favor the use of neoadjuvant therapy even in selected high-risk resectable patients, while also selecting patients previously categorized as unresectable or even oligometastatic, as candidates for surgical resection with favorable outcomes. Patient management decisions should therefore be made in a multidisciplinary team setting, considering both the anatomic staging and additional prognostic factors.

3.6. Alternative staging classifications

Other staging classifications have been developed, including additional prognostic factors in the decision-making process. The MD Anderson Cancer Center developed a well-known classification incorporating anatomic criteria, tumor biology and patient performance status for patient categorization [101,102]. This type of classification has been used later in a consensus meeting to categorize borderline resectable and locally advanced patients in different types, according to anatomic, biological, and conditional factors [103]. Here, in addition to the anatomic classification (resectable, borderline resectable and locally advanced), biological factors (serum CA 19–9 >500 IU/mL and/or positive regional lymph node metastases) and conditional factors (performance status) were added for an integrative patient stratification.

Additionally, other classifications were developed based on anatomic criteria, but without such widespread use as the NCCN classification. These include the American Society of Clinical Oncology, Intergroup Alliance, and Americas Hepato-Pancreato-Biliary Association / Society of Surgical Oncology / Society for Surgery of the

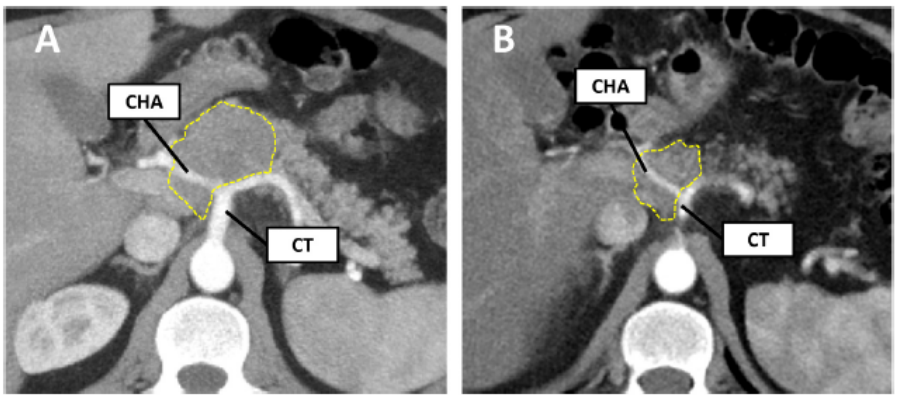


Fig. 12. Response to neoadjuvant therapy. (A) reveals a locally advanced PDAC (dashed line) with common hepatic artery (CHA) encasement up to the celiac trunk bifurcation (CT). After the completion of neoadjuvant chemotherapy, the tumor had reduced in size (B, dashed line), but maintained a long encasement of the CHA. The patient underwent surgery, with an R0 resection.

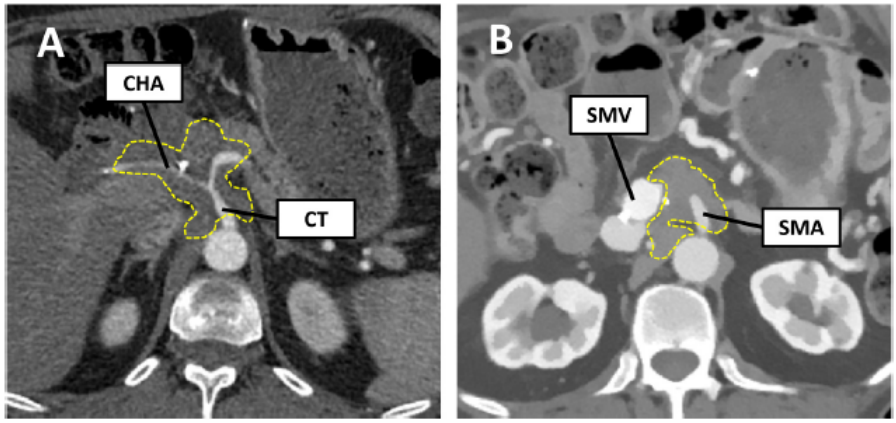


Fig. 13. Recurrence of PDAC. Two cases of local recurrence of PDAC (dashed lines), in (A) encasing the celiac trunk (CT) and common hepatic artery (CHA), and in (B) encasing the superior mesenteric artery (SMA) and invading the superior mesenteric vein (SMV) with a teardrop sign.

Alimentary Tract [7,104,105]. These classifications also use the resectable, borderline resectable and unresectable / locally advanced categories, but with different criteria, which were highlighted in a consensus meeting [103].

4. Response to neoadjuvant therapy

Assessing response to neoadjuvant therapy for PDAC is a difficult task in clinical practice. Tumor size criteria are not useful for this purpose, as the fibrotic tumoral stroma remains, even when a response has occurred in cancer cells [106–108]. The current methods for evaluating response to neoadjuvant therapy reside on tumoral markers evolution (serum CA19–9 concentration) and the absence of disease progression as evidenced by imaging studies [3,9,109]. If progression is not apparent – the pancreatic tumor is stable or has reduced in size, and tumor markers have not increased – then a response is presumed and the patient can be proposed for surgery, in the case of initial borderline or even locally advanced disease (Fig. 12). Also, standard criteria for vascular resectability based on the amount of tumor-vessel contact are not useful post-neoadjuvant therapy, and an improvement of tumor-vascular involvement is highly predictive of an R0 resection, even if partial [109]. Furthermore, the presence of tumor regression after neoadjuvant therapy was not correlated with survival, in a cohort of patients with R0 resections [110]. Disease extension as observed on CT should not just be disregarded, however. Smaller tumor size and reduction of arterial contact, as well as imaging scores based on arterial involvement and resectability status, performed both before and after neoadjuvant therapy, were correlated with probability of R0 resection [111,112].

Some studies have evaluated the role of DWI for response assessment, reporting a correlation of apparent diffusion coefficient (ADC) with histopathological response, but others have not found it useful [113–117]. The value of DWI in this context remains undetermined, and further studies are needed to provide recommendations for clinical practice [118].

The role of FDG-PET for neoadjuvant therapy response assessment has also been evaluated. Both CT and MRI FDG-PET's metabolic response has been reported to be associated with pathologic response, being superior than CA19–9 for this purpose [119,120]. FDG-PET MRI added to contrast-enhanced CT showed improved accuracy for determining resectability status when compared with contras-enhanced CT alone, in a retrospective study [121]. A recent systematic review reported FDG-PET's potential for predicting and assessing response to neoadjuvant therapy; however, the small numbers of patients enrolled in each study and methodological heterogeneity prompt the need for well-designed prospective trials [122].

Recent developments in molecular imaging provided potential biomarkers for response to neoadjuvant therapy evaluation, as well as improving diagnostic and staging accuracy, with encouraging results [123]. However, these require validation and thus cannot yet be recommended for clinical practice.

Considering current limited tools for response assessment, the therapeutic decision after neoadjuvant therapy should always be made by a multidisciplinary team, taking into account imaging, biochemical and patient fitness data. The surgical decision is heavily dependent on the surgical team expertise, especially in cases of initially advanced disease or extensive vascular involvement [3,6].

5. Patient surveillance after resection

First, some important issues regarding pathologic assessment of PDAC resection margin should be discussed. The R0 definition for PDAC resection has been debated, and controversy regarding microscopic margin involvement has contributed to variability in reported R1 rates [124–126]. Although UICC's classification considers R0 as absence of tumor cells at the resection margin, a free resection margin of ≥ 1 mm defining R0 is also frequently used, and was associated with better survival when compared with < 1 mm [127,128]. Despite this, in the presence of lymph node positive disease, recurrence patterns were reportedly similar for both R0 and R1 patients [129]. Also, free margins larger than 1.5 mm have been reported to correlate with survival, as explained by the dispersed growth pattern of PDAC [125,130]. Other issues including challenges in specimen grossing and sampling, and the variable R0 definitions used in published literature, have been considered as important factors undermining the data quality of reported clinical outcomes of PDAC resection [125].

Evidence for recommending specific surveillance methods after PDAC resection is lacking, and the value of surveillance has been debated [131,132]. Nevertheless, patients undergoing post-resection surveillance have been reported to have improved detection of disease recurrence at asymptomatic stages, were more likely to receive treatment for the recurrence and presented longer overall survival [133,134]. A tumoral recurrence is usually found in the surgical bed, in the mesenteric root or the pancreatic remnant (Fig. 13). Local perivascular densification is common post-resection; however, a perivascular densification increasing in size in serial imaging or leading to a *de novo* change in the caliber or regularity of the vessel should be considered suspicious for local recurrence [135]. Distant recurrence is most commonly found in the liver or lungs [136]. A surveillance scheme including serum CA19–9 and CT (chest, abdomen and pelvis) every 3–6 months for 2 years after surgical resection has been recommended, and is followed in our institution [6]. MRI is usually not included in a surveillance setting but can be used for disease staging if a recurrence is

suspected.

6. Conclusion

Imaging plays a central role in all stages of patient management for PDAC: diagnosis, staging, response to neoadjuvant therapy and post-surgical surveillance. Diagnostic and staging performance of current imaging modalities is high; however, there are unresolved issues when staging patients and assessing response to neoadjuvant therapy, and evidence is lacking for dedicated patient surveillance protocols. Nevertheless, an experienced radiologist remains essential in the multidisciplinary team caring for patients with PDAC.

CRediT authorship contribution statement

Matos Celso: Writing – review & editing, Methodology, Conceptualization. **Marques Rui Mateus:** Writing – review & editing, Methodology. **Santiago Inês:** Writing – review & editing. **Andrade Luísa:** Writing – review & editing, Methodology, Investigation, Data curation, Conceptualization. **Bilreiro Carlos:** Writing – review & editing, Writing – original draft, Visualization, Resources, Methodology, Formal analysis, Data curation, Conceptualization.

Declaration of Competing Interest

The authors declare that they have no known competing financial interests or personal relationships that could have appeared to influence the work reported in this paper.

Acknowledgements

This work did not receive any specific grant from funding agencies in the public, commercial, or not-for-profit sectors.

References

[1] R.L. Siegel, K.D. Miller, H.E. Fuchs, A. Jemal, Cancer statistics, 2022, Ca. Cancer J. Clin. 72 (2022) 7–33, https://doi.org/10.3322/CAAC.21708.
[2] M. Ducreux, A.S. Cuhna, C. Caramella, A. Hollebecque, P. Burtin, D. Goéré, T. Seufferlein, K. Haustermans, J.L. Van Laethem, T. Conroy, D. Arnold, Cancer of the pancreas: ESMO clinical practice guidelines for diagnosis, treatment and follow-up, Ann. Oncol. . J. Eur. Soc. Med. Oncol. 26 (Suppl 5) (2015) v56–v68, https://doi.org/10.1093/ANNONC/MDV295.
[3] O. Strobel, J. Neoptolemos, D. Jäger, M.W. Büchler, Optimizing the outcomes of pancreatic cancer surgery, Nat. Rev. Clin. Oncol. 16 (2019) 11–26, https://doi.org/10.1038/S41571-018-0112-1.
[4] T.A. Sohn, C.J. Yeo, J.L. Cameron, L. Koniaris, S. Kaushal, R.A. Abrams, P. K. Sauter, J. Coleman, R.H. Hruban, K.D. Lillemoe, Resected adenocarcinoma of the pancreas-616 patients: results, outcomes, and prognostic indicators, J. Gastrointest. Surg. 4 (2000) 567–579, https://doi.org/10.1016/S1091-255X(00)80105-5.
[5] J.D. Kang, S.E. Clarke, A.F. Costa, Factors associated with missed and misinterpreted cases of pancreatic ductal adenocarcinoma, Eur. Radiol. 31 (2021) 2422–2432, https://doi.org/10.1007/S00330-020-07307-5.
[6] M.A. Tempero, M.P. Mokenge, A.B. Benson III, R.H. Lurie, D.B. Cardin, E. Gabriela Chiorean, F.A. Hutchinson Cancer Center Jared Christensen, V. Chung, B. Czito, M. Del Chiaro, T.R. Donahue, E. Dotan, C. Fountzilas, E.S. Glazer, J. Hardacre, W.G. Hawkins, K. Klute, A.H. Ko, J.W. Kunstman, N. LoConte, A.M. Lowy, A. Masood, L. Nardo, ϕ Φ, J. Obando, P.M. Polanco, S. Reddy, M. Reyngold, C. Scaife, J. Shen, M.J. Truty, C. Vollmer Jr, R.A. Wolff, B.M. Wolpin, N. Susan Darlow, S. Kurtoglu Lubin, M.R. Beth McCullough, NCCN Guidelines Version 2.2023 Pancreatic Adenocarcinoma, (2023). https://www.nccn.org/home/member- (Accessed 19 September 2023).
[7] A.A. Khorana, M. Shapiro, P.B. Mangu, J. Berlin, A. Engebretson, T.S. Hong, A. Maitra, M.H.G. Katz, S.G. Mohile, M. Mumber, R. Schulick, S. Urba, H.J. Zeh, Potentially curable pancreatic cancer: American society of clinical oncology clinical practice guideline update, J. Clin. Oncol. 35 (2017) 2324–2328, https://doi.org/10.1200/JCO.2017.72.4948.
[8] G.R. Varadhachary, E.P. Tamm, J.L. Abbruzzese, H.Q. Xiong, C.H. Crane, H. Wang, J.E. Lee, P.W.T. Pisters, D.B. Evans, R.A. Wolff, Borderline resectable pancreatic cancer: definitions, management, and role of preoperative therapy, Ann. Surg. Oncol. 13 (2006) 1035–1046, https://doi.org/10.1245/ASO.2006.08.011.
[9] M. Zins, C. Matos, C. Cassinotto, Pancreatic adenocarcinoma staging in the era of preoperative chemotherapy and radiation therapy, Radiology 287 (2018) 374–390, https://doi.org/10.1148/RADIOL.2018171670.
[10] C. Zaharia, K. Søreide, Call for better response evaluation after neoadjuvant therapy in pancreatic cancer, Br. J. Surg. 110 (2023) 294–296, https://doi.org/10.1093/BJS/ZNAC452.
[11] J. Xu, H. Zhan, F. Li, S. Hu, L. Wang, Neoadjuvant therapy for pancreatic cancer: limitations and advances of response assessment (Review), Oncol. Rep. 45 (2021), https://doi.org/10.3892/OR.2021.7977.
[12] E.V. Soloff, M.M. Al-Hawary, T.S. Desser, E.K. Fishman, R.M. Minter, M. Zins, Imaging assessment of pancreatic cancer resectability after neoadjuvant therapy: AJR expert panel narrative review, Ajr. Am. J. Roentgenol. 218 (2022) 570–581, https://doi.org/10.2214/AJR.21.26931.
[13] A. Dallongeville, L. Corno, S. Silvera, I. Boulay-Coletta, M. Zins, Initial diagnosis and staging of pancreatic cancer including main differentials, Semin. Ultrasound, CT Mri. 40 (2019) 436–468, https://doi.org/10.1053/J.SULT.2019.08.001.
[14] N. El Kayal, S. Lennartz, S. Ekdawi, J. Holz, K. Slebocki, S. Haneder, C. Wybranski, A. Mohallel, M. Eid, H. Grüll, T. Persigehl, J. Borggrefe, D. Maintz, C. Heneweer, Value of spectral detector computed tomography for assessment of pancreatic lesions, Eur. J. Radiol. 118 (2019) 215–222, https://doi.org/10.1016/J.EJRAD.2019.07.016.
[15] L. Beer, M. Toepker, A. Ba-Ssalamah, C. Schestak, A. Dutschke, M. Schindl, A. Wressnegger, H. Ringl, P. Apfaltrer, Objective and subjective comparison of virtual monoenergetic vs. polychromatic images in patients with pancreatic ductal adenocarcinoma, Eur. Radiol. 29 (2019), https://doi.org/10.1007/S00330-019-06116-9.
[16] J.A. Decker, J. Becker, M. Härting, B. Jehs, F. Risch, L. Canalini, C. Wollny, C. Scheurig-Muenkler, T. Kroencke, F. Schwarz, S. Bette, Optimal conspicuity of pancreatic ductal adenocarcinoma in virtual monochromatic imaging reconstructions on a photon-counting detector CT: comparison to conventional MDCT, Abdom. Radiol. 49 (2023) 103–116, https://doi.org/10.1007/S00261-023-04042-5/FIGURES/6.
[17] B.M. Karlson, A. Ekbom, P.G. Lindgren, V. Källskog, J. Rastad, Abdominal US for diagnosis of pancreatic tumor: prospective cohort analysis, Radiology 213 (1999) 107–111, https://doi.org/10.1148/RADIOLOGY.213.1.R99OC25107.
[18] L.C. Chu, M.G. Goggins, E.K. Fishman, Diagnosis and detection of pancreatic cancer, Cancer J. (U. S.) 23 (2017) 333–342, https://doi.org/10.1097/PPO.0000000000000290.
[19] A.P. Rijkers, R. Valkema, H.J. Duivenvoorden, C.H.J. Van Eijck, Usefulness of F-18-fluorodeoxyglucose positron emission tomography to confirm suspected pancreatic cancer: a meta-analysis, Eur. J. Surg. Oncol. 40 (2014) 794–804, https://doi.org/10.1016/J.EJSO.2014.03.016.
[20] A. Zakaria, B. Al-Share, J.B. Klapman, A. Dam, The role of endoscopic ultrasonography in the diagnosis and staging of pancreatic cancer, Cancers 14 (2022), https://doi.org/10.3390/CANCERS14061373.
[21] J. DeWitt, B.M. Devereaux, G.A. Lehman, S. Sherman, T.F. Imperiale, Comparison of endoscopic ultrasound and computed tomography for the preoperative evaluation of pancreatic cancer: a systematic review, Clin. Gastroenterol. Hepatol. 4 (2006) 717–725, https://doi.org/10.1016/J.CGH.2006.02.020.
[22] K.T. Bae, Intravenous contrast medium administration and scan timing at CT: considerations and approaches, Radiology 256 (2010) 32–61, https://doi.org/10.1148/RADIOL.10090908.
[23] L. Loizou, N. Albiin, B. Leidner, E. Axelsson, M.A. Fischer, A. Grigoriadis, M. Del Chiaro, R. Segersvärd, C. Verbeke, A. Sundin, N. Kartalis, Multidetector CT of pancreatic ductal adenocarcinoma: Effect of tube voltage and iodine load on tumour conspicuity and image quality, Eur. Radiol. 26 (2016) 4021–4029, https://doi.org/10.1007/S00330-016-4273-Y.
[24] D. Placido, B. Yuan, J.X. Hjaltelin, C. Zheng, A.D. Haue, P.J. Chmura, C. Yuan, J. Kim, R. Umeton, G. Antell, A. Chowdhury, A. Franz, L. Brais, E. Andrews, D. S. Marks, A. Regev, S. Ayandeh, M.T. Brophy, N.V. Do, P. Kraft, B.M. Wolpin, M. H. Rosenthal, N.R. Fillmore, S. Brunak, C. Sander, A deep learning algorithm to predict risk of pancreatic cancer from disease trajectories, 2023 295, Nat. Med. 29 (2023) 1113–1122, https://doi.org/10.1038/s41591-023-02332-5.
[25] K. Cao, Y. Xia, J. Yao, X. Han, L. Lambert, T. Zhang, W. Tang, G. Jin, H. Jiang, X. Fang, I. Nogues, X. Li, W. Guo, Y. Wang, W. Fang, M. Qiu, Y. Hou, T. Kovarnik, M. Vocka, Y. Lu, Y. Chen, X. Chen, Z. Liu, J. Zhou, C. Xie, R. Zhang, H. Lu, G. D. Hager, A.L. Yuille, L. Lu, C. Shao, Y. Shi, Q. Zhang, T. Liang, L. Zhang, J. Lu, Large-scale pancreatic cancer detection via non-contrast CT and deep learning, 2023 2912, Nat. Med. 29 (2023) 3033–3043, https://doi.org/10.1038/s41591-023-02640-w.
[26] R.W. Prokesch, L.C. Chow, C.F. Beaulieu, R. Bammer, R.B. Jeffrey, Isoattenuating pancreatic adenocarcinoma at multi-detector row CT: secondary signs, Radiology 224 (2002) 764–768, https://doi.org/10.1148/RADIOL.2243011284.
[27] S. Gangi, J.G. Fletcher, M.A. Nathan, J.A. Christensen, W.S. Harmsen, B. S. Crownhart, S.T. Chari, Time interval between abnormalities seen on CT and the clinical diagnosis of pancreatic cancer: retrospective review of CT scans obtained before diagnosis, Ajr. Am. J. Roentgenol. 182 (2004) 897–903, https://doi.org/10.2214/AJR.182.4.1820897.
[28] J.H. Kim, S.H. Park, E.S. Yu, M.H. Kim, J. Kim, J.H. Byun, S.S. Lee, H.J. Hwang, J. Y. Hwang, S.S. Lee, M.G. Lee, Visually isoattenuating pancreatic adenocarcinoma at dynamic-enhanced CT: frequency, clinical and pathologic characteristics, and diagnosis at imaging examinations, Radiology 257 (2010) 87–96, https://doi.org/10.1148/RADIOL.10100015/-/DC1.
[29] Y. Fukukura, Y. Kumagae, Y. Fujisaki, R. Yamagishi, S. Nakamura, J. Kamizono, M. Nakajo, K. Kamimura, H. Nagano, K. Takumi, T. Yoshiura, Adding delayed phase images to dual-phase contrast-enhanced CT increases sensitivity for small

pancreatic ductal adenocarcinoma, Ajr. Am. J. Roentgenol. 217 (2021) 888–897, https://doi.org/10.2214/AJR.20.25430.
[30] F. Toshima, R. Watanabe, D. Inoue, N. Yoneda, T. Yamamoto, N. Sasahira, T. Sasaki, M. Matsuyama, K. Minehiro, U. Tateishi, T. Gabata, Ct abnormalities of the pancreas associated with the subsequent diagnosis of clinical stage i pancreatic ductal adenocarcinoma more than 1 year later: a case-control study, Am. J. Roentgenol. 217 (2021) 1353–1364, https://doi.org/10.2214/AJR.21.26014/SUPPL_FILE/12_21_26014_SUPPL.PDF.
[31] F. Donati, C. Casini, R. Cervelli, R. Morganti, P. Boraschi, Diffusion-weighted MRI of solid pancreatic lesions: comparison between reduced field-of-view and large field-of-view sequences, Eur. J. Radiol. 143 (2021) 109936, https://doi.org/10.1016/J.EJRAD.2021.109936.
[32] F. Donati, P. Boraschi, R. Cervelli, F. Pacciardi, C. Lombardo, U. Boggi, F. Falaschi, D. Caramella, 3 T MR perfusion of solid pancreatic lesions using dynamic contrast-enhanced DISCO sequence: usefulness of qualitative and quantitative analyses in a pilot study, Magn. Reson. Imaging 59 (2019) 105–113, https://doi.org/10.1016/J.MRI.2019.03.001.
[33] W. Wang, A. Shpaner, S.G. Krishna, W.A. Ross, M.S. Bhutani, E.P. Tamm, G. S. Raju, L. Xiao, R.A. Wolff, J.B. Fleming, J.H. Lee, Use of EUS-FNA in diagnosing pancreatic neoplasm without a definitive mass on CT, Gastrointest. Endosc. 78 (2013) 73–80, https://doi.org/10.1016/J.GIE.2013.01.040.
[34] M. Kitano, M. Kudo, K. Yamao, T. Takagi, H. Sakamoto, T. Komaki, K. Kamata, H. Imai, Y. Chiba, M. Okada, T. Murakami, Y. Takeyama, Characterization of small solid tumors in the pancreas: the value of contrast-enhanced harmonic endoscopic ultrasonography, Am. J. Gastroenterol. 107 (2012) 303–310, https://doi.org/10.1038/AJG.2011.354.
[35] Y.J. Choi, J.H. Byun, J.Y. Kim, M.H. Kim, S.J. Jang, H.K. Ha, M.G. Lee, Diffuse pancreatic ductal adenocarcinoma: characteristic imaging features, Eur. J. Radiol. 67 (2008) 321–328, https://doi.org/10.1016/j.ejrad.2007.07.010.
[36] T. Ichikawa, H. Sou, T. Araki, A.S. Arbab, T. Yoshikawa, K. Ishigame, H. Haradome, J. Hachiya, Duct-penetrating sign at MRCP: usefulness for differentiating inflammatory pancreatic mass from pancreatic carcinomas, Radiology 221 (2001) 107–116, https://doi.org/10.1148/RADIOL.2211001157.
[37] G. Carbognin, V. Girardi, C. Biasiutti, L. Camera, R. Manfredi, L. Frulloni, J. J. Hermans, R. Pozzi Mucelli, Autoimmune pancreatitis: imaging findings on contrast-enhanced MR, MRCP and dynamic secretin-enhanced MRCP, Radiol. Med. 114 (2009) 1214–1231, https://doi.org/10.1007/S11547-009-0452-0.
[38] A.A. Pozdzik, C. Matos, S. Rorive, I. Brocheriou, M. Delhaye, J.L. Nortier, Diffusion-weighted magnetic resonance imaging: a non-nephrotoxic prompt assessment of kidney involvement in IgG4-related disease, Kidney Int 85 (2014) 981, https://doi.org/10.1038/KI.2013.540.
[39] N. Hafezi-Nejad, V.K. Singh, C. Fung, N. Takahashi, A. Zaheer, MR imaging of autoimmune pancreatitis, Magn. Reson. Imaging Clin. N. Am. 26 (2018) 463–478, https://doi.org/10.1016/j.mric.2018.03.008.
[40] S.Y. Choi, S.H. Kim, T.W. Kang, K.D. Song, H.J. Park, Y.H. Choi, Differentiating mass-forming autoimmune pancreatitis from pancreatic ductal adenocarcinoma on the basis of contrast-enhanced MRI and DWI findings, Am. J. Roentgenol. 206 (2016) 291–300, https://doi.org/10.2214/AJR.15.14974/ASSET/IMAGES/LARGE/02_15_14974_05.JPEG.
[41] H.S. Tran Cao, A. Balachandran, H. Wang, G.M. Nogueras-González, C.E. Bailey, J.E. Lee, P.W.T. Pisters, D.B. Evans, G. Varadhachary, C.H. Crane, T.A. Aloia, J. N. Vauthey, J.B. Fleming, M.H.G. Katz, Radiographic tumor-vein interface as a predictor of intraoperative, pathologic, and oncologic outcomes in resectable and borderline resectable pancreatic cancer, J. Gastrointest. Surg. 18 (2014) 269–278, https://doi.org/10.1007/S11605-013-2374-3.
[42] D.S.K. Lu, H.A. Reber, R.M. Krasny, B.M. Kadell, J. Sayre, Local staging of pancreatic cancer: criteria for unresectability of major vessels as revealed by pancreatic-phase, thin-section helical CT, Ajr. Am. J. Roentgenol. 168 (1997) 1439–1443, https://doi.org/10.2214/AJR.168.6.9168704.
[43] A.M. Zaky, C.L. Wolfgang, M.J. Weiss, A.A. Javed, E.K. Fishman, A. Zaheer, Tumor-vessel relationships in pancreatic ductal adenocarcinoma at multidetector CT: different classification systems and their influence on treatment planning, Radiographics 37 (2017) 93–112, https://doi.org/10.1148/RG.2017160054.
[44] T.J. Hough, V. Raptopoulos, B. Siewert, J.B. Matthews, Teardrop superior mesenteric vein: CT sign for unresectable carcinoma of the pancreas, Ajr. Am. J. Roentgenol. 173 (1999) 1509–1512, https://doi.org/10.2214/AJR.173.6.10584793.
[45] M.P. Malafa, Defining borderline resectable pancreatic cancer: emerging consensus for an old challenge, J. Natl. Compr. Canc. Netw. 13 (2015) 501–504, https://doi.org/10.6004/JNCCN.2015.0068.
[46] M.A. Tempero, M.P. Malafa, M. Al-Hawary, H. Asbun, A. Bain, S.W. Behrman, B. Al Benson, E. Binder, D.B. Cardin, C. Cha, E.G. Chiorean, V. Chung, B. Czito, M. Dillhoff, E. Dotan, C.R. Ferrone, J. Hardacre, W.G. Hawkins, J. Herman, A. H. Ko, S. Komanduri, A. Koong, N. LoConte, A.M. Lowy, C. Moravek, E. K. Nakakura, E.M. O'Reilly, J. Obando, S. Reddy, C. Scaife, S. Thayer, C. D. Weekes, R.A. Wolff, B.M. Wolpin, J. Burns, S. Darlow, Pancreatic adenocarcinoma, version 2.2017, NCCN clinical practice guidelines in oncology, J. Natl. Compr. Canc. Netw. 15 (2017) 1028–1061, https://doi.org/10.6004/JNCCN.2017.0131.
[47] S.J. Park, S. Jang, J.K. Han, H. Kim, W. Kwon, J.Y. Jang, K.B. Lee, H. Kim, D. H. Lee, Preoperative assessment of the resectability of pancreatic ductal adenocarcinoma on CT according to the NCCN guidelines focusing on SMA/SMV branch invasion, Eur. Radiol. 31 (2021) 6889–6897, https://doi.org/10.1007/S00330-021-07847-4/FIGURES/3.
[48] P.J. Shukla, S.G. Barreto, A. Kulkarni, G. Nagarajan, A. Fingerhut, Vascular anomalies encountered during pancreatoduodenectomy: do they influence outcomes? Ann. Surg. Oncol. 17 (2010) 186–193, https://doi.org/10.1245/S10434-009-0757-1.
[49] F. Yang, J. Long, D.L. Fu, C. Jin, X.J. Yu, J. Xu, Q.X. Ni, Aberrant hepatic artery in patients undergoing pancreaticoduodenectomy, Pancreatology 8 (2008) 50–54, https://doi.org/10.1159/000114867.
[50] P. Appanraj, A.P. Mathew, D. Kandasamy, M. Venugopal, CT reporting of relevant vascular variations and its implication in pancreatoduodenectomy, Abdom. Radiol. 46 (2021) 3935–3945, https://doi.org/10.1007/s00261-021-02983-3.
[51] S. Gaujoux, A. Sauvanet, M.P. Vullierme, A. Cortes, S. Dokmak, A. Sibert, V. Vilgrain, J. Belghiti, Ischemic complications after pancreaticoduodenectomy: incidence, prevention, and management, Ann. Surg. 249 (2009) 111–117, https://doi.org/10.1097/SLA.0B013E3181930249.
[52] I. Kurosaki, K. Hatakeyama, K.E. Nihei, M. Oyamatsu, Celiac axis stenosis in pancreaticoduodenectomy, J. Hepatobiliary. Pancreat. Surg. 11 (2004) 119–124, https://doi.org/10.1007/S00534-003-0871-6.
[53] J.M. Farma, J.P. Hoffman, Nonneoplastic celiac axis occlusion in patients undergoing pancreaticoduodenectomy, Am. J. Surg. 193 (2007) 341–344, https://doi.org/10.1016/J.AMJSURG.2006.09.027.
[54] K.M. Horton, M.A. Talamini, E.K. Fishman, Median arcuate ligament syndrome: evaluation with CT angiography, Radiographics 25 (2005) 1177–1182, https://doi.org/10.1148/RG.255055001.
[55] M.M. Al-Hawary, I.R. Francis, S.T. Chari, E.K. Fishman, D.M. Hough, D.S. Lu, M. Macari, A.J. Megibow, F.H. Miller, K.J. Mortele, N.B. Merchant, R.M. Minter, E.P. Tamm, D.V. Sahani, D.M. Simeone, Pancreatic ductal adenocarcinoma radiology reporting template: consensus statement of the Society of Abdominal Radiology and the American Pancreatic Association, Radiology 270 (2014) 248–260, https://doi.org/10.1148/RADIOL.13131184.
[56] P.D. James, Z.W. Meng, M. Zhang, P.J. Belletrutti, R. Mohamed, W. Ghali, D. J. Roberts, G. Martel, S.J. Heitman, The incremental benefit of EUS for identifying unresectable disease among adults with pancreatic adenocarcinoma: a meta-analysis, PLoS One 12 (2017), https://doi.org/10.1371/JOURNAL.PONE.0173687.
[57] Z. Kala, V. Válek, J. Hlavsa, K. Hana, A. Váňová, The role of CT and endoscopic ultrasound in pre-operative staging of pancreatic cancer, Eur. J. Radiol. 62 (2007) 166–169, https://doi.org/10.1016/J.EJRAD.2007.01.039.
[58] H. Nawaz, C. Yi-Fan, J. Kloke, A. Khalid, K. McGrath, D. Landsittel, G. I. Papachristou, Performance characteristics of endoscopic ultrasound in the staging of pancreatic cancer: a meta-analysis, JOP 14 (2013) 484–497, https://doi.org/10.6092/1590-8577/1512.
[59] I. Somers, S. Bipat, Contrast-enhanced CT in determining resectability in patients with pancreatic carcinoma: a meta-analysis of the positive predictive values of CT, Eur. Radiol. 27 (2017) 3408–3435, https://doi.org/10.1007/S00330-016-4708-5.
[60] U. Motosugi, T. Ichikawa, H. Morisaka, H. Sou, A. Muhi, K. Kimura, K. Sano, T. Araki, Detection of pancreatic carcinoma and liver metastases with gadoxetic acid-enhanced MR imaging: comparison with contrast-enhanced multi-detector row CT, Radiology 260 (2011) 446–453, https://doi.org/10.1148/RADIOL.11103548.
[61] A.M. Marion-Audibert, M.P. Vullierme, M. Ronot, J.Y. Mabrut, A. Sauvanet, M. Zins, M. Cuilleron, A. Sa-Cunha, P. Lévy, A. Rode, Routine MRI with DWI sequences to detect liver metastases in patients with potentially resectable pancreatic ductal carcinoma and normal liver CT: a prospective multicenter study, Ajr. Am. J. Roentgenol. 211 (2018) W217–W225, https://doi.org/10.2214/AJR.18.19640.
[62] K. Holzapfel, C. Reiser-Erkan, A.A. Fingerle, M. Erkan, M.J. Eiber, E.J. Rummeny, H. Friess, J. Kleeff, J. Gaa, Comparison of diffusion-weighted MR imaging and multidetector-row CT in the detection of liver metastases in patients operated for pancreatic cancer, Abdom. Imaging 36 (2011) 179–184, https://doi.org/10.1007/S00261-010-9633-5.
[63] S. Altmayer, L.M. Armelin, J.S. Pereira, L.V. Carvalho, J. Tse, P. Balthazar, M. Z. Francisco, G. Watte, B. Hochhegger, MRI with DWI improves detection of liver metastasis and selection of surgical candidates with pancreatic cancer: a systematic review and meta-analysis, Eur. Radiol. 34 (2024), https://doi.org/10.1007/S00330-023-10069-5.
[64] H. Duan, L. Baratto, A. Iagaru, The role of PET/CT in the imaging of pancreatic neoplasms, Semin. Ultrasound Ct. Mr. 40 (2019) 500–508, https://doi.org/10.1053/J.SULT.2019.04.006.
[65] K. Arai, K. Kawai, W. Kohda, H. Tatsu, O. Matsui, T. Nakahama, Dynamic CT of acute cholangitis: early inhomogeneous enhancement of the liver, Am. J. Roentgenol. 181 (2003) 115–118, https://doi.org/10.2214/AJR.181.1.1810115/ASSET/IMAGES/07_AC1349_03C_NEW_1.JPEG.
[66] B.T. Everett, S. Naud, R.S. Zubarik, Risk factors for the development of stent-associated cholangitis following endoscopic biliary stent placement, Dig. Dis. Sci. 64 (2019) 2300–2307, https://doi.org/10.1007/S10620-019-05533-6.
[67] J.G. Oh, S.Y. Choi, M.H. Lee, J.E. Lee, B.H. Yi, S.S. Kim, J.H. Min, B. Lee, Differentiation of hepatic abscess from metastasis on contrast-enhanced dynamic computed tomography in patients with a history of extrahepatic malignancy: emphasis on dynamic change of arterial rim enhancement, Abdom. Radiol. (N. Y.) 44 (2019) 529–538, https://doi.org/10.1007/S00261-018-1766-Y.
[68] N. Wang, Y. Ju, J. Wu, A. Liu, A. Chen, J. Liu, Y. Liu, J. Li, Differentiation of liver abscess from liver metastasis using dual-energy spectral CT quantitative parameters, Eur. J. Radiol. 113 (2019) 204–208, https://doi.org/10.1016/j.ejrad.2019.02.024.
[69] H.J. Park, S.H. Kim, K.M. Jang, S.J. Lee, M.J. Park, D. Choi, Differentiating hepatic abscess from malignant mimickers: Value of diffusion-weighted imaging

with an emphasis on the periphery of the lesion, J. Magn. Reson. Imaging 38 (2013) 1333–1341, https://doi.org/10.1002/JMRI.24112.
[70] J.A. Pietryga, D.E. Morgan, Imaging preoperatively for pancreatic adenocarcinoma, J. Gastrointest. Oncol. 6 (2015) 343, https://doi.org/10.3978/J.ISSN.2078-6891.2015.024.
[71] A. Qayyum, E.P. Tamm, I.R. Kamel, P.J. Allen, H. Arif-Tiwari, V. Chernyak, T. A. Gonda, J.R. Grajo, N.M. Hindman, J.M. Horowitz, H. Kaur, M.M. McNamara, R.B. Noto, P.K. Srivastava, T. Lalani, ACR Appropriateness Criteria® Staging of Pancreatic Ductal Adenocarcinoma, J. Am. Coll. Radiol. 14 (2017) S560–S569, https://doi.org/10.1016/J.JACR.2017.08.050.
[72] E. Tapper, B. Kalb, D.R. Martin, D. Kooby, N.V. Adsay, J.M. Sarmiento, Staging laparoscopy for proximal pancreatic cancer in a magnetic resonance imaging-driven practice: what's it worth? HPB (Oxf.) 13 (2011) 732–737, https://doi.org/10.1111/J.1477-2574.2011.00366.X.
[73] V.B. Allen, K.S. Gurusamy, Y. Takwoingi, A. Kalia, B.R. Davidson, Diagnostic accuracy of laparoscopy following computed tomography (CT) scanning for assessing the resectability with curative intent in pancreatic and periampullary cancer, Cochrane Database Syst. Rev. (7) (2016), https://doi.org/10.1002/14651858.CD009323.PUB3.
[74] H. Gudmundsdottir, J.A. Yonkus, R. Alva-Ruiz, M.L. Kendrick, R.L. Smoot, S. G. Warner, P. Starlinger, C.A. Thiels, D.M. Nagorney, S.P. Cleary, T.E. Grotz, M. J. Truty, Yield of staging laparoscopy for pancreatic cancer in the modern era: analysis of more than 1,000 consecutive patients, J. Am. Coll. Surg. 237 (2023) 49–57, https://doi.org/10.1097/XCS.0000000000000704.
[75] W.T. Mehtsun, F.E. Chipidza, C. Fernández-del Castillo, K. Hemingway, Z. V. Fong, D.C. Chang, P. Pandharipande, J.W. Clark, J. Allen, T.S. Hong, J.Y. Wo, A.L. Warshaw, K.D. Lillemoe, C.R. Ferrone, Are staging computed tomography (CT) scans of the chest necessary in pancreatic adenocarcinoma? Ann. Surg. Oncol. 25 (2018) 3936–3942, https://doi.org/10.1245/S10434-018-6764-3.
[76] S. Downs-Canner, M. Zenati, B.A. Boone, P.R. Varley, J. Steve, M.E. Hogg, A. Zureikat, H.J. Zeh, K.K.W. Lee, The indolent nature of pulmonary metastases from ductal adenocarcinoma of the pancreas, J. Surg. Oncol. 112 (2015) 80–85, https://doi.org/10.1002/JSO.23943.
[77] C.J. Roche, M.L. Hughes, C.J. Garvey, F. Campbell, D.A. White, L. Jones, J. P. Neoptolemos, CT and pathologic assessment of prospective nodal staging in patients with ductal adenocarcinoma of the head of the pancreas, Ajr. Am. J. Roentgenol. 180 (2003) 475–480, https://doi.org/10.2214/AJR.180.2.1800475.
[78] F.N. Loch, P. Asbach, M. Haas, H. Seeliger, K. Beyer, C. Schineis, C.E. Degro, G. A. Margonis, M.E. Kreis, C. Kamphues, Accuracy of various criteria for lymph node staging in ductal adenocarcinoma of the pancreatic head by computed tomography and magnetic resonance imaging, World J. Surg. Oncol. 18 (2020) 1–10, https://doi.org/10.1186/S12957-020-01951-3/FIGURES/4.
[79] M. Röhrich, P. Naumann, F.L. Giesel, P.L. Choyke, F. Staudinger, A. Wefers, D. P. Liew, C. Kratochwil, H. Rathke, J. Liermann, K. Herfarth, D. Jäger, J. Debus, U. Haberkorn, M. Lang, S.A. Koerber, Impact of 68Ga-FAPI PET/CT imaging on the therapeutic management of primary and recurrent pancreatic ductal adenocarcinomas, J. Nucl. Med. 62 (2021) 779, https://doi.org/10.2967/JNUMED.120.253062.
[80] Y. Bian, Z. Zheng, X. Fang, H. Jiang, M. Zhu, J. Yu, H. Zhao, L. Zhang, J. Yao, L. Lu, J. Lu, C. Shao, Artificial intelligence to predict lymph node metastasis at CT in pancreatic ductal adenocarcinoma, Radiology 306 (2023) 160–169, https://doi.org/10.1148/RADIOL.220329/ASSET/IMAGES/LARGE/RADIOL.220329.TBL3.JPEG.
[81] S. Adham, M. Ferri, S.Y. Lee, N. Larocque, O.A. Alwahbi, L. Ruo, C.B. van der Pol, Pancreatic ductal adenocarcinoma (PDAC) regional nodal disease at standard lymphadenectomy: is MRI accurate for identifying node-positive patients? Eur. Radiol. 33 (2023) 5976–5983, https://doi.org/10.1007/S00330-023-09597-X/FIGURES/3.
[82] S.O. Bratlie, J. Wennerblom, C. Vilhav, J. Persson, E. Rangelova, Resectable, borderline, and locally advanced pancreatic cancer-"the good, the bad, and the ugly" candidates for surgery? J. Gastrointest. Oncol. 12 (2021) 2450–2460, https://doi.org/10.21037/JGO-2020-SLAPC-04.
[83] T. Imamura, Y. Yamamoto, T. Sugiura, Y. Okamura, T. Ito, R. Ashida, K. Ohgi, A. Todaka, A. Fukutomi, T. Aramaki, K. Uesaka, Prognostic role of the length of tumour-vein contact at the portal-superior mesenteric vein in patients having surgery for pancreatic cancer, Br. J. Surg. 106 (2019) 1649–1656, https://doi.org/10.1002/BJS.11328.
[84] B. Saka, S. Balci, O. Basturk, P. Bagci, L.M. Postlewait, S. Maithel, J. Knight, B. El-Rayes, D. Kooby, J. Sarmiento, T. Muraki, I. Oliva, S. Bandyopadhyay, G. Akkas, M. Goodman, M.D. Reid, A. Krasinskas, R. Everett, V. Adsay, Pancreatic ductal adenocarcinoma is spread to the peripancreatic soft tissue in the majority of resected cases, rendering the AJCC T-stage protocol (7th edition) inapplicable and insignificant: a size-based staging system (pT1: ≤2, pT2: >2-≤4, pT3: >4 cm) is more valid and clinically relevant, Ann, Surg. Oncol. 23 (2016) 2010–2018, https://doi.org/10.1245/S10434-016-5093-7.
[85] G. Marchegiani, S. Andrianello, G. Malleo, L. De Gregorio, A. Scarpa, M. Mino-Kenudson, L. Maggino, C.R. Ferrone, K.D. Lillemoe, C. Bassi, C.F. Del Castillo, R. Salvia, Does size matter in pancreatic cancer?: reappraisal of tumour dimension as a predictor of outcome beyond the TNM, Ann. Surg. 266 (2017) 142–148, https://doi.org/10.1097/SLA.0000000000001837.
[86] C. Liu, Y. Lu, G. Luo, H. Cheng, M. Guo, Z. Liu, J. Xu, J. Long, L. Liu, D. Fu, Q. Ni, M. Li, X. Yu, Which patients with para-aortic lymph node (LN16) metastasis will truly benefit from curative pancreaticoduodenectomy for pancreatic head cancer? Oncotarget 7 (2016) 29177–29186, https://doi.org/10.18632/ONCOTARGET.8690.
[87] S. Hempel, V. Plodeck, F. Mierke, M. Distler, D.E. Aust, H.D. Saeger, J. Weitz, T. Welsch, Para-aortic lymph node metastases in pancreatic cancer should not be considered a watershed for curative resection, Sci. Rep. 7 (2017), https://doi.org/10.1038/S41598-017-08165-W.
[88] T. Komo, Y. Murakami, N. Kondo, K. Uemura, Y. Hashimoto, N. Nakagawa, K. Urabe, S. Takahashi, T. Sueda, Prognostic impact of para-aortic lymph node micrometastasis in pancreatic ductal adenocarcinoma, Ann. Surg. Oncol. 23 (2016) 2019–2027, https://doi.org/10.1245/S10434-016-5120-8.
[89] M. Sho, Y. Murakami, F. Motoi, S. Satoi, I. Matsumoto, M. Kawai, G. Honda, K. Uemura, H. Yanagimoto, M. Kurata, T. Fukumoto, T. Akahori, S. Kinoshita, M. Nagai, S. Nishiwada, M. Unno, H. Yamaue, Y. Nakajima, Postoperative prognosis of pancreatic cancer with para-aortic lymph node metastasis: a multicenter study on 822 patients, J. Gastroenterol. 50 (2015) 694–702, https://doi.org/10.1007/S00535-014-1005-4.
[90] J.A.M.G. Tol, D.J. Gouma, C. Bassi, C. Dervenis, M. Montorsi, M. Adham, A. Andrén-Sandberg, H.J. Asbun, M. Bockhorn, M.W. Büchler, K.C. Conlon, L. Fernández-Cruz, A. Fingerhut, H. Friess, W. Hartwig, J.R. Izbicki, K. D. Lillemoe, M.N. Milicevic, J.P. Neoptolemos, S.V. Shrikhande, C.M. Vollmer, C. J. Yeo, R.M. Charnley, Definition of a standard lymphadenectomy in surgery for pancreatic ductal adenocarcinoma: a consensus statement by the International Study Group on Pancreatic Surgery (ISGPS), Surgery 156 (2014) 591–600, https://doi.org/10.1016/J.SURG.2014.06.016.
[91] T. Hackert, W. Niesen, U. Hinz, C. Tjaden, O. Strobel, A. Ulrich, C.W. Michalski, M.W. Büchler, Radical surgery of oligometastatic pancreatic cancer, Eur. J. Surg. Oncol. 43 (2017) 358–363, https://doi.org/10.1016/J.EJSO.2016.10.023.
[92] S. Crippa, A. Bittoni, E. Sebastiani, S. Partelli, S. Zanon, A. Lanese, K. Andrikou, F. Muffatti, G. Balzano, M. Reni, S. Cascinu, M. Falconi, Is there a role for surgical resection in patients with pancreatic cancer with liver metastases responding to chemotherapy? Eur. J. Surg. Oncol. 42 (2016) 1533–1539, https://doi.org/10.1016/J.EJSO.2016.06.398.
[93] O. De Simoni, M. Scarpa, M. Tonello, P. Pilati, F. Tolin, Y. Spolverato, M. Gruppo, Oligometastatic pancreatic cancer to the liver in the era of neoadjuvant chemotherapy: which role for conversion surgery? a systematic review and meta-analysis, Cancers (Basel) 12 (2020) 1–14, https://doi.org/10.3390/CANCERS12113402.
[94] V.P. Groot, G. Gemenetzis, A.B. Blair, R.J. Rivero-Soto, J. Yu, A.A. Javed, R. A. Burkhart, I.H.M.B. Rinkes, I.Q. Molenaar, J.L. Cameron, M.J. Weiss, C. L. Wolfgang, J. He, Defining and predicting early recurrence in 957 patients with resected pancreatic ductal adenocarcinoma, Ann. Surg. 269 (2019) 1154–1162, https://doi.org/10.1097/SLA.0000000000002734.
[95] H. Kurahara, K. Maemura, Y. Mataki, M. Sakoda, S. Iino, Y. Kawasaki, T. Arigami, S. Mori, Y. Kijima, S. Ueno, H. Shinchi, S. Natsugoe, A therapeutic strategy for resectable pancreatic cancer based on risk factors of early recurrence, Pancreas 47 (2018) 753–758, https://doi.org/10.1097/MPA.0000000000001066.
[96] R.A. Snyder, L.R. Prakash, G.M. Nogueras-Gonzalez, M.P. Kim, T.A. Aloia, J. N. Vauthey, J.E. Lee, J.B. Fleming, M.H.G. Katz, C.W.D. Tzeng, Vein resection during pancreaticoduodenectomy for pancreatic adenocarcinoma: patency rates and outcomes associated with thrombosis, J. Surg. Oncol. 117 (2018) 1648–1654, https://doi.org/10.1002/JSO.25067.
[97] D.L. Birrer, H. Golcher, R. Casadei, S.R. Haile, R. Fritsch, S. Hussung, T. B. Brunner, R. Fietkau, T. Meyer, R. Grützmann, S. Merkel, C. Ricci, C. Ingaldi, M. Di Marco, A. Guido, C. Serra, F. Minni, B. Pestalozzi, H. Petrowsky, M. Deoliveira, W.O. Bechstein, C.J. Bruns, C.E. Oberkofler, M. Puhan, M. Lesurtel, S. Heinrich, P.A. Clavien, Neoadjuvant therapy for resectable pancreatic cancer: a new standard of care. pooled data from 3 randomized controlled trials, Ann. Surg. 274 (2021) 713–720, https://doi.org/10.1097/SLA.0000000000005126.
[98] M. Vivarelli, F. Mocchegiani, D. Nicolini, A. Vecchi, G. Conte, E. Dalla Bona, R. Rossi, A. Benedetti Cacciaguerra, Neoadjuvant treatment in resectable pancreatic cancer. is it time for pushing on it? Front. Oncol. 12 (2022) 914203 https://doi.org/10.3389/FONC.2022.914203/BIBTEX.
[99] J.L. van Dam, Q.P. Janssen, M.G. Besselink, M.Y.V. Homs, H.C. van Santvoort, G. van Tienhoven, R.F. de Wilde, J.W. Wilmink, C.H.J. van Eijck, B. Groot Koerkamp, Neoadjuvant therapy or upfront surgery for resectable and borderline resectable pancreatic cancer: A meta-analysis of randomised controlled trials, Eur. J. Cancer 160 (2022) 140–149, https://doi.org/10.1016/j.ejca.2021.10.023.
[100] K.J. Labori, S.O. Bratlie, B. Andersson, J.-H. Angelsen, C. Björnerud, B. Björnsson, E.A. Bringeland, N. Elander, H. Garresori, J.E. Grønbech, J. Haux, O. Hemmingsson, M.G. Liljefors, T.Å. Myklebust, L.S. Nymo, K. Peltola, P. Pfeiffer, V. Sallinen, P. Sandström, E. Sparrelid, H. Stenvold, K. Søreide, B. Tingstedt, C. Verbeke, D. Öhlund, L. Klint, S. Dueland, K. Lassen, E.K. Aahlin, C. Bratthäll, A. Halimi, I. Hatlevoll, M. Heby, A. Kokkola, M. Kordes, S. Lindblad, L. Lundgren, M.B. Mortensen, K.E. Mortensen, J. Persson, E. Rangelova, E. Rønne, O.M. Sandvik, J.A. Søreide, C. Vilhav, K. Waardal, J. Wennerblom, C. Williamsson, S. Yaqub, Neoadjuvant FOLFIRINOX versus upfront surgery for resectable pancreatic head cancer (NORPACT-1): a multicentre, randomised, phase 2 trial, Lancet Gastroenterol. Hepatol. (2024), https://doi.org/10.1016/S2468-1253(23)00405-3.
[101] Y.D. Seo, M.H.G. Katz, Preoperative therapy for pancreatic adenocarcinoma—precision beyond anatomy, Cancer 128 (2022) 3041–3056, https://doi.org/10.1002/CNCR.34273.
[102] A.J. Jain, J.E. Maxwell, M.H.G. Katz, R.A. Snyder, Surgical considerations for neoadjuvant therapy for pancreatic adenocarcinoma, Cancers 15 (2023), https://doi.org/10.3390/CANCERS15164174.
[103] S. Isaji, S. Mizuno, J.A. Windsor, C. Bassi, C. Fernández-del Castillo, T. Hackert, A. Hayasaki, M.H.G. Katz, S.W. Kim, M. Kishiwada, H. Kitagawa, C.W. Michalski, C.L. Wolfgang, International consensus on definition and criteria of borderline

resectable pancreatic ductal adenocarcinoma 2017, Pancreatology 18 (2018) 2–11, https://doi.org/10.1016/J.PAN.2017.11.011.
[104] J.N. Vauthey, E. Dixon, AHPBA/SSO/SSAT consensus conference on resectable and borderline resectable pancreatic cancer: rationale and overview of the conference, Ann. Surg. Oncol. 16 (2009) 1725–1726, https://doi.org/10.1245/S10434-009-0409-5.
[105] M.H.G. Katz, R. Marsh, J.M. Herman, Q. Shi, E. Collison, A.P. Venook, H. L. Kindler, S.R. Alberts, P. Philip, A.M. Lowy, P.W.T. Pisters, M.C. Posner, J. D. Berlin, S.A. Ahmad, Borderline resectable pancreatic cancer: need for standardization and methods for optimal clinical trial design, Ann. Surg. Oncol. 20 (2013) 2787–2795, https://doi.org/10.1245/S10434-013-2886-9.
[106] M. Wagner, C. Antunes, D. Pietrasz, C. Cassinotto, M. Zappa, A. Sa Cunha, O. Lucidarme, J.B. Bachet, CT evaluation after neoadjuvant FOLFIRINOX chemotherapy for borderline and locally advanced pancreatic adenocarcinoma, Eur. Radiol. 27 (2017) 3104–3116, https://doi.org/10.1007/S00330-016-4632-8.
[107] C. Cassinotto, J. Cortade, G. Belleannée, B. Lapuyade, E. Terrebonne, V. Vendrely, C. Laurent, A. Sa-Cunha, An evaluation of the accuracy of CT when determining resectability of pancreatic head adenocarcinoma after neoadjuvant treatment, Eur. J. Radiol. 82 (2013) 589–593, https://doi.org/10.1016/J.EJRAD.2012.12.002.
[108] Y. Matsuda, Y. Inoue, M. Hiratsuka, S. Kawakatsu, T. Arai, K. Matsueda, A. Saiura, Y. Takazawa, Encapsulating fibrosis following neoadjuvant chemotherapy is correlated with outcomes in patients with pancreatic cancer, PLoS One 14 (2019), https://doi.org/10.1371/JOURNAL.PONE.0222155.
[109] C. Cassinotto, A. Mouries, J.P. Lafourcade, E. Terrebonne, G. Belleannée, J. F. Blanc, B. Lapuyade, V. Vendrely, C. Laurent, L. Chiche, T. Wagner, A. Sa-Cunha, D. Gaye, H. Trillaud, F. Laurent, M. Montaudon, Locally advanced pancreatic adenocarcinoma: reassessment of response with CT after neoadjuvant chemotherapy and radiation therapy, Radiology 273 (2014) 108–116, https://doi.org/10.1148/RADIOL.14132914.
[110] Y. Guo, F. Czeyda-Pommersheim, J.A. Miccio, S. Mahalingam, M. Cecchini, J. Pahade, Can a simplified CT response criteria for vascular involvement in pancreatic adenocarcinoma after neoadjuvant therapy predict survival in patients who achieved subsequent R0 resection? Abdom. Radiol. 46 (2021) 5609–5617, https://doi.org/10.1007/S00261-021-03284-5.
[111] Y. Noda, N. Pisuchpen, N.D. Mercaldo, Y. Sekigami, T. Michelakos, A. Parakh, J. Y. Wo, M. Qadan, C. Ferrone, K.D. Lillemoe, D.P. Ryan, J.W. Clark, C. Fernandez-Del Castillo, T.S. Hong, A.R. Kambadakone, Arterial involvement and resectability scoring system to predict R0 resection in patients with pancreatic ductal adenocarcinoma treated with neoadjuvant chemoradiation therapy, Eur. Radiol. 32 (2022) 2470–2480, https://doi.org/10.1007/S00330-021-08304-Y.
[112] S.K. Jeon, J.M. Lee, E.S. Lee, M.H. Yu, I. Joo, J.H. Yoon, J.Y. Jang, K.B. Lee, S. H. Lee, How to approach pancreatic cancer after neoadjuvant treatment: assessment of resectability using multidetector CT and tumor markers, Eur. Radiol. 32 (2022) 56–66, https://doi.org/10.1007/S00330-021-08108-0.
[113] N. Hussien, R.S. Hussien, D.H.A. Saad, M. El Kassas, W.F. Elkhatib, M. Ezz El Din, The role of MRI pancreatic protocol in assessing response to neoadjuvant therapy for patients with borderline resectable pancreatic cancer, Front. Oncol. 11 (2022), https://doi.org/10.3389/FONC.2021.796317.
[114] K. ichi Okada, M. Kawai, S. Hirono, F. Kojima, K. Tanioka, M. Terada, M. Miyazawa, Y. Kitahata, Y. Iwahashi, M. Ueno, S. Hayami, S. ichi Murata, T. Shimokawa, H. Yamaue, Diffusion-weighted MRI predicts the histologic response for neoadjuvant therapy in patients with pancreatic cancer: a prospective study (DIFFERENT trial), Langenbeck's Arch. Surg. 405 (2020) 23–33, https://doi.org/10.1007/S00423-020-01857-4.
[115] F.N. Harder, F. Jungmann, G.A. Kaissis, F.K. Lohöfer, S. Ziegelmayer, D. Havel, M. Quante, M. Reichert, R.M. Schmid, I.E. Demir, H. Friess, M. Wildgruber, J. Siveke, A. Muckenhuber, K. Steiger, W. Weichert, I. Rauscher, M. Eiber, M. R. Makowski, R.F. Braren, 18F]FDG PET/MRI enables early chemotherapy response prediction in pancreatic ductal adenocarcinoma, EJNMMI Res 11 (2021), https://doi.org/10.1186/S13550-021-00808-4.
[116] J.H. Kang, S.S. Lee, J.H. Kim, J.H. Byun, H.J. Kim, C. Yoo, K. pyo Kim, B.Y. Ryoo, S.C. Kim, Multiparametric MRI for prediction of treatment response to neoadjuvant FOLFIRINOX therapy in borderline resectable or locally advanced pancreatic cancer, Eur. Radiol. 31 (2021) 864–874, https://doi.org/10.1007/S00330-020-07134-8.
[117] M.A. Bali, S. Pullini, T. Metens, J. Absil, S.L. Chao, R. Marechal, C. Matos, B. M. Peerboccus, J.L. Van Laethem, Assessment of response to chemotherapy in pancreatic ductal adenocarcinoma: comparison between diffusion-weighted MR quantitative parameters and RECIST, Eur. J. Radiol. 104 (2018) 49–57, https://doi.org/10.1016/J.EJRAD.2018.04.024.
[118] C. Bilreiro, L. Andrade, R.M. Marques, C. Matos, Diffusion-weighted imaging for determining response to neoadjuvant therapy in pancreatic cancer: a systematic review and meta-analysis, Eur. Radiol. (2023), https://doi.org/10.1007/s00330-023-10381-0.
[119] A.M. Abdelrahman, A.H. Goenka, R. Alva-Ruiz, J.A. Yonkus, J.L. Leiting, R. P. Graham, K.W. Merrell, C.A. Thiels, C.L. Hallemeier, S.G. Warner, M. G. Haddock, T.E. Grotz, N.H. Tran, R.L. Smoot, W.W. Ma, S.P. Cleary, R. R. McWilliams, D.M. Nagorney, T.R. Halfdanarson, M.L. Kendrick, M.J. Truty, FDG-PET predicts neoadjuvant therapy response and survival in borderline resectable/locally advanced pancreatic adenocarcinoma, J. Natl. Compr. Canc. Netw. 20 (2022) 1023–1032, https://doi.org/10.6004/JNCCN.2022.7041.
[120] A. Panda, I. Garg, M.J. Truty, T.L. Kline, M.P. Johnson, E.C. Ehman, G. Suman, D. A. Anaam, B.J. Kemp, G.B. Johnson, T.R. Halfdanarson, S.K. Venkatesh, J. L. Fidler, A.H. Goenka, Borderline resectable and locally advanced pancreatic cancer: FDG PET/MRI and CT tumor metrics for assessment of pathologic response to neoadjuvant therapy and prediction of survival, Ajr. Am. J. Roentgenol. 217 (2021) 730–740, https://doi.org/10.2214/AJR.20.24567.
[121] J. Yoo, J.M. Lee, I. Joo, D.H. Lee, J.H. Yoon, M.H. Yu, J.Y. Jang, S.H. Lee, Post-neoadjuvant treatment pancreatic cancer resectability and outcome prediction using CT, 18F-FDG PET/MRI and CA 19–9, Cancer Imaging 23 (2023) 1–13, https://doi.org/10.1186/S40644-023-00565-8/TABLES/4.
[122] L. Evangelista, P. Zucchetta, L. Moletta, S. Serafini, G. Cassarino, N. Pegoraro, F. Bergamo, C. Sperti, D. Cecchin, The role of FDG PET/CT or PET/MRI in assessing response to neoadjuvant therapy for patients with borderline or resectable pancreatic cancer: a systematic literature review, Ann. Nucl. Med. 35 (2021) 767–776, https://doi.org/10.1007/S12149-021-01629-0.
[123] M.A. Van Dam, F.A. Vuijk, J.A. Stibbe, R.D. Houvast, S.A.C. Luelmo, S. Crobach, S.S. Feshtali, L.F. De Geus-Oei, B.A. Bonsing, C.F.M. Sier, P.J.K. Kuppen, R. J. Swijnenburg, A.D. Windhorst, J. Burggraaf, A.L. Vahrmeijer, J.S.D. Mieog, Overview and future perspectives on tumor-targeted positron emission tomography and fluorescence imaging of pancreatic cancer in the era of neoadjuvant therapy, Cancers 13 (2021), https://doi.org/10.3390/CANCERS13236088.
[124] I. Esposito, J. Kleeff, F. Bergmann, C. Reiser, E. Herpel, H. Friess, P. Schirmacher, M.W. Büchler, Most pancreatic cancer resections are R1 resections, Ann. Surg. Oncol. 15 (2008) 1651–1660, https://doi.org/10.1245/S10434-008-9839-8.
[125] E.C. Soer, C.S. Verbeke, Pathology reporting of margin status in locally advanced pancreatic cancer: challenges and uncertainties, J. Gastrointest. Oncol. 12 (2021) 2512–2520, https://doi.org/10.21037/JGO-20-391.
[126] C.S. Verbeke, K.V. Menon, Redefining resection margin status in pancreatic cancer, HPB (Oxf.) 11 (2009) 282, https://doi.org/10.1111/J.1477-2574.2009.00055.X.
[127] O. Strobel, T. Hank, U. Hinz, F. Bergmann, L. Schneider, C. Springfeld, D. Jäger, P. Schirmacher, T. Hackert, M.W. Büchler, Pancreatic cancer surgery: the new R-status counts, Ann. Surg. 265 (2017) 565–573, https://doi.org/10.1097/SLA.0000000000001731.
[128] F. Campbell, R.A. Smith, P. Whelan, R. Sutton, M. Raraty, J.P. Neoptolemos, P. Ghaneh, Classification of R1 resections for pancreatic cancer: the prognostic relevance of tumour involvement within 1 mm of a resection margin, Histopathology 55 (2009) 277–283, https://doi.org/10.1111/J.1365-2559.2009.03376.X.
[129] W.S. Tummers, J.V. Groen, B.G. Sibinga Mulder, A. Farina-Sarasqueta, J. Morreau, H. Putter, C.J. van de Velde, A.L. Vahrmeijer, B.A. Bonsing, J. S. Mieog, R.J. Swijnenburg, Impact of resection margin status on recurrence and survival in pancreatic cancer surgery, Br. J. Surg. 106 (2019) 1055–1065, https://doi.org/10.1002/BJS.11115.
[130] J.R. Delpero, F. Jeune, P. Bachellier, N. Regenet, Y.P. Le Treut, F. Paye, N. Carrere, A. Sauvanet, M. Adham, A. Autret, F. Poizat, O. Turrini, J.M. Boher, Prognostic value of resection margin involvement after pancreaticoduodenectomy for ductal adenocarcinoma: updates from a french prospective multicenter study, Ann. Surg. 266 (2017) 787–796, https://doi.org/10.1097/SLA.0000000000002432.
[131] L.A. Daamen, V.P. Groot, M.P.W. Intven, M.G. Besselink, O.R. Busch, B. G. Koerkamp, N.H. Mohammad, J.J. Hermans, H.W.M. van Laarhoven, J. J. Nuyttens, J.W. Wilmink, H.C. van Santvoort, I.Q. Molenaar, M.W.J. Stommel, Postoperative surveillance of pancreatic cancer patients, Eur. J. Surg. Oncol. 45 (2019) 1770–1777, https://doi.org/10.1016/J.EJSO.2019.05.031.
[132] E.R. Witkowski, J.K. Smith, E. Ragulin-Coyne, S.C. Ng, S.A. Shah, J.F. Tseng, Is it worth looking? abdominal imaging after pancreatic cancer resection: a national study, J. Gastrointest. Surg. 16 (2012) 121–128, https://doi.org/10.1007/S11605-011-1699-Z.
[133] J.M. Halle-Smith, L. Hall, L.A. Daamen, J. Hodson, R. Pande, A. Young, N. B. Jamieson, A. Lamarca, H.C. van Santvoort, I.Q. Molenaar, J.W. Valle, K. J. Roberts, Clinical benefit of surveillance after resection of pancreatic ductal adenocarcinoma: a systematic review and meta-analysis, Eur. J. Surg. Oncol. 47 (2021) 2248–2255, https://doi.org/10.1016/J.EJSO.2021.04.031.
[134] C.W.D. Tzeng, J.B. Fleming, J.E. Lee, X. Wang, P.W.T. Pisters, J.N. Vauthey, G. Varadhachary, R.A. Wolff, M.H.G. Katz, Yield of clinical and radiographic surveillance in patients with resected pancreatic adenocarcinoma following multimodal therapy, HPB 14 (2012) 365–372, https://doi.org/10.1111/J.1477-2574.2012.00445.X.
[135] K. Ishigami, K. Yoshimitsu, H. Irie, T. Tajima, Y. Asayama, M. Hirakawa, D. Kakihara, Y. Shioyama, Y. Nishihara, K. Yamaguchi, H. Honda, Significance of perivascular soft tissue around the common hepatic and proximal superior mesenteric arteries arising after pancreaticoduodenectomy: evaluation with serial MDCT studies, Abdom. Imaging 33 (2008) 654–661, https://doi.org/10.1007/S00261-008-9359-9.
[136] V.P. Groot, N. Rezaee, W. Wu, J.L. Cameron, E.K. Fishman, R.H. Hruban, M. J. Weiss, L. Zheng, C.L. Wolfgang, J. He, Patterns, timing, and predictors of recurrence following pancreatectomy for pancreatic ductal adenocarcinoma, Ann. Surg. 267 (2018) 936–945, https://doi.org/10.1097/SLA.0000000000002234.

1.3.2. Diffusion-weighted imaging of the pancreas

This section reviews the current literature on diffusion-weighted imaging (DWI) of the pancreas and exemplifies its value with clinical cases. It has been published as a book chapter [62]: “Bilreiro C, Matos C. (2021) Diffusion-Weighted Imaging of the Pancreas. In: Matos C, Papanikolaou N (eds) Diffusion Weighted Imaging of the Hepatobiliary System. Springer, Cham”.

© Springer Nature Switzerland AG 2021
C. Matos, N. Papanikolaou (eds.), *Diffusion Weighted Imaging of the Hepatobiliary System*
https://doi.org/10.1007/978-3-319-62977-3_6

6. Diffusion-Weighted Imaging of the Pancreas

Carlos Bilreiro[1] and Celso Matos[1] ✉
(1) Department of Radiology, Champalimaud Centre for the Unknown, Lisbon, Portugal

✉ **Celso Matos**
Email: celso.matos@fundacaochampalimaud.pt

6.1 Introduction

MRI has become an established imaging modality of the pancreas due to recent technological advances, and diffusion-weighted imaging (DWI) is one major contributor to its success. DWI is sensitive to the Brownian movement of water molecules in tissues, which is a thermally driven process [1, 2]. Different tissues have different degrees of restriction to the Brownian movement of water molecules, due to different intracellular and extracellular compartments' composition and cell density [3, 4]. Thus, in DWI, tissues appear with higher signal intensity depending on the presence of restriction to diffusion. The physics behind DWI are explained in a previous chapter.

DWI is usually performed with a T2-weighted spin-echo echo planar imaging (SE-EPI) sequence, so the images obtained are both sensitive to T2 and diffusion. By increasing the *b* values (usually up to 1000 s/mm^2 in abdominal imaging), the images obtained are increasingly sensitive to water diffusion and less sensitive to T2 [5]. When performing DWI in the clinical setting, an apparent diffusion coefficient (ADC) map is automatically calculated on modern MRI workstations, which provides visual information

of quantification of apparent diffusion coefficients in the images obtained, without influence of T2.

Because the pancreas is an organ with high blood perfusion, under low *b* values (<150 s/mm^2), intravoxel incoherent motion (IVIM) due to blood flow in microcirculation network becomes an important source of pseudo diffusion (perfusion), which can be used to derive flowing blood volume fraction, perfusion free diffusion coefficient and perfusion coefficient [6]. Promising results on the use of IVIM have been reported, however, at the present moment, it is not yet implemented in routine clinical practice [7–9].

6.2 Image Acquisition and Technical Aspects

As stated before, DWI is usually performed over a T2-weighted SE-EPI sequence, preferably using parallel imaging for reduced acquisition times. Fat signal suppression is usually performed, either with spectral fat saturation or spectral adiabatic inversion recovery sequence (SPAIR) [10].

DWI is known for a low in-plane resolution and suffers from susceptibility and motion artifacts [10]. A reduced field of view (FOV) has been shown to improve image quality and reduce these artifacts, however with a reduced signal-to-noise ratio (SNR) [11, 12]. With the increasingly common use of 3 T MRI, one can expect higher SNR with high resolution images [13].

An example of DWI sequence parameters at 3 T is shown in Table 6.1.

Table 6.1 Suggested parameters for acquiring DWI of the pancreas at 3 T scanners

MR parameters for DWI of the pancreas at 3 T	
Transmission technology	Multi transmit radiofrequency
Body coil	Phased-array 16 channel
FOV	260 × 303 mm
Voxel size	1.8 × 1.8 × 5 mm^3
Sequence	SE EPI DWI
EPI factor	63
B values	0, 150, 1000
Number of signal averages	3 (2, 2, 8)
Parallel imaging	Sense RL 2.6 and POS 1.5 = S total 3.9

MR parameters for DWI of the pancreas at 3 T	
Breathing motion	Free breathing with respiratory triggering
TR	1200 ms
TE	82 ms
Fat suppression	SPAIR

Abbreviations: *FOV* field of view, *SE* spin-echo, *EPI* echo planar imaging, *DWI* diffusion weighted imaging, *Sense* sensitivity encoding, *RL* right to left, *TR* repetition time, *TE* echo time, *SPAIR* spectral adiabatic inversion recovery

6.3 DWI in the Normal Pancreas

The normal disease-free pancreas is basically homogeneous on DWI and should serve as tissue background when identifying focal lesions and abnormalities (Fig. 6.1) [10]. Slightly decreasing ADC values in the different anatomical segments (from head to body to tail) have been reported [14, 15]. However, other studies found variable or no differences in ADC values measured in different pancreatic anatomical segments [10, 16–18].

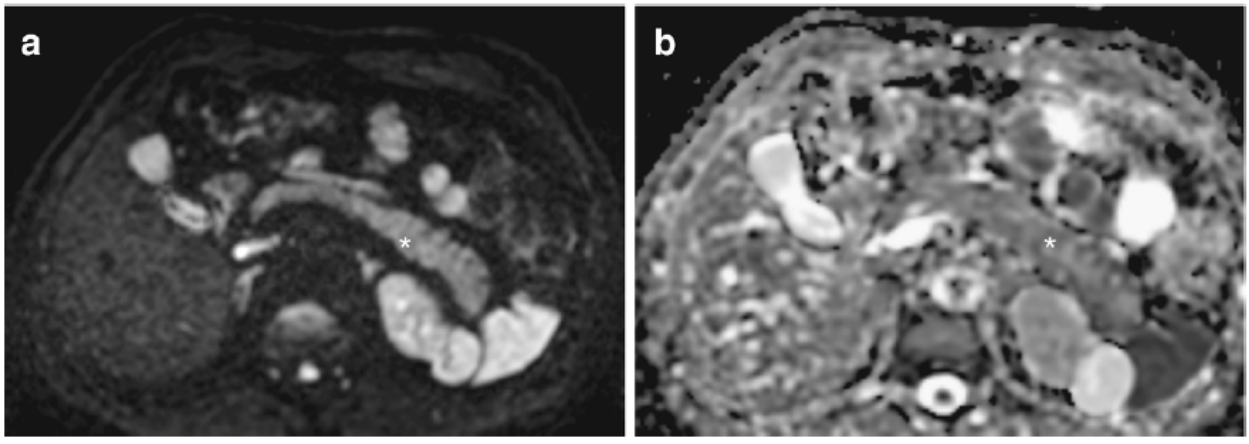


Fig. 6.1 Normal pancreas on DWI b600 (**a**) with respective ADC map (**b**). The healthy pancreatic parenchyma is basically homogeneous (asterisk), serving as tissue background for identification of focal lesions

DWI has been used to evaluate pancreatic exocrine function. Increased and peaking ADC values have been reported, mainly in the pancreatic head,

early after secretin administration in healthy subjects, with a subsequent gradual decrease to baseline values [19, 20].

6.4 DWI of Pancreatic Pathological Conditions

6.4.1 Inflammatory Conditions

6.4.1.1 Acute Pancreatitis

In the setting of acute pancreatitis, the role of DWI is not yet clear. The diagnosis, based on the 2012 revised Atlanta consensus, relies in the presence of two of the following criteria: acute onset of persistent, severe epigastric pain; serum lipase activity (or amylase activity) at least three times greater than the upper limit of normal; characteristic imaging features on contrast-enhanced CT, MRI, or ultrasound [21]. Imaging studies, therefore, are frequently not necessary for the diagnosis and when they are actually performed, MRI is usually not the first option, due to low availability in the emergency setting and higher financial costs.

Acute inflammatory changes in the pancreatic parenchyma have been reported to cause restricted diffusion, with lower ADC values than the healthy pancreatic parenchyma [22]. More importantly, DWI may have a role in identifying infection in acute pancreatic and acute necrotic fluid collections (Figs. 6.2, 6.3 and 6.4). These have been shown to present with restricted diffusion in the collection periphery, a finding reported in one study to have 100% sensitivity and 90.9% specificity when differentiating from sterile collections [23]. The same study reported better DWI MRI performance for this diagnosis when compared to CT (60% sensitivity and 100% specificity). In another study, the addition of DWI to a standard MRI protocol significantly increased diagnostic accuracy for infected pancreatic fluid collections [24]. These authors also suggested a possible increase in diagnostic confidence level for inexperienced readers, probably due to the straightforward nature of DWI interpretation.

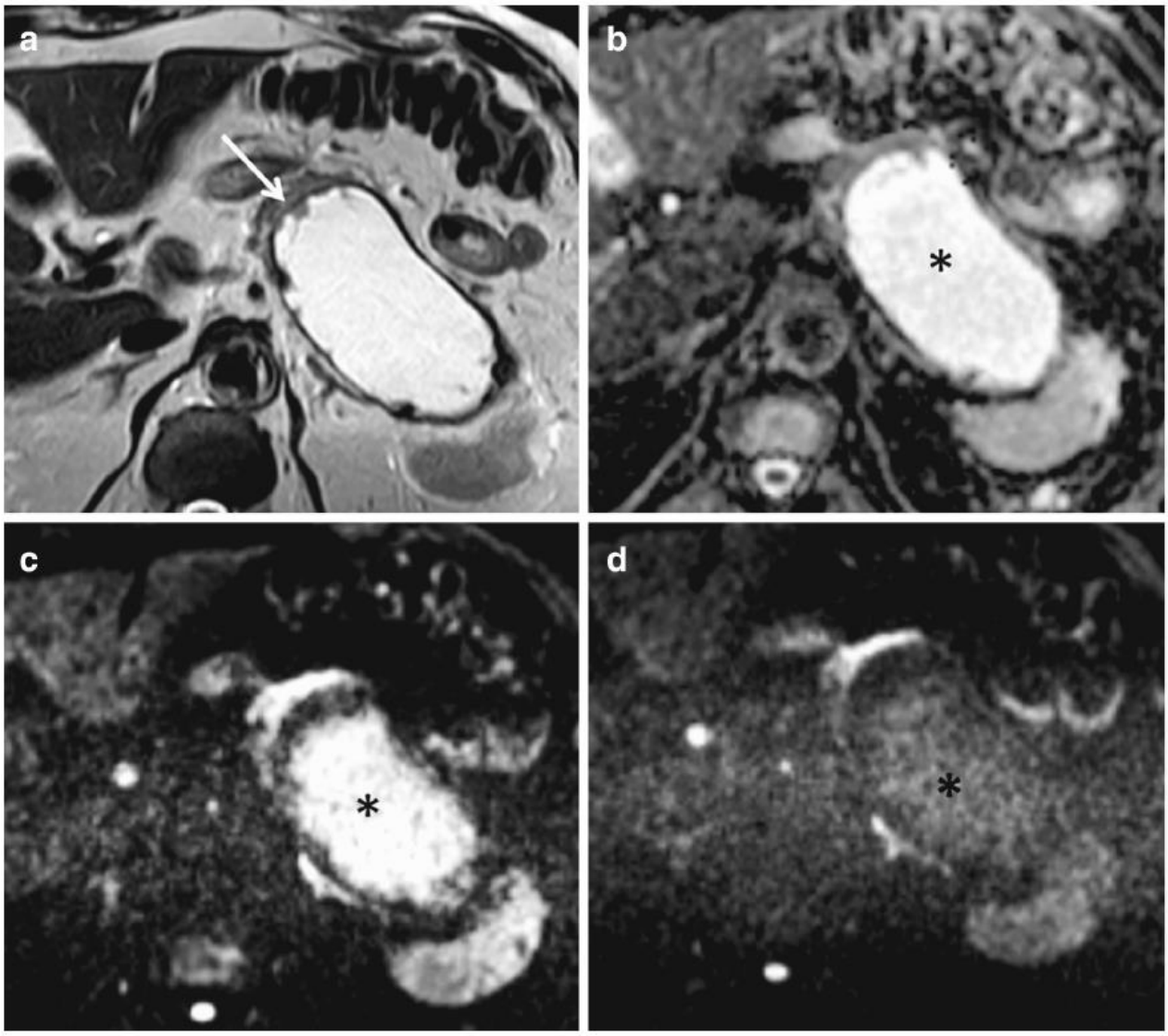


Fig. 6.2 Sterile acute pancreatic fluid collection. There is a large collection in the tail of the pancreas (**a**, arrow), well depicted in T2WI. The lesion shows high signal intensity on DWI b1000, suspicious for possible infection (**c**, asterisk). However, in DWI b1600 the lesion shows low signal intensity (**d**, asterisk), exemplifying the importance of high *b* value DWI to minimize T2 shine-through effects, as confirmed with high ADC values in the lesion (**b**, asterisk)

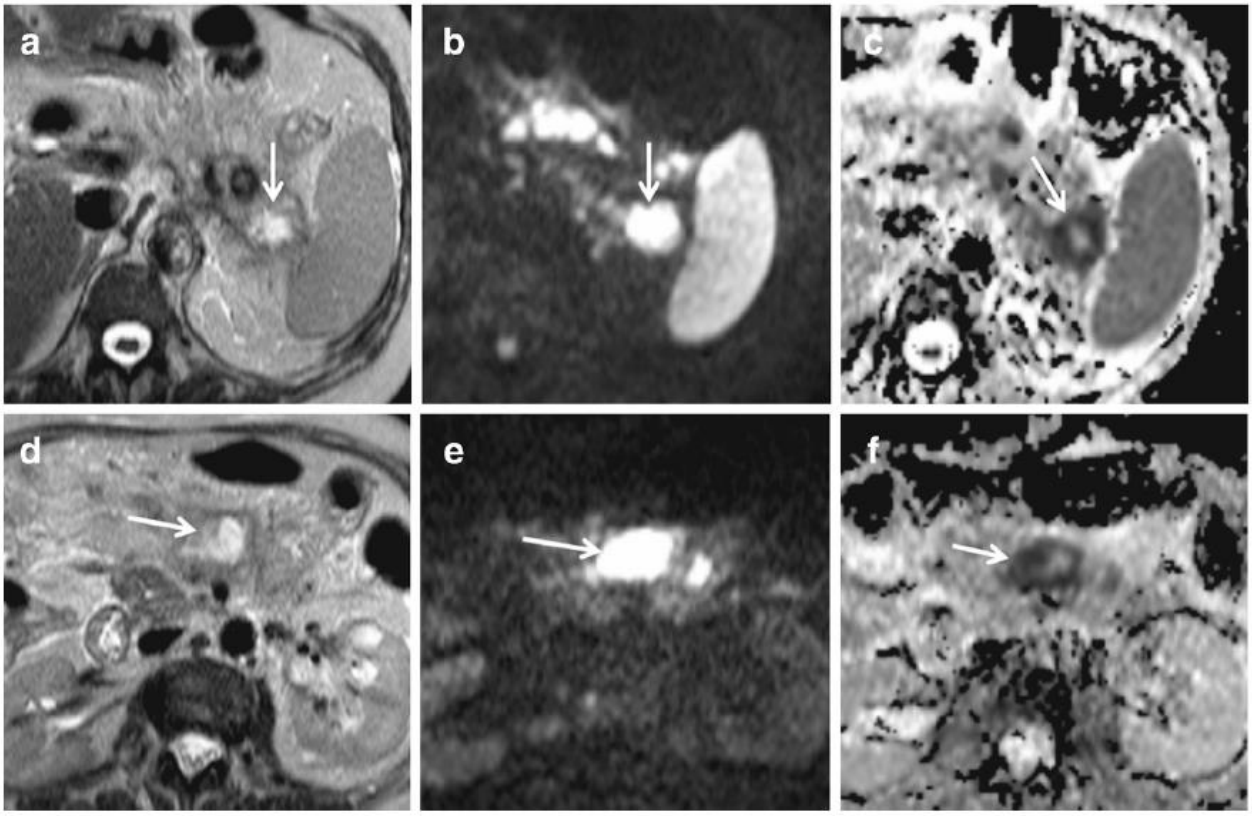


Fig. 6.3 Infected acute pancreatic fluid collections. This patient with acute pancreatitis presented several fluid collections (**a** and **d**, arrows). These collections show restricted diffusion mainly in the periphery, with high signal intensity in b1000 DWI (**b** and **e**, arrows) and low ADC values (**c** and **f**, arrows). These collections were drained and the presence of infection was confirmed

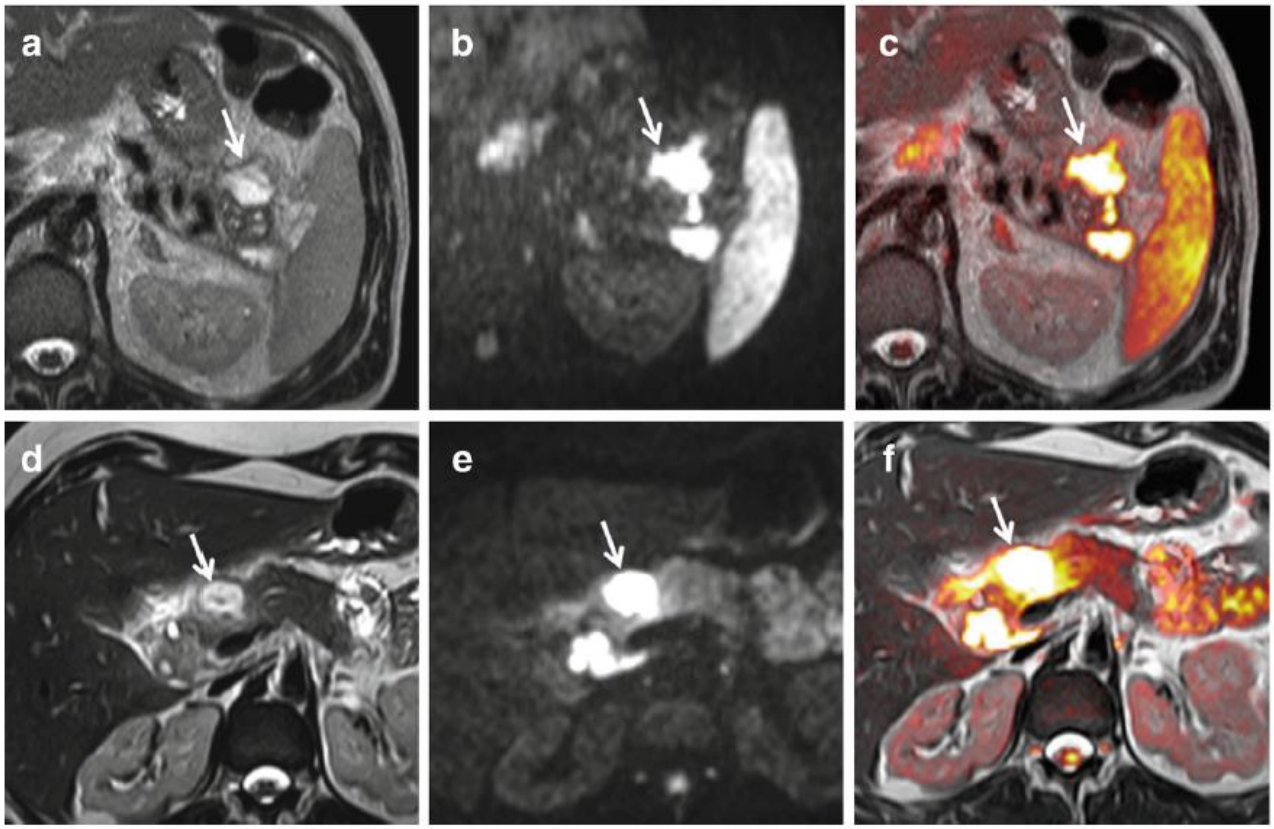


Fig. 6.4 Infected acute pancreatic fluid collections in two different patients (**a–c** and **d–f**). In both patients, the pancreatic collections (**a** and **d**, arrows) show restricted diffusion with high signal intensity in high *b* value DWI (**b** and **e**, arrows). The T2-DWI fusion images clearly depict the lesions with restricted diffusion (**c** and **f**, arrows)

6.4.1.2 Chronic Pancreatitis

ADC values of the pancreatic parenchyma have been shown to be lower in chronic pancreatitis compared with healthy pancreas [16, 25]. One study reported an ADC cutoff value of 2.2×10^{-3} mm^2/s with 100% sensitivity and 73% specificity for this purpose, at 3 T MRI [24]. However, in the same studies, when trying to differentiate between patients with severe and mild chronic pancreatitis, ADC values have not proven useful.

The use of secretin in conjunction with DWI has also been studied for chronic pancreatitis. Delayed and absent peak of ADC values after secretin administration have been correlated with the presence of chronic alcohol abuse and severe chronic pancreatitis, respectively [20].

6.4.1.3 Autoimmune Pancreatitis

Autoimmune pancreatitis may have a variable appearance in MRI studies. The classical description is a diffusely enlarged, “sausage-like” pancreas

with decreased signal on T1- and increased signal on T2-weighted images and delayed enhancement after intravenous contrast administration [26–28]. However, different imaging presentations of autoimmune pancreatitis are described, most frequently a focal mass-like enlargement, which poses a diagnostic challenge. Also, signal changes with absent pancreatic enlargement may be seen, although less frequently [26–28].

DWI may help in the diagnosis of autoimmune pancreatitis (Figs. 6.5 and 6.6). When compared to healthy pancreatic parenchyma, ADC values of autoimmune pancreatitis are known to be lower [29–32]. Also, in the setting of IgG4-related pancreatitis, the involvement of other organs (especially the kidneys) can accurately be detected by DWI, providing additional clues for the differential diagnosis [33].

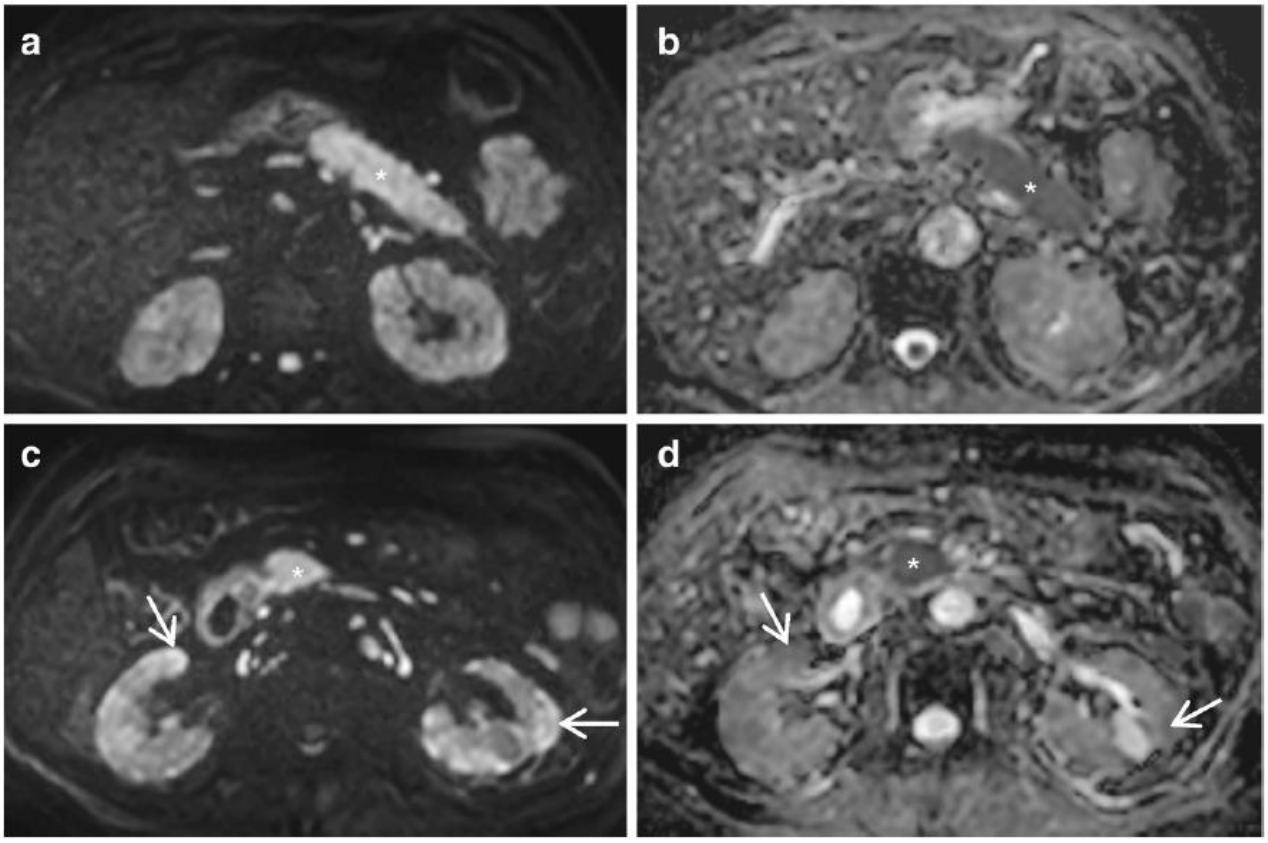


Fig. 6.5 Autoimmune pancreatitis (IgG4-related disease). Note the diffusely enlarged pancreatic parenchyma, with restricted diffusion on DWI b900 (**a** and **c**, asterisks) and consequently low values on ADC map (**b** and **d**, asterisks). There is also bilateral kidney involvement (**c** and **d**, arrows)

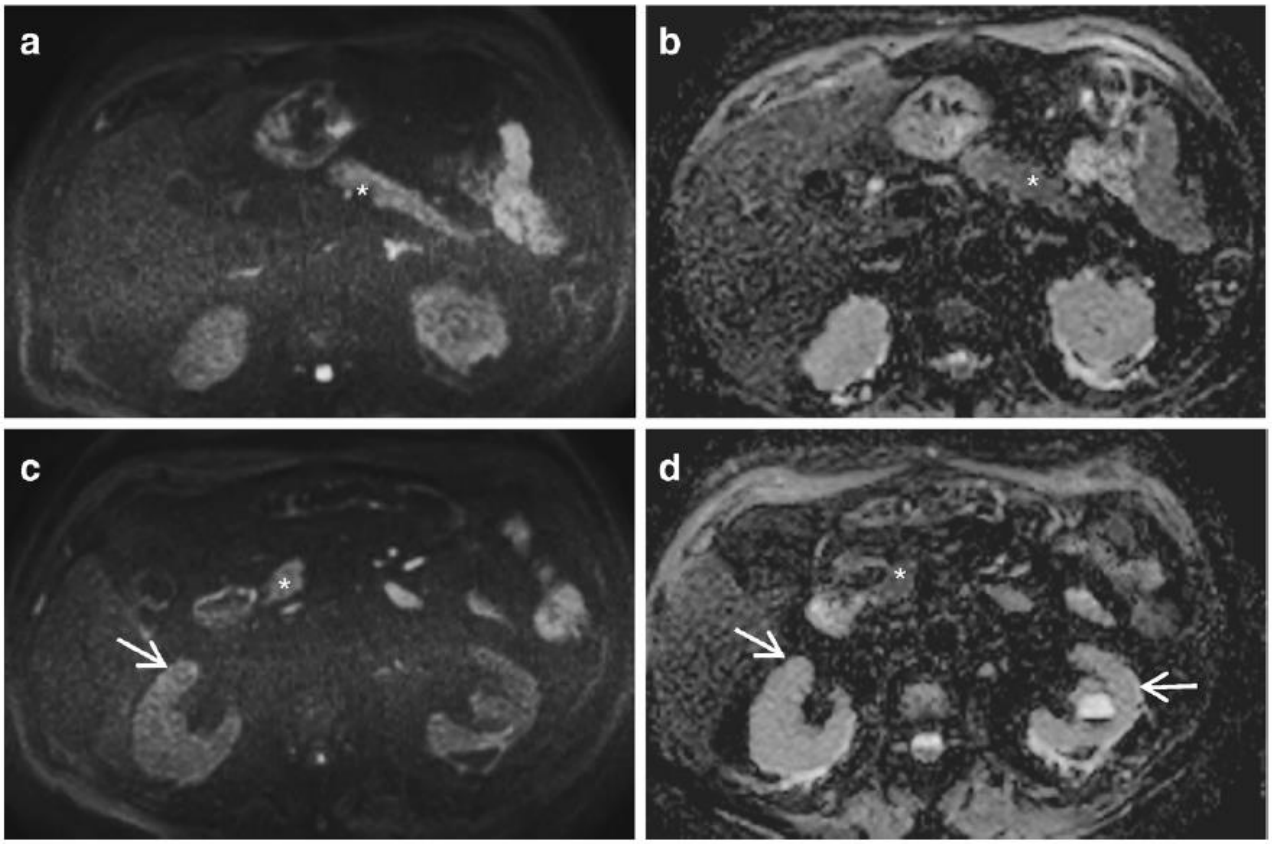


Fig. 6.6 Same patient from Fig. 6.5, after corticosteroid therapy. The pancreatic parenchyma is no longer enlarged and there is no restricted diffusion on DWI b900 (**a**, **c**) with corresponding normal ADC map (**b**, **d**) (asterisks). The kidney lesions seen previously have also resolved with therapy (arrows)

Another potential role of ADC values in the setting of autoimmune pancreatitis is evaluation of disease activity and response to therapy. One study reported lower ADC values in symptomatic patients when compared with asymptomatic patients [34]. Others reported increasing ADC values correlate with response to steroid administration [35]. IVIM-based models might also help in assessing response to therapy, with perfusion fraction showing progressively increasing values with steroid administration, possibly serving as an imaging biomarker [36].

6.4.1.4 Differentiating Mass Forming Pancreatitis from Pancreatic Adenocarcinoma

An important diagnostic challenge arises when differentiating mass forming pancreatitis from pancreatic adenocarcinoma. ADC values have been studied as a tool to perform the differential diagnosis, however with conflicting success in literature reports. Some studies reported lower ADC

values in pancreatic adenocarcinoma than mass forming pancreatitis [29–31]. One study even reported a sensitivity of 100% and a specificity of 98% when using ADC cutoff values of 0.88×10^{-3} mm^2/s together with morphologic findings and delayed parenchymal enhancement [30]. However, others found ADC values unable to differentiate both conditions, or even lower ADC values in pancreatic adenocarcinoma [32, 37]. Due to these conflicting reports, the role of ADC values in differentiating mass forming pancreatitis from pancreatic adenocarcinoma remains unclear.

The use of intravoxel incoherent motion (IVIM)-based models for characterization of pancreatic lesions has been proposed in the differentiation of mass forming pancreatitis and pancreatic adenocarcinoma. The perfusion fraction has been reported as the most valuable IVIM derived parameter for differentiating these entities, with pancreatic adenocarcinoma presenting significantly lower values than pancreatitis [8, 36, 38, 39]. Another study evaluated IVIM-derived parameter maps (diffusivity, perfusion fraction and ADC), reporting good discrimination of pancreatic adenocarcinoma from pancreatitis and neuroendocrine tumors [9]. However, one study reported conflicting results, with perfusion fraction and fast diffusion unable to differentiate these conditions [40]. These results require further studies for clarification, validation and standardization of protocols, before IVIM-based models can be recommended for clinical practice.

6.4.2 Cystic Pancreatic Lesions

Cystic pancreatic lesions include lesions with an invariably benign course (pancreatic fluid collection/pseudocyst, serous cystadenoma, cystic lymphangioma) and lesions with malignant potential (mucinous cystadenoma and intraductal papillary mucinous neoplasm—IPMN).

As discussed previously, DWI may help in the diagnosis of infected pancreatic fluid collection [23, 24]. However, DWI has been reported to be of little value in differentiating pancreatic cystic lesions, with conflicting results in the literature [10]. Several researchers have studied DWI for differentiating mucinous from non-mucinous lesions, malignant from benign lesions and inflammatory from non-inflammatory lesions; however their results were conflicting or showed DWI unable to confidently differentiate these conditions [41–46].

A possible role of DWI with measurement of ADC values in pancreatic cystic lesions might be the differentiation of high-grade/invasive IPMN from low-grade IPMN, with high-grade/invasive lesions presenting significantly lower values than low-grade lesions, as reported in one study (Fig. 6.7) [43]. Another study reported significantly higher specificity for DWI MRI compared with conventional MRI, when differentiating malignant from benign IPMN lesions, mainly due to identification of restricted diffusion on the cyst wall, internal septations, mural nodules or solid components [47]. However, further studies are required to confirm these results.

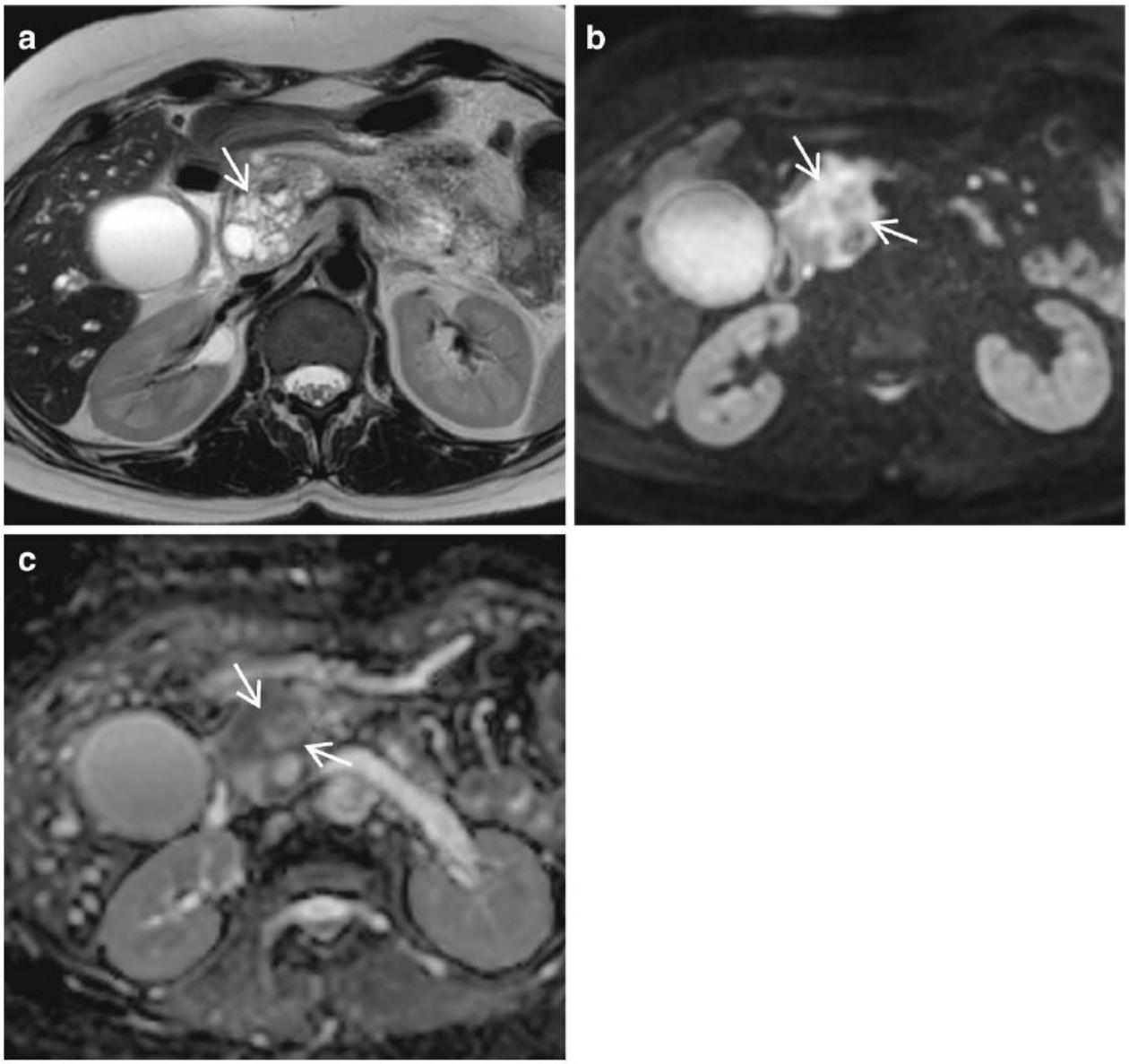


Fig. 6.7 Malignant mixed-type IPMN. There is a large complex cystic lesion in the pancreatic head, as seen on T2 weighted images (**a**, arrow). On DWI b900 (**b**), there are internal septa and solid components with restricted diffusion (arrows) and corresponding low values on ADC map (**c**)

6.4.3 Pancreatic Ductal Adenocarcinoma

DWI MRI has a major role in diagnosing pancreatic adenocarcinoma, with lesions presenting restricted diffusion (Figs. 6.8 and 6.9). High sensitivity and specificity have been reported (96.2% and 98.6%, respectively) using *b* value of 1000 s/mm^2 [48]. DWI is also comparable to a contrast-enhanced comprehensive MRI for diagnosis of pancreatic adenocarcinoma, with similar accuracy [49].

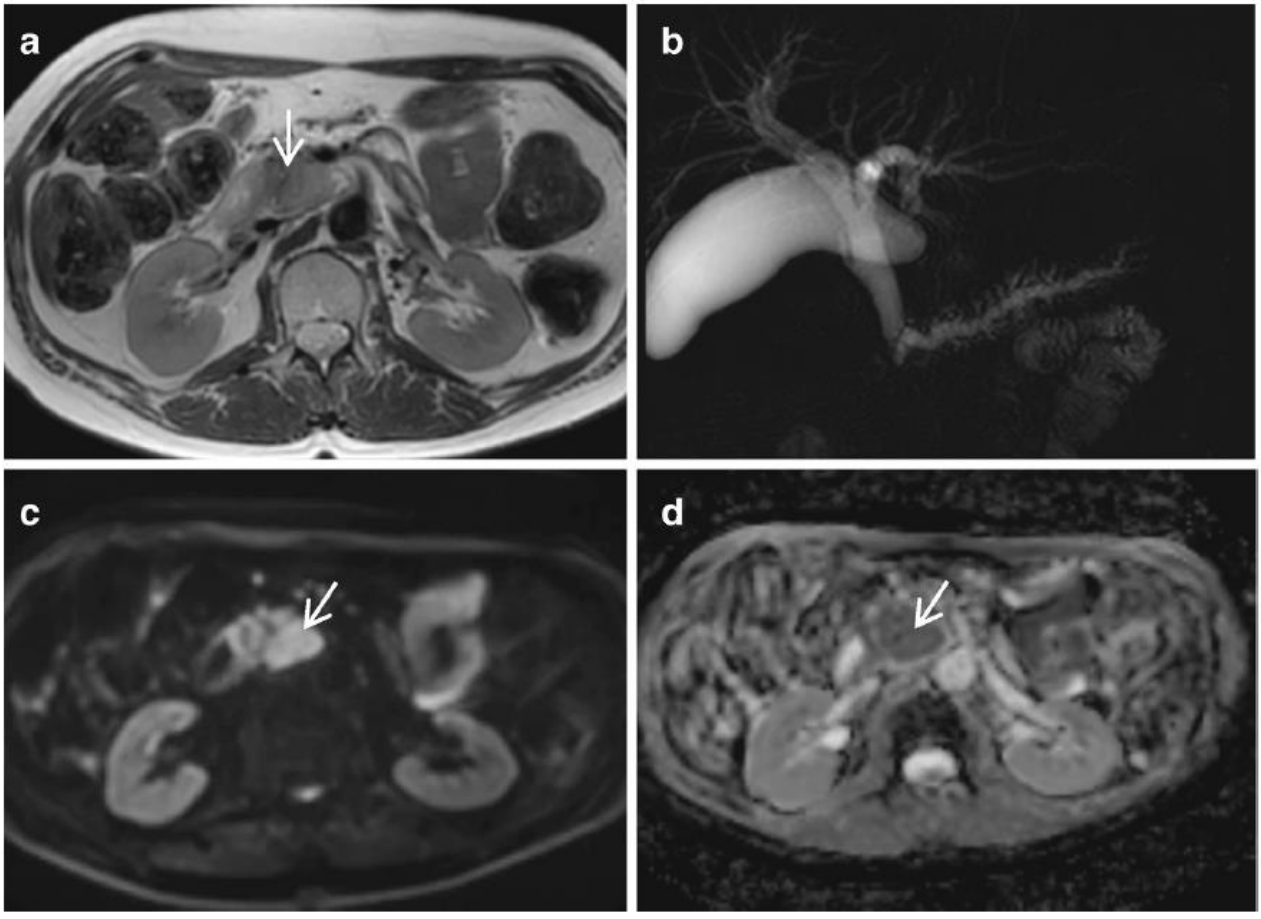


Fig. 6.8 Ductal adenocarcinoma of the pancreatic head. This is a typical case, with a mass in the pancreatic head, identified on T2 weighted images (**a**), causing diffuse dilatation of the biliary tree and the main pancreatic duct, clearly visible on MRCP (**b**). On DWI b900, the mass presents with restricted diffusion (**c**, arrow) with consequent low values on ADC map (**d**, arrow)

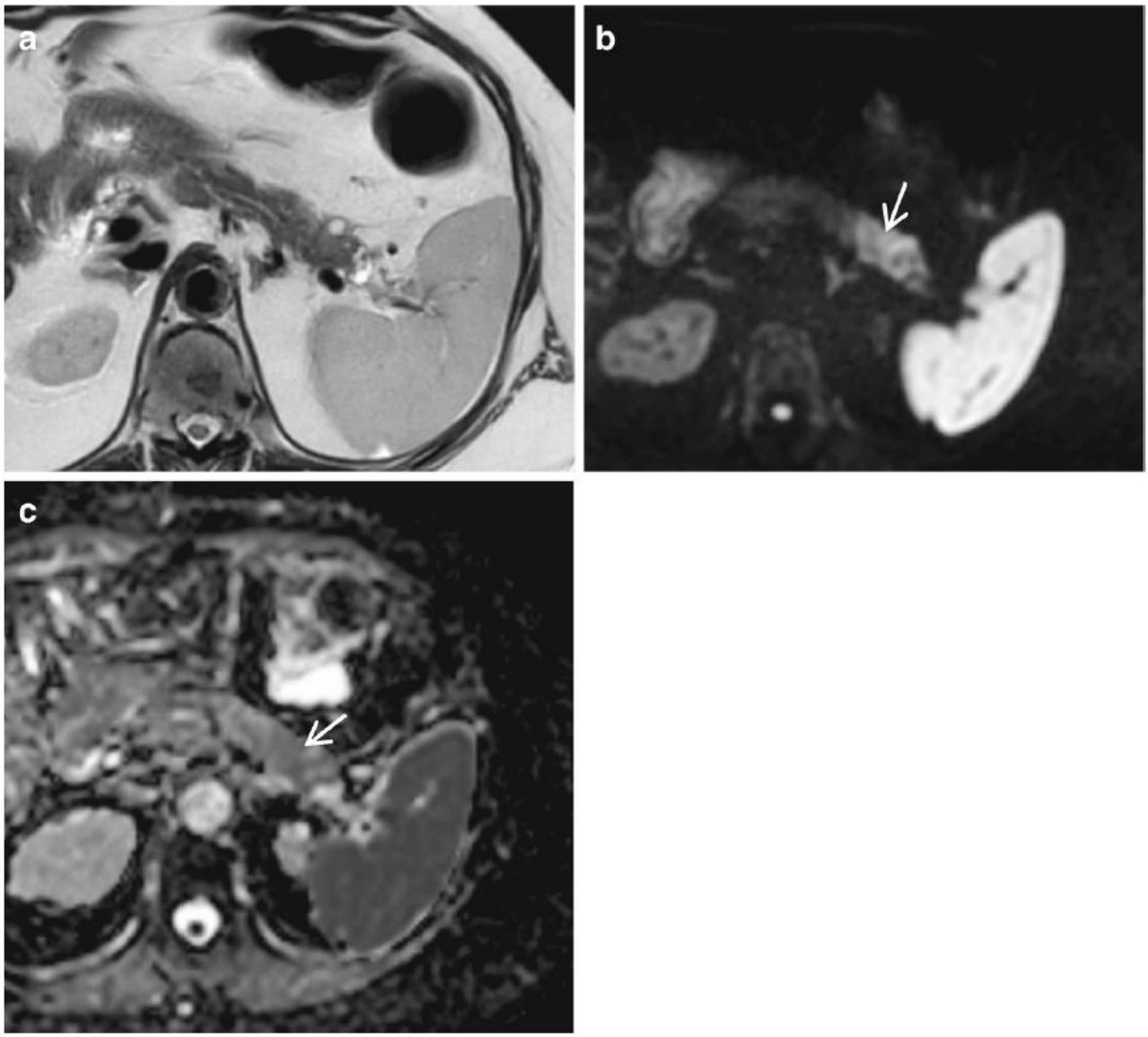


Fig. 6.9 Ductal adenocarcinoma of the pancreatic tail. The tumor is difficult to identify on T2 weighted images (**a**), mainly because of its location in the pancreatic tail, where it doesn't cause typical dilatation of the main pancreatic duct. On DWI b900, it is clearly seen with restricted diffusion (**b**, arrow), with corresponding low values on ADC map (**c**, arrow)

DWI was studied regarding its ability to evaluate tumor grading, but with conflicting results. One study reported significantly lower ADC values in poorly differentiated adenocarcinoma with dense fibrosis compared to well/moderately differentiated adenocarcinomas [50]. However, another study reported no association between ADC values of pancreatic adenocarcinoma and tumor grade or other adverse pathological features [51].

The role of DWI in the diagnostic challenge of differentiating mass forming pancreatitis from pancreatic adenocarcinoma has been discussed

previously in this chapter.

DWI may be useful in the prediction of tumor response to neoadjuvant therapy. Two studies reported that tumors of patients without response to neoadjuvant chemotherapy or radio-chemotherapy present lower ADC values, in comparison with patients with response [52, 53].

Another role of DWI may be the imaging assessment of tumor response to neoadjuvant therapy. One study reported reduction of 39% in tumor DW volume (a software assisted DWI tumor volume measurement) as having great performance to assess response to neoadjuvant chemotherapy, with 93% sensitivity and 100% specificity [54]. The same study evaluated IVIM derived parameters and reported increasing diffusivity and ADC values after neoadjuvant chemotherapy in patients with response to therapy, whereas no changes were seen in patients without response to therapy. Perfusion fraction, however, did not show any significant increase in responding patients, as might have been expected. These are promising results; further studies should help define the role of DWI in assessing response to neoadjuvant chemotherapy.

6.4.4 Pancreatic Neuroendocrine Tumors

Typically, pancreatic neuroendocrine tumors are small lesions with early enhancement in the arterial phase of contrast-enhanced imaging studies [55, 56]. However, variable imaging findings are common, posing diagnostic challenges. DWI MRI has been proposed for the detection and characterization of these lesions. Tumor detection was reported to significantly improve with the addition of DWI to T2-weighted images, with the tumors showing restricted diffusion (Fig. 6.10) [57–59]. One of these studies used fusion T2 and DWI images, reporting improved lesion detection especially for small isointense lesions on T2-weighted images [58].

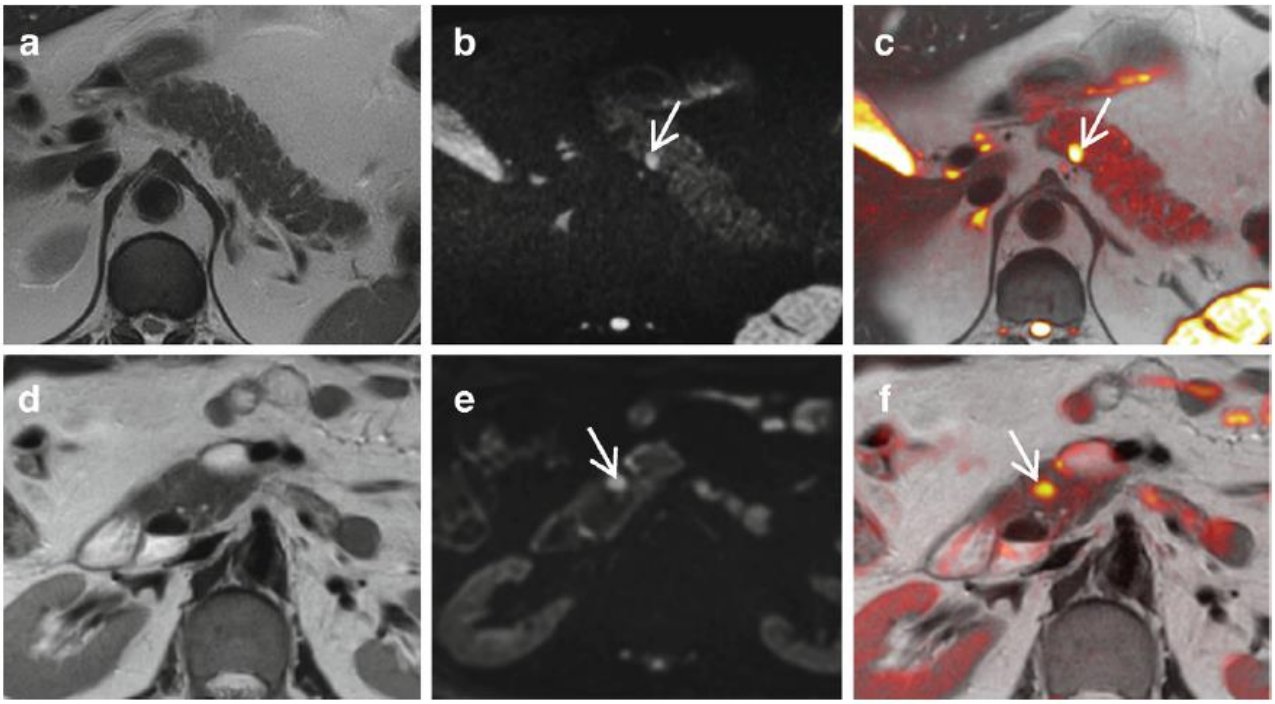


Fig. 6.10 Pancreatic neuroendocrine tumors in two patients (**a–c**, **d–f**). In both patients, there are no visible pancreatic lesions on T2 weighted images (**a**, **d**). On DWI, a focal lesion is clearly identified in both patients (**b** and **c**, arrows). On fusion T2-DWI images, the lesions are also clearly visible (**c** and **f**, arrows)

DWI has also been studied for its ability to predict tumor grade according to the 2010 World Health Organization classification [60]. A recent meta-analysis reviewed nine studies on this topic, more specifically the role of ADC, using cutoff values of 0.95–1.27 × 10^{-3} mm^2/s [61–70]. A high diagnostic accuracy was reported, with higher grade tumors (G2 and G3) showing lower ADC values, with pooled sensitivity of 84% and pooled specificity of 87%, when compared with low grade tumors (G1). The same study revealed that 3 T devices had higher sensitivity (93%); additionally, using a *b* value of 1000 s/mm^2 and an ADC cutoff of 1.0 × 10^{-3} mm^2/s had the highest specificity (95%). Once standardized imaging parameters are adopted and validation studies are performed, DWI might be used to predict tumor grade in clinical practice.

When trying to differentiate pancreatic neuroendocrine tumors from pancreatic adenocarcinoma, IVIM based models might prove useful. Perfusion fraction and incoherent microcirculation (fast diffusion) have been reported as the most valuable parameters, with neuroendocrine tumors presenting significantly higher values in comparison with adenocarcinoma [8, 39, 40].

Another role of DWI in the setting of pancreatic neuroendocrine tumors is identification of liver metastasis, with high sensitivity (Fig. 6.11) [10, 71].

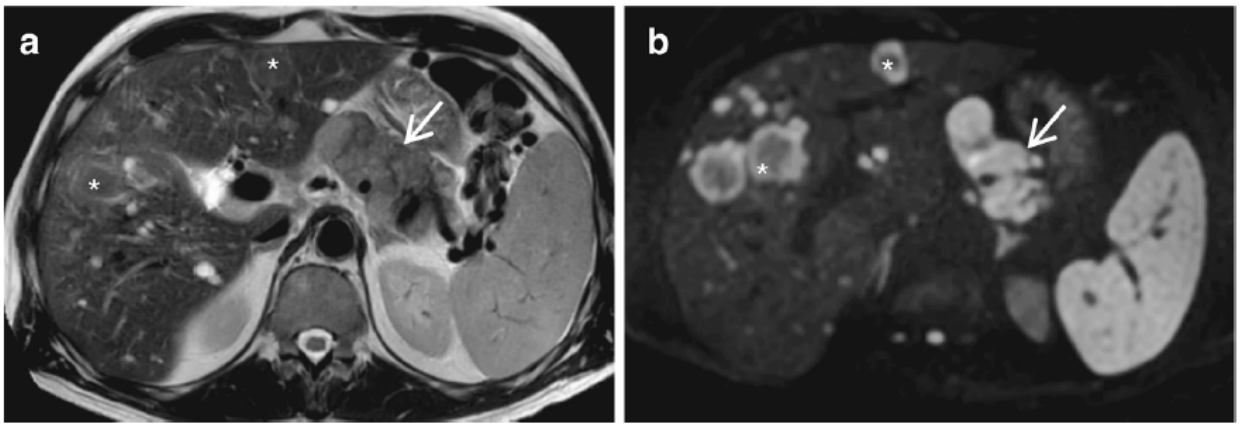


Fig. 6.11 Pancreatic neuroendocrine tumor with liver metastasis. A large mass in the pancreatic body and tail is seen in T2 weighted images and DWI (**a** and **b**, arrows). The liver metastases are visible on T2 weighted images, but badly defined (**a**, asterisks). On DWI, the liver metastases are much clearly depicted (**b**, asterisks)

6.4.5 Rare Conditions

Rare pancreatic lesions not included in the previous discussions comprise solid pseudopapillary neoplasm and intrapancreatic accessory spleen.

Solid pseudopapillary neoplasm has been reported to present lower ADC vales compared with normal pancreatic parenchyma [18, 72, 73]. However, the role of DWI in diagnosis and management of these tumors remains unclear.

Intrapancreatic spleen is usually diagnosed in MRI by comparing the lesion with the spleen, as signal intensities should be similar in all sequences. DWI may further help in this setting, with two studies reporting excellent diagnostic accuracy by visually comparing findings in the focal pancreatic lesion and the spleen [74, 75].

6.5 Conclusion

DWI MRI is a useful tool for the diagnosis of focal and diffuse pancreatic pathological conditions. DWI may further help evaluating tumor grade (neuroendocrine tumor and IPMN) and predicting and assessing therapeutic response (pancreatic ductal adenocarcinoma and autoimmune pancreatitis).

IVIM-based models are promising methods of lesion characterization and may be further developed in the near future. Table 6.2 provides a short summary of key aspects from this chapter.

Table 6.2 Short summary of main aspects for DW MRI of the pancreas

Condition	Relevant aspects
Normal pancreas	Homogeneous DWI signal Peak ADC values after secretin administration, with subsequent gradual decrease to baseline
Acute pancreatitis	Low ADC values in the parenchyma Restricted diffusion in the periphery of fluid collections indicates infection
Chronic pancreatitis	Low ADC values in the parenchyma Delayed or absent peak in ADC values after secretin administration
Autoimmune pancreatitis	Low ADC values in the parenchyma ADC and IVIM perfusion fraction values may correlate with symptoms and response to therapy
Differentiating mass forming pancreatitis from pancreatic adenocarcinoma	ADC values unable to differentiate IVIM-based models appear useful with perfusion fraction as the best parameter
Cystic lesions	DWI unable to differentiate lesions ADC values lower in malignant/high-grade IPMN, especially components of complex lesions
Ductal adenocarcinoma	DWI has high sensitivity and accuracy for diagnosis ADC values and IVIM-based models may help predict and assess response to neoadjuvant therapy
Neuroendocrine tumors	DWI improves tumor detection ADC values correlate with tumor grading IVIM-based models with perfusion fraction and incoherent diffusivity may help differentiate from adenocarcinoma DWI identifies liver metastases
Solid pseudopapillary neoplasm	Low ADC values in the tumor
Intrapancreatic spleen	DWI with identical findings to the spleen

References

1. Paul L. Sur la théorie du mouvement brownien. C R Acad Sci. 1908;146:530–2.

2. Albert E. Über die von der molekularkinetischen Theorie der Wärme geforderte Bewegung von in ruhenden Flüssigkeiten suspendierten Teilchen. Ann Phys. 1905;322(8):549–60.

3. Stejskal EO, Tanner JE. Spin diffusion measurements: spin-echo in the presence of a time dependent field gradient. J Chem Phys. 1965;42:288–92.

4. Qayyum A. Diffusion-weighted imaging in the abdomen and pelvis: concepts and applications. Radiographics. 2009;29(6):1797–810.

5. Koh DM, Collins DJ. Diffusion-weighted MRI in the body: applications and challenges in oncology. AJR Am J Roentgenol. 2007;188(6):1622–35.

6. Le Bihan D, Breton E, Lallemand D, Aubin ML, Vignaud J, Laval-Jeantet M. Separation of diffusion and perfusion in intravoxel incoherent motion MR imaging. Radiology. 1988;168(2):497–505.

7. Klau M, Mayer P, Bergmann F, Maier-Hein K, Hase J, Hackert T, Kauczor HU, Grenacher L, Stieltjes B. Correlation of histological vessel characteristics and diffusion-weighted imaging Intravoxel incoherent motion-derived parameters in pancreatic ductal adenocarcinomas and pancreatic neuroendocrine tumors. Investig Radiol. 2015;50(11):792–7.

8. Kang KM, Lee JM, Yoon JH, Kiefer B, Han JK, Choi BI. Intravoxel incoherent motion diffusion-weighted MR imaging for characterization of focal pancreatic lesions. Radiology. 2014;270(2):444–53.

9. Concia M, Sprinkart AM, Penner AH, Brossart P, Gieseke J, Schild HH, Willinek WA, Mürtz P. Diffusion-weighted magnetic resonance imaging of the pancreas: diagnostic benefit from an intravoxel incoherent motion model-based 3 b-value analysis. Investig Radiol. 2014;49(2):93–100.

10. Barral M, Taouli B, Guiu B, Koh DM, Luciani A, Manfredi R, Vilgrain V, Hoeffel C, Kanematsu M, Soyer P. Diffusion-weighted MR imaging of the pancreas: current status and recommendations. Radiology. 2015;274(1):45–63.

11. Riffel P, Michaely HJ, Morelli JN, Pfeuffer J, Attenberger UI, Schoenberg SO, Haneder S. Zoomed EPI-DWI of the pancreas using two-dimensional spatially-selective radiofrequency excitation pulses. PLoS One. 2014;9(3):e89468.

12. Thierfelder KM, Sommer WH, Dietrich O, Meinel FG, Theisen D, Paprottka PM, Strobl FF, Pfeuffer J, Reiser MF, Nikolaou K. Parallel-transmit-accelerated spatially selective excitation MRI for reduced-fov diffusion-weighted-imaging of the pancreas. Eur J Radiol. 2014;83(10):1709–14.

13. Ma C, Li YJ, Pan CS, Wang H, Wang J, Chen SY, Lu JP. High resolution diffusion weighted magnetic resonance imaging of the pancreas using reduced field of view single-shot echo-planar imaging at 3 T. Magn Reson Imaging. 2014;32(2):125–31.

14. Ye XH, Gao JY, Yang ZH, Liu Y. Apparent diffusion coefficient reproducibility of the pancreas measured at different MR scanners using diffusion-weighted imaging. J Magn Reson Imaging. 2014;40(6):1375–81.

15. Schoennagel BP, Habermann CR, Roesch M, Hahne JD, Arndt C, Kleibeler L, Petersen KU, Graessner J, Adam G, Herrmann J. Diffusion-weighted imaging of the healthy pancreas: apparent diffusion coefficient values of the normal head, body, and tail calculated from different sets of b-values. J Magn Reson Imaging. 2011;34(4):861–5.

16. Akisik MF, Aisen AM, Sandrasegaran K, Jennings SG, Lin C, Sherman S, Lin JA, Rydberg M. Assessment of chronic pancreatitis: utility of diffusion-weighted MR imaging with secretin enhancement. Radiology. 2009;250(1):103–9.

17. Barral M, Soyer P, Ben Hassen W, Gayat E, Aout M, Chiaradia M, Rahmouni A, Luciani A. Diffusion-weighted MR imaging of the normal pancreas: reproducibility and variations of apparent diffusion coefficient measurement at 1.5- and 3.0-tesla. Diagn Interv Imaging. 2013;94(4):418–27.

18. Barral M, Sebbag-Sfez D, Hoeffel C, Chaput U, Dohan A, Eveno C, Boudiaf M, Soyer P. Characterization of focal pancreatic lesions using normalized apparent diffusion coefficient at 1.5-Tesla: preliminary experience. Diagn Interv Imaging. 2013;94(6):619–27.

19. Wathle GK, Tjora E, Ersland L, Dimcevski G, Salvesen ØO, Molven A, Njølstad PR, Haldorsen IS. Assessment of exocrine pancreatic function by secretin-stimulated magnetic resonance cholangiopancreaticography and diffusion-weighted imaging in healthy controls. J Magn Reson Imaging. 2014;39(2):448–54.

20. Erturk SM, Ichikawa T, Motosugi U, Sou H, Araki T. Diffusion-weighted MR imaging in the evaluation of pancreatic exocrine function before and after secretin stimulation. Am J Gastroenterol. 2006;101(1):133–6.

21. Banks PA, Bollen TL, Dervenis C, Gooszen HG, Johnson CD, Sarr MG, Tsiotos GG, Vege SS, Acute Pancreatitis Classification Working Group. Classification of acute pancreatitis—2012: revision of the Atlanta classification and definitions by international consensus. Gut. 2013;62(1):102–11.

22. Thomas S, Kayhan A, Lakadamyali H, Oto A. Diffusion MRI of acute pancreatitis and comparison with normal individuals using ADC values. Emerg Radiol. 2012;19(1):5–9.

23. Islim F, Salik AE, Bayramoglu S, Guven K, Alis H, Turhan AN. Non-invasive detection of infection in acute pancreatic and acute necrotic collections with diffusion-weighted magnetic resonance imaging: preliminary findings. Abdom Imaging. 2014;39(3):472–81.

24. Borens B, Arvanitakis M, Absil J, El Bouchaibi S, Matos C, Eisendrath P, Toussaint E, Deviere J, Bali MA. Added value of diffusion-weighted magnetic resonance imaging for the detection of pancreatic fluid collection infection. Eur Radiol. 2017;27(3):1064–73.

25. Akisik MF, Sandrasegaran K, Jennings SG, Aisen AM, Lin C, Sherman S, Rydberg MP. Diagnosis of chronic pancreatitis by using apparent diffusion coefficient measurements at 3.0-T MR following secretin stimulation. Radiology. 2009;252(2):418–25.

26. Irie H, Honda H, Baba S, Kuroiwa T, Yoshimitsu K, Tajima T, Jimi M, Sumii T, Masuda K. Autoimmune pancreatitis: CT and MR characteristics. AJR Am J Roentgenol. 1998;170(5):1323–7.

27.

Sahani DV, Kalva SP, Farrell J, Maher MM, Saini S, Mueller PR, Lauwers GY, Fernandez CD, Warshaw AL, Simeone JF. Autoimmune pancreatitis: imaging features. Radiology. 2004;233(2):345–52.

28. Hafezi-Nejad N, Singh VK, Fung C, Takahashi N, Zaheer A. MR imaging of autoimmune pancreatitis. Magn Reson Imaging Clin N Am. 2018;26(3):463–78.

29. Kamisawa T, Takuma K, Anjiki H, Egawa N, Hata T, Kurata M, Honda G, Tsuruta K, Suzuki M, Kamata N, Sasaki T. Differentiation of autoimmune pancreatitis from pancreatic cancer by diffusion-weighted MRI. Am J Gastroenterol. 2010;105(8):1870–5.

30. Muhi A, Ichikawa T, Motosugi U, Sou H, Sano K, Tsukamoto T, Fatima Z, Araki T. Mass-forming autoimmune pancreatitis and pancreatic carcinoma: differential diagnosis on the basis of computed tomography and magnetic resonance cholangiopancreatography, and diffusion-weighted imaging findings. J Magn Reson Imaging. 2012;35(4):827–36.

31. Hur BY, Lee JM, Lee JE, Park JY, Kim SJ, Joo I, Shin CI, Baek JH, Kim JH, Han JK, Choi BI. Magnetic resonance imaging findings of the mass-forming type of autoimmune pancreatitis: comparison with pancreatic adenocarcinoma. J Magn Reson Imaging. 2012;36(1):188–97.

32. Wiggermann P, Grützmann R, Weissenböck A, Kamusella P, Dittert DD, Stroszczynski C. Apparent diffusion coefficient measurements of the pancreas, pancreas carcinoma, and mass-forming focal pancreatitis. Acta Radiol. 2012;53(2):135–9.

33. Pozdzik AA, Matos C, Rorive S, Brocheriou I, Delhaye M, Nortier JL. Diffusion-weighted magnetic resonance imaging: a non-nephrotoxic prompt assessment of kidney involvement in IgG4-related disease. Kidney Int. 2014 Apr;85(4):981.

34. Oki H, Hayashida Y, Oki H, Kakeda S, Aoki T, Taguchi M, Harada M, Korogi Y. DWI findings of autoimmune pancreatitis: comparison between symptomatic and asymptomatic patients. J Magn Reson Imaging. 2015;41(1):125–31.

35. Taniguchi T, Kobayashi H, Nishikawa K, Iida E, Michigami Y, Morimoto E, Yamashita R, Miyagi K, Okamoto M. Diffusion-weighted magnetic resonance imaging in autoimmune pancreatitis. Jpn J Radiol. 2009;27(3):138–42.

36. Klauß M, Maier-Hein K, Tjaden C, Hackert T, Grenacher L, Stieltjes B. IVIM DW-MRI of autoimmune pancreatitis: therapy monitoring and differentiation from pancreatic cancer. Eur Radiol. 2016;26(7):2099–106.

37. Fattahi R, Balci NC, Perman WH, Hsueh EC, Alkaade S, Havlioglu N, Burton FR. Pancreatic diffusion-weighted imaging (DWI): comparison between mass-forming focal pancreatitis (FP), pancreatic cancer (PC), and normal pancreas. J Magn Reson Imaging. 2009;29(2):350–6.

38. Klauss M, Lemke A, Grünberg K, Simon D, Re TJ, Wente MN, Laun FB, Kauczor HU, Delorme S, Grenacher L, Stieltjes B. Intravoxel incoherent motion MRI for the differentiation between mass forming chronic pancreatitis and pancreatic carcinoma. Investig Radiol. 2011;46(1):57–63.

39. De Robertis R, Cardobi N, Ortolani S, Tinazzi Martini P, Stemmer A, Grimm R, Gobbo S, Butturini G, D'Onofrio M. Intravoxel incoherent motion diffusion-weighted MR imaging of solid pancreatic masses: reliability and usefulness for characterization. Abdom Radiol (NY). 2019;44(1):131–9.

40. Kim B, Lee SS, Sung YS, Cheong H, Byun JH, Kim HJ, Kim JH. Intravoxel incoherent motion diffusion-weighted imaging of the pancreas: characterization of benign and malignant pancreatic pathologies. J Magn Reson Imaging. 2017;45(1):260–9.

41. Inan N, Arslan A, Akansel G, Anik Y, Demirci A. Diffusion-weighted imaging in the differential diagnosis of cystic lesions of the pancreas. AJR Am J Roentgenol. 2008;191(4):1115–21.

42. Fatima Z, Ichikawa T, Motosugi U, Muhi A, Sano K, Sou H, Haradome H, Kiryu S, Araki T. Magnetic resonance diffusion-weighted imaging in the characterization of pancreatic mucinous cystic lesions. Clin Radiol. 2011;66(2):108–11.

43. Sandrasegaran K, Akisik FM, Patel AA, Rydberg M, Cramer HM, Agaram NP, Schmidt CM. Diffusion-weighted imaging in characterization of cystic pancreatic lesions. Clin Radiol. 2011;66(9):808–14.

44. Yamashita Y, Namimoto T, Mitsuzaki K, Urata J, Tsuchigame T, Takahashi M, Ogawa M. Mucin-producing tumor of the pancreas: diagnostic value of diffusion-weighted echo-planar MR imaging. Radiology. 1998;208(3):605–9.

45. Mottola JC, Sahni VA, Erturk SM, Swanson R, Banks PA, Mortele KJ. Diffusion-weighted MRI of focal cystic pancreatic lesions at 3.0-Tesla: preliminary results. Abdom Imaging. 2012;37(1):110–7.

46. Schraibman V, Goldman SM, Ardengh JC, Goldenberg A, Lobo E, Linhares MM, Gonzales AM, Abdala N, Abud TG, Ajzen SA, Jackowsky A, Szejnfeld J. New trends in diffusion-weighted magnetic resonance imaging as a tool in differentiation of serous cystadenoma and mucinous cystic tumor: a prospective study. Pancreatology. 2011;11(1):43–51.

47. Jang KM, Kim SH, Min JH, Lee SJ, Kang TW, Lim S, Choi D. Value of diffusion-weighted MRI for differentiating malignant from benign intraductal papillary mucinous neoplasms of the pancreas. AJR Am J Roentgenol. 2014;203(5):992–1000.

48. Ichikawa T, Erturk SM, Motosugi U, Sou H, Iino H, Araki T, Fujii H. High-b value diffusion-weighted MRI for detecting pancreatic adenocarcinoma: preliminary results. AJR Am J Roentgenol. 2007;188(2):409–14.

49. Kartalis N, Lindholm TL, Aspelin P, Permert J, Albiin N. Diffusion-weighted magnetic resonance imaging of pancreas tumours. Eur Radiol. 2009;19(8):1981–90.

50. Wang Y, Chen ZE, Nikolaidis P, McCarthy RJ, Merrick L, Sternick LA, Horowitz JM, Yaghmai V, Miller FH. Diffusion-weighted magnetic resonance imaging of pancreatic adenocarcinomas: association with histopathology and tumor grade. J Magn Reson Imaging. 2011;33(1):136–42.

51. Rosenkrantz AB, Matza BW, Sabach A, Hajdu CH, Hindman N. Pancreatic cancer: lack of association between apparent diffusion coefficient values and adverse pathological features. Clin Radiol. 2013;68(4):e191–7.

52. Cuneo KC, Chenevert TL, Ben-Josef E, Feng MU, Greenson JK, Hussain HK, Simeone DM, Schipper MJ, Anderson MA, Zalupski MM, Al-Hawary M, Galban CJ, Rehemtulla A, Feng FY, Lawrence TS, Ross BD. A pilot study of diffusion-weighted MRI in patients undergoing neoadjuvant chemoradiation for pancreatic cancer. Transl Oncol. 2014;7(5):644–9.

53. Niwa T, Ueno M, Ohkawa S, Yoshida T, Doiuchi T, Ito K, Inoue T. Advanced pancreatic cancer: the use of the apparent diffusion coefficient to predict response to chemotherapy. Br J Radiol. 2009;82(973):28–34.

54. Bali MA, Pullini S, Metens T, Absil J, Chao SL, Marechal R, Matos C, Peerboccus BM, Van Laethem JL. Assessment of response to chemotherapy in pancreatic ductal adenocarcinoma: comparison between diffusion-weighted MR quantitative parameters and RECIST. Eur J Radiol. 2018;104:49–57.

55. Herwick S, Miller FH, Keppke AL. MRI of islet cell tumors of the pancreas. AJR Am J Roentgenol. 2006;187(5):W472–80.

56. Ichikawa T, Peterson MS, Federle MP, Baron RL, Haradome H, Kawamori Y, Nawano S, Araki T. Islet cell tumor of the pancreas: biphasic CT versus MR imaging in tumor detection. Radiology. 2000;216(1):163–71.

57. Schmid-Tannwald C, Schmid-Tannwald CM, Morelli JN, Neumann R, Haug AR, Jansen N, Nikolaou K, Schramm N, Reiser MF, Rist C. Comparison of abdominal MRI with diffusion-weighted imaging to 68Ga-DOTATATE PET/CT in detection of neuroendocrine tumors of the pancreas. Eur J Nucl Med Mol Imaging. 2013;40(6):897–907.

58. Brenner R, Metens T, Bali M, Demetter P, Matos C. Pancreatic neuroendocrine tumor: added value of fusion of T2-weighted imaging and high b-value diffusion-weighted imaging for tumor detection. Eur J Radiol. 2012;81(5):e746–9.

59. Bakir B, Salmaslioğlu A, Poyanli A, Rozanes I, Acunas B. Diffusion weighted MR imaging of pancreatic islet cell tumors. Eur J Radiol. 2010;74(1):214–20.

60. Klimstra DS, Arnold R, Capella C. Neuroendocrine neoplasms of the pancreas. In: Bosman FT, Carneiro F, Hruban RH, Theise ND, editors. WHO classification of tumours of the digestive system. Lyon: International Agency for Research on Cancer (IARC); 2010. p. 322–6.

61. Zong RL, Geng L, Wang X, Xie D. Diagnostic performance of apparent diffusion coefficient for prediction of grading of pancreatic neuroendocrine tumors: a systematic review and meta-analysis. Pancreas. 2019;48(2):151–60.

62. Wang Y, Chen ZE, Yaghmai V, Nikolaidis P, McCarthy RJ, Merrick L, Miller FH. Diffusion-weighted MR imaging in pancreatic endocrine tumors correlated with histopathologic characteristics. J Magn Reson Imaging. 2011;33(5):1071–9.

63. De Robertis R, Cingarlini S, Tinazzi Martini P, Ortolani S, Butturini G, Landoni L, Regi P, Girelli R, Capelli P, Gobbo S, Tortora G, Scarpa A, Pederzoli P, D'Onofrio M. Pancreatic neuroendocrine neoplasms: magnetic resonance imaging features according to grade and stage. World J Gastroenterol. 2017;23(2):275–85.

64. Guo C, Zhuge X, Chen X, Wang Z, Xiao W, Wang Q. Value of diffusion-weighted magnetic resonance imaging in predicting World Health Organization grade in G1/G2 pancreatic neuroendocrine tumors. Oncol Lett. 2017;13(6):4141–6.

65. Pereira JA, Rosado E, Bali M, Metens T, Chao SL. Pancreatic neuroendocrine tumors: correlation between histogram analysis of apparent diffusion coefficient maps and tumor grade.

Abdom Imaging. 2015;40(8):3122–8.

66. Kim JH, Eun HW, Kim YJ, Han JK, Choi BI. Staging accuracy of MR for pancreatic neuroendocrine tumor and imaging findings according to the tumor grade. Abdom Imaging. 2013;38(5):1106–14.

67. Jang KM, Kim SH, Lee SJ, Choi D. The value of gadoxetic acid-enhanced and diffusion-weighted MRI for prediction of grading of pancreatic neuroendocrine tumors. Acta Radiol. 2014;55(2):140–8.

68. Kulali F, Semiz-Oysu A, Demir M, Segmen-Yilmaz M, Bukte Y. Role of diffusion-weighted MR imaging in predicting the grade of nonfunctional pancreatic neuroendocrine tumors. Diagn Interv Imaging. 2018;99(5):301–9.

69. Lotfalizadeh E, Ronot M, Wagner M, Cros J, Couvelard A, Vullierme MP, Allaham W, Hentic O, Ruzniewski P, Vilgrain V. Prediction of pancreatic neuroendocrine tumour grade with MR imaging features: added value of diffusion-weighted imaging. Eur Radiol. 2017;27(4):1748–59.

70. Guo C, Chen X, Xiao W, Wang Q, Sun K, Wang Z. Pancreatic neuroendocrine neoplasms at magnetic resonance imaging: comparison between grade 3 and grade 1/2 tumors. Onco Targets Ther. 2017;10:1465–74.

71. d'Assignies G, Fina P, Bruno O, Vullierme MP, Tubach F, Paradis V, Sauvanet A, Ruszniewski P, Vilgrain V. High sensitivity of diffusion-weighted MR imaging for the detection of liver metastases from neuroendocrine tumors: comparison with T2-weighted and dynamic gadolinium-enhanced MR imaging. Radiology. 2013;268(2):390–9.

72. Yao XZ, Yun H, Zeng MS, Wang H, Sun F, Rao SX, Ji Y. Evaluation of ADC measurements among solid pancreatic masses by respiratory-triggered diffusion-weighted MR imaging with inversion-recovery fat-suppression technique at 3.0T. Magn Reson Imaging. 2013;31(4):524–8.

73. Jang KM, Kim SH, Kim YK, Park MJ, Lee MH, Hwang J, Rhim H. Imaging features of small (≤3 cm) pancreatic solid tumors on gadoxetic-acid-enhanced MR imaging and diffusion-weighted imaging: an initial experience. Magn Reson Imaging. 2012;30(7):916–25.

74. Kang BK, Kim JH, Byun JH, Lee SS, Kim HJ, Kim SY, Lee MG. Diffusion-weighted MRI: usefulness for differentiating intrapancreatic accessory spleen and small hypervascular neuroendocrine tumor of the pancreas. Acta Radiol. 2014;55(10):1157–65.

75. Jang KM, Kim SH, Lee SJ, Park MJ, Lee MH, Choi D. Differentiation of an intrapancreatic accessory spleen from a small (<3-cm) solid pancreatic tumor: value of diffusion-weighted MR imaging. Radiology. 2013;266(1):159–67.

1.4. Advanced Diffusion-weighted MRI techniques

1.4.1. Conventional Diffusion-weighted imaging

Diffusion-weighted imaging (DWI) is sensitive to the thermally-driven random motion of water molecules in tissues. This type of motion was first observed by Robert Brown in 1827, who reported the erratic motion of pollen particles, henceforth being often called Brownian motion [63]. Brownian motion was later studied by others, with landmark works by Einstein and Langevin during the first decade of the 20th century [64, 65]. Fundamental to our understanding of the diffusion process, the relation between mean square displacement of water molecules (r^2), the diffusion coefficient (D), and the diffusion time (t) was first described by Einstein:

$$\langle r^2 \rangle = 6Dt$$

Simply put, the diffusion coefficient of water molecules will be higher with higher temperatures, and lower with higher friction or viscosity of the medium on which it travels; and the longer one observes water molecules, the further they can travel from a starting point to any point along the surface of a sphere.

Following the initial developments of MRI, the effects of the diffusion process on the signal of water molecules and related concepts were soon explored by pioneer MRI developers [66–68]. Stejskal and Tanner provided a landmark development for DWI in 1965, when describing how MRI could become sensitive to the diffusion of water molecules by using a pair of time-dependent magnetic field gradients on a spin-echo pulse sequence [69]. This method became a gold standard for DWI in body and neuroimaging, and is widely used today in clinical practice, in conjunction with spin-echo echo planar imaging (SE-EPI) allowing for fast acquisitions, as represented in a pulse sequence diagram in Figure 5.

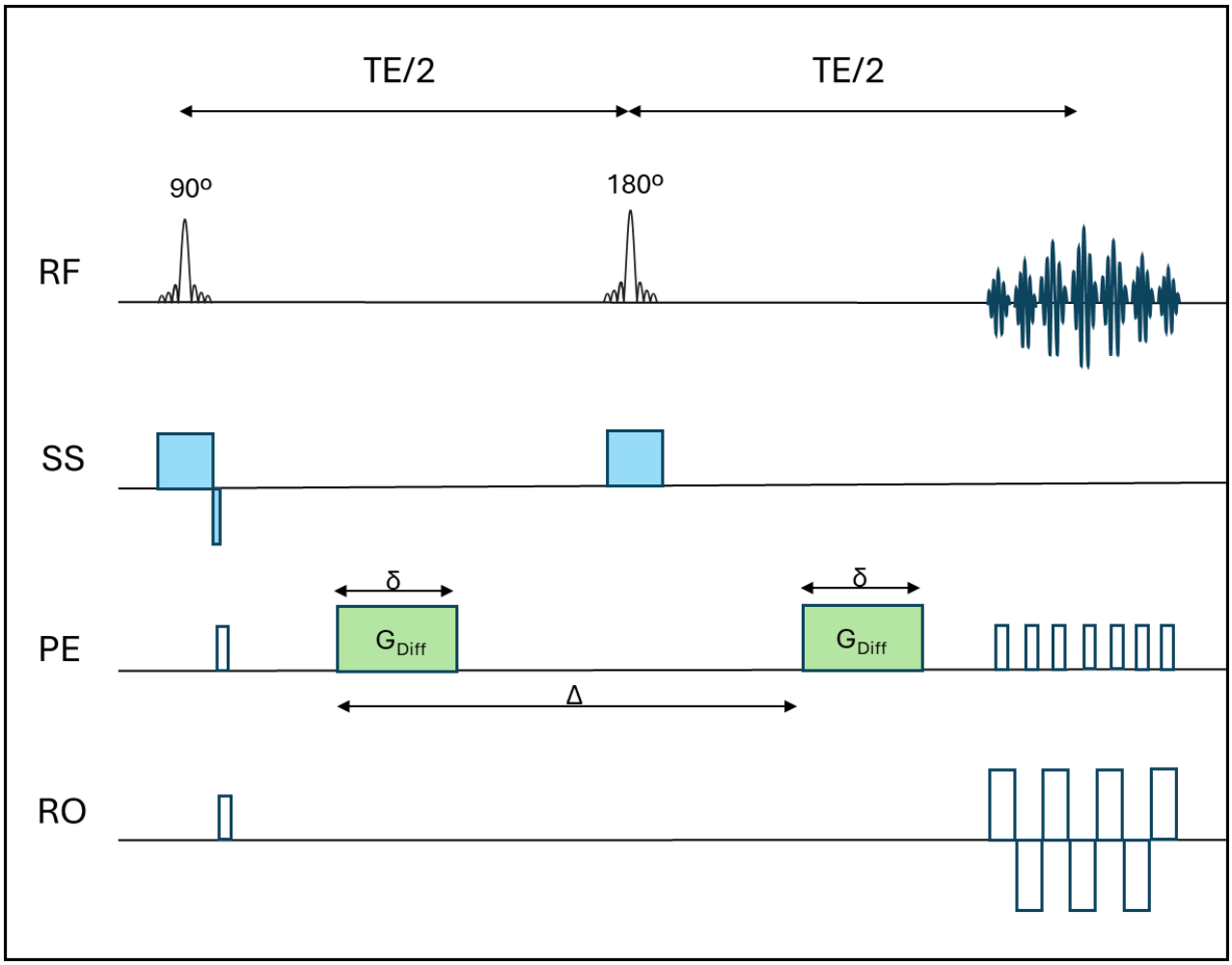


Figure 5. DWI pulse sequence diagram using a pair of diffusion sensitizing gradients on spin-echo echo planar imaging (SE-EPI). The first diffusion gradient (G_{Diff}) is placed before, and the second after the 180º pulse. Then, MR signal is acquired using an EPI echo train. RF: radiofrequency; SS: slice selection; PE: phase encoding; RO: readout; G_{Diff}: diffusion gradient; δ: diffusion gradient duration; Δ: diffusion time.

Through the above method, the apparent diffusion coefficient (ADC) can be calculated using the diffusion-weighted signal (S) as follows:

$$S(b) = S_0 e^{(-bADC)}$$

Here, the obtained signal depends on the apparent (measured) diffusion coefficient, and the b value. Since the b value is controlled by the operator, performing at least one diffusion-weighted - S(b), and one non-diffusion-weighted acquisition – S_0, allows us to estimate the ADC value. The b value represents the amount of diffusion-weighting,

which is dependent on the proton gyromagnetic ratio (γ) and the following variables - gradient amplitude (G), diffusion time (Δ), and the duration of diffusion gradients (δ):

$$b = (\gamma G \delta)^2 (\Delta - \frac{\delta}{3})$$

This way, the amount of diffusion weighting can be predetermined using operator-controlled parameters, when performing DWI acquisitions.

DWI has become a staple in current medical imaging [70, 71]. In the human body, different tissues and focal alterations in parenchymal organs have different degrees of restriction to the Brownian motion of water molecules, reflecting aspects at the microscopic level: cellular density and intracellular and extracellular compartments' composition [72–74]. As water molecules in tissues encounter more and more obstacles at these microscopic levels, their ability to travel in space is hindered or restricted. This simple yet robust diffusion model has been the basis for many of DWI's applications in clinical practice. DWI is routinely used for diagnosis, staging and response to therapy in benign and malignant diseases throughout the human body, ranging from cancer to auto-immune diseases [70]. A review of DWI applications for pancreatic imaging is presented in chapter 1.3.2[62]. Despite the robustness and usefulness of DWI as an imaging technique sensitive to microstructure, the full complexity of microstructure is not captured by ADC. Other aspects of the diffusion process in tissues which are not considered in conventional DWI include its directional dependence (i.e. anisotropy) and the non-Gaussian behavior of diffusion.

1.4.2. Diffusion tensor imaging

Diffusion tensor imaging (DTI) has been developed as a method for exploring diffusion directionality dependence in tissues, i.e. anisotropy. This method provides a rotationally invariant representation of the diffusion process, by applying several diffusion gradient directions in three-dimensional space, and was first described by Basser et al in 1994 [75]. A pulse sequence diagram for DTI using SE-EPI is represented in Figure 6.

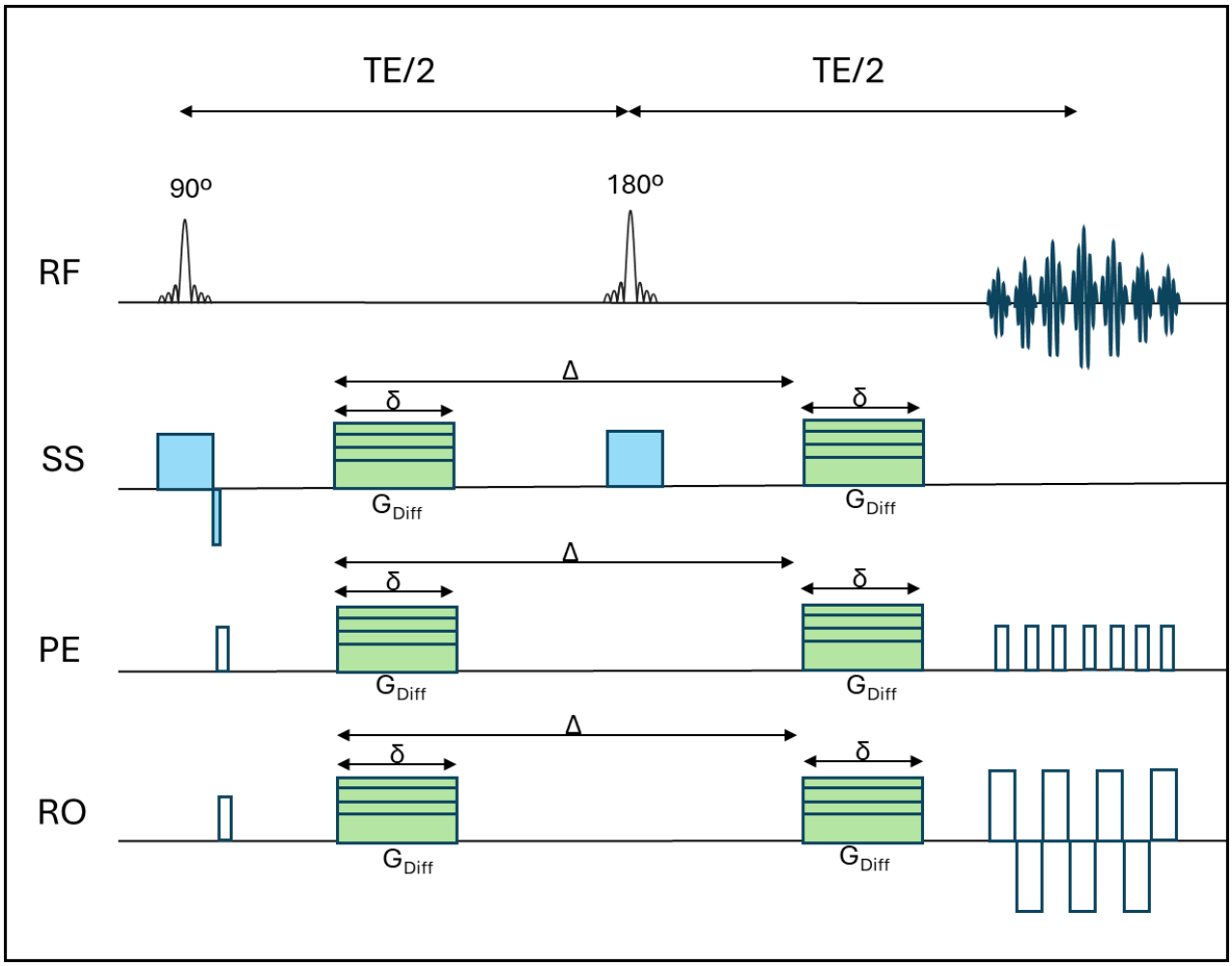


Figure 6. DTI pulse sequence diagram using three pairs of diffusion sensitizing gradients, one for each spatial axis (x, y, z), on spin-echo echo planar imaging (SE-EPI). Diffusion gradients (G_{Diff}) for each spatial axis occur simultaneously with varying amplitudes. MR signal is acquired using an EPI echo train. RF: radiofrequency; SS: slice selection; PE: phase encoding; RO: readout; G_{Diff}: diffusion gradient; δ: diffusion gradient duration; Δ: diffusion time.

In DTI, the signal measured with each diffusion direction for each voxel is then used to build a diffusion (D) tensor with diagonal and off-diagonal elements, which will be used to represent the directionality of diffusion in tissues:

$$D = \begin{bmatrix} D_{xx} & D_{xy} & D_{xz} \\ D_{yx} & D_{yy} & D_{yz} \\ D_{zx} & D_{zy} & D_{zz} \end{bmatrix}$$

Since off-diagonal elements in the tensor are symmetric ($D_{xy} = D_{yx}$, $D_{xz} = D_{zx}$, $D_{yz} = D_{zy}$), the diffusion tensor has six unique parameters that need to be estimated, three diagonal (D_{xx}, D_{yy}, D_{zz}) and three off-diagonal (D_{xy}, D_{xz}, D_{yz}). This can be achieved with a minimum acquisition of 6 non-collinear diffusion directions, but increasing the number of acquired directions will improve estimations' accuracy [76–78].

From the diffusion tensor, three principal eigenvectors can be extracted (ε_1, ε_2, ε_3), each with a corresponding eigenvalue. These eigenvalues (λ_1, λ_2, λ_3) numbered from largest to smallest, represent the three orthogonal diffusion coefficients in the diffusion frame of each voxel. In an isotropic diffusion scenario, the three eigenvalues would be equal, while this would not be the case for anisotropic scenarios, as represented in Figure 7.

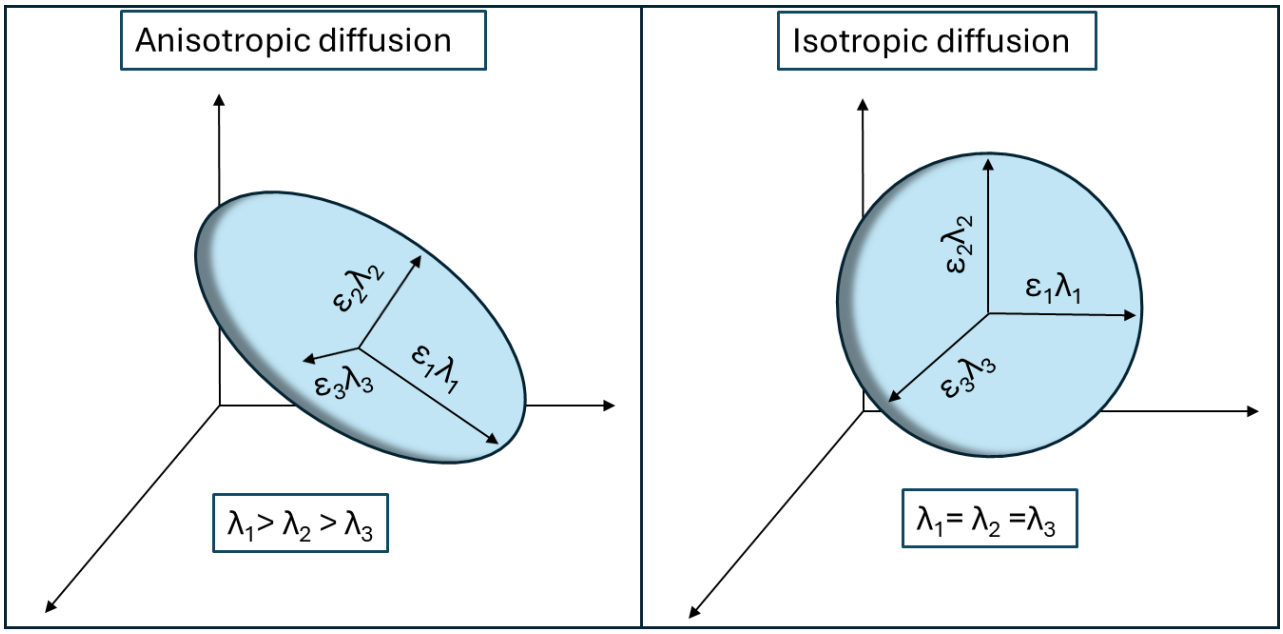


Figure 7. Anisotropic and isotropic diffusion representation. $\varepsilon_{1\text{-}3}$ represent the three principal eigenvectors of the diffusion frame of reference, and $\lambda_{1\text{-}3}$ represent the corresponding eigenvalues. The eigenvalues differ from each other in an anisotropic scenario - represented as an ellipse, while being equal in an isotropic scenario – represented as a sphere.

From the diffusion coefficients, mean diffusivity (MD), axial diffusivity (AD), radial diffusivity (RD) and fractional anisotropy (FA) maps can be calculated. MD is calculated as the average diffusion coefficient:

$$MD = \frac{\lambda_1 + \lambda_2 + \lambda_3}{3}$$

AD is the largest diffusion coefficient of each voxel, as such equal to λ_1. If considering tubular microstructures (ex.: axons in the nervous system), AD would represent the diffusion along the long axis of these structures. In the same scenario, the short axis of tubular structures can be represented as RD, which is calculated as the average of the two smaller diffusion coefficients:

$$RD = \frac{\lambda_2 + \lambda_3}{2}$$

Using the diffusion tensor, one can also quantify the amount of diffusion anisotropy, i.e., how much the measured diffusion differs from a perfectly isotropic scenario, as fractional anisotropy (FA) [76]:

$$FA = \sqrt{{}^{3}/_{2}\left((\lambda_1 - \mathrm{MD})^2 + (\lambda_2 - \mathrm{MD})^2 + (\lambda_3 - \mathrm{MD})^2\right)/(\lambda_1^2 + \lambda_2^2 + \lambda_3^2)}$$

Making use of its ability to characterize microstructure, and especially tubular structures (such as axonal bundles), DTI has become a well-established technique for neuroimaging, mainly for tractography, but has also been studied for brain tumors, schizophrenia, neurodegenerative diseases, epilepsy, and peripheral nerve imaging [79–83]. Besides neuroimaging, its use is still very limited, with some studies revealing potential for breast and musculoskeletal imaging and reporting preliminary data on abdominal organs [83–86]. Specifically for the pancreas, DTI has been determined as a feasible technique and explored for characterizing acute pancreatitis [86, 87].

1.4.3. Diffusion kurtosis imaging

Diffusion kurtosis imaging (DKI) explores the deviation of diffusion measurements from a Gaussian distribution. The net displacement of water molecules presents a Gaussian distribution when diffusing in a homogeneous medium. However, in biological tissues, water molecules are located in a heterogeneous medium, with different microscopic compartments, which pose multiple obstacles for diffusion. Thus, water molecules' ability to travel long distances (the extremes in a Gaussian distribution), becomes limited due to microstructural complexity. In such scenarios, the probability distribution of water molecules becomes more peaked, i.e., with positive kurtosis (Figure 8).

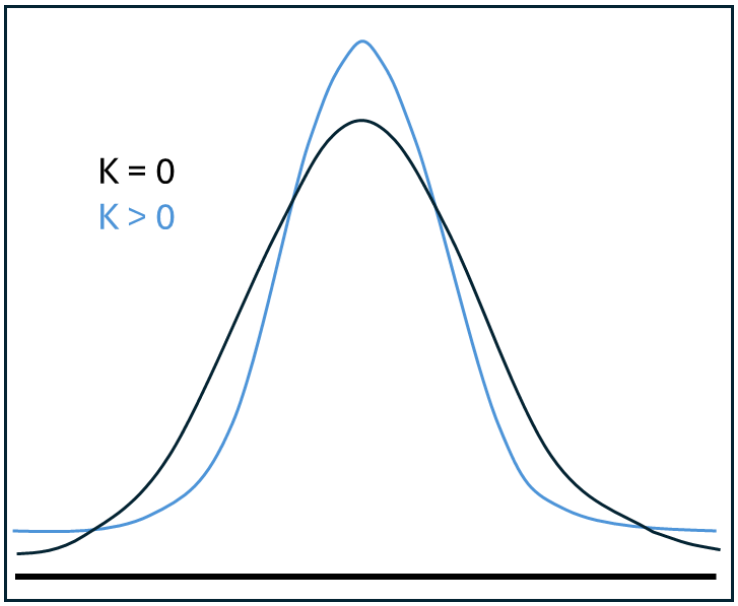


Figure 8. Representation of Gaussian distribution and positive Kurtosis. Note the peaked distribution with positive kurtosis (blue).

Using DKI, one can quantify the apparent kurtosis coefficient (K) from diffusion-weighted signal for any given direction, and determine the apparent diffusion coefficient (D) separate from excess kurtosis [88]:

$$S(b) = S_0 e^{(-bD+\frac{1}{6}b^2D^2K)}$$

Importantly, not any b values can be used for DKI acquisitions. The kurtosis effects on diffusion-weighted signal attenuation are only observed with high b values, from approximately 1500 s/mm^2 and above, and acquiring at least 3 different b values (ex.: 0,

1000, 2000 s/mm^2) is recommended for fitting the DKI parameters [89, 90]. The representation of kurtosis effects on diffusion-weighted signal attenuation as a function of b value is presented in Figure 9.

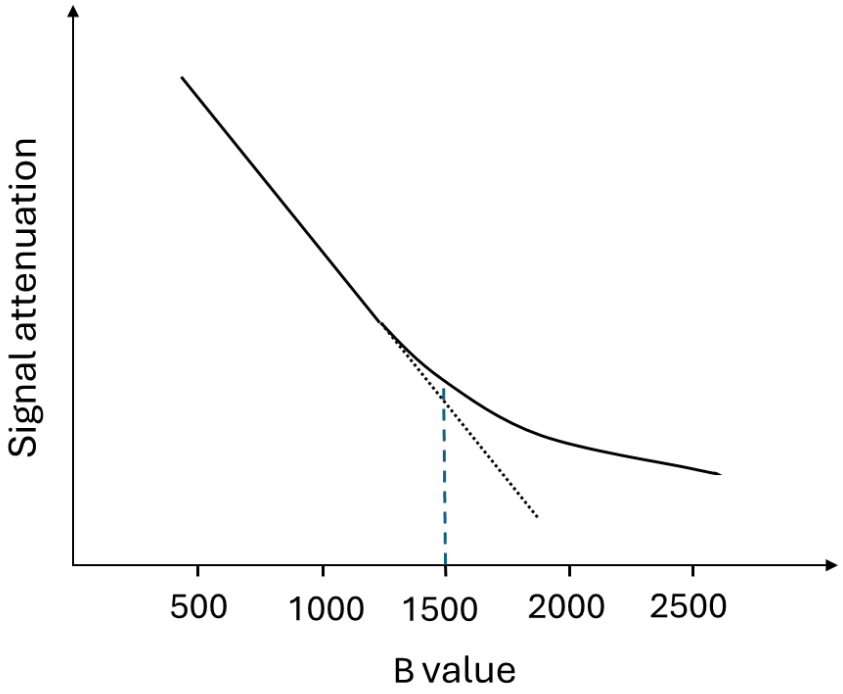


Figure 9. Signal attenuation as a function of b value for demonstrating kurtosis effects. The measured signal attenuation rate becomes reduced from high b values, of approximately 1500 s/mm^2 upwards, deviating from the expected attenuation in the linear diffusion model (dashed line). This lower attenuation at high b values translates into kurtosis excess.

Diffusion kurtosis also entails directional dependence; as such, a diffusion kurtosis tensor can be built for DKI, where kurtosis excess (K) is measured for each spatial axis along an apparent diffusion coefficient (D). From this tensor, and analogous to DTI, the following metrics can be derived: axial kurtosis (AK), radial kurtosis (RK) and mean kurtosis (MK). DKI acquisitions can then become quite demanding, with a minimum number of 15 diffusion directions and 3 b values [89]. Nevertheless, a scalar kurtosis quantification surrogate to MK can be robustly estimated from the averaged signals of all diffusion directions, without calculating the full kurtosis tensor, and facilitating acquisition demands [91–93].

Several studies have explored DKI in a variety of clinical settings; however, it has not yet reached the widespread usage of DTI. For neuroimaging, DKI has been shown to be useful in characterizing ischemia and infarction, neoplasms and neurodegenerative diseases [94–99]. For body imaging, DKI has been explored with promising results for cancers of the prostate, head and neck, breast and liver, and for assessing pancreatic changes associated with Diabetes Mellitus [100–105].

Chapter II.

Rationale and Aims

2.1. Response assessment to neoadjuvant therapy in pancreatic cancer

Assessing response to neoadjuvant therapy (NAT) in pancreatic cancer remains a clinical challenge. Radiological assessment is still based on size measurements, which are known to be inadequate. DWI has been used for pancreatic imaging for a long time, and several studies reported its use as a biomarker for NAT response assessment, but with conflicting results. Thus, clarification of DWI's role for assessing response to neoadjuvant therapy in pancreatic cancer was needed. For this, a systematic review and meta-analysis of the literature on this topic was conducted.

Aim: to determine the role of DWI for predicting response NAT in pancreatic cancer.

Published study [106]: Bilreiro C, Andrade L, Marques RM, Matos C. Diffusion-weighted imaging for determining response to neoadjuvant therapy in pancreatic cancer: a systematic review and meta-analysis. Eur Radiol. 2024; 34(5):3238-3248. doi: 10.1007/s00330-023-10381-0.

2.2. Imaging of the most relevant precursor lesions for pancreatic cancer – PanIN

Detecting the most important premalignant lesions for pancreatic ductal adenocarcinoma, mainly pancreatic intraepithelial neoplasia (PanIN), could provide opportunities for early diagnosis, and allow a further understanding of PanIN biology. Here, efforts were directed at developing methods for imaging PanIN in a pre-clinical context.

2.2.1. Development of a bowel motion reduction protocol for mouse abdominal MRI

Performing MRI of the mouse abdomen is a technical challenge due to image artifacts, which become especially relevant for diffusion-weighted techniques. One of the major contributors to these artifacts is physiologic bowel motion, which is not adequately addressed by current motion prevention or correction methods. We explored the use of different dosages of hyoscine butylbromide (BUSC) for bowel motion reduction in mice, and compared it with a commonly reported fasting protocol. The protocols' efficacy and duration were assessed visually and quantitatively using cine-like acquisitions, and the occurrence of motion artifacts was recorded for each protocol.

Aim: to develop a bowel motion reduction protocol for mouse abdominal MRI, comparing fasting and administration of different dosages of hyoscine butylbromide (Buscopan®).

Published study [107]: Bilreiro C, Fernandes FF, Andrade L, Chavarrías C, Simões RV, Matos C, Shemesh N. Effective bowel motion reduction in mouse abdominal MRI using hyoscine butylbromide. Magn Reson Med. 2021; 86(4):2146-2155. doi: 10.1002/mrm.28824.

2.2.2. Longitudinal assessment of PanIN and PDAC development onset

Based on PanIN's histology, we hypothesized that diffusion tensor imaging (DTI) and T2* contrasts could be used to detect and characterize PanIN, due to the grossly lamellar organization of fibrosis around PanIN and to its mucin content, as observed on preliminary findings. After developing the protocol for bowel motion reduction in mouse MRI described in 2.1, we set our efforts on imaging genetically engineered mouse models (GEMM), specifically the KC and KPC models which develop PanIN and pancreatic ductal adenocarcinoma (PDAC).

First, we needed to determine when pancreatic changes occur during the lifetime of GEMM, in order to validate our mouse models and to plan the following *in vivo* and *ex vivo* DTI experiments. A longitudinal study with periodical anatomical (T2-weighted) imaging after weaning of the GEMM was therefore conducted.

Aim: to determine the onset of detectable pancreatic abnormalities on GEMM with MRI.

2.2.3. In vivo DTI of the pancreas

After determining the age of onset of pancreatic changes in our GEMM, a DTI evaluation of GEMM and healthy controls was then planned for PanIN and PDAC detection, in live animals. We wanted to explore DTI's diagnostic usefulness in live animals, to assess its potential as a noninvasive tool for PanIN and PDAC detection and characterization. Such a tool could become useful in pre-clinical studies for PanIN / PDAC carcinogenesis and therapeutic response assessment.

Aim: to determine the feasibility and diagnostic usefulness of DTI for *in vivo* imaging of the pancreas of GEMM.

2.2.4. Magnetic Resonance Microscopy of GEMM pancreatic specimens

Our previous *in vivo* results revealed the diagnostic potential of DTI for PanIN, with DTI-derived maps providing image contrasts for the diseased and normal pancreas of the GEMM and control mice, respectively. Further characterization of these contrasts could facilitate understanding of their underlying pathological processes, and validate our diagnostic assumptions for PanIN. This was achieved through MR Microscopy – ultrahigh resolution imaging, enabling a direct correlation with microscopic findings in histology slides. Furthermore, histological characterizations of disease burden and severity allowed us to quantitatively correlate MRI biomarkers with histology.

Aim: to investigate the pathological sources of DTI contrasts in pancreatic specimens of GEMM, using MR Microscopy with histological correlation.

2.2.5. Human pancreatic specimens

Fundamental to determining clinical translation potential, the efficacy of DTI in the human pancreas needed to be explored. As GEMM do not fully recapitulate human pathology, the question of whether the DTI contrasts would still be useful for humans, as they were for mice, was crucial. Thus, we imaged pancreatic specimens from patients subjected to surgical resection, using MR Microscopy with histological correlation as a validation method.

Aim: to assess the usefulness of DTI contrasts in the human pancreas for PanIN detection.

Published study [108]: Bilreiro C, Fernandes FF, Simões RV, Henriques R, Chavarrías C, Ianus A, Castillo-Martin M, Carvalho T, Matos C, Shemesh N. Pancreatic Intraepithelial

Neoplasia Revealed by Diffusion-Tensor MRI. Invest Radiol. 2024. doi: 10.1097/RLI.0000000000001142.

2.3. Diffusion tensor imaging and Diffusion kurtosis imaging of the pancreas in the clinical setting

DTI and Diffusion Kurtosis Imaging (DKI) are largely unexplored for pancreatic imaging. Before being tested in a clinical setting for specific pathologies, issues such as optimal acquisition parameters, technical feasibility, image quality, repeatability and inter-reader variability should be determined.

Aim: to determine the feasibility, image quality, intra-subject repeatability and inter-reader variability of DTI and DKI for pancreatic imaging using different protocols and report normative values in healthy individuals.

Study accepted for publication in Abdominal Radiology on 10/03/2025: Bilreiro C, Andrade L, Henriques R, Loução N, Shemesh N, Matos C. Diffusion Tensor Imaging and Diffusion Kurtosis Imaging of the Pancreas - Feasibility, Robustness and Protocol comparison in a Healthy population.

Chapter III.

Results

3.1. Diffusion-weighted imaging for determining response to neoadjuvant therapy in pancreatic cancer: a systematic review and meta-analysis.

Bilreiro C, Andrade L, Marques RM, Matos C.

Eur Radiol. 2024; 34(5):3238-3248.

doi: 10.1007/s00330-023-10381-0

Bilreiro *et al. European Radiology* (2024) 34:3238–3248
https://doi.org/10.1007/s00330-023-10381-0

EUROPEAN SOCIETY OF RADIOLOGY
European Radiology

HEPATOBILIARY-PANCREAS

Diffusion-weighted imaging for determining response to neoadjuvant therapy in pancreatic cancer: a systematic review and meta-analysis

Carlos Bilreiro[1,2,3*], Luísa Andrade[1], Rui Mateus Marques[3,4] and Celso Matos[1,2]

Abstract

Objectives To determine the role of diffusion-weighted imaging (DWI) for predicting response to neoadjuvant therapy (NAT) in pancreatic cancer.

Materials and methods MEDLINE, EMBASE, and Cochrane Library databases were searched for studies evaluating the performance of apparent diffusion coefficient (ADC) to assess response to NAT. Data extracted included ADC pre- and post-NAT, for predicting response as defined by imaging, histopathology, or clinical reference standards. ADC values were compared with standardized mean differences. Risk of bias was assessed using the Quality Assessment of Diagnostic Studies (QUADAS-2).

Results Of 337 studies, 7 were included in the analysis (161 patients). ADC values reported for the pre- and post-NAT assessments overlapped between responders and non-responders. One study reported inability of ADC increase after NAT for distinguishing responders and non-responders. A correlation with histopathological response was reported for pre- and post-NAT ADC in 4 studies. DWI's diagnostic performance was reported to be high in three studies, with a 91.6–100% sensitivity and 62.5–94.7% specificity. Finally, heterogeneity and high risk of bias were identified across studies, affecting the domains of patient selection, index test, reference standard, and flow and timing.

Conclusion DWI might be useful for determining response to NAT in pancreatic cancer. However, there are still too few studies on this matter, which are also heterogeneous and at high risk for bias. Further studies with standardized procedures for data acquisition and accurate reference standards are needed.

Clinical relevance statement Diffusion-weighted MRI might be useful for assessing response to neoadjuvant therapy in pancreatic cancer. However, further studies with robust data are needed to provide specific recommendations for clinical practice.

Key Points

- *The role of DWI with ADC measurements for assessing response to neoadjuvant therapy in pancreatic cancer is still unclear.*
- *Pre- and post-neoadjuvant therapy ADC values overlap between responders and non-responders.*
- *DWI has a reported high diagnostic performance for determining response when using histopathological or clinical reference standards; however, studies are still few and at high risk for bias.*

Keywords Diffusion magnetic resonance imaging, Neoadjuvant therapy, Pancreatic carcinoma, Meta-analysis

*Correspondence:
Carlos Bilreiro
carlosbilreiro@hotmail.com
Full list of author information is available at the end of the article

Springer

© The Author(s) 2023. **Open Access** This article is licensed under a Creative Commons Attribution 4.0 International License, which permits use, sharing, adaptation, distribution and reproduction in any medium or format, as long as you give appropriate credit to the original author(s) and the source, provide a link to the Creative Commons licence, and indicate if changes were made. The images or other third party material in this article are included in the article's Creative Commons licence, unless indicated otherwise in a credit line to the material. If material is not included in the article's Creative Commons licence and your intended use is not permitted by statutory regulation or exceeds the permitted use, you will need to obtain permission directly from the copyright holder. To view a copy of this licence, visit http://creativecommons.org/licenses/by/4.0/.

Introduction

Pancreatic cancer is one of the most lethal cancers worldwide, with surgical resection as the only potentially curative therapeutic option [1, 2]. Nevertheless, most patients are not surgical candidates, many presenting with locally advanced disease. These patients can undergo neoadjuvant chemotherapy or chemoradiotherapy, attempting to downstage the disease and allowing a successful surgical resection [3]. Evaluating these patients, however, is a difficult task, as imaging studies do not accurately reflect response to neoadjuvant therapy (NAT) [4–7]. Traditional size criteria in cross-sectional imaging are known to be unreliable, as the primary pancreatic lesion may undergo minimal or no size reduction, due to remaining tumoral fibrotic stroma even when a response in the cancer cells has already occurred [8].

Diffusion-weighted MRI (DWI), quantified by apparent diffusion coefficient (ADC), is a cornerstone in the MRI evaluation of pancreatic cancer, especially for diagnostic purposes [9]. This technique probes microstructural characteristics of biological tissues, namely cell density and extracellular compartment's composition, therefore being regarded as a useful biomarker for characterizing neoplastic lesions [10, 11]. However, its value in the assessment of response to NAT in pancreatic cancer is still undetermined, as studies have reported inconclusive and diverse results, both regarding the classification of patients as responders and non-responders and the correlation with histopathological response [12–16].

This study aims to determine the role of DWI in the evaluation of response to NAT in pancreatic cancer, by systematically reviewing the published literature and performing a meta-analysis of reported data.

Materials and methods

This study is presented according to the Preferred Reporting Items for Systematic Reviews and Meta-Analyses (PRISMA) [17]. The study protocol was registered in an international database prior to data search and collection — PROSPERO: CRD42022309467 [18]. Eligibility criteria were defined according to the following PICOs: (P) patients with pancreatic cancer undergoing neoadjuvant chemotherapy, radiotherapy, or chemoradiotherapy; (I) diffusion-weighted MRI (DWI) is the index test; (C) no comparison is to be performed; (O) outcome is assessed with an acceptable reference standard for determining response status to NAT — post-operative histopathology, clinical follow-up, imaging follow-up.

Search strategy

MEDLINE, EMBASE, and Cochrane Library (Cochrane Database of Systematic Reviews, Cochrane Central Register of Controlled Trials, Cochrane Clinical Answers) databases were used for the literature search, and the final search was undertaken on 17/01/2023. The search strategy was first defined by an abdominal radiologist with 4 years of experience (C.B.), and reviewed by two radiologists (L.A. and C.M., with 7 and 35 years of experience, respectively). The search query including title and abstract was the following: "pancreatic OR pancreas AND neoadjuvant OR chemotherapy OR radiotherapy OR chemoradiotherapy AND diffusion OR apparent diffusion coefficient OR ADC OR diffusion-weighted MRI OR DWI." Only studies in the English literature were included; study publication dates were not restricted to a certain period.

The search results were first filtered for relevance by title and abstract review by two reviewers (C.B. and L.A.); the same reviewers then independently performed the full-text reviews of the resulting studies, determining if these fulfilled the criteria for inclusion and solving discrepancies in a consensus meeting. Finally, reference lists of the included studies were additionally searched for more relevant studies.

Inclusion criteria

Patients were included according to the following: diagnosis of pancreatic cancer; NAT was performed with chemo-, radio-, or chemoradiotherapy; DWI with retrievable ADC measurements was reported for tumor imaging before, after, or before and after NAT; a measure of response to NAT was provided, including histopathological response scores, clinical follow-up evaluation, correlation with RECIST criteria.

Exclusion criteria

If studies were found using overlapping groups of patients, one of the studies would be excluded to avoid duplication of included patients. Studies where a reference standard was not used to determine response to NAT were excluded. Studies including metastatic (stage IV) patients were excluded, in order to exclude patients undergoing palliative and not neoadjuvant therapy. As only human data was collected, studies performed in animals were excluded. Conference abstracts, letters, and comments were excluded from the analysis.

Risk of bias assessment

A QUADAS-2 assessment tool was used, based on the domains of patient selection, index test, reference standard, and flow and timing [19]. The tool was adapted to the current review by C.B. and L.A. in consensus, defining quality standards for each of the domains assessed, and then applied by both authors independently to the included studies. Discrepancies in evaluation between both readers were solved in a consensus meeting.

Data extraction

Two authors (C.B. and L.A.) independently extracted the following data: first author name, year of publication, journal name, type of study (retrospective, prospective), institution(s) and study dates, number of patients, patients' age, resectability status, chemotherapy and/or radiotherapy details (protocols and timings), MR system field strength, DWI acquisition *b* values, DWI timing (before and/or after NAT), MRI readers' experience, tumor location in the pancreas, tumor size pre- and post-NAT, ADC values pre- and post-NAT for responders and non-responders, histopathological analysis for NAT response grading, clinical follow-up data when used to determine response to NAT.

Whenever possible, ADC data was retrieved as a 2×2 table, as defined: true positives were cases where a positive index text was confirmed with the reference standard; true negatives were cases where a negative index test was confirmed with the reference standard; false positives were cases where a positive index test was not confirmed with the reference standard; false negatives were cases where a negative index test was not confirmed with the reference standard.

When available, Pearson's correlation coefficient values between ADC and histological response grades were retrieved, including ADC measurement timing (pre- or post-NAT) and histological grading system (based either on Evans or College of American Pathologists classification systems) [20, 21].

When the published data for any specific study was considered insufficient or incomplete, an attempt to contact the study's corresponding author by e-mail was conducted, and the new data added to the analysis, if then provided.

Data analysis

The collected data regarding pre-NAT ADC values in responders and non-responders were summarized in forest plots.

Standardized mean differences with random effects and *Z* test for overall effects were used for comparing ADC values in the pre-NAT period, between responders and non-responders.

Sources of heterogeneity between studies were recorded and qualitatively discussed [22].

Data extraction and analysis were performed using Microsoft Excel® and Review Manager (RevMan) 5.4. (The Cochrane Collaboration, 2020).

Results

The initial search yielded 337 studies; after removal of duplicates, title and abstract screening, and full-text screening, 7 studies with 161 patients (6–41 patients per study) were finally included (Fig. 1) [12–14, 23–26]. One study's corresponding author was contacted with a request for further information: however, a reply was not obtained.

Studies' and patients' characteristics

The included studies' characteristics are described in Table 1. Most studies were recent (6/7 from 2017 onwards; date range of publication: 2014–2022), and

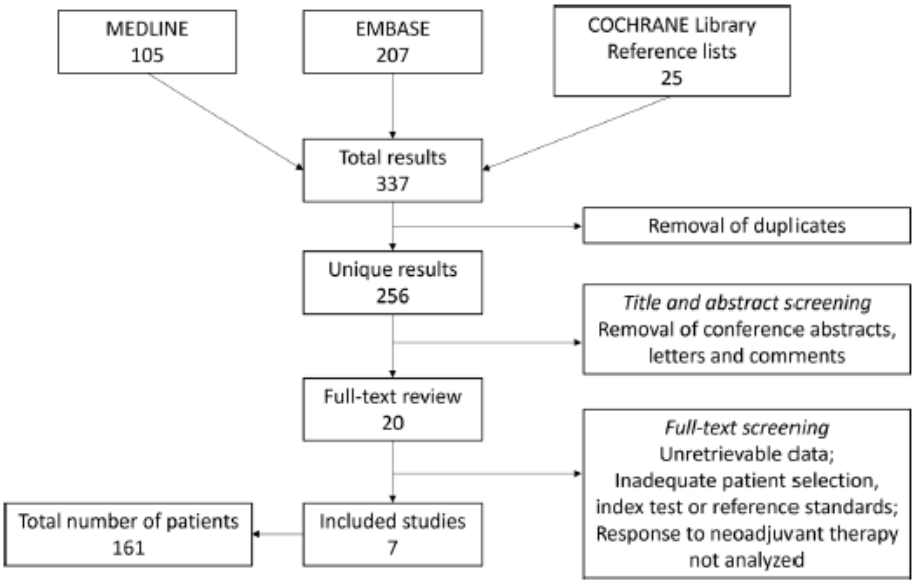


Fig. 1 Study flowchart

Table 1 Studies characteristics

Study	Journal	Year	Study design	Magnetic field	*B* values (s/mm^2)	Number of readers	Readers experience	ROI drawing process	DWI timing	Reference standard
Cuneo KC, et al [23]	*Transl Oncol*	2014	Prospective	ND	0, 100, 500, 800	2	Radiologist + researcher (ND)	Manual delineation of tumor volume	Before NT	Pathological (Evans)
Dalah E, et al [24]	*Transl Oncol*	2018	Retrospective	3 T	0, 500, 1000	ND	ND	Manual delineation of tumor volume	After NT	Pathological (CAP)
Hussien N, et al [12]	*Front Oncol*	2022	Prospective	3 T	0, 400, 800	ND	ND	ND	Before and after NT	Clinical (multidisciplinary — surgical indication)
Kang JH, et al [14]	*Eur Radiol*	2021	Prospective	3 T	0, 30, 60, 120, 200, 400, 800	2	Radiologists (8+ 10 years)	Average of two largest manual cross-sectional ROIs; intra- and inter-observer variability assessed	Before and after NT	RECIST 1.1 + tumor-vessel contact
Kinh Do R, et al [25]	*Tomography*	2020	Prospective	3 T	0, 500	ND	Radiologists + radiation oncologists (ND)	Manual delineation of tumor ROIs	Before and after NT	RECIST 1.1
Okada KI, et al [26]	*J Hepatobiliary Pancreat Sci*	2017	Retrospective	1.5 T	0, 50, 800	2	Radiologists (2)	Manual ROI: largest cross-sectional area based on CT	Before and after NT	Pathological (Evans)
Okada KI, et al [13]	*Langenbecks Arch Surg*	2020	Prospective	3 T	0, 50, 1000	1	Radiologist (1)	Manual ROIs: 3–4 largest cross-sectional areas based on CT	Before and after NT	Pathological (Evans and CAP)

ND, non-disclosed; *NT*, neoadjuvant therapy; *NM*, nuclear medicine consultant; *CAP*, College of American Pathologists; *CT*, computerized tomography; *ROI*, region of interest

prospective (5/7 prospective). Five out of seven studies were performed on 3-T MRI systems, and most (6/7) used high *b* values for DWI (800 s/mm^2 and higher). All studies used mono-exponential models for ADC calculations. The number and experience of readers were inconsistently reported. Most studies (5/7) performed DWI before and after NAT. For determining response to NAT, 4 studies used histopathological criteria (3 using a modified Evans classification, 1 using the College of American Pathologists classification), 2 studies used RECIST 1.1 criteria, and 1 study used clinical criteria (multidisciplinary assessment of surgical indication).

Included patients' characteristics are summarized in Table 2. The number of patients included in each study ranged from 6 to 41, and the patients' mean age ranged from 52.5 to 69 years. Most studies (5/7) included borderline resectable patients; 2/7 included locally advanced patients. Six studies described tumor locations, most often in the head of the pancreas (5/6). Mean tumor size pre-NAT ranged from 27.8 to 51.5 mm, and post-NAT ranged from 22.3 to 55.5 mm. Chemotherapy regimens varied, gemcitabine being included in most studies (6/7); 4 studies included radiotherapy.

DWI for response assessment

Table 3 summarizes ADC measurements and their performance in assessing response to NAT. ADC values overlapped for responders and non-responders between studies: in the pre-NAT period, these ranged from 1.0 to 1.61×10^{-3} mm^2/s for responders, and from 1.25 to 1.5×10^{-3} mm^2/s for non-responders. In the post-NAT period, only one included study reported ADC values: 1.4×10^{-3} mm^2/s for responders, and 1.3×10^{-3} mm^2/s for non-responders. One study reported ADC increase from the pre- to the post-NAT period: 14.9% for responders and 10.3% for non-responders.

Two studies, both using RECIST 1.1 criteria for assessing response status, reported no significant differences in ADC values for differentiating responders from non-responders [14, 25]. All other studies (5/7) reported ADC being able to determine response status, using histopathological or clinical criteria as reference standard. The 4 studies evaluating histopathological response (Table 4) reported a correlation between both pre- and post-NAT ADC values and response grade, which was positive when using the modified Evan's classification and negative when using the College of American Pathologists' classification [13, 23, 24, 26].

Three studies reported DWI's diagnostic performance, with sensitivity values ranging from 91.6 to 100% and specificity values from 62.5 to 94.7% [12, 13, 26]. Noteworthy, these studies used different criteria for determining response status: stationary vs. regressive ADC; pre-NAT ADC$\geq1.2\times10^{-3}$ mm^2/s; post-NAT ADC$\geq1.4\times10^{-3}$ mm^2/s.

Synthesis of collected data

Figure 2 summarizes the pooled analysis for pre-NAT ADC values reported in responders and non-responders. When testing for overall effects, ADC values were not significantly different between groups of patients ($Z=1.39$, $p=0.16$, $I^2=30\%$).

Studies were considered too few and heterogeneous to perform a pooled analysis regarding post-NAT ADC values (1 study), ADC variance from pre- to post-NAT (1 study), and diagnostic performance with summary ROC statistics (3 studies with high heterogeneity).

Risk of bias and heterogeneity

Figure 3 illustrates the QUADAS-2 evaluation results, regarding risk of bias and applicability concerns. High risk of bias and applicability concerns were identified across studies, especially for patient selection, but also for the other domains. The main causes for concern regarding patient selection were the exclusion of borderline or locally advanced stages, retrospective studies, non-disclosure of resectability criteria, and patients excluded due to missing or inadequate index test. For the reference standard, the dependance on RECIST criteria, interpretation of the reference standard with knowledge of the index test (DWI), and the use of clinical multidisciplinary evaluation were considered the major causes of concern. Regarding the index test, the major sources of concern stemmed from reader's number and experience not being disclosed, region of interest (ROI) drawing process not being disclosed or vaguely described, the use of poorly defined diagnostic criteria, and the use of highest *b* values lower than the usual standards (500 s/mm^2). Finally, in the flow and timing domain, concerns were expressed due to widely variable MRI timings both before and after NAT.

Heterogeneity was also analyzed in a qualitative manner across studies. Regarding the reference standard, the use of RECIST 1.1 criteria was considered a probable source of heterogeneity, as the two studies using it did not report ADC to be of diagnostic value while all others did, when using either clinical or histopathological criteria. For the studies using histopathological response assessment, the correlation coefficients with ADC values were positive when using the modified Evans classification and negative when using the College of American Pathologists classification [20, 21]. Since these classifications' gradings are the inverse of each other — higher tumor cell destruction translates into higher degrees in the Evans but lower degrees in the College of American Pathologists classifications — the results between

Table 2 Patient, disease, and treatment data collected

Study	Number of patients	Age (years)	Initial staging	Resectability criteria	Tumor size (pre-NT)	Tumor size (post-NT)	Tumor location	Resection surgery	Chemotherapy	Radiotherapy
Cuneo KC, et al [23]	10 (7*)	60.7	Resectable	ND	ND	ND	ND	All patients	Gemcitabine + oxaliplatin	30 Gy in 2 fractions (method ND)
Dalah E, et al [24]	25	ND	Resectable and borderline	ND	37.79 ± 12.1 cc	9.75 ± 5.93 cc	100% head	All patients	Gemcitabine or Capecitabine + FOLFIRINOX or gemcitabine-Abraxane	50.4 Gy in 28 fractions, IMRT
Hussien N, et al [12]	30	52.5	Borderline	NCCN (v2.2012)	ND	ND	23.3% head 76.7% body/tail	11 patients	63.3% FOLFIRINOX 36.7% gemcitabine/cisplatin	No
Kang JH, et al [14]	41	60.3	Borderline and locally advanced	NCCN (v2.2017)	36 ± 8	ND	65.9% head 34.1% body/tail	25 patients	FOLFIRINOX	No
Kinh Do R, et al [25]	10 (6*)	64	Locally advanced	ND	51.5 ± 24.3	R: 42 ± 2.8 NR: 55.5 ± 26	50% head 50% body/tail	None	80% FOLFIRINOX 10% GEM/NAB 10% FOLFIRINOX + GEM/NAB	27–33 Gy in 3 fractions, SBRT
Okada KI, et al (2017) [26]	24	67	Borderline	NCCN (v2.2015)	28.9 ± 12.5	26.9 ± 12.2	54.2% head 45.8% body/tail	All patients	S-1 + gemcitabine or FIRINOX or GEM/NAB or S-1 + radiation	50 Gy, EBRT (4 patients)
Okada KI, et al (2020) [13]	28	69	Borderline	NCCN (v2.2015)	27.8 ± 9.36	22.3 ± 9.8	68% head 32% body/tail	All patients	GEM/NAB	No

* Number of patients eligible for response assessment. If not otherwise mentioned, tumor size is expressed in mm. *ND*, non-disclosed; *R*, responders; *NR*, non-responders; *pre-NT*, pre-neoadjuvant therapy; *post-NT*, post-neoadjuvant therapy; *NCCN*, National Comprehensive Cancer Network

Table 3 ADC measurements and response assessment

Study	R: pre-ADC	NR: pre-ADC	R: post-ADC	NR: post-ADC	R: ADC increase	NR: ADC increase	Response assessment	Diagnostic performance	
								Criteria	Sensitivity/specificity
Cuneo KC, et al [23]	1.61 ± 0.05	1.25 ± 0.16	ND	ND	ND	ND	Pre-ADC correlates with pathological response grade	NA	NA
Dalah E, et al [24]	ND	ND	ND	ND	ND	ND	Post-ADC correlates with pathological response	NA	NA
Hussien N, et al [12]	1.0 (1.0–1.3)	1.4 (1.0–1.4)	1.4 (1.3–1.7)	1.3 (1.0–1.7)	ND	ND	ADC increase in responders	Stationary vs. regressive ADC	100%/94.7%
Kang JH, et al [14]	1.46 ± 0.23	1.40 ± 0.19	ND	ND	14.9 ± 13.8%	10.3 ± 27.6%	No significant differences in ADC	NA	NA
Kinh Do R, et al [25]	1.60 ± 0.17	1.50 ± 0.05	ND	ND	ND	ND	No significant differences in ADC	NA	NA
Okada KI, et al (2017) [26]	ND	ND	ND	ND	ND	ND	Pre- and post-ADC correlate with pathological response grade	Pre-ADC (≥ 1.2)	100%/75%
Okada KI, et al (2020) [13]	ND	ND	ND	ND	ND	ND	Pre-ADC, post-ADC, and ADC increase correlate with pathological response grade	Pre-ADC (≥ 1.2) Post-ADC (≥ 1.4)	91.6%/62.5% 100%/81%

R, responders; *NR*, non-responders; *pre-ADC*, ADC value pre-neoadjuvant therapy; *post-ADC*, ADC value post-neoadjuvant therapy; *ND*, non-disclosed; *NA*, not assessed. ADC values ($\times 10^{-3}$ mm^2/s) are expressed as means ± standard deviations or medians and ranges (in parentheses)

Table 4 Correlation coefficients of studies using histopathological criteria to determine response to neoadjuvant therapy

Study	Classification	DWI timing	Correlation coefficient
Cuneo KC, et al [23]	Evans*	Pre	0.94* (p=0.001)
Dalah E, et al [24]	College of American Pathologists	Post	−0.52 (p<0.05)
Okada KI, et al (2017) [26]	Evans*	Pre	0.63 (p=0.001)
		Post	0.41 (p=0.144)
Okada KI, et al (2020) [13]	Evans*	Pre	0.63 (p<0.001)
		Post	0.71 (p<0.001)
		Pre/Post Difference	0.29 (p=0.138)

* Modified version of the Evans classification [20]. *Pre*, pre-neoadjuvant therapy; *Post*, post-neoadjuvant therapy

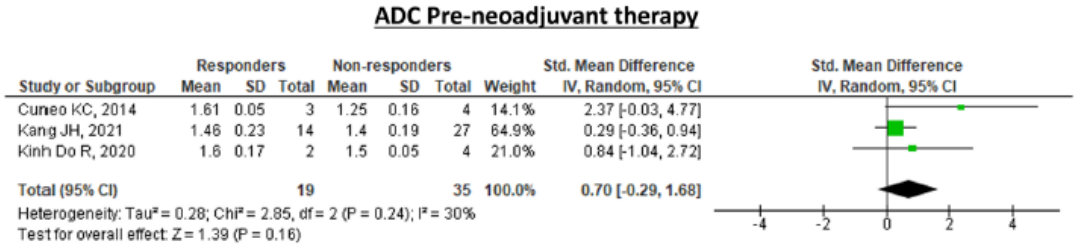


Fig. 2 Pooled analysis results of ADC values pre-neoadjuvant therapy. Test for overall effects was not statistically significant, with $Z = 1.39$ ($p = 0.16$)

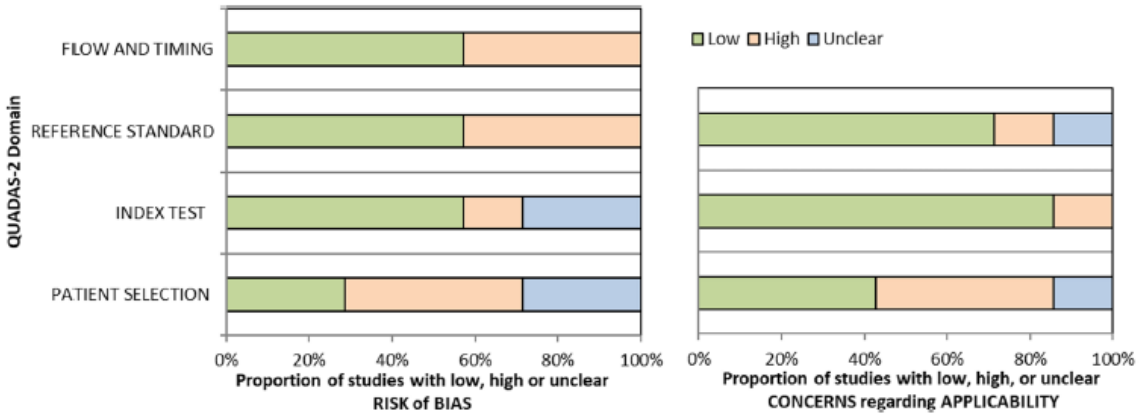


Fig. 3 QUADAS-2 chart, representing the estimated risk for bias and applicability concerns for all studies included

studies can be considered concordant, as higher pre- and post-NAT ADC values correlate with higher tumor cell destruction. Another identified source of heterogeneity directly influencing ADC values obtained in each study was the variability in *b* values used for ADC calculation. Although 1/7 studies used low *b* values for ADC calculation, also used for IVIM (intravascular incoherent motion) assessment, this study also used a mono-exponential calculation method for ADC. Also, 1/7 studies used highest *b* values lower than the usual standards (500 s/mm^2), while all other studies used *b* values of 800–1000 s/mm^2.

Discussion

This systematic review determines that DWI with ADC values for the assessment of response to NAT in pancreatic cancer may be useful, with reported high diagnostic performance. However, the included number of studies was small and high risk for bias was identified across studies, prompting a cautious interpretation of these results.

As ADC values observed across studies overlapped for responders and non-responders and no overall effects were seen in the pre-NAT period, an evaluation of absolute ADC values for this purpose appears to not be useful. The reproducibility of ADC values in the pancreas has been shown to be imperfect, and some variability should be expected across individuals, MRI scanners, and even anatomical regions of the pancreas [27–31]. Despite this, a correlation between ADC values and histopathological response was reported in 4 studies, both for the pre- and post-NAT assessments; therefore, high ADC values may still have a role in predicting response to NAT, but more studies providing further characterization in this regard are needed.

Technical issues affecting the reproducibility of ADC values were an important concern in this study, with values varying widely between studies, for both responders and non-responders. For future studies, the use of standardized protocols for image acquisition with motion-robust techniques, post-processing and corrective methods should be effective for diminishing these differences and improve ADC values' reproducibility [32–37]. Also, the process of ROI placement for ADC measurement, which was inconsistently reported in studies in this review, is known to have inherent variability [38, 39]. This is another aspect that could be improved in further studies, exploring the variability of ADC measurements

derived from the measurement process itself, and its effect on the magnitude of ADC differences between groups of responders and non-responders.

The diagnostic performance of DWI for determining response to NAT was high in all three included studies, which is encouraging for implementing its use in clinical practice. Nevertheless, studies used both different DWI-based metrics (1/3 used an ADC increase measure; 2/3 used cutoff ADC values) and different reference standards for this purpose (1/3 clinical; 2/3 histopathological). Therefore, the most adequate methodology when using DWI to differentiate responders from non-responders remains undetermined.

Response assessment after NAT in pancreatic cancer remains a challenge in clinical practice, with most centers relying on both analytical (serum CA19-9 concentration) and imaging data to assess response, the latter based on traditional size criteria: increase in tumor size being suggestive of progressive disease, stability or reduction in tumor size being considered a response and warranting surgical exploration [4, 40, 41]. This approach, however, may lead to unnecessary surgery being performed in cases of persistent advanced disease, or potentially resectable patients being excluded from surgery. Novel biomarkers have therefore been sought, with DWI emerging as a potential imaging candidate, but with inconclusive/insufficient results thus far [42–44]. Our analysis helps establishing DWI with ADC measurement as useful biomarker for assessing response, but current data is still not enough to recommend its implementation in clinical practice.

This systematic review and meta-analysis is limited by the small number of studies, which precluded subgroup analysis and statistical exploration of heterogeneity factors. Studies were also considered heterogeneous and at high risk for bias. We identified similar important sources for both heterogeneity and risk for bias, the most obvious being the variability in resectability status of patients included in each study, NAT regimens, DWI *b* values, readers' experience, and reference standards (RECIST, clinical and histopathological). In an ideal world, we would expect studies to replicate the best clinical practice and control for interfering variables — include all patients undergoing NAT, use only standardized NAT regimens and DWI acquisition parameters with experienced readers, and use the most accurate reference standards. However, these studies provide real-world data, reflecting the difficulties in managing patients with pancreatic cancer, with imperfect staging systems after NAT, and the evolution of NAT regimens and treatment recommendations in recent years [45, 46].

In conclusion, this systematic review and meta-analysis helps establish DWI as a useful biomarker for determining response to NAT in pancreatic cancer. However, few studies were included and were considered heterogeneous and at high risk for bias. Further data, best provided by studies with standardized procedures for data acquisition and accurate reference standards, are needed.

Abbreviations

ADC	Apparent diffusion coefficient
DWI	Diffusion-weighted imaging
MRI	Magnetic resonance imaging
NAT	Neoadjuvant therapy
NCCN	National Comprehensive Cancer Network
ROC	Receiver operating characteristics
ROI	Region of interest

Acknowledgements
The authors would like to thank the collaboration of Prof. Tiago Bilhim (Interventional Radiology Unit, Centro Hospitalar Universitário de Lisboa Central, Portugal) in the initial elaboration of the study's protocol, and the collaboration of Prof. Thierry Metens (Université Libre de Bruxelles, Brussels) in the final manuscript review with insightful discussions.

Funding
Open access funding provided by FCT|FCCN (b-on). The authors state that this work has not received any funding.

Declarations

Guarantor
The scientific guarantor of this publication is Dr. Celso Matos.

Conflict of interest
Carlos Bilreiro is a member of European Radiology's Editorial Board – Oncology section. They have not taken part in the review or selection process.
The other authors of this manuscript declare no relationships with any companies, whose products or services may be related to the subject matter of the article.

Statistics and biometry
One of the authors has significant statistical expertise.

Informed consent
Written informed consent was not required for this study because it is a systematic review and meta-analysis.

Ethical approval
Institutional Review Board approval was not required because this study is a systematic review and meta-analysis.

Study subjects or cohorts overlap
Since this study is a systematic review and meta-analysis, all data was collected from previously published studies.

Methodology
- diagnostic or prognostic study
- multicentre study

Author details
[1]Radiology Department, Champalimaud Foundation, Lisbon, Portugal. [2]Champalimaud Research, Champalimaud Foundation, Lisbon, Portugal. [3]Nova Medical School, Lisbon, Portugal. [4]Radiology Department, Hospital de S. José, Lisbon, Portugal.

Received: 4 August 2023 Revised: 15 September 2023
Accepted: 11 October 2023 Published: 1 November 2023

References

1. Siegel RL, Miller KD, Fuchs HE, Jemal A (2022) Cancer statistics, 2022. CA Cancer J Clin 72:7–33. https://doi.org/10.3322/CAAC.21708
2. Ducreux M, Cuhna AS, Caramella C et al (2015) Cancer of the pancreas: ESMO Clinical Practice Guidelines for diagnosis, treatment and follow-up. Ann Oncol 26(Suppl 5):v56–v68. https://doi.org/10.1093/ANNONC/MDV295
3. Gillen S, Schuster T, Meyer Zum Büschenfelde C, Friess H, Kleeff J (2010) Preoperative/neoadjuvant therapy in pancreatic cancer: a systematic review and meta-analysis of response and resection percentages. PLoS Med 7(4):e1000267. https://doi.org/10.1371/JOURNAL.PMED.1000267
4. Zins M, Matos C, Cassinotto C (2018) Pancreatic adenocarcinoma staging in the era of preoperative chemotherapy and radiation therapy. Radiology 287:374–390. https://doi.org/10.1148/RADIOL.2018171670
5. Cassinotto C, Cortade J, Belleannée G et al (2013) An evaluation of the accuracy of CT when determining resectability of pancreatic head adenocarcinoma after neoadjuvant treatment. Eur J Radiol 82:589–593. https://doi.org/10.1016/J.EJRAD.2012.12.002
6. Katz MHG, Fleming JB, Bhosale P et al (2012) Response of borderline resectable pancreatic cancer to neoadjuvant therapy is not reflected by radiographic indicators. Cancer 118:5749–5756. https://doi.org/10.1002/CNCR.27636
7. Wagner M, Antunes C, Pietrasz D et al (2017) CT evaluation after neoadjuvant FOLFIRINOX chemotherapy for borderline and locally advanced pancreatic adenocarcinoma. Eur Radiol 27:3104–3116. https://doi.org/10.1007/S00330-016-4632-8
8. Matsuda Y, Inoue Y, Hiratsuka M et al (2019) Encapsulating fibrosis following neoadjuvant chemotherapy is correlated with outcomes in patients with pancreatic cancer. PLoS One 14(9):e0222155. https://doi.org/10.1371/JOURNAL.PONE.0222155
9. Barral M, Taouli B, Guiu B et al (2015) Diffusion-weighted MR imaging of the pancreas: current status and recommendations. Radiology 274:45–63
10. Qayyum A (2009) Diffusion-weighted imaging in the abdomen and pelvis: concepts and applications. Radiographics 29:1797–1810. https://doi.org/10.1148/RG.296095521
11. Morone M, Bali MA, Tunariu N et al (2017) Whole-body MRI: current applications in oncology. AJR Am J Roentgenol 209:W336–W349. https://doi.org/10.2214/AJR.17.17984
12. Hussien N, Hussien RS, Saad DHA, El Kassas M, Elkhatib WF, Ezz El Din M (2022) The role of MRI pancreatic protocol in assessing response to neoadjuvant therapy for patients with borderline resectable pancreatic cancer. Front Oncol 11:796317. https://doi.org/10.3389/FONC.2021.796317
13. Okada Kichi, Kawai M, Hirono S et al (2020) Diffusion-weighted MRI predicts the histologic response for neoadjuvant therapy in patients with pancreatic cancer: a prospective study (DIFFERENT trial). Langenbecks Arch Surg 405:23–33. https://doi.org/10.1007/S00423-020-01857-4
14. Kang JH, Lee SS, Kim JH et al (2021) Multiparametric MRI for prediction of treatment response to neoadjuvant FOLFIRINOX therapy in borderline resectable or locally advanced pancreatic cancer. Eur Radiol 31:864–874. https://doi.org/10.1007/S00330-020-07134-8
15. Bali MA, Pullini S, Metens T et al (2018) Assessment of response to chemotherapy in pancreatic ductal adenocarcinoma: comparison between diffusion-weighted MR quantitative parameters and RECIST. Eur J Radiol 104:49–57. https://doi.org/10.1016/J.EJRAD.2018.04.024
16. Harder FN, Jungmann F, Kaissis GA, Lohöfer FK, Ziegelmayer S, Havel D, Quante M, Reichert M, Schmid RM, Demir IE, Friess H, Wildgruber M, Siveke J, Muckenhuber A, Steiger K, Weichert W, Rauscher I, Eiber M, Makowski MR, Braren RF (2021) [18F]FDG PET/MRI enables early chemotherapy response prediction in pancreatic ductal adenocarcinoma. EJNMMI Res 11(1):70. https://doi.org/10.1186/S13550-021-00808-4
17. Page MJ, Moher D, Bossuyt PM et al (2021) PRISMA 2020 explanation and elaboration: updated guidance and exemplars for reporting systematic reviews. BMJ 372:n160. https://doi.org/10.1136/BMJ.N160
18. Bilreiro C, Andrade L, Bilhim T, Matos C (2022) Diffusion-weighted MRI for assessing response to neoadjuvant therapy in pancreatic cancer: a systematic review and meta-analysis. PROSPERO CRD42022309467. Available from: https://www.crd.york.ac.uk/prospero/display_record.php?ID=CRD42022309467
19. Whiting PF, Rutjes AWS, Westwood ME et al (2011) QUADAS-2: a revised tool for the quality assessment of diagnostic accuracy studies. Ann Intern Med 155:529–536. https://doi.org/10.7326/0003-4819-155-8-201110180-00009
20. Evans DB, Rich TA, Byrd DR et al (1992) Preoperative chemoradiation and pancreaticoduodenectomy for adenocarcinoma of the pancreas. Arch Surg 127:1335–1339. https://doi.org/10.1001/ARCHSURG.1992.01420110083017
21. Kakar S, Shi C, Adsay V et al (2017) Protocol for the examination of specimens from patients with carcinoma of the pancreas, version pancreas exocrine 4.0.0.1. College of American Pathologists. Available at: https://documents.cap.org/protocols/cp-pancreas-exocrine-17protocol-4001.pdf
22. Deeks JJ, Bossuyt PM, Leeflang MM, Takwoingi Y (eds) (2023) Cochrane handbook for systematic reviews of diagnostic test accuracy. Version 2.0 (updated July 2023). Cochrane. Available from https://training.cochrane.org/handbook-diagnostic-test-accuracy/current
23. Cuneo KC, Chenevert TL, Ben-Josef E et al (2014) A pilot study of diffusion-weighted MRI in patients undergoing neoadjuvant chemoradiation for pancreatic cancer. Transl Oncol 7:644–649. https://doi.org/10.1016/J.TRANON.2014.07.005
24. Dalah E, Erickson B, Oshima K et al (2018) Correlation of ADC with pathological treatment response for radiation therapy of pancreatic cancer. Transl Oncol 11:391–398. https://doi.org/10.1016/J.TRANON.2018.01.018
25. Do RK, Reyngold M, Paudyal R et al (2020) Diffusion-weighted and dynamic contrast-enhanced MRI derived imaging metrics for stereotactic body radiotherapy of pancreatic ductal adenocarcinoma: preliminary findings. Tomography 6:261–271. https://doi.org/10.18383/J.TOM.2020.00015
26. Okada KI, Hirono S, Kawai M et al (2017) Value of apparent diffusion coefficient prior to neoadjuvant therapy is a predictor of histologic response in patients with borderline resectable pancreatic carcinoma. J Hepatobiliary Pancreat Sci 24:161–168. https://doi.org/10.1002/JHBP.430
27. Malyarenko D, Galbán CJ, Londy FJ et al (2013) Multi-system repeatability and reproducibility of apparent diffusion coefficient measurement using an ice-water phantom. J Magn Reson Imaging 37:1238–1246. https://doi.org/10.1002/JMRI.23825
28. Donati OF, Chong D, Nanz D et al (2014) Diffusion-weighted MR imaging of upper abdominal organs: field strength and intervendor variability of apparent diffusion coefficients. Radiology 270:454–463. https://doi.org/10.1148/RADIOL.13130819
29. Ye XH, Gao JY, Yang ZH, Liu Y (2014) Apparent diffusion coefficient reproducibility of the pancreas measured at different MR scanners using diffusion-weighted imaging. J Magn Reson Imaging 40:1375–1381. https://doi.org/10.1002/JMRI.24492
30. Rosenkrantz AB, Oei M, Babb JS et al (2011) Diffusion-weighted imaging of the abdomen at 3.0 tesla: image quality and apparent diffusion coefficient reproducibility compared with 1.5 tesla. J Magn Reson Imaging 33:128–135. https://doi.org/10.1002/jmri.22395
31. Schoennagel BP, Habermann CR, Roesch M et al (2011) Diffusion-weighted imaging of the healthy pancreas: apparent diffusion coefficient values of the normal head, body, and tail calculated from different sets of b-values. J Magn Reson Imaging 34:861–865. https://doi.org/10.1002/JMRI.22743
32. McTavish S, Van AT, Peeters JM et al (2022) Gradient nonlinearity correction in liver DWI using motion-compensated diffusion encoding waveforms. MAGMA 35:827–841. https://doi.org/10.1007/S10334-021-00981-6/FIGURES/8
33. Hu L, Zhou DW, Fu CX et al (2021) Calculation of apparent diffusion coefficients in prostate cancer using deep learning algorithms: a pilot study. Front Oncol 11:697721. https://doi.org/10.3389/FONC.2021.697721/BIBTEX
34. Sedlaczek OL, Kleesiek J, Gallagher FA et al (2022) Quantification and reduction of cross-vendor variation in multicenter DWI MR imaging: results of the Cancer Core Europe imaging task force. Eur Radiol 32:8617–8628. https://doi.org/10.1007/S00330-022-08880-7/FIGURES/6
35. Barral M, Taouli B, Guiu B et al (2014) Diffusion-weighted MR imaging of the pancreas: current status and recommendations. Radiology 274:45–63. https://doi.org/10.1148/RADIOL.14130778
36. Virostko J, Craddock RC, Williams JM et al (2021) Development of a standardized MRI protocol for pancreas assessment in humans. PLoS One 16(8):e0256029. https://doi.org/10.1371/JOURNAL.PONE.0256029
37. Geng R, Zhang Y, Starekova J et al (2021) Characterization and correction of cardiovascular motion artifacts in diffusion-weighted imaging of the

pancreas. Magn Reson Med 86:1956–1969. https://doi.org/10.1002/MRM.28846
38. Ma C, Li J, Boukar MB et al (2017) Optimized ROI size on ADC measurements of normal pancreas, pancreatic cancer and mass-forming chronic pancreatitis. Oncotarget 8:99085–99092. https://doi.org/10.18632/ONCOTARGET.18457
39. Ma C, Guo X, Liu L et al (2017) Effect of region of interest size on ADC measurements in pancreatic adenocarcinoma. Cancer Imaging 17:1–7. https://doi.org/10.1186/S40644-017-0116-6/TABLES/5
40. Cassinotto C, Mouries A, Lafourcade JP et al (2014) Locally advanced pancreatic adenocarcinoma: reassessment of response with CT after neoadjuvant chemotherapy and radiation therapy. Radiology 273:108–116. https://doi.org/10.1148/RADIOL.14132914
41. Strobel O, Neoptolemos J, Jäger D, Büchler MW (2019) Optimizing the outcomes of pancreatic cancer surgery. Nat Rev Clin Oncol 16:11–26. https://doi.org/10.1038/S41571-018-0112-1
42. Zaharia C, Søreide K (2023) Call for better response evaluation after neoadjuvant therapy in pancreatic cancer. Br J Surg 110:294–296. https://doi.org/10.1093/BJS/ZNAC452
43. Xu J, Zhan H, Li F, Hu S, Wang L (2021) Neoadjuvant therapy for pancreatic cancer: limitations and advances of response assessment (Review). Oncol Rep 45(4):26. https://doi.org/10.3892/OR.2021.7977
44. Soloff EV, Al-Hawary MM, Desser TS et al (2022) Imaging assessment of pancreatic cancer resectability after neoadjuvant therapy: AJR expert panel narrative review. AJR Am J Roentgenol 218:570–581. https://doi.org/10.2214/AJR.21.26931
45. Isaji S, Mizuno S, Windsor JA et al (2018) International consensus on definition and criteria of borderline resectable pancreatic ductal adenocarcinoma 2017. Pancreatology 18:2–11. https://doi.org/10.1016/J.PAN.2017.11.011
46. Tempero MA, Malafa MP, Al-Hawary M et al (2021) Pancreatic adenocarcinoma, version 2.2021, NCCN clinical practice guidelines in oncology. J Natl Compr Canc Netw 19:439–457. https://doi.org/10.6004/JNCCN.2021.0017

Publisher's note

Springer Nature remains neutral with regard to jurisdictional claims in published maps and institutional affiliations.

3.2. Effective bowel motion reduction in mouse abdominal MRI using hyoscine butylbromide.

Bilreiro C, Fernandes FF, Andrade L, Chavarrías C, Simões RV, Matos C, Shemesh N.

Magn Reson Med. 2021; 86(4):2146-2155.

doi: 10.1002/mrm.28824.

Received: 17 January 2021 | Revised: 15 March 2021 | Accepted: 12 April 2021

DOI: 10.1002/mrm.28824

TECHNICAL NOTE

Magnetic Resonance in Medicine

Effective bowel motion reduction in mouse abdominal MRI using hyoscine butylbromide

Carlos Bilreiro[1,2,3] | **Francisca F. Fernandes**[1] | **Luísa Andrade**[2] | **Cristina Chavarrías**[1] | **Rui V. Simões**[1] | **Celso Matos**[1,2] | **Noam Shemesh**[1]

[1]Champalimaud Research, Champalimaud Centre for the Unknown, Lisbon, Portugal

[2]Radiology Department, Champalimaud Clinical Centre, Lisbon, Portugal

[3]Nova Medical School, Lisbon, Portugal

Correspondence
Noam Shemesh, Champalimaud Research, Champalimaud Centre for the Unknown, Av. Brasilia 1400-038, Lisbon, Portugal.
Email: noam.shemesh@neuro.fchampalimaud.org

Funding information
Champalimaud Foundation, Grant/Award Number: H2020-MSCA-IF-2018, ref: 844776. CONGENTO LISBOA-01-0145-FEDER-022170

Purpose: Bowel motion is a significant source of artifacts in mouse abdominal MRI. Fasting and administration of hyoscine butylbromide (BUSC) have been proposed for bowel motion reduction but with inconsistent results and limited efficacy assessments. Here, we evaluate these regimes for mouse abdominal MRI at high field.

Methods: Thirty-two adult C57BL/6J mice were imaged on a 9.4T scanner with a FLASH sequence, acquired over 90 min with ~19 s temporal resolution. During MRI acquisition, 8 mice were injected with a low-dose and 8 mice with a high-dose bolus of BUSC (0.5 and 5 mg/kg, respectively). Eight mice were food deprived for 4.5-6.5 hours before MRI and another group of eight mice was injected with saline during MRI acquisition. Two expert readers reviewed the images and classified bowel motion, and quantitative voxel-wise analyses were performed for identification of moving regions. After defining the most effective protocol, high-resolution T_2-weighted and diffusion-weighted images were acquired from 4 mice.

Results: High-dose BUSC was the most effective protocol for bowel motion reduction, for up to 45 min. Fasting and saline protocols were not effective in suppressing bowel motion. High-resolution abdominal MRI clearly demonstrated improved image quality and ADC quantification with the high-dose BUSC protocol.

Conclusion: Our data show that BUSC administration is advantageous for abdominal MRI in the mouse. Specifically, it endows significant bowel motion reduction, with relatively short onset timings after injection (~8.5 min) and relatively long duration of the effect (~45 min). These features improve the quality of high-resolution images of the mouse abdomen.

KEYWORDS
abdominal MRI, bowel, Buscopan, hyoscine butylbromide, mouse

Carlos Bilreiro and Francisca F. Fernandes contributed equally to this work.

© 2021 International Society for Magnetic Resonance in Medicine

1 | INTRODUCTION

Abdominal MRI in the mouse is challenged by physiological motion, including breathing and bowel motility, causing multiple artifacts such as blurring and ghosting.[1] Respiratory motion compensation is routinely achieved by techniques including respiratory triggering or placing animals in supine position.[2,3] However, despite the importance of suppressing bowel motion, there is no consensus on how to achieve it in the mouse.[4-8] Fasting and administration of hyoscine butylbromide (BUSC), trademarked Buscopan, have been proposed, but the efficacy of these methods has never been thoroughly assessed. Food deprivation of at least 4 hours was reported to decrease peristalsis because of the absence of digestion and gut relaxation.[4,7] Moreover, BUSC is a spasmolytic agent routinely used in the clinical setting to reduce motion artifacts from intestinal peristaltic motion.[9-13] In the mouse, however, a consensus does not exist on its efficacy, and reported dosage regimens vary by several orders of magnitude, specifically from 0.5 to ≈80-100 mg/kg.[4-6,8] Furthermore, the motion reduction window with BUSC was reportedly very short (≈5-10 min),[4,7] and some authors suggest that only a partial suppression of bowel movements can be achieved.[6] Clearly, suppressing bowel motion over longer periods can be imperative for high-quality abdominal MRI. The aim of this study was thus to define a protocol for consistent bowel motion reduction (BMR) in the mouse and comprehensively evaluate its efficacy.

2 | METHODS

All experiments were in accordance with European Directive 2010/63 and preapproved by the Institution's Review Board and the national competent authority. Our workflow is summarized in Figure 1, which included 4 animal groups with different BMR protocols: low- and high-dose BUSC,[4,8] food deprivation, and saline. BMR was assessed using dynamic MRI of the abdomen in 32 mice, followed by high-resolution MRI with the most effective protocol in 4 animals. Below, we elaborate on each phase. Animal weights and ages are reported as mean ± SD.

2.1 | Animal preparation

Wild-type male mice ($n = 36$) on a C57BL/6J background weighing 27.8 ± 2.3 g and aged 14.8 ± 4.6 weeks were used. Details on animal rearing and isoflurane-induced anesthesia can be found in Supporting Information.

A 24G × ¾″ catheter was inserted intraperitoneally in $n = 24$ animals for BUSC or saline administration for characterizing the different BMR protocols, and in $n = 4$ extra animals for high-resolution imaging. All volumes were injected over 10 s using a syringe pump (GenieTouch, Kent Scientific, Torrington, CT), resulting in a 12-18 µL/s injection rate.

2.2 | MRI setup

Animals were imaged using a 9.4T BioSpec MRI scanner (Bruker, Karlsruhe, Germany) equipped with an AVANCE III HD console, producing isotropic pulsed field gradients of up to 660 mT/m (120 µs rise time), and a 40-mm ID linear transmit-receive volume coil. All acquisitions began with routine adjustments: center frequency, RF calibration, acquisition of B_0 maps, and automatic shimming.

2.3 | Characterization of BMR

2.3.1 | MRI protocol

A FLASH sequence with two 1-mm thick coronal slices positioned in the abdomen and ~19 s temporal resolution (detailed in Supporting Information) was acquired in $n = 32$ animals.

2.3.2 | BMR protocols

Mice were divided into 4 groups. In the food deprivation group, 8 animals (16.5 ± 2.1 weeks old, 28.7 ± 1.3 g) were fasted between 4 h 30 min to 6 h 30 min before the experiment. In the low-dose BUSC group, 8 animals (15.3 ± 3.1 weeks old, 28.1 ± 1.9 g) were injected with a 5 mL/kg bolus of 0.5 mg/kg[4] BUSC (Buscopan, Boehringer Ingelheim, Barcelona, Spain; 20 mg/mL, diluted 1:200 in saline) after 10 min of acquisition. In the high-dose BUSC group, 8 animals (12.4 ± 4.2 weeks old, 27.9 ± 3.8 g) were injected with a 5 mL/kg bolus of 5 mg/kg[8] BUSC (1:20 dilution) after 10 min of acquisition. Finally, in the saline control group, 8 animals (12.7 ± 6.0 weeks old, 26.5 ± 0.8 g) received an injection of 5 mL/kg saline after 10 min of acquisition.

2.3.3 | Data analysis

The data analysis included 2 main parts: a qualitative analysis of the images, performed by 2 readers, aiming to identify, and define periods with BMR; and a quantitative analysis of the data, aiming to produce motion maps and time courses.

Qualitative analysis

Two gastrointestinal radiologists (7 and 9 years of experience) reviewed the acquired images, blinded to the interventions

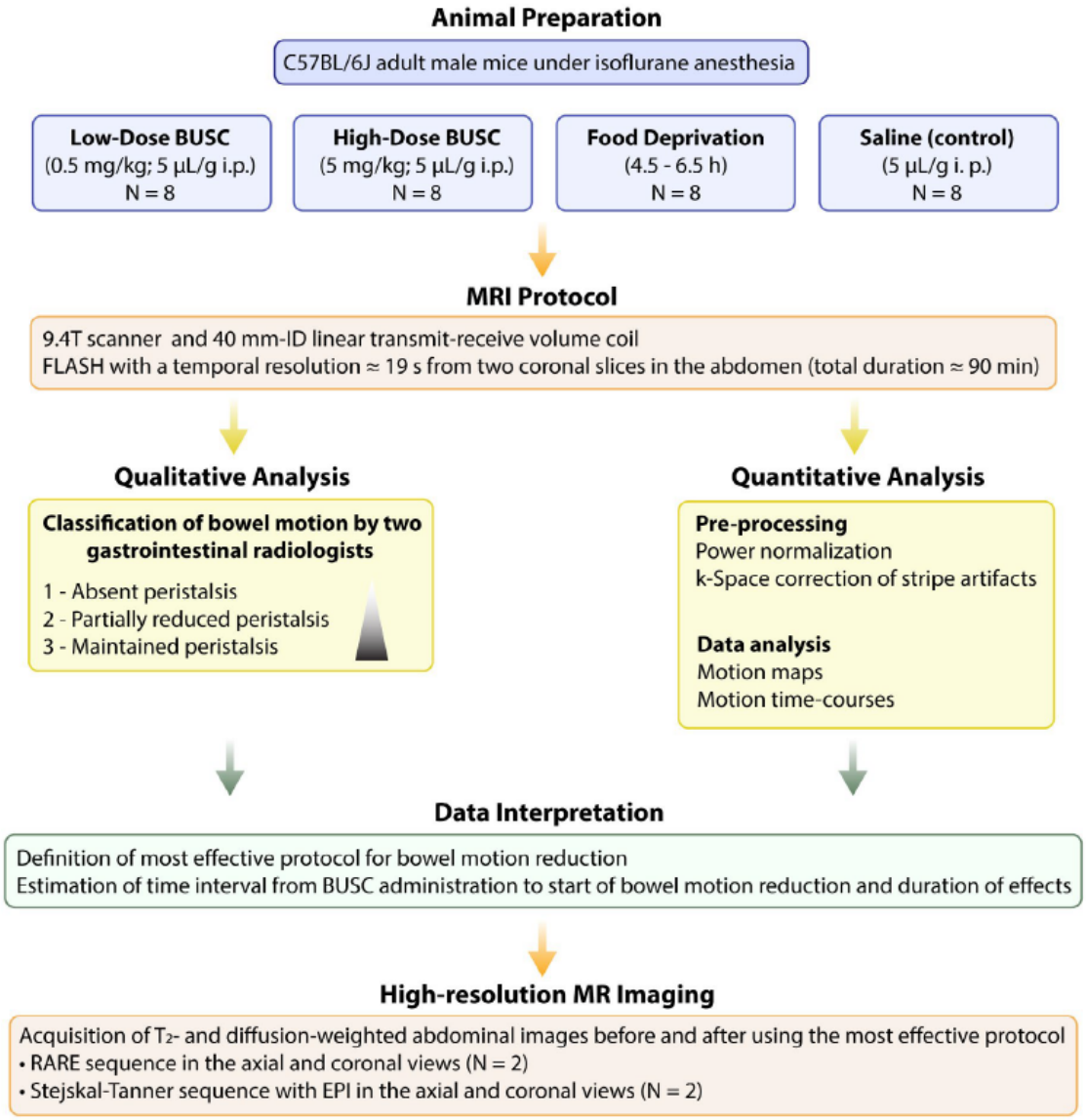


FIGURE 1 Study flowchart. Thirty-two C57BL/6J mice were subjected to 4 different bowel motion reduction protocols and underwent MRI scans under isoflurane anesthesia. Images were qualitatively and quantitatively assessed for the presence and degree of bowel motion in each condition. After determining the most effective protocol, high-resolution MR images of the entire abdomen were acquired in 4 animals, before and after using that protocol

performed on the animals, and separately divided the time course of every slice into time blocks with different degrees of peristaltic motion: 1 - strongly reduced peristalsis; 2 - partial reduction of peristalsis with residual movement of bowel content; 3 - persistent peristalsis. Blocks with a classification of 1 and 2 were then merged to define periods with BMR and obtain 2 relevant timings: the time from the beginning of acquisition to the start of BMR (T_{mr}); and the duration of BMR (D_{mr}).

To evaluate interrater variability, T_{mr} and D_{mr} were compared between readers with single score intra-class correlation coefficient (ICC) assessing absolute agreement and using a 2-way random effects model, using SPSS (SPSS, NY). In cases where bowel motion was maintained throughout the entire scan (classification = always 3), values of 90 min and 0 min were assigned to T_{mr} and D_{mr}, respectively.

Finally, both readers defined in consensus time blocks and classifications for each animal, and T_{mr} and D_{mr} were recalculated. The duration of halted motion (D_{mh}), that is, the time under a classification of 1, was also calculated. For the low- and high-dose BUSC groups, the time from the injection of BUSC to the start of BMR (T_{mrb}) and the duration of BUSC effects (D_{mrb}) were also computed. T_{mrb} was calculated by subtracting 10 min from T_{mr} because BUSC was injected after 10 min of acquisition and $D_{mrb} = D_{mr}$.

Mann-Whitney test was used to evaluate differences between BUSC protocols on T_{mrb} and D_{mrb} and the Kruskal-Wallis test was used for differences between the 4 groups on D_{mh} (significance at 0.05).

Quantitative analysis

Data sets were pre-processed (details in Supporting Information) and analyzed in MATLAB (The MathWorks, Natick, MA). The absolute differences between consecutive images were computed voxel-by-voxel, summed for 10-11 min intervals throughout the acquisition and mapped voxel-wise for identification of moving regions. These absolute differences were thresholded at 20% of the highest difference obtained from all scans for identification of significantly moving pixels at each time instant, and the differences from the pixels surviving the thresholding were summed to create motion time courses for each animal. Individual motion time courses were then averaged for each group to generate group time courses.

To investigate anesthesia depth and temperature as possible confounding factors, influencing BMR and contributing to the differences observed between groups in the 20- to 50-min period after the beginning of MRI, respiratory rate and rectal temperature values averaged for each animal in that period were tested with analysis of variance (significance at 0.05).

2.4 | High-resolution MRI

After determining the most effective protocol for BMR, we chose to demonstrate its value with high-resolution MRI. T_2-weighted and diffusion-weighted images were acquired in the abdomen of $n = 4$ mice before and ~6.5 min after the administration of high-dose BUSC using rapid acquisition with relaxation enhancement (RARE) and EPI-based Stejskal-Tanner DWI, respectively (detailed in Supporting Information). ADC maps were calculated using MATLAB. ImageJ (United States National Institutes of Health) was used for manual drawing of regions of interest (ROIs) for comparing results between ADC measurements.

3 | RESULTS

3.1 | Agreement between readers

Supporting Information Video S1 shows the FLASH images obtained throughout 90-min scans from 1 representative animal of each experimental group, revealing periods with different degrees of motion. Figure 2 shows different degrees of peristaltic motion, assigned by the readers to time blocks of each animal. Reliability analysis (Supporting Information Figure S2) revealed a very high agreement

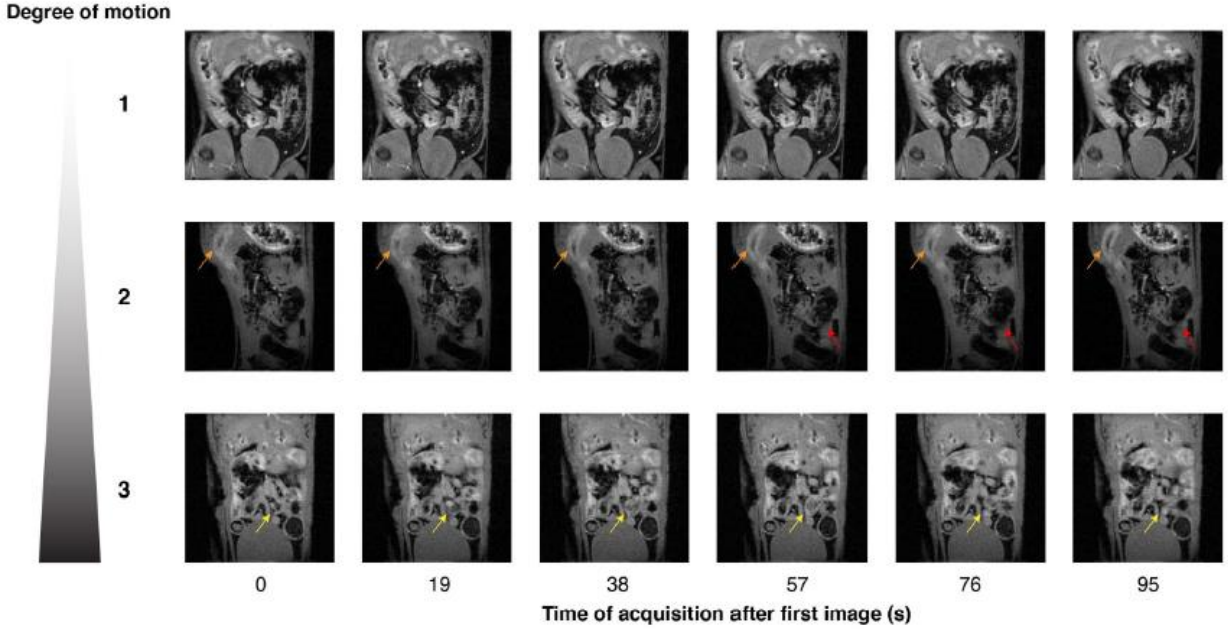


FIGURE 2 Classification of images according to the degree of motion. Three examples of 6 consecutive images from the mouse abdomen acquired with a FLASH sequence in the coronal plane. Each row represents a time period of ~1.5 min. Upper row: no noticeable peristalsis is observed (classification = 1). Middle row: residual motion of bowel content without peristaltic motion, causing intensity changes (orange arrows) and susceptibility artifacts (red arrows) (classification = 2). Lower row: peristaltic bowel motion. Notice the variability of luminal diameter in 1 bowel loop along this time period (yellow arrows) (classification = 3)

between readers for T_{mr} (ICC [2,1] = 0.984) and D_{mr} (ICC [2,1] = 0.951).

3.2 | Readers' consensus on the efficacy of each protocol

Supporting Information Table S1 shows T_{mr}, D_{mr}, and D_{mh} for each animal. Most mice in the food deprivation and saline groups never showed significant BMR. In contrast, animals under low- or high-dose BUSC showed sustained BMR after injection. In particular, T_{mrb} and D_{mrb} in the low-dose BUSC group were 12.9 (±9.6) min and 46.8 (±18.3) min, respectively. T_{mrb} was less variable in the high-dose BUSC group (8.5 ± 2.8 min), whereas D_{mrb} was similar (40.8 ± 17.8 min) without significant differences (T_{mrb}, $P = .59$; D_{mrb}, $P = .33$). Nevertheless, half of the mice under high-dose BUSC showed absent peristalsis, whereas this was observed in only 1 animal in the low-dose BUSC and in none of the animals from other groups. Most animals (7 of 8) under low-dose BUSC showed a reduced but residual peristalsis. Kruskal-Wallis test revealed significant differences on D_{mh} ($P < .03$) between the 4 groups. After pairwise comparisons, significant differences were only found between the high-dose BUSC and both food deprivation and saline groups (both $P = .04$). No significant differences were observed between the low-dose and the high-dose BUSC, saline, or food deprivation groups ($P = .25$, $P = .87$ and $P = .87$, respectively).

3.3 | Motion maps and time courses

The quantitative analysis of bowel motion was mostly consistent with the readers' analysis. Figure 3 shows strongly reduced bowel motion in 1 representative animal from the high-dose BUSC group (from 18-28 min to 53-63 min), an effect noticeably more intense compared to the others. This effect was reproducible throughout the entire high-dose BUSC group (Supporting Information Figure S3) and in the individual and group motion time courses (Supporting Information Figure S4 and Figure 4, respectively). The animal-averaged time course from the high-dose BUSC group shows a robust decrease in motion for the longest period of time in comparison to the others. A maintained peristalsis is observed throughout the entire acquisition in all food deprivation and most saline groups' animals. Notably, a sudden increase in motion was consistent in both BUSC and saline groups during the first 5 min after injection (Figure 4, Supporting Information Figure S4).

3.4 | Animals' welfare

No side effects of BUSC administration were observed for either dosages, and all animals quickly recovered from sedation. Group-averaged respiratory rate and rectal temperature values recorded during MRI acquisition are plotted in Supporting Information Figure S5. Analysis of variance did not reveal significant differences between groups (respiratory rate, $P = .28$; rectal temperature, $P = .39$).

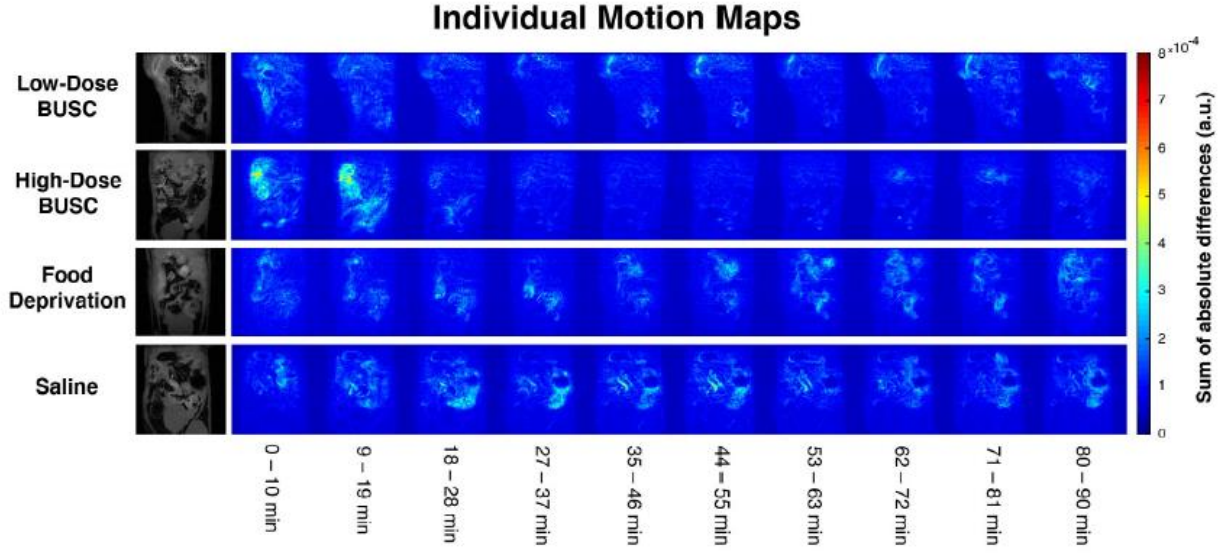


FIGURE 3 Representative individual motion maps. Voxel-by-voxel motion maps obtained for 1 representative slice of 1 animal from each group (specifically, from animals 3, 14, 17, and 30), representing the calculated sum of the absolute differences between consecutive images for 10- to 11-min intervals throughout the acquisition. Dark blue areas represent regions without significant bowel motility. A raw image from the slice is presented on the left of each map for anatomic region definition

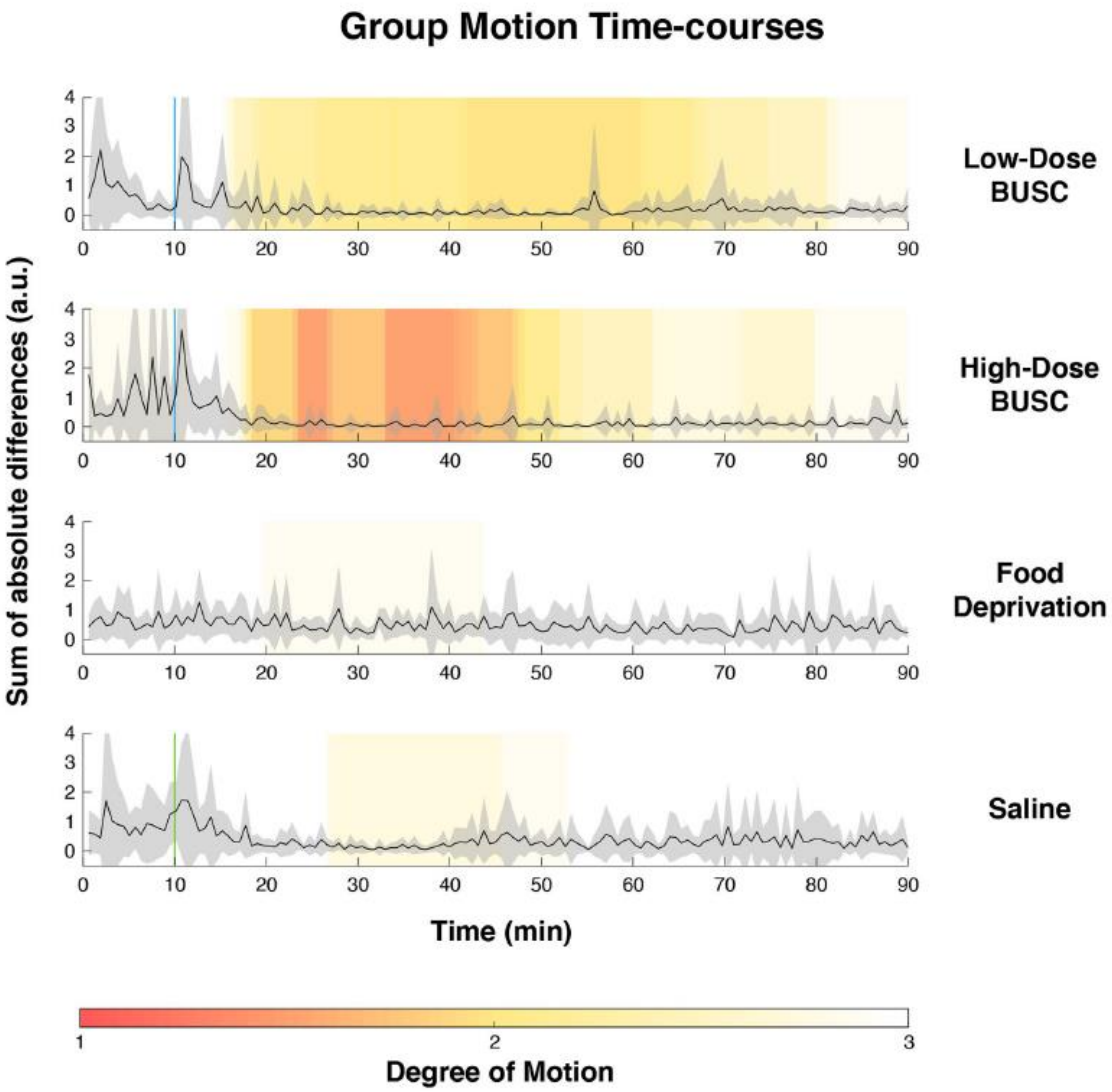


FIGURE 4 Group motion time courses. Estimated group-averaged motion time courses obtained from both slices of all animals from each group, depicting the sum of absolute differences between consecutive images for ~38-s intervals throughout the acquisition from significantly moving pixels, (ie, pixels whose absolute difference was higher than 20% of the highest difference at each time instant). Gray shaded areas represent the standard deviation of the estimated motion. The degrees of motion defined in consensus by the 2 readers for each time interval of each animal were averaged for each group and are color coded behind each time course, where white represents maintained peristalsis (classification = 3), bright yellow represents reduced but residual peristalsis (classification = 2), and red represents strongly reduced peristalsis (classification = 1). Blue lines indicate i.p. injection of a BUSC bolus, whereas the green line represents i.p. injection of saline

3.5 | High-resolution MRI

The introduction of high-dose BUSC clearly improved image quality regarding structural definition, organ detail, and reduction of motion artifacts. These effects are noticeable in both T_2-weighted RARE (Figure 5A and Supporting Information Figures S6 and S7) and DWI (Figure 5B and Supporting Information Figures S8 and S9), when comparing depiction of bowel walls and parenchymal organs (kidneys, pancreas, spleen, and liver). Regarding DWI, BUSC effect is mostly noted in b1000 images, representing a powder average of 14 directions, acquired over ~30 min. BUSC provided reduced data variability derived from motion artifacts in ADC measurements from ROIs in the kidney parenchyma and renal pelvis (Figure 5B and Supporting Information Figure S10).

4 | DISCUSSION

Our study reveals that BUSC is effective for BMR in the mouse for an average duration of 40-45 min. Its effects were consistent in both qualitative and quantitative analyses, with reduced bowel motion using both BUSC dosages. However,

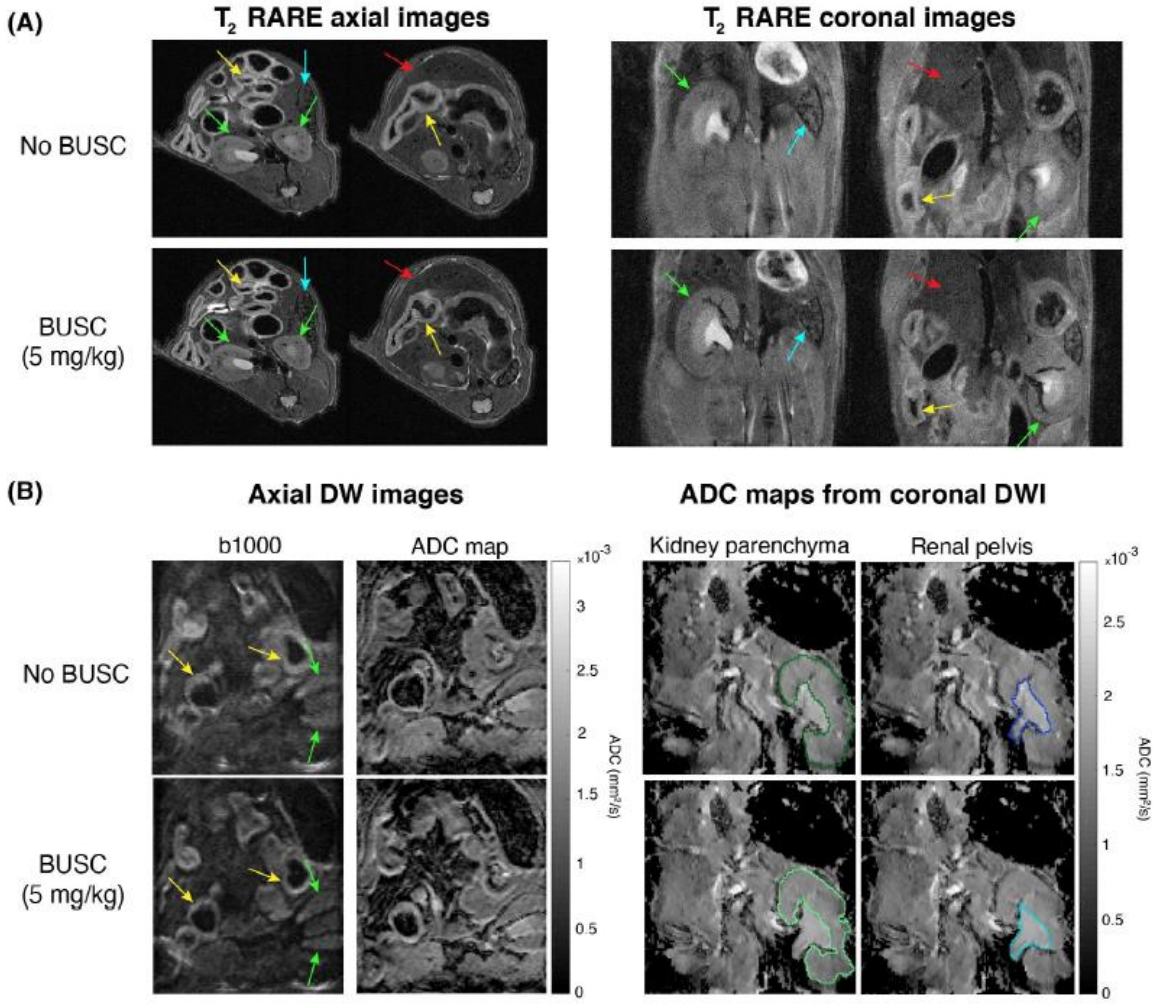


FIGURE 5 High-resolution T_2 RARE and diffusion-weighted images of the abdomen, with corresponding ADC maps, before and after high-dose BUSC injection. Representative axial and coronal T_2-weighted (A) and diffusion-weighted (B) images of the mouse abdomen acquired without BUSC and 6.5 min after BUSC i.p. injection. Yellow arrows point to the bowel, green arrows to the kidneys, blue arrows to the spleen, and red arrows to the liver. The ROIs performed for ADC values quantification in the renal pelvis and parenchyma are presented in (B), on the right, with blue and green contours, respectively

strongly reduced peristalsis was best achieved with the high-dose protocol, significantly improving abdominal imaging quality by reducing motion artifacts. This study provides the first thorough characterization of BMR strategies for abdominal MRI in the mouse.

These results reveal a longer duration of BUSC effects on mouse bowel peristalsis than previously reported by Grimm et al.[4] Additionally, fasting, suggested by others[4,7] to have comparable effects to BUSC, was not effective (Figure 3). These differences likely result from our motion quantification strategy involving both subjective and objective criteria, whereas previous studies did not report such quantification of bowel motion. BUSC works as a blocker of muscarinic receptors for acetylcholine in smooth muscle cells in the gastrointestinal tract, reducing motility in a dose-dependent manner.[14] This effect is evidently more intense and reliable than the motility reduction obtained with fasting.

Our motion quantification strategy did not always correlate with the readers' evaluation. Discrepancies between both methods are apparent in the time course graphs (Supporting Information Figure S4). The readers' evaluation was more specific in detecting peristaltic motion, because the quantitative analysis mostly reflects the magnitude of motion in the entire FOV. Therefore, it does not strikingly reflect the presence of motion when it happens in a small number of voxels or if it does not translate into large differences in voxel intensity (eg, Supporting Information Figure S4: animal no. 29). Susceptibility artifacts caused by bowel gas are very noticeable in the quantitative analysis, creating "spikes" in the time course that do not actually correspond to bowel motion. These can be recognized by human readers

as artifacts and classified as residual motion of bowel content (eg, Supporting Information Figure S4: animals 7, 16, 27, and 28). Therefore, both strategies are complementary: the qualitative focuses on the detection and classification of peristaltic motion and the quantitative represents objectively measured data, highly sensitive to motion, allowing its representation over time. Moreover, it should be noted that these case-by-case discrepancies were partially attenuated by averaging (Figure 4).

Considering the motion time courses, a shorter magnitude of motion can be observed in the food deprivation group, before injections occurred. This, however, did not translate into significant BMR in the readers' evaluation. Nevertheless, it might be hypothesized that a combination of food deprivation and BUSC administration, especially at higher dosages, could provide even greater BMR. Because the high-dose BUSC protocol provided satisfactory results without side effects, this combination might not be worth the additional time and preparation.

Isoflurane-induced anesthesia has been reported to suppress gastrointestinal motility in rodents.[15,16] In this study, the anesthesia depth did not vary substantially between groups, because the respiratory rate and rectal temperature values recorded during MRI acquisition (Supporting Information Figure S5) were on the same ranges, including the period with stronger BUSC effects (20-50 min after beginning of acquisition). Therefore, the use of isoflurane should not have contributed to the differences observed in bowel motion.

The high-resolution data acquired under high-dose BUSC reveals well-defined and detailed abdominal organs such as the bowel, kidneys, pancreas, spleen, and liver (Figure 5 and Supporting Information Figures S6-S9). Previous studies reported T_2-weighted turbo spin-echo abdominal images with in-plane resolutions as high as 75 × 156 μm^2 (1-mm slice thickness),[6] 117 × 70 μm^2 (0.5-mm slice thickness),[4] and 100 × 100 μm^2 (1-mm slice thickness).[17] Our results show that higher resolutions (85 × 85 μm^2) with reduced slice thickness (0.3 mm) can be achieved without motion artifacts when using high-dose BUSC. Similarly, although previously reported DWI resolutions reached 1300 × 1300 μm^2 (2-mm slice thickness),[18] 250 × 250 μm^2 (1-mm slice thickness),[19] 700 × 700 μm^2 (1.5-mm slice thickness),[20] and 1250 × 1250 μm^2 (1.3-mm slice thickness),[21] we achieved a significantly higher resolution (150 × 150 μm^2; 0.65-mm slice thickness) free of motion artifacts.

These results favor the use of BUSC for long acquisitions using several repetitions/averages for producing a single image, exemplified by the DW images presented. The longer the acquisition time, the longer the data will be exposed to the occurrence of motion and, because each repetition is uniquely affected by motion, the resulting artifacts increase when a powder-average of several diffusion directions is used to create DW images. Moreover, ADC maps or other quantifiable measurements are expected to be more accurately calculated with the reduction of motion-dependent artifacts.[22,23] Our results reflect this, with more precise ADC measurements in the kidney using high-dose BUSC (Figure 5 and Supporting Information Figure S10), demonstrating how BUSC administration is useful for motion-sensitive organs (kidneys, bowels, and pancreas) in quantitative MRI.

As established for humans, glucagon might be an alternative to BUSC, a hormone known to have a similar, although shorter, effect.[24] Further studies should investigate its use as an alternative to BUSC in the mouse.

As in every work, we acknowledge several relevant limitations in this study. First, the statistical evaluation was limited, probably because of insufficient power; trends were observed favoring the high-dose compared with the low-dose BUSC protocol for more reliable initiation and duration of BMR, without reaching statistical significance. Nevertheless, significant differences were observed between the high-dose BUSC and the food deprivation/saline groups on D_{mh}, whereas the low-dose BUSC did not show significant differences with any other groups. Second, the injections performed at room temperature (~20°C) might have caused the short-duration motion increases observed immediately after all injections. This should be taken into account when considering repeated bolus protocols for long periods of BMR, because the motion caused by each injection could be detrimental to data acquisitions. In this context, a priori warming the solution to body temperature or using continuous infusion protocols might prove beneficial. Third, the only route for BUSC administration was intraperitoneal because of the ease of catheter placement; other routes of administration (intravenous or intramuscular) might provide different results.[25] Last, because no side effects were observed with our dosage protocols, future studies could investigate mice's capability to tolerate higher dosages and their efficacy on BMR.

5 | CONCLUSIONS

BUSC administered in a single 5 mg/kg bolus is effective for BMR in the mouse for up to 45 min, enabling robust imaging in the abdomen and allowing high-resolution imaging in this challenging region. Our results are promising for future studies in motion susceptible organs (bowels, pancreas, and kidneys), either for diagnostic or quantification purposes.

ACKNOWLEDGMENTS

Funding Support: Champalimaud Foundation; H2020-MSCA-IF-2018, ref: 844776. CONGENTO LISBOA-01-0145-FEDER-022170.

ORCID

Noam Shemesh https://orcid.org/0000-0001-6681-5876

REFERENCES

1. Wood ML, Henkelman RM. MR image artifacts from periodic motion. *Med Phys*. 1985;12:143-151.
2. Cassidy PJ, Schneider JE, Grieve SM, Lygate C, Neubauer S, Clarke K. Assessment of motion gating strategies for mouse magnetic resonance at high magnetic fields. *J Magn Reson Imaging*. 2004;19:229-237.
3. Kinchesh P, Allen PD, Gilchrist S, et al. Reduced respiratory motion artefact in constant TR multi-slice MRI of the mouse. *Magn Reson Imaging*. 2019;60:1-6.
4. Grimm J, Potthast A, Wunder A, Moore A. Magnetic resonance imaging of the pancreas and pancreatic tumors in a mouse orthotopic model of human cancer. *Int J Cancer*. 2003;106:806-811.
5. Dear JW, Kobayashi H, Jo S-K, et al. Dendrimer-enhanced MRI as a diagnostic and prognostic biomarker of sepsis-induced acute renal failure in aged mice. *Kidney Int*. 2005;67:2159-2167.
6. Ellmann S, Langer V, Britzen-Laurent N, et al. Application of machine learning algorithms for multiparametric MRI-based evaluation of murine colitis. *PLoS One*. 2018;13:e0206576.
7. Partecke IL, Kaeding A, Sendler M, et al. In vivo imaging of pancreatic tumours and liver metastases using 7 Tesla MRI in a murine orthotopic pancreatic cancer model and a liver metastases model. *BMC Cancer*. 2011;11:11-40.
8. Larsson AE, Melgar S, Rehnström E, et al. Magnetic resonance imaging of experimental mouse colitis and association with inflammatory activity. *Inflamm Bowel Dis*. 2006;12:478-485.
9. Johnson W, Taylor MB, Carrington BM, Bonington SC, Swindell R. The value of hyoscine butylbromide in pelvic MRI. *Clin Radiol*. 2007;62:1087-1093.
10. Slough RA, Caglic I, Hansen NL, Patterson AJ, Barrett T. Effect of hyoscine butylbromide on prostate multiparametric MRI anatomical and functional image quality. *Clin Radiol*. 2018;73:216.e9-216.e14.
11. Dyde R, Chapman AH, Gale R, Mackintosh A, Tolan DJM. Precautions to be taken by radiologists and radiographers when prescribing hyoscine-N-butylbromide. *Clin Radiol*. 2008;63:739-743.
12. Laniado M, Grönewäller E, Kopp AF, et al. The value of hyoscine butylbromide in abdominal MR imaging with and without oral magnetic particles. *Abdom Imaging*. 1997;22:381-388.
13. Venkatanarasimha N, Jenkins SJ, Yang N, Colak E, Kirpalani A. Impact of butylscopolamine on image quality of magnetic resonance cholangiopancreatography. *Eur J Radiol*. 2013;82:583-588.
14. Krueger D, Michel K, Allam S, et al. Effect of hyoscine butylbromide (Buscopan®) on cholinergic pathways in the human intestine. *Neurogastroenterol Motil*. 2013;25:e530-e539.
15. Torjman MC, Joseph JI, Munsick C, Morishita M, Grunwald Z. Effects of Isoflurane on gastrointestinal motility after brief exposure in rats. *Int J Pharm*. 2005;294:65-71.
16. Dryn D, Luo J, Melnyk M, Zholos A, Hu H. Inhalation anaesthetic isoflurane inhibits the muscarinic cation current and carbachol-induced gastrointestinal smooth muscle contractions. *Eur J Pharmacol*. 2018;820:39-44.
17. He Z, Evelhoch JL, Mohammad RM, et al. Magnetic resonance imaging to measure therapeutic response using an orthotopic model of human pancreatic cancer. *Pancreas*. 2000;21:69-76.
18. Sun J, Zhang X-P, Li X-T, et al. Applicable apparent diffusion coefficient of an orthotopic mouse model of gastric cancer by improved clinical MRI diffusion weighted imaging. *Sci Rep*. 2014;4:6072.
19. Haldorsen IS, Popa M, Fonnes T, et al. Multimodal imaging of orthotopic mouse model of endometrial carcinoma. *PLoS One*. 2015;10:e0135220.
20. Heid I, Steiger K, Trajkovic-Arsic M, et al. Co-clinical assessment of tumor cellularity in pancreatic cancer. *Clin Cancer Res*. 2017;23:1461-1470.
21. Wu L, Li J, Fu C, Kühn B, Wang X. Chemotherapy response of pancreatic cancer by diffusion-weighted imaging (DWI) and intravoxel incoherent motion DWI (IVIM-DWI) in an orthotopic mouse model. *Magn Reson Mater Phys Biol Med*. 2019;32:501-509.
22. le Bihan D, Poupon C, Amadon A, Lethimonnier F. Artifacts and pitfalls in diffusion MRI. *J Magn Reson Imaging*. 2006;24:478-488.
23. Ozaki M, Inoue Y, Miyati T, et al. Motion artifact reduction of diffusion-weighted MRI of the liver: use of velocity-compensated diffusion gradients combined with tetrahedral gradients. *J Magn Reson Imaging*. 2013;37:172-178.
24. Froehlich JM, Daenzer M, von Weymarn C, Erturk SM, Zollikofer CL, Patak MA. Aperistaltic effect of hyoscine N-butylbromide versus glucagon on the small bowel assessed by magnetic resonance imaging. *Eur Radiol*. 2009;19:1387-1393.
25. Gutzeit A, Binkert CA, Koh D-M, et al. Evaluation of the antiperistaltic effect of glucagon and hyoscine on the small bowel: Comparison of intravenous and intramuscular drug administration. *Eur Radiol*. 2012;22:1186-1194.

SUPPORTING INFORMATION

Additional Supporting Information may be found online in the Supporting Information section.

FIGURE S1 Pre-processing of abdominal MR images. (A) Correction of transient global signal increases on 5 consecutive frames from a representative animal through power normalization, where power represents the sum of signal intensities from all voxels in each slice frame. Upper row: raw images with different powers. Lower row: images with unitary power after normalization, revealing a significant reduction of global signal variations. (B) Correction of stripe artifacts on 2 representative frames from a single animal through elimination of spurious signals at high-frequency regions of the k-space. White boxes delineate regions prone to correction that were manually selected for that animal

FIGURE S2 Reliability analysis. (A) Time from the beginning of acquisition to the start of bowel motion reduction (T_{mr}) and (B) duration of small motion period (D_{mr}) measured by 2 readers for all animal slices ($N = 64$ slices) and respective measures of inter-rater agreement (ICC [2,1] = 0.984 and ICC [2,1] = 0.951). The calculated ICCs reveal a very high agreement between readers

FIGURE S3 Individual motion maps. Voxel-by-voxel motion maps obtained for 1 representative slice of each animal, representing the calculated sum of the absolute differences between consecutive images for 10- to 11-min intervals throughout the

acquisition. Dark blue areas represent regions without significant bowel motility. A raw image from the slice is presented on the left of each map for anatomic region definition

FIGURE S4 Individual motion time courses. Estimated motion time courses obtained from both slices of each animal, depicting the sum of absolute differences between consecutive images for 19-s intervals throughout the acquisition from significantly moving pixels, (ie, pixels whose absolute difference was higher than 20% of the highest difference) at each time instant. Yellow areas represent time intervals with reduced but residual peristalsis (classification = 2) and red areas represent time intervals where peristalsis was strongly reduced (classification = 1), both defined in consensus by the 2 readers. Blue lines indicate i.p. injection of a BUSC bolus, whereas green lines represent i.p. injection of saline

FIGURE S5 Group-averaged vital signs. Respiratory rate and rectal temperature values recorded throughout MRI acquisition and averaged between animals of each group. Shaded areas represent the SDs of these measures

FIGURE S6 Axial images of the abdomen after BUSC injection. High-resolution T_2-weighted images of a mouse abdomen acquired 6.5 min after BUSC i.p. injection, from caudal to cranial. Note the high definition and detail of abdominal organs: bowels (yellow arrows), kidneys (green arrows), pancreas (orange arrows), spleen (blue arrows), and liver (red arrows)

FIGURE S7 Coronal images of the abdomen after BUSC injection. High-resolution T_2-weighted images of a mouse abdomen acquired 6.5 min after BUSC i.p. injection, from dorsal to ventral. Note the high definition and detail of abdominal organs: bowels (yellow arrows), kidneys (green arrows), pancreas (orange arrows), spleen (blue arrows), and liver (red arrows)

FIGURE S8 Axial images of the abdomen after BUSC injection. DW (b1000) images of a mouse abdomen acquired 6.5 min after BUSC i.p. injection, from cranial to caudal. The abdominal organs are easily identified and well defined: bowels (yellow arrows), kidneys (green arrows), pancreas (orange arrows), and liver (red arrows)

FIGURE S9 Coronal images of the abdomen after BUSC injection. DW (b1000) images of a mouse abdomen acquired 6.5 min after BUSC i.p. injection, from dorsal to ventral. The abdominal organs are easily identified and well defined: bowels (yellow arrows), kidneys (green arrows), and liver (red arrows)

FIGURE S10 Histograms and boxplots of ADC values measured in kidney ROIs. A higher variability of data can be observed in measurements performed before injecting BUSC, as represented by higher frequency of extreme values in both parenchymal (A) and renal pelvis (B) histograms and boxplots, when compared with measurements performed after injecting BUSC. These measurements exemplify the applicability of BUSC for performing segmentation/quantification studies in the mouse abdomen, by reducing the rate of motion-derived artifactual measurements

TABLE S1 Relevant timings defined in consensus for each animal. Time from the beginning of acquisition to the start of noticeable bowel motion reduction (T_{mr}), as well as the duration of those effects (D_{mr}), that is, the time under a classification of 1 or 2. The duration of halted motion (D_{mh}), that is, the time under a classification of 1, is also included. For the low- and high-dose BUSC groups, T_{mrb} was calculated by subtracting 10 min from T_{mr}, because BUSC bolus injection was performed after 10 min of acquisition, and D_{mrb} was equal to D_{mr} (not in the table). Because bowel motion reduction in animal 9 started before the injection of BUSC, its T_{mrb} and D_{mrb} values were 7.1 min and 34.9 min, respectively. NR, no reduction

VIDEO S1 Videos from each experimental group. FLASH images obtained during 90 min from 1 representative slice of 4 animals (specifically, from animals 3, 14, 17, and 30). The intraperitoneal injections at 10 min after the start of each scan are represented by a blue (BUSC) or gray (saline) circle in the left top corner of each video, when applicable. The low-dose BUSC scan shows a period with reduced but residual peristalsis after the injection, classified by the readers with a degree of motion of 2. The high-dose BUSC scan shows a strongly reduced peristalsis after the injection, whose period was classified as 1. At the end of both these scans, there is a return to normal peristaltic motion as the BUSC effects wear off. Both the food deprivation and saline scans show continuous motion throughout the entire scan and were, therefore, classified with a degree of motion of 3. All images displayed were corrected for transient global signal changes and stripe artifacts

How to cite this article: Bilreiro C, Fernandes FF, Andrade L, et al. Effective bowel motion reduction in mouse abdominal MRI using hyoscine butylbromide. *Magn Reson Med*. 2021;86:2146–2155. https://doi.org/10.1002/mrm.28824

Supplementary Information for:
Effective bowel motion reduction in mouse abdominal MRI using hyoscine butylbromide

Carlos Bilreiro[1,2,3]*, Francisca F. Fernandes[1]*, Luísa Andrade[2], Cristina Chavarrías[1], Rui V. Simões[1], Celso Matos[1,2], Noam Shemesh[1†].

[1]Champalimaud Research, Champalimaud Centre for the Unknown, Lisbon, Portugal.

[2]Radiology Department, Champalimaud Clinical Centre, Lisbon, Portugal.

[3]Nova Medical School, Lisbon, Portugal.

[†]Corresponding author:

Dr. Noam Shemesh, Champalimaud Research, Champalimaud Centre for the Unknown

Av. Brasilia 1400-038, Lisbon, Portugal**.**

E-mail: noam.shemesh@neuro.fchampalimaud.org ;

Phone number: +351 210 480 000 ext. #4467.

Running Head: High-resolution mouse abdominal MRI using hyoscine butylbromide administration.

*Carlos Bilreiro and Francisca F. Fernandes contributed equally to this work.

In this Supplementary Information, Methods' details are presented regarding animal preparation, MRI protocols used for dynamic MRI and high-resolution images and image pre-processing methods used for correction of artifacts.

Also, Results from motion qualitative assessments are presented in Video S1 and Table S1, as well as from reliability analysis (Figure S2), individual motion maps (Figure S3) and time-courses (Figure S4), group-averaged vital signs (Figure S5), axial and coronal T_2- and diffusion-weighted images of the abdomen after BUSC injection (Figures S6-9), and histograms and boxplots representations of ADC values measured in kidney ROIs (Figure S10).

METHODS

Animal preparation

Animals were reared in a temperature-controlled room and held under a 12h/12h light/dark regimen with *ad libitum* access to food and water.

Anesthesia was induced with 5% isoflurane (Vetflurane™, Virbac, France) mixed with oxygen-enriched (28%) air. Mice were then weighed, moved to the animal bed (Bruker BioSpin™, Germany) and isoflurane was reduced to 1.5-2.5%. Breathing rate and rectal temperature were monitored and recorded throughout the MRI sessions using a pillow sensor and an optic fiber probe (SA Instruments Inc., Stony Brook, USA), respectively. The readings were kept stable throughout the experiment via small adjustments to isoflurane levels (maintaining respiratory rates between 40-70 bpm) and a warm-water recirculating pad for body temperature control (maintaining temperatures between 35.0-37.0 ºC). Ophthalmic gel (Vidisic® Gel, Bausch+Lomb, Canada) was applied in the beginning of the experiment to prevent eye dryness.

Characterization of BMR

MRI protocol

For abdominal dynamic MRI, a FLASH sequence was acquired in n=32 animals with two 1-mm thick coronal slices positioned in the abdomen: TR/TE = 19/2 ms, flip angle = 20°, FOV = 25 x 25 mm^2, in-plane resolution = 120 x 120 μm^2, respiratory triggering, 284 repetitions, in a total duration of approximately 90 min (temporal resolution ~19 s).

Data analysis - Quantitative Analysis

Datasets were pre-processed in MATLAB® (MathWorks Inc., Natick, MA). Transient global signal increases caused by variations in the breathing rate were corrected by normalizing each single image to the sum of all of its voxel intensities (Figure S1A). Subsequently, images were corrected for sporadic stripe artifacts by calculating their 2D Fourier transform and eliminating spurious signal that appeared at high-frequency regions of the k-space. Affected regions of the k-space were first manually selected and then voxels in those regions were nulled whenever their values were higher than 1.5 times the standard deviation of their time-course. This value accurately selected all the strongly deviating k-space voxels that contributed to the artifacts, while still being permissible to voxels with weaker visual influence on the transformed images. In a single outlying case (Animal #16), a value of one standard deviation was chosen as the nulling criterion, because the stripe artifacts were less sporadic and more persistent during the entire scan. k-Space images were then 2D inverse-Fourier transformed to obtain the final corrected spatial images (Figure S1B).

High-resolution MRI

T_2-weighted images were acquired with Rapid Acquisition with Refocused Echoes (RARE), with the following parameters: TR/TE = 3500/25 ms, RARE factor = 8, in-plane resolution = 85 x 85 μm^2, FOV = 26 x 26 mm^2 (axial slices) or 20 x 26 mm^2 (coronal slices), number of slices = 42, slice thickness = 0.3 mm, slice gap = 0.25 mm, respiratory triggering; acquisition time: 49 min.

Diffusion-weighted images were acquired with a Stejskal-Tanner sequence with EPI: TR/TE = 2000/13.6 ms, 10 averages, 4 segments, double sampling, in-plane resolution = 150 x 150 μm^2,

FOV = 16 x 18 mm^2 (if axial slices) or 18 x 18 mm^2 (if coronal slices), number of slices = 24 (axial slices) or 22 (coronal slices), slice thickness = 0.65 mm, slice gap = 0.2 mm, respiratory triggering, fat suppression, 14 directions of b = 1000 s/mm^2 (powder averaged), 2 acquisitions of b = 0; acquisition time: 30 min.

RESULTS

Supporting Information Table S1 – **Relevant timings defined in consensus for each animal**. Time from the beginning of acquisition to the start of noticeable bowel motion reduction (T_{mr}), as well as the duration of those effects (D_{mr}), i.e. the time under a classification of 1 or 2. The duration of halted motion (D_{mh}), i.e. the time under a classification of 1, is also included. For the low- and high-dose BUSC groups, T_{mrb} was calculated by subtracting 10 min from T_{mr}, since BUSC bolus injection was performed after 10 min of acquisition, and D_{mrb} was equal to D_{mr} (not in the table). Since bowel motion reduction in Animal #9 started before the injection of BUSC, its T_{mrb} and D_{mrb} values were 7.1 min and 34.9 min, respectively. NR: No reduction.

Group	Animal	Time to start motion reduction (T_{mr}, min)	Duration of motion reduction (D_{mr}, min)	Duration of halted motion (D_{mh}, min)
Low-Dose BUSC	**1**	15.5	74.5	0.0
	2	41.2	41.2	
	3	25.4	49.4	
	4	18.1	49.8	
	5	16.2	65.0	65.0
	6	33.3	33.3	0.0
	7	14.9	46.3	
	8	19.0	14.9	
High-Dose BUSC	**9**	0.0	52.0	29.2
	10	17.1	37.4	0.0
	11	17.7	29.5	29.5
	12	15.2	33.0	0.0
	13	18.1	61.8	61.8
	14	23.1	39.0	39.0
	15	22.5	18.4	0.0
	16	17.1	72.9	
Food Deprivation	**17**	NR	0.0	0.0
	18			
	19			
	20			
	21			
	22	19.3	24.4	
	23	NR	0.0	
	24			
Saline	**25**	NR	0.0	
	26			
	27	26.3	19.3	
	28	26.6	26.3	
	29	NR	0.0	
	30			
	31			
	32			

Video S1 – **Videos from each experimental group**. FLASH images obtained during 90 min from one representative slice of four animals (specifically, from Animals #3, #14, #17 and #30). The

intraperitoneal injections at 10 minutes after the start of each scan are represented by a blue (BUSC) or gray (saline) circle in the left top corner of each video, when applicable. The low-dose BUSC scan shows a period with reduced but residual peristalsis after the injection, classified by the readers with a degree of motion of 2. The high-dose BUSC scan shows a strongly reduced peristalsis after the injection, whose period was classified as 1. At the end of both these scans, there is a return to normal peristaltic motion as the BUSC effects wear off. Both the food deprivation and saline scans show continuous motion throughout the entire scan and were therefore classified with a degree of motion of 3. All images displayed were corrected for transient global signal changes and stripe artifacts.

SUPPLEMENTARY FIGURES

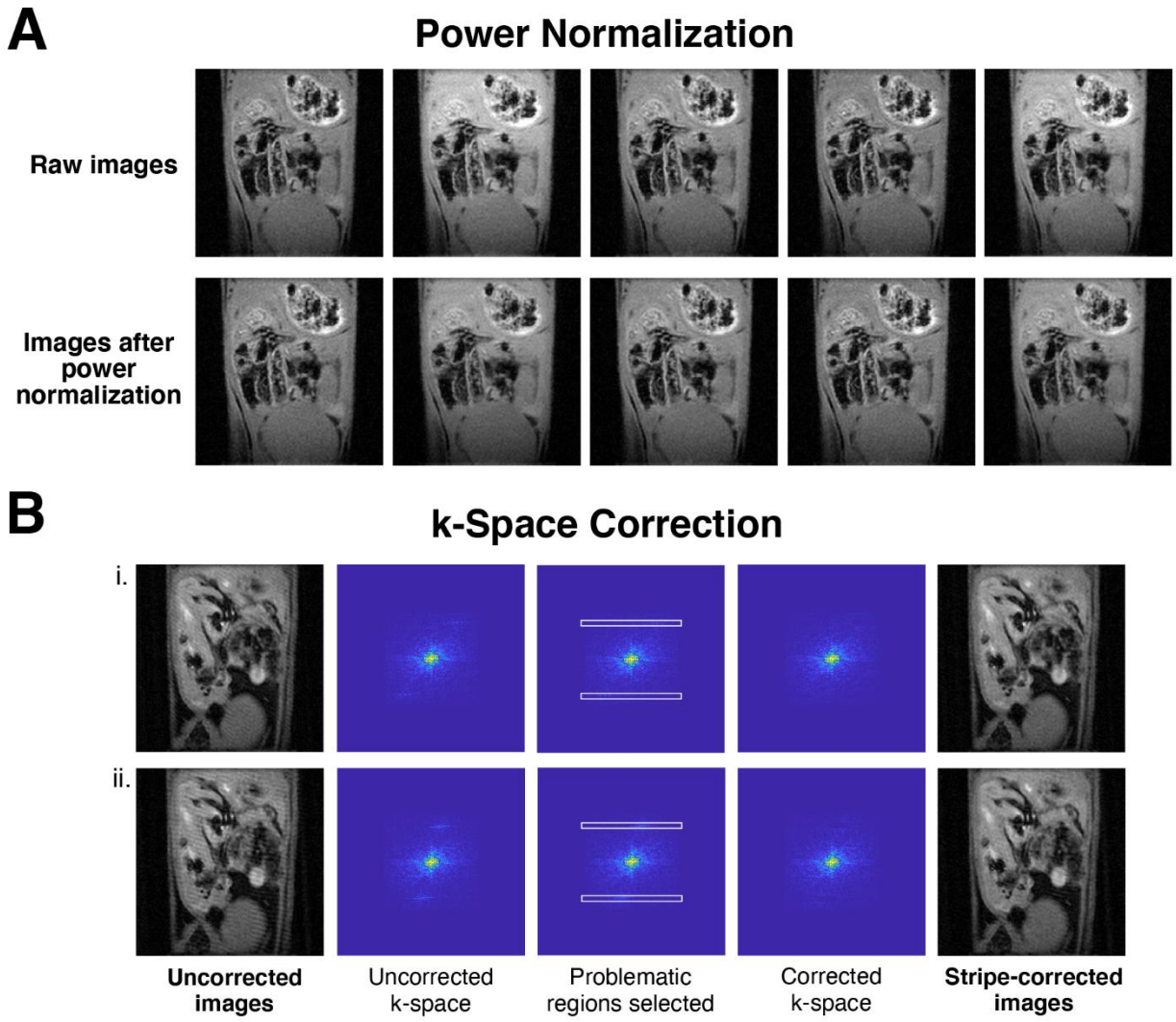


Figure S1 – **Pre-processing of abdominal MR images**. (A) Correction of transient global signal increases on 5 consecutive frames from a representative animal through power normalization, where power represents the sum of signal intensities from all voxels in each slice frame. Upper row: Raw images with different powers. Lower row: Images with unitary power after normalization, revealing a significant reduction of global signal variations. (B) Correction of stripe artifacts on 2 representative frames from a single animal through elimination of spurious signals at high-frequency regions of the k-space. White boxes delineate regions prone to correction that were manually selected for that animal.

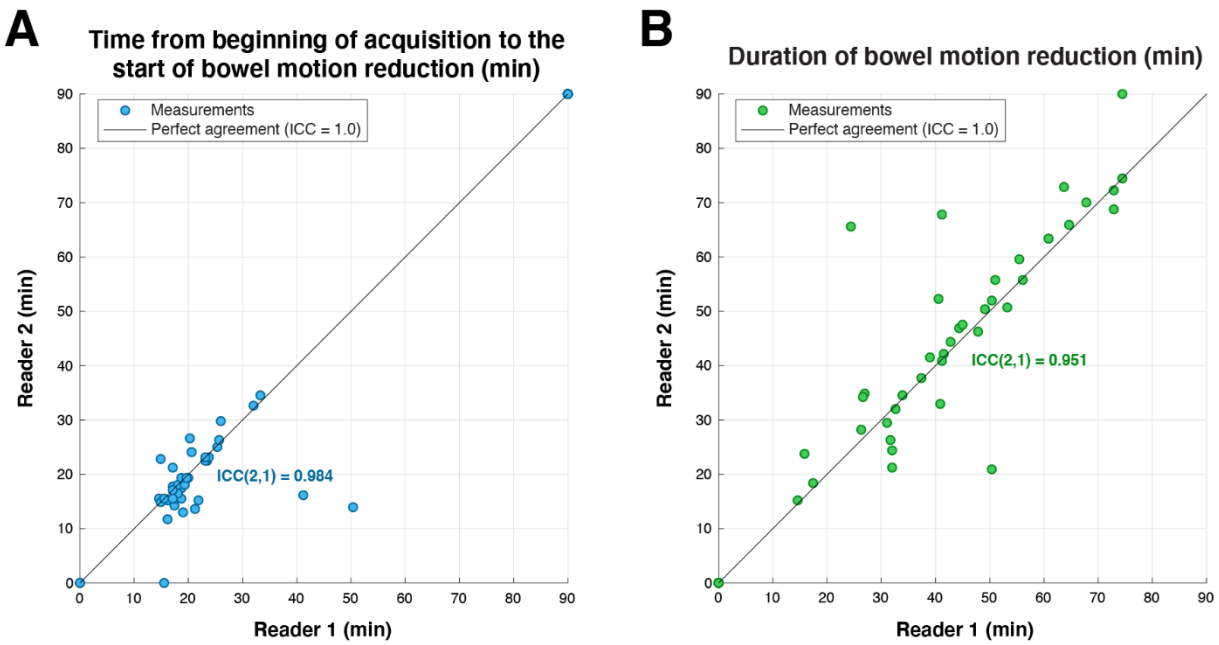


Figure S2 - **Reliability analysis**. (A) Time from the beginning of acquisition to the start of bowel motion reduction (T_{mr}) and (B) duration of small motion period (D_{mr}) measured by two readers for all animal slices (N = 64 slices) and respective measures of inter-rater agreement (ICC(2,1) = 0.984 and ICC(2,1) = 0.951). The calculated ICCs reveal a very high agreement between readers.

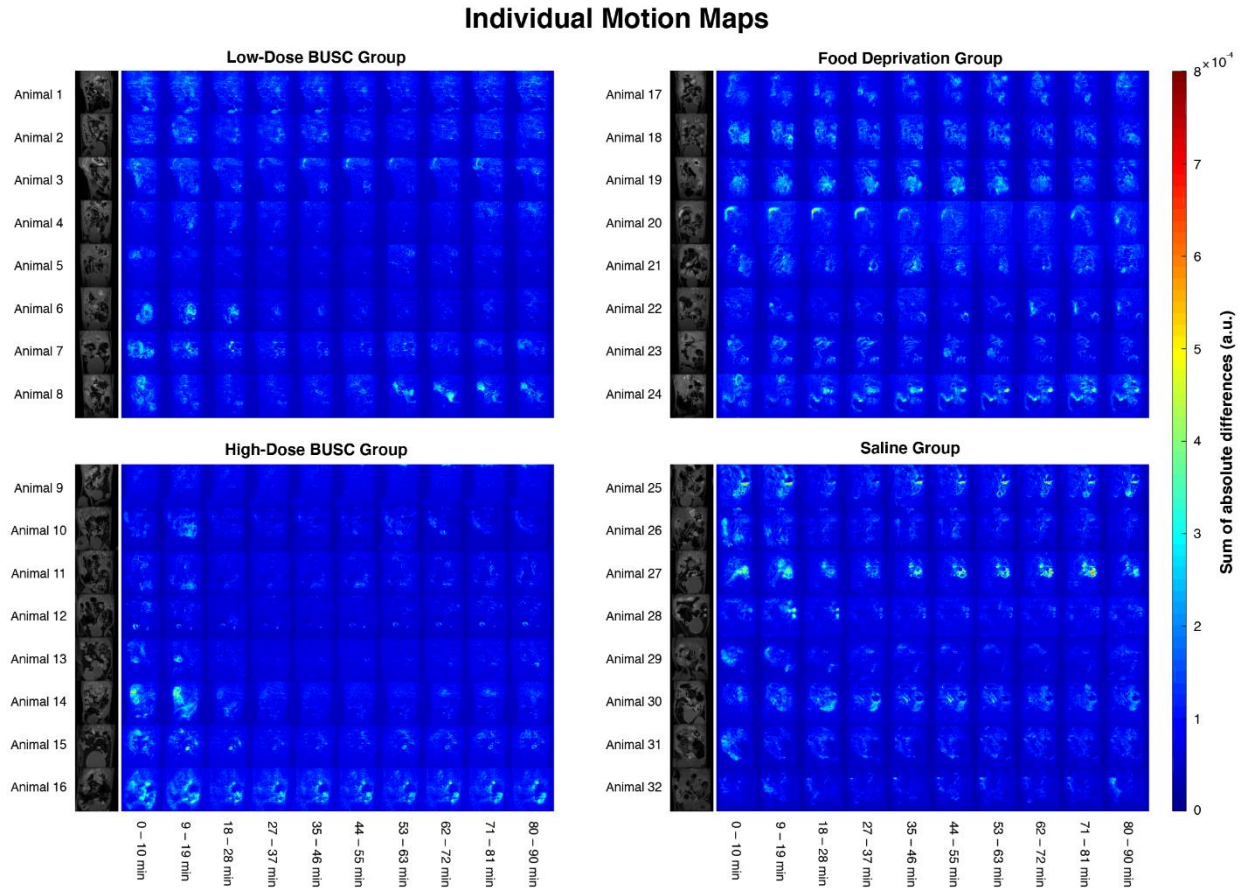


Figure S3 - **Individual motion maps**. Voxel-by-voxel motion maps obtained for one representative slice of each animal, representing the calculated sum of the absolute differences between consecutive images for 10-11 min intervals throughout the acquisition. Dark blue areas represent regions without significant bowel motility. A raw image from the slice is presented on the left of each map for anatomical region definition.

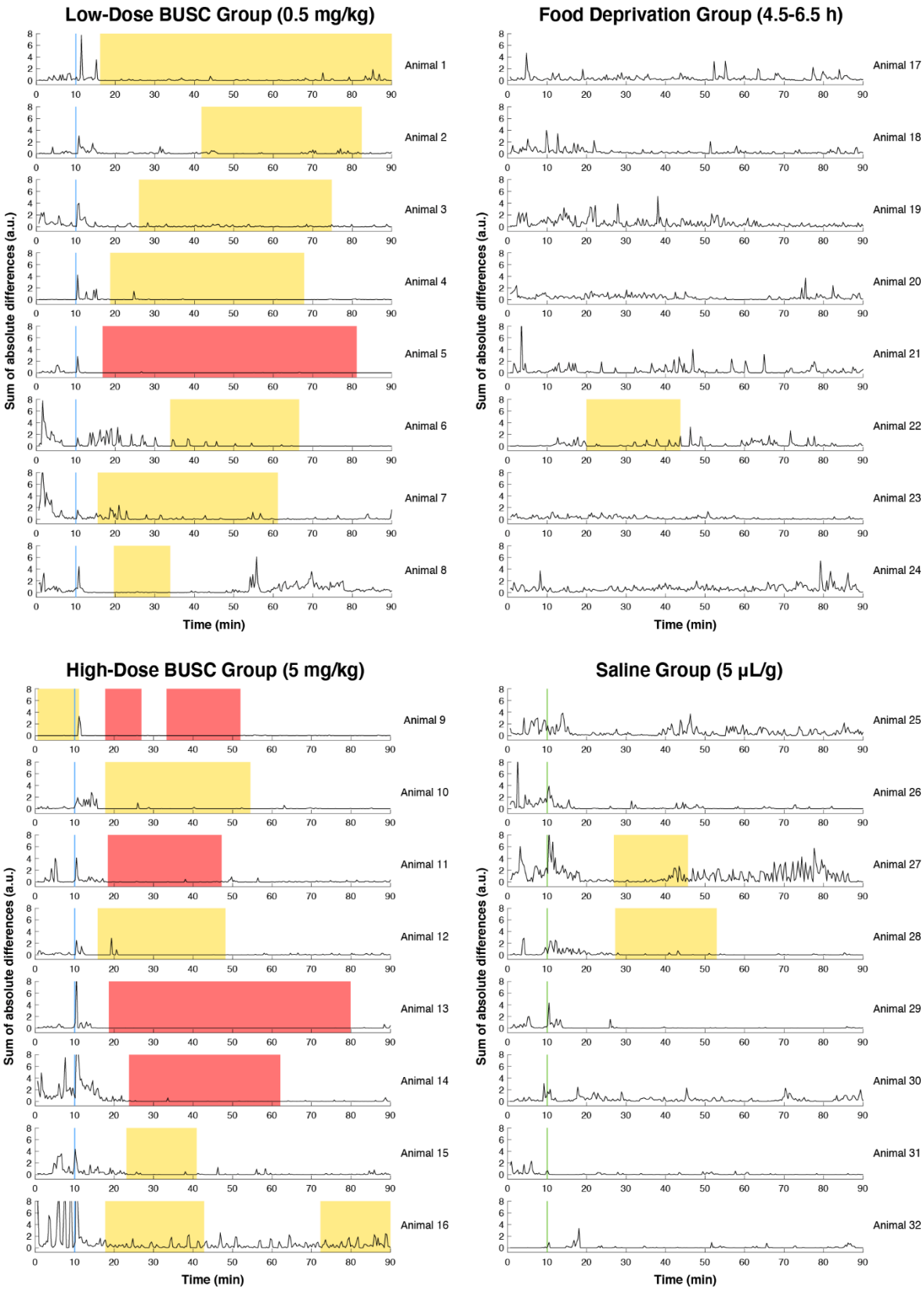


Figure S4 – **Individual motion time-courses**. Estimated motion time-courses obtained from both slices of each animal, depicting the sum of absolute differences between consecutive images for 19 sec intervals throughout the acquisition from significantly moving pixels, i.e. pixels whose absolute

difference was higher than 20% of the highest difference, at each time instant. Yellow areas represent time intervals with reduced but residual peristalsis (classification = 2) and red areas represent time intervals where peristalsis was strongly reduced (classification = 1), both defined in consensus by the two readers. Blue lines indicate i.p. injection of a BUSC bolus whereas green lines represent i.p. injection of saline.

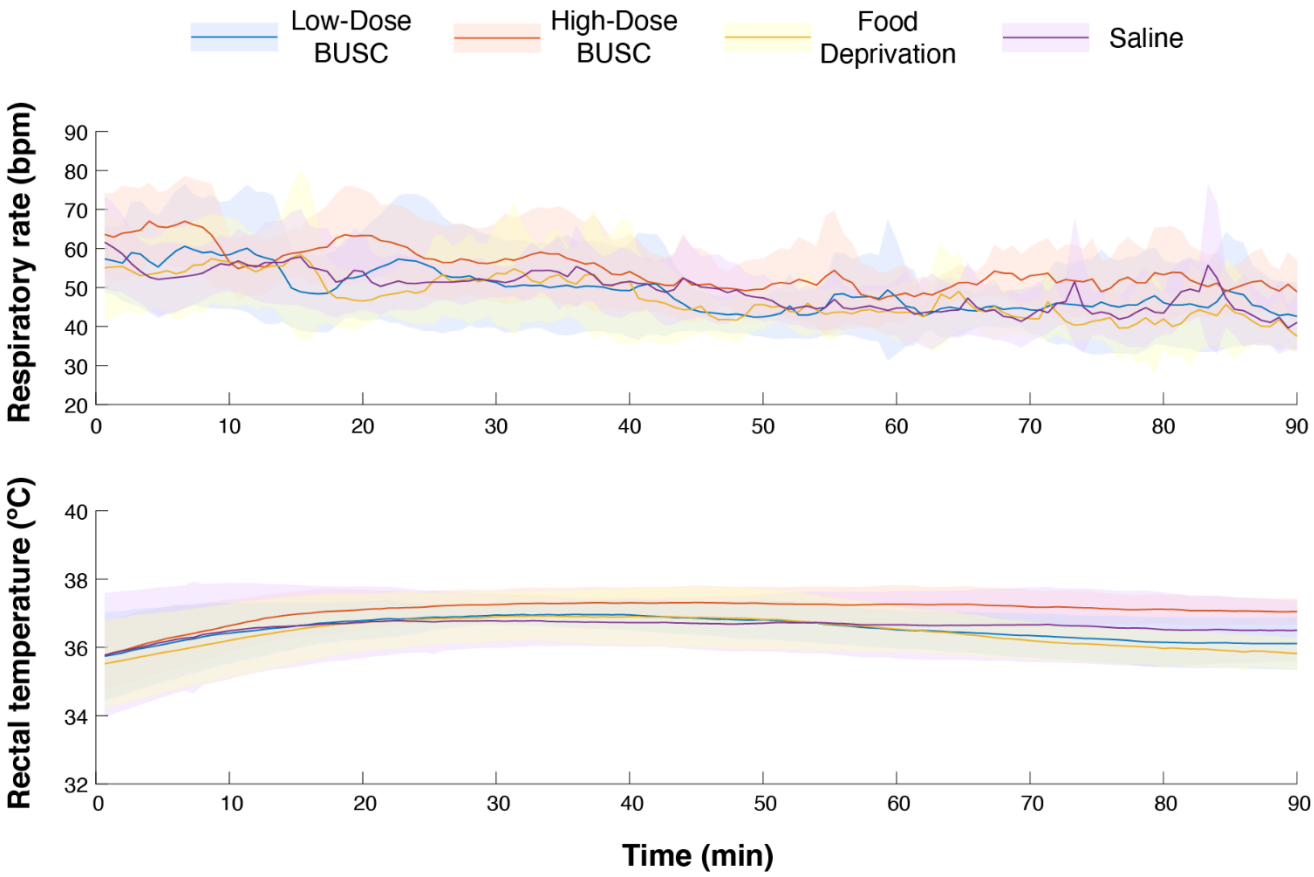


Figure S5 – **Group-averaged vital signs.** Respiratory rate and rectal temperature values recorded throughout MRI acquisition and averaged between animals of each group. Shaded areas represent the standard deviations of these measures.

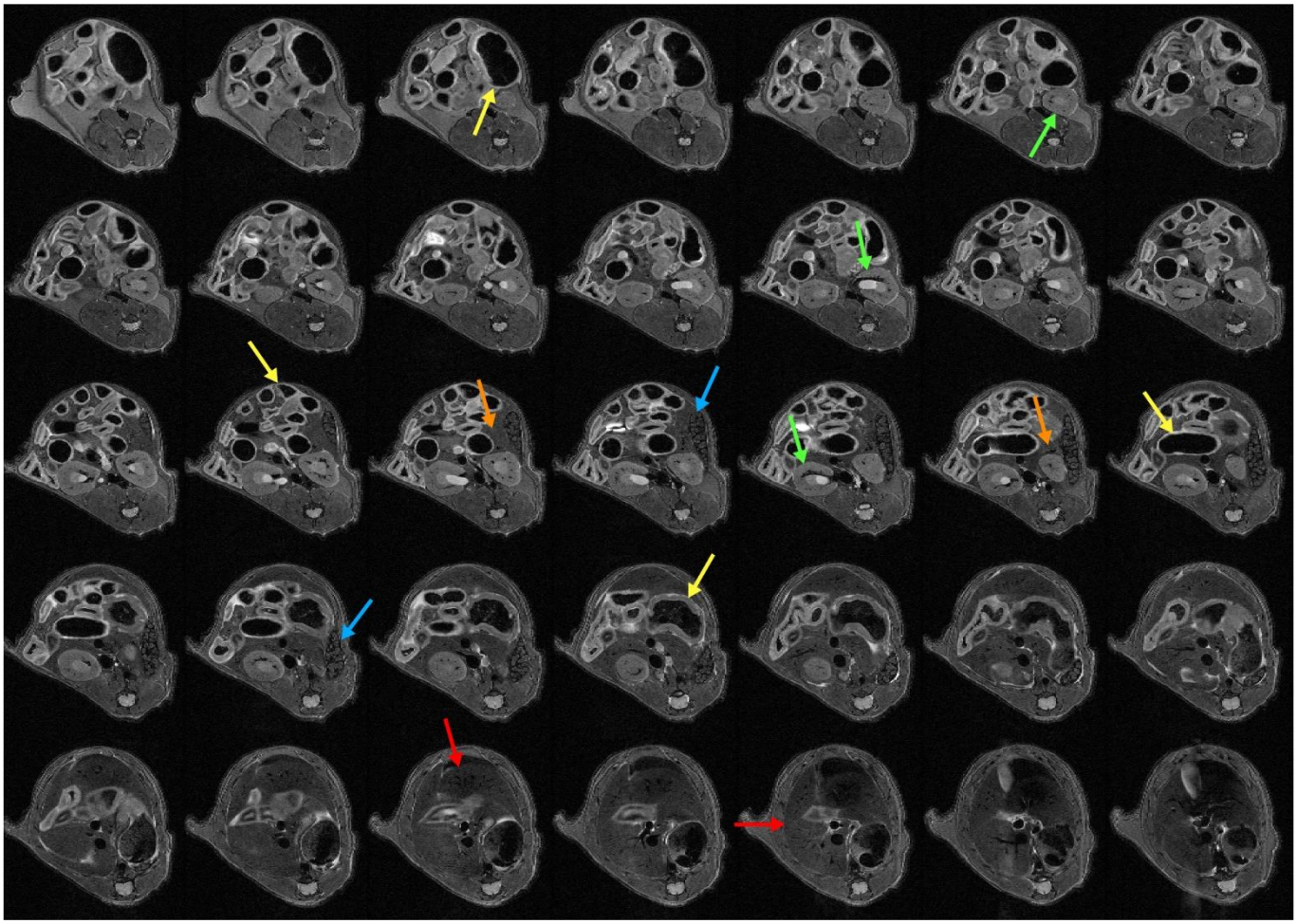


Figure S6 – **Axial images of the abdomen after BUSC injection**. High-resolution T_2-weighted images of a mouse abdomen acquired 6.5 min after BUSC i.p. injection, from caudal to cranial. Note the high definition and detail of abdominal organs: bowels (yellow arrows), kidneys (green arrows), pancreas (orange arrows), spleen (blue arrows) and liver (red arrows).

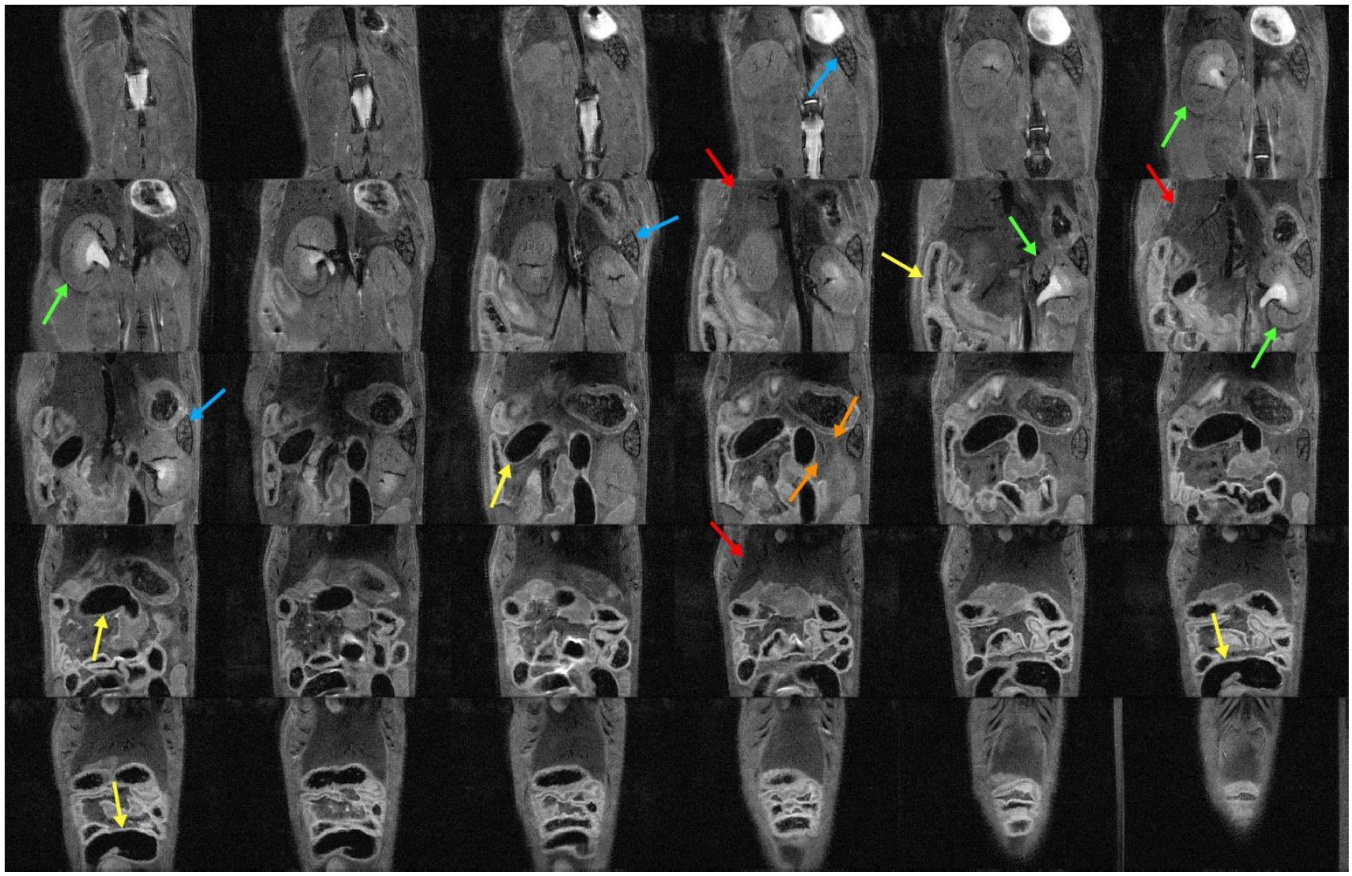


Figure S7 – **Coronal images of the abdomen after BUSC injection**. High-resolution T_2-weighted images of a mouse abdomen acquired 6.5 min after BUSC i.p. injection, from dorsal to ventral. Note the high definition and detail of abdominal organs: bowels (yellow arrows), kidneys (green arrows), pancreas (orange arrows), spleen (blue arrows) and liver (red arrows).

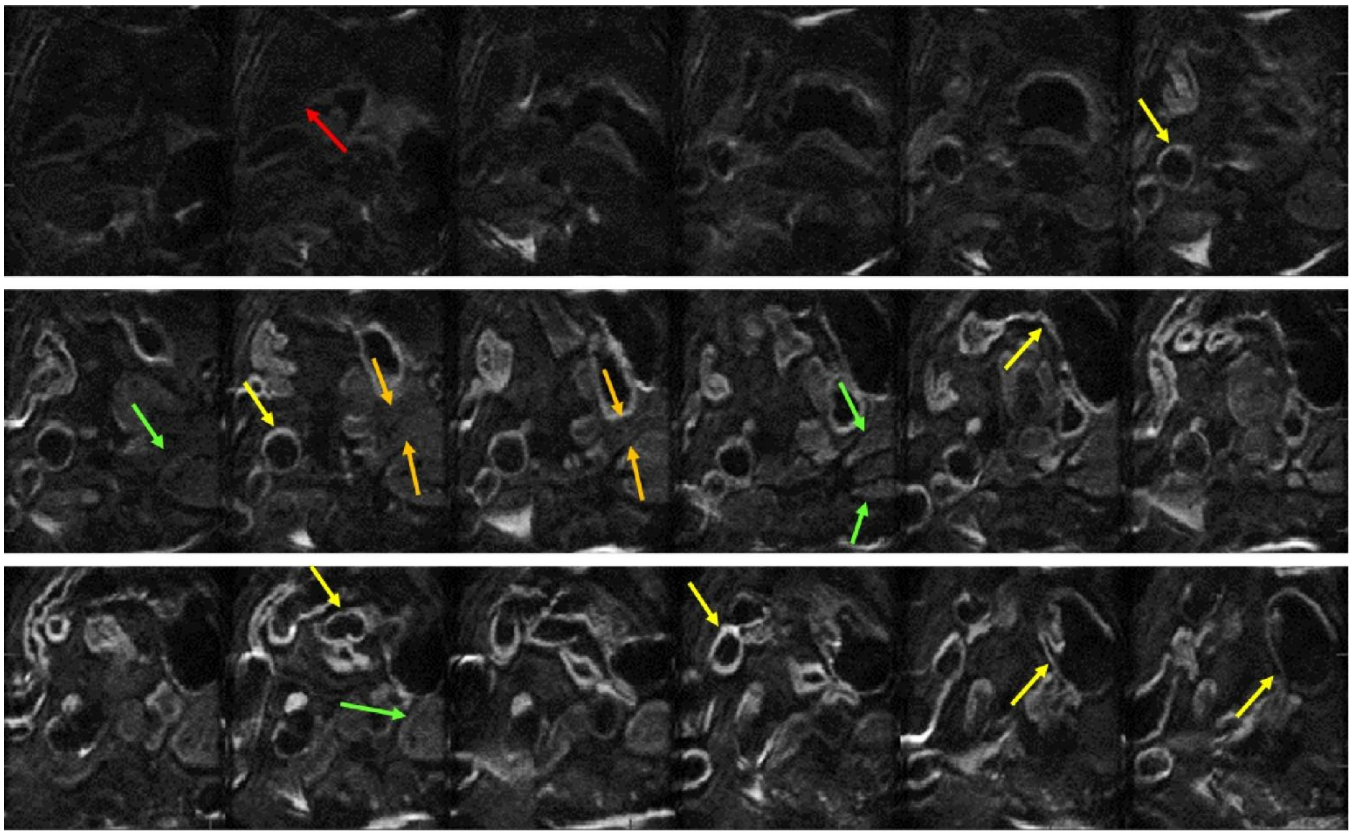


Figure S8 – **Axial images of the abdomen after BUSC injection.** DW (b1000) images of a mouse abdomen acquired 6.5 min after BUSC i.p. injection, from cranial to caudal. The abdominal organs are easily identified and well defined: bowels (yellow arrows), kidneys (green arrows), pancreas (orange arrows) and liver (red arrows).

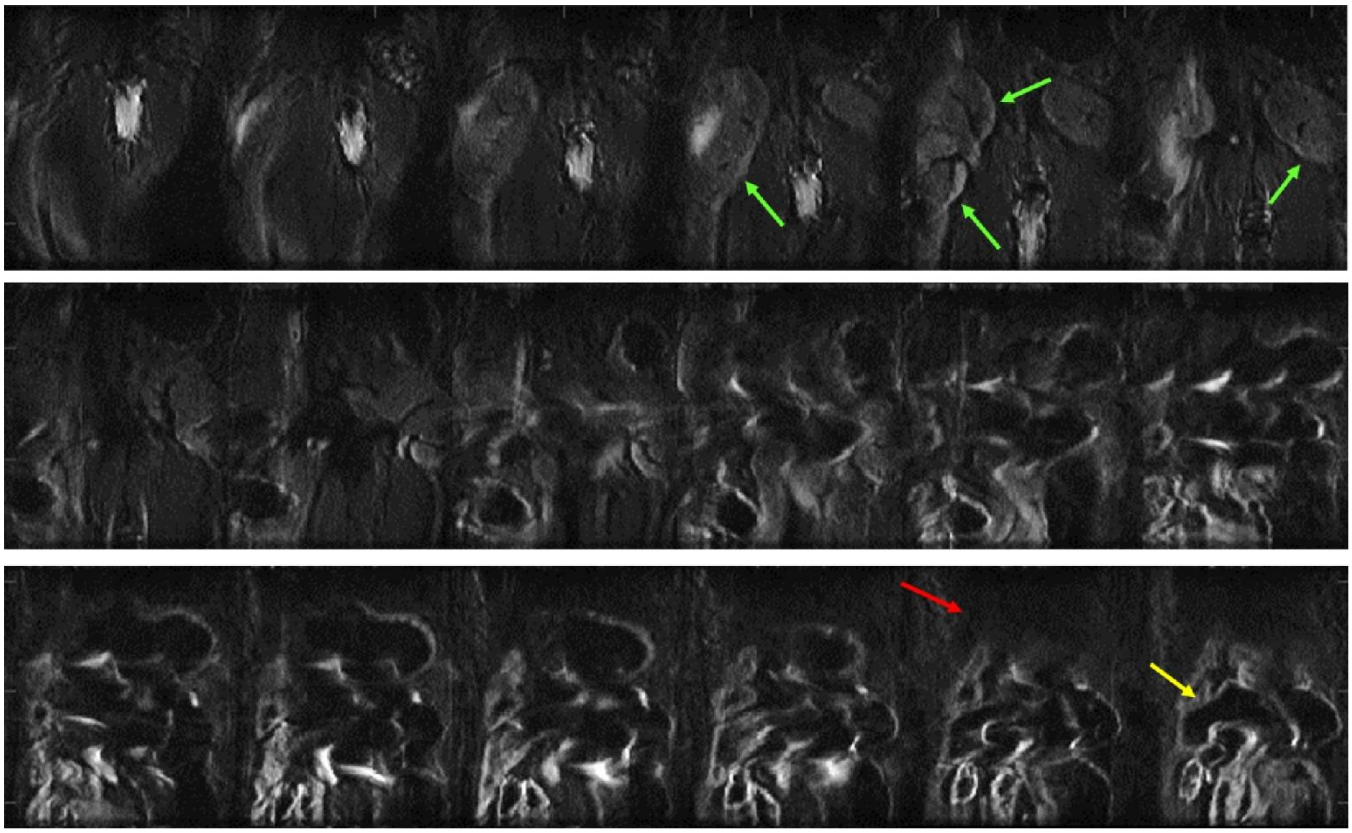


Figure S9 – **Coronal images of the abdomen after BUSC injection.** DW (b1000) images of a mouse abdomen acquired 6.5 min after BUSC i.p. injection, from dorsal to ventral. The abdominal organs are easily identified and well defined: bowels (yellow arrows), kidneys (green arrows) and liver (red arrows).

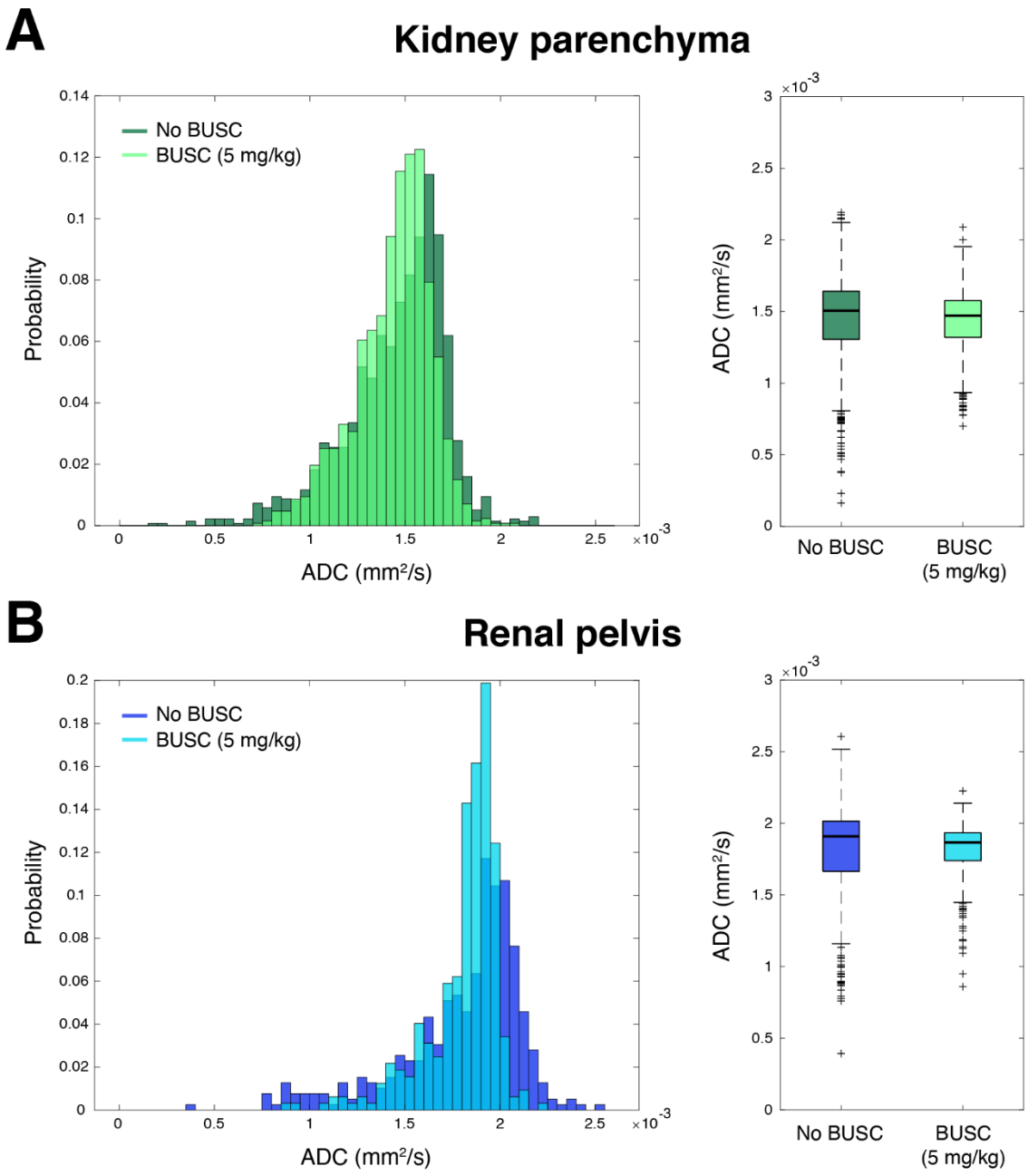


Figure S10 – **Histograms and boxplots of ADC values measured in kidney ROIs.** A higher variability of data can be observed in measurements performed before injecting BUSC, as represented by higher frequency of extreme values in both parenchymal (A) and renal pelvis (B) histograms and boxplots, when compared with measurements performed after injecting BUSC. These measurements exemplify the applicability of BUSC for performing segmentation/quantification studies in the mouse abdomen, by reducing the rate of motion-derived artifactual measurements.

3.3. Pancreatic Intraepithelial Neoplasia Revealed by Diffusion-Tensor MRI.

Bilreiro C, Fernandes FF, Simões RV, Henriques R, Chavarrías C, Ianus A, Castillo-Martin M, Carvalho T, Matos C, Shemesh N. Invest Radiol. 2024.
doi: 10.1097/RLI.0000000000001142

OPEN

Pancreatic Intraepithelial Neoplasia Revealed by Diffusion-Tensor MRI

Carlos Bilreiro, MD, Francisca F. Fernandes, MSc, Rui V. Simões, PhD, Rafael Henriques, PhD, Cristina Chavarrías, PhD, Andrada Ianus, PhD, Mireia Castillo-Martin, MD, PhD, Tânia Carvalho, DVM, PhD, Celso Matos, MD, and Noam Shemesh, PhD

Objectives: Detecting premalignant lesions for pancreatic ductal adenocarcinoma, mainly pancreatic intraepithelial neoplasia (PanIN), is critical for early diagnosis and for understanding PanIN biology. Based on PanIN's histology, we hypothesized that diffusion tensor imaging (DTI) and T2* could detect PanIN.

Materials and Methods: DTI was explored for the detection and characterization of PanIN in genetically engineered mice (KC, KPC). Following in vivo DTI, ex vivo ultrahigh-field (16.4 T) MR microscopy using DTI, T2* was performed with histological validation. Sources of MR contrasts and histological features were investigated, including histological scoring for disease burden (lesion span) and severity (adjusted score). To test if findings in mice can be translated to humans, human pancreas specimens were imaged.

Results: DTI detected PanIN and pancreatic ductal adenocarcinoma in vivo (6 KPC, 4 KC, 6 controls) with high discriminative ability: fractional anisotropy (FA) and radial diffusivity with area under the curve = 0.983 (95% confidence interval: 0.932–1.000); mean diffusivity and axial diffusivity (AD) with area under the curve = 1 (95% confidence interval: 1.000–1.000). MR microscopy with histological correlation (20 KC/KPC; 5 controls) revealed that sources of MR contrasts likely arise from microarchitectural signatures: high FA, AD in fibrotic areas surrounding lesions, high diffusivities within cysts, and high T2* within lesions' stroma. The strongest histological correlations for lesion span and adjusted score were obtained with AD ($R = 0.708$, $P < 0.001$; $R = 0.789$, $P < 0.001$, respectively). Ex vivo observations in 5 human pancreases matched our findings in mice, revealing substantial contrast between PanIN and normal pancreas.

Conclusions: DTI and T2* are useful for detecting and characterizing PanIN in genetically engineered mice and in the human pancreas, especially with AD and FA. These are encouraging findings for future clinical applications of pancreatic imaging.

Key Words: diffusion tensor imaging, carcinoma in situ, pancreatic neoplasms, pancreatic intraepithelial neoplasia, animals, genetically modified

(*Invest Radiol* 2024;00: 00–00)

Pancreatic cancer, mainly represented by ductal adenocarcinoma (PDAC), is the third leading cause of cancer-related death in the United States, with an estimated 11% survival rate at 5 years.[1] As symptoms develop late in the course of the disease, most patients are diagnosed at advanced stages precluding pancreatic resection surgery, which remains the only potentially curative therapeutic option.[2] Moreover, when patients are diagnosed in the early disease stages and subjected to tumor resection, the 5-year survival rate reaches 25%–50%.[3,4] Therefore, identifying precursor lesions for PDAC, mainly composed of pancreatic intraepithelial neoplasia (PanIN), could provide opportunities for early diagnosis and development of more effective therapies.[5,6] However, PanINs are not diagnosed by current imaging modalities, with a single study describing small cystic lesions in magnetic resonance cholangiopancreatography in a subset of patients with these lesions.[7] The absence of noninvasive diagnostic tools also prevents the investigation of PanIN's biology and tumorigenesis in humans, which remains largely unknown and mostly driven by research using genetically engineered mouse models (GEMMs) and histopathological analyses.[8–10] Therefore, there is an urgent need for developing imaging methods for PanIN diagnosis and characterization, which could enable early diagnosis before PDAC is established.

Diffusion-weighted MRI (DWI) provides insights into tissue microstructure and is routinely used for diagnosis, staging, and evaluation of response to therapy in benign and malignant diseases, mostly based on apparent diffusion coefficients (ADCs).[11–14] Given the potential of DWI, diffusion tensor imaging (DTI) was developed and explored in the clinical setting to provide a rotationally invariant representation of the diffusion process in biological tissues.[11] In the pancreas, DWI has been used in the past for characterizing benign and malignant processes, but studies exploring DTI for pancreatic disease characterization remain lacking, including for the detection of PanIN and early PDAC.[15,16]

We hypothesized that high-resolution DTI, with its ability to characterize diffusion anisotropy and sensitivity toward microarchitecture, could detect and characterize microstructural changes expected in PanIN and early PDAC. To test this hypothesis, we imaged GEMM developing PanIN and PDAC in vivo and harnessed ex vivo MR microscopy at ultrahigh field and direct histological validation to understand the sources of contrast. Similar techniques were previously successful in characterizing malignant lymph nodes with high resolution.[17,18] Here, we used 2 well-established mouse models of pancreatic cancer: KC, mostly displaying PanIN lesions, and KPC, with complete penetrance of PDAC.[19] Finally, we tested our hypothesis in human pancreas samples.

Received for publication September 12, 2024; and accepted for publication, after revision, October 11, 2024.

From the Radiology Department, Champalimaud Foundation, Lisbon, Portugal (C.B., C.M.); Champalimaud Research, Champalimaud Foundation, Lisbon, Portugal (C.B., F.F.F., R.H., C.C., A.I., M.C.-M., T.C., C.M., N.S.); Nova Medical School, Lisbon, Portugal (C.B.); i3S—Instituto de Investigação e Inovação em Saúde, Universidade do Porto, Porto, Portugal (R.V.S.); and Pathology Department, Champalimaud Foundation, Lisbon, Portugal (M.C.-M.).

Conflicts of interest and sources of funding: N.S. serves on the Scientific Advisory Board of Bruker Biospin. No other potential conflicts of interest are reported from remaining authors. Champalimaud Foundation funded this work; R.V.S.'s work was supported by H2020-MSCA-IF-2018, ref: 844776; A.I.'s work received the support of a fellowship from "La Caixa" Foundation (ID 100010434) and from the European Union's Horizon 2020 research and innovation programme under the Marie Skłodowska-Curie grant agreement no. 847648, fellowship code LCF/BQ/PI20/11760029.

Correspondence to: Noam Shemesh, PhD, Champalimaud Research, Champalimaud Foundation, Av. Brasilia 1400-038, Lisbon, Portugal. E-mail: noam.shemesh@neuro.fchampalimaud.org.

Data availability statement: The data generated in this study are available upon request from the corresponding author. Any human-derived data are completely anonymized.

Supplemental digital contents are available for this article. Direct URL citations appear in the printed text and are provided in the HTML and PDF versions of this article on the journal's Web site (www.investigativeradiology.com).

Copyright © 2024 The Author(s). Published by Wolters Kluwer Health, Inc. This is an open-access article distributed under the terms of the Creative Commons Attribution-Non Commercial-No Derivatives License 4.0 (CCBY-NC-ND), where it is permissible to download and share the work provided it is properly cited. The work cannot be changed in any way or used commercially without permission from the journal.

ISSN: 1536-0210/24/0000–0000
DOI: 10.1097/RLI.0000000000001142

MATERIALS AND METHODS

Ethics Statement

Animals were handled in agreement with European FELASA guidelines. Animal procedures were conducted according to European Directive 2010/63 and preapproved by institutional and national authorities. The study protocol involving human biological tissue was preapproved by the institutional ethics committee. All participants provided signed informed consent before tissue collection, and personal identity was kept private through pseudonymization in the institution's Biobank.

Genetically Engineered Mouse Models

The KC (Pdx1-Cre, LSL-Kras^{G12D}/Ptf1a-Cre, LSL-Kras^{G12D}) and KPC (Ptf1a-Cre, LSL-Kras^{G12D}, p53^{LoxP}) mouse models were used: KC mice develop PanIN and progress to PDAC; KPC mice develop PanIN and PDAC with complete penetrance.[19] Healthy mice (C57BL/6 J background) were used as controls. All animals' rearing was undertaken in a specific pathogen-free facility in a temperature-controlled room, with a 12-hour light/dark cycle with ad libitum access to food and water. The animals' cages were enriched with plastic igloos and shredded paper. Given the potential of GEMM for developing advanced pancreatic disease, the animals were continuously monitored for signs of malaise, namely, weight loss/cachexia, fur thinning, and apathetic or aggressive behavior. Whenever these signs were observed, the animals were humanely sacrificed.

Anatomical In Vivo Imaging

In a first exploratory phase (Fig. 1A), KC (n = 9) and KPC (n = 6) mice were imaged monthly from 4 months old, to assess the development onset of pancreatic abnormalities. Animals were imaged until abnormalities were observed, with a T2-weighted turbo spin-echo sequence (Table 1), in 1 T and 9.4 T scanners (respectively, Icon and BioSpec; Bruker, Germany; 40-mm ID linear transmit-receive volume coil) depending on scanner availability: 41 scans were performed in 1 T; 15 scans were performed in 9.4 T scanners. Animal characteristics are described in Table 2. Anesthesia was induced with 5% isoflurane (Vetflurane; Virbac, France) mixed with oxygen-enriched (28%) air. Isoflurane dosage was reduced to 1.5%–2.5% during animal preparation and for the duration of MRI scanning. Breathing rate and rectal temperature were monitored and recorded throughout scans using a pillow pressure sensor and an optic fiber temperature probe (SA Instruments Inc, Stony Brook, USA). A warm-water recirculating pad was used for body temperature control, maintaining rectal temperature between 35.0°C and 37.0°C. Ophthalmic gel (Vidisic Gel; Bausch+Lomb, Canada) was applied to the animals' eyes before each acquisition for preventing eye dryness. All acquisitions began with routine adjustments: center frequency, radiofrequency calibration, and automatic shimming.

In Vivo DTI Animals Selection

KPC mice presented early-onset disease with pancreatic abnormalities in anatomical T2-weighted in vivo imaging and physical signs of malaise. In contrast, KC mice presented pancreatic abnormalities later in their development. Considering these preliminary findings, we decided to use young animals from the KPC and older animals from the KC transgenic lines for this part of the study: 6 KPC, 4 KC, and 6 controls (Supplemental Digital Content 1, Table with sample characteristics, http://links.lww.com/RLI/A980), with an estimated statistical power of 0.95 ($\alpha = 0.05$; estimated effect size = 2.2). The predicted number of KC mice was 6; however, due to unexpected deaths of 2 KC mice before pancreas extraction, these animals could not be used for histopathological analysis and were excluded from the study.

In Vivo DTI

KPC (n = 6), KC (n = 4), and control (n = 6) mice were imaged in a 9.4 T scanner (BioSpec; Bruker, Germany; 40-mm ID linear transmit-receive volume coil). Intraperitoneal hyoscine butylbromide (5 mg/kg; Buscopan; Boehringer Ingelheim, Spain) was administered 8 minutes before acquisition for bowel motion reduction.[20] A diffusion-weighted spin-echo echo-planar-imaging was used for imaging the animals' abdomen (Table 1). Datasets were analyzed using in-house developed

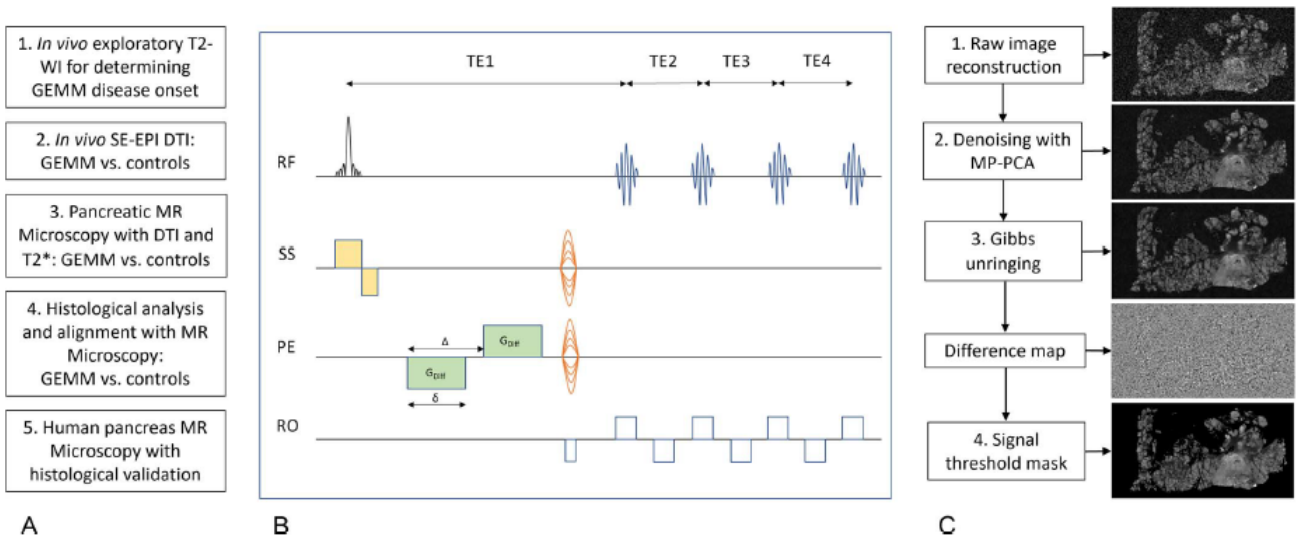


FIGURE 1. Study design, diffusion-weighted multi-gradient-echo pulse sequence diagram, and preprocessing pipeline. A, Study design with major steps performed in chronological order. B, Diffusion-weighted multi-gradient-echo sequence used for the ex vivo MRI acquisition, which includes a small flip-angle slab-selective excitation followed by diffusion gradients and phase encoding, and a multiple-gradient-echo readout echo-train (RF, radiofrequency; SS, slice selection; PE, phase encoding; RO, readout; GDiff, diffusion gradients; δ, diffusion gradient duration; Δ, diffusion time; TE2 = TE3 = TE4). C, Data preprocessing pipeline, with a respective example image obtained in each step (MP-PCA = Marchenko-Pastur principal component analysis). Difference map is the resulting subtraction of pixel values between the raw image and the processed image after denoising and unringing, displaying the removal of image noise and ringing artifacts.

© 2024 The Author(s). Published by Wolters Kluwer Health, Inc.

TABLE 1. MRI Acquisition Parameters

Pulse Sequence	T2-TSE	SE-EPI	DMGE
Magnetic field strength	1 T; 9.4 T	9.4 T	16.4 T
In-plane resolution (mm^2)	0.150 × 0.150 (1 T) 0.125 × 0.125 (9.4 T)	0.125 × 0.125	-
Slice thickness (mm)	0.7 (1 T) 0.3 (9.4 T)	0.25	-
No. slices	20–36	36	-
3D resolution (mm)	-	-	0.08 × 0.08 × 0.08
TR (ms)	3825 (1 T) 1500–2700 (9.4 T)	2300–2600	125
TE (ms)	60 (1 T) 20–22 (9.4 T)	15.6–16.5	9.2–10.2
Signal averages	30 (1 T) 10–16 (9.4 T)	16	1
Acceleration factor	8	-	-
Multishot segments	-	4	-
Partial Fourier reduction factor	-	1.7	-
EPI sampling bandwidth (kHz)	-	395	-
Fat suppression	No	Yes	Yes
No. DTI B values	-	1	1
B values (s/mm^2)	-	1000	775–1200
No. B = 0 s/mm^2	-	2	2
Diffusion directions	-	10	10
Respiratory triggering	Yes	Yes	-
Scan duration	44–50 min (1 T) 12–21 min (9.4 T)	31–33 min	5 h 54 min–16 h 33 min

T2-TSE, T2-weighted turbo spin echo; SE-EPI, spin-echo echo planar imaging; DMGE, diffusion-weighted multi-gradient-echo.

code in MATLAB (MathWorks Inc, Natick, MA). Data preprocessing included denoising based on Marchenko-Pastur principal component analysis (MP-PCA) and Gibbs unringing.[21,22] Fractional anisotropy (FA), mean diffusivity (MD), axial diffusivity (AD), and radial diffusivity (RD) maps were produced, fitting DTI to diffusion-weighted images using a weighted-least-squares solution.[23] The images obtained were analyzed by a gastrointestinal radiologist, who segmented the entire pancreas in each slice, using MATLAB's built-in segmentation tools. Measurements obtained from pancreatic segmentation were used for groupwise comparisons. After MRI, all animals had their pancreases harvested and subjected to histopathological diagnosis, so disease status (presence of PanIN, PDAC) was known for each animal.

Pancreas Specimens' Preparation for MR Microscopy

Pancreases from additional KPC (n = 8), KC (n = 12), and control (n = 5) mice were prepared for MR microscopy. As pancreatic abnormalities were evident in T2-weighted images at 8.5 (interquartile range [IQR] = 0.75) months of age for KC mice, these animals were studied at this age (n = 12), whereas n = 8 KPC mice were studied at 4.25 (IQR = 0.25) months old, right after the first exploratory MRI scans, due to early aggressive disease.[19] Preliminary findings were used for calculating the number of animals in each group: pancreases harvested from 3 KC mice and 1 healthy control were imaged and FA maps were produced. According to a comparison of median FA measurements, effect size was estimated at 1.6, and a similar effect size was assumed for KPC mice. With a statistical power of 0.95, each animal group was initially aimed at 10 animals. However, due to unpredictable events when developing the colonies, 12 KC (available surplus in litter production) and 8 KPC mice were finally used (3 KPC mice suffered premature deaths and their pancreases could not be harvested on time). GEMM and n = 5 controls were sacrificed with cervical dislocation, and their pancreases dissected and removed through median laparotomy. Pancreatic specimens were subjected to fixation: immersion in

TABLE 2. Sample Characteristics in Anatomical Longitudinal T2-Weighted Imaging of GEMM

Animal Model	KC	KPC
No. animals	9	6
Pancreatic abnormalities onset (months old)	8.5 (IQR = 0.75)	4.25 (IQR = 0.25)
Animal weight (g)	30.4 (IQR = 11.2)	22.9 (IQR = 4.1)
Animal sex	4/9 females	4/6 females

Continuous variables expressed as medians and IQR. Pancreatic abnormalities onset was assessed from 4 months old.

TABLE 3. Lesion Adjusted Score Calculation, Adapted From Veite-Schmahl et al[25] and Basturk et al[26]

Score	Grade	Distribution
1	Low-grade	Focal
2	High-grade	Multifocal
3	PDAC	Diffuse

The final adjusted score for each pancreatic specimen was determined using the following distribution-adjusted lesion grade = (low-grade × distribution) + (high-grade × distribution) + (PDAC × distribution).

© 2024 The Author(s). Published by Wolters Kluwer Health, Inc.

4% paraformaldehyde for 48 hours and then in phosphate-buffered saline with 0.01% sodium azide for 24 hours. After fixation, pancreases were immersed in Fluorinert within a 10-mm NMR tube for ex vivo MRI, with special care for removing air bubbles and animal hair in the sample.

Ex Vivo MR Microscopy

Pancreases were imaged in a 16.4 T MRI scanner (Ascend Aeon; Bruker, Germany), using a diffusion-weighted multi-gradient-echo sequence, providing ultrahigh-resolution 3D images with both diffusion and T2* weighting (Fig. 1B, Table 1).[24] Two 10-mm probes were used (Micro5, Cryoprobe; Bruker, Germany) depending on availability; sample temperature was maintained at 37°C. Datasets were preprocessed as previously described (MP-PCA denoising, Gibbs unringing, Fig. 1C).[21,22] After preprocessing, images were masked to remove low-signal areas. T2*, DTI (FA, MD, AD, RD), and ADC maps were then obtained from the preprocessed datasets.[23]

Histological Analysis

Following MRI, mouse pancreas samples were serially sectioned (4-µm thickness, 0.5-mm spacing) and stained with hematoxylin and eosin. Slides were digitally scanned in Ultra-Fast Scanner (Philips) or AxioScan Z1 (Zeiss) and examined by a veterinary pathologist.

The classification of pancreatic lesions—acinar-to-ductal metaplasia (ADM), low-grade PanIN, high-grade PanIN, and PDAC—was based on specific criteria (Supplemental Digital Content 2, Table with classification, http://links.lww.com/RLI/A980), adapted from Veite-Schmahl et al[25] and Basturk et al.[26] Disease severity scoring was performed on the slide where the extent of the lesions was higher. A distribution-adjusted lesion grade with equal contribution from each lesion type was developed, ensuring that all lesions contribute equally to the final score, rendering a continuous range of scores, adapted from Berman-Booty et al[27] and Knoblaugh and Himmel.[28] This system calculates the score by summing the product of the scores for grade and distribution of each lesion, as shown in Table 3: distribution-adjusted lesion grade = (low-grade PanIN × distribution) + (high-grade PanIN-distribution) + (PDAC × distribution) with ascribed scores of 1, 2, and 3 for low-grade PanIN, high-grade PanIN, and PDAC, respectively, and for focal, multifocal, and diffuse lesions, respectively. The same histological slide was also used to calculate lesion span (ie, lesion burden for each specimen), through digital segmentation using QuPath v. 0.4.3 semimanual segmentation tools, by annotating area of the lesions and area of normal pancreas.[28,29]

Lesion span and adjusted score were correlated with MRI data, assessing if DTI and T2* measurements scale with disease extension and severity.

Imaging and Histology Alignment

The alignment between MRI and histology was manually performed by a gastrointestinal radiologist. For this, the Volume Viewer tool from ImageJ (US National Institutes of Health) was used for reconstructing the 3D datasets in real time and searching for image planes corresponding to histology slides using the powder-averaged diffusion-weighted images. Specimens' structures (lymph nodes, large blood vessels, cystic lesions, and large masses) were used as landmarks for searching for the most adequate image plane. When the manually reconstructed image plane and slice were deemed the most approximate as possible to the corresponding histological slide, the reconstruction coordinates were used in all DTI and T2* maps, and the corresponding images were exported for a visual comparison between both histology and MRI. Image contrasts were therefore attributed to the corresponding histological changes, as directly observed.

Human Pancreas

Pancreas specimens (n = 5) obtained from patients with PDAC, from the institution's Biobank (formalin-fixed leftovers after diagnostic procedures following resection surgery), were analyzed searching for PanIN.[30] Specimens were sliced and placed inside a 10-mm MR tube. Sample preparation, imaging acquisition, and processing methods described above for MR microscopy were used. Histological slides were sectionized, stained,

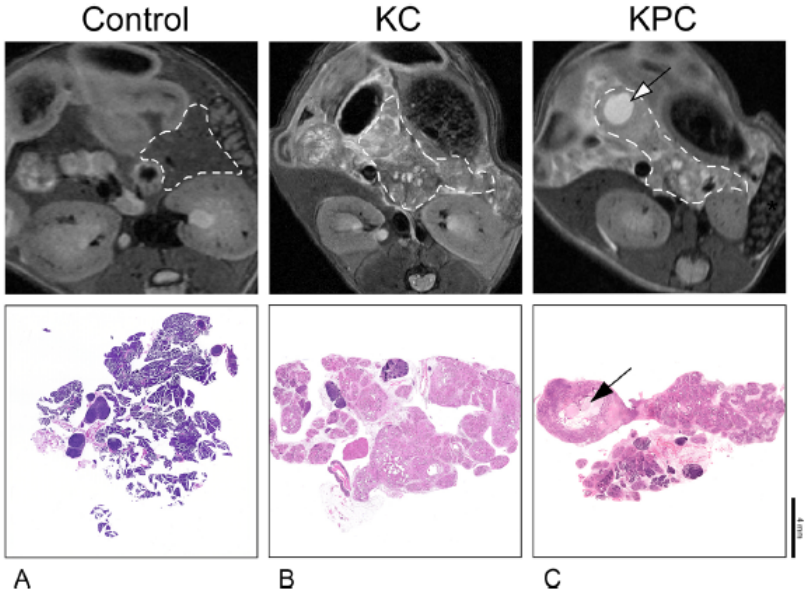


FIGURE 2. Pancreatic abnormalities with cystic changes are seen in vivo in KPC (4.75 months old) and KC (8.5 months old) mice, using conventional TSE-T2-weighted images, with corresponding histological diagnosis, including acinar-to-ductal metaplasia, PanIN, and PDAC lesions. The healthy control (2 months old) pancreas is homogeneous without focal or diffuse changes. C, A necrotic/cystic area inside a large tumor (arrows) is directly correlated with histology. All 3 images were acquired in a 9.4 T scanner (BioSpec).

© 2024 The Author(s). Published by Wolters Kluwer Health, Inc.

and digitized, as described above, and evaluated by a gastrointestinal pathologist. Alignment was performed manually by a gastrointestinal radiologist, as previously described, for a visual comparison.

Statistical Analysis

IBM SPSS statistics v.23 was used. Kolmogorov-Smirnov test was used to assess the distribution of continuous variables, revealing nonnormal distributions throughout. Kruskal-Wallis test was used for groupwise comparisons, with post hoc pairwise comparisons, and Mann-Whitney *U* test for comparisons between 2 groups. Bonferroni correction was applied when comparing multiple test metrics, namely, different DTI, T2*, and ADC maps, by multiplying the *P* values by the number of metrics. Receiver operating characteristics analysis was performed for assessing the discriminative value of DTI. Pearson correlation coefficient was used for evaluating MRI measurements and lesion span/adjusted score. All tests were bilateral; *P* values <0.05 were considered significant.

RESULTS

Longitudinal MRI Assessment of PanIN and PDAC Development Onset

Exploratory anatomical in vivo T2-weighted images revealed variably enlarged pancreases with high signal intensity and cystic lesions for GEMM, whereas the pancreas of control mice was homogeneous with low signal intensity (Fig. 2A). These findings were evident at 8.5 months old for KC mice and at first scans (4.25 months old) for KPC mice (Table 2), as confirmed with histopathology (Fig. 2B).

DTI Noninvasively Detects PanIN and PDAC In Vivo

Both KC and KPC mice presented pancreases with high FA, MD, AD, and RD; large PDAC; and small cystic lesions, contrasting visually with control mice which presented low values in the pancreas in all parameters (Fig. 3A).

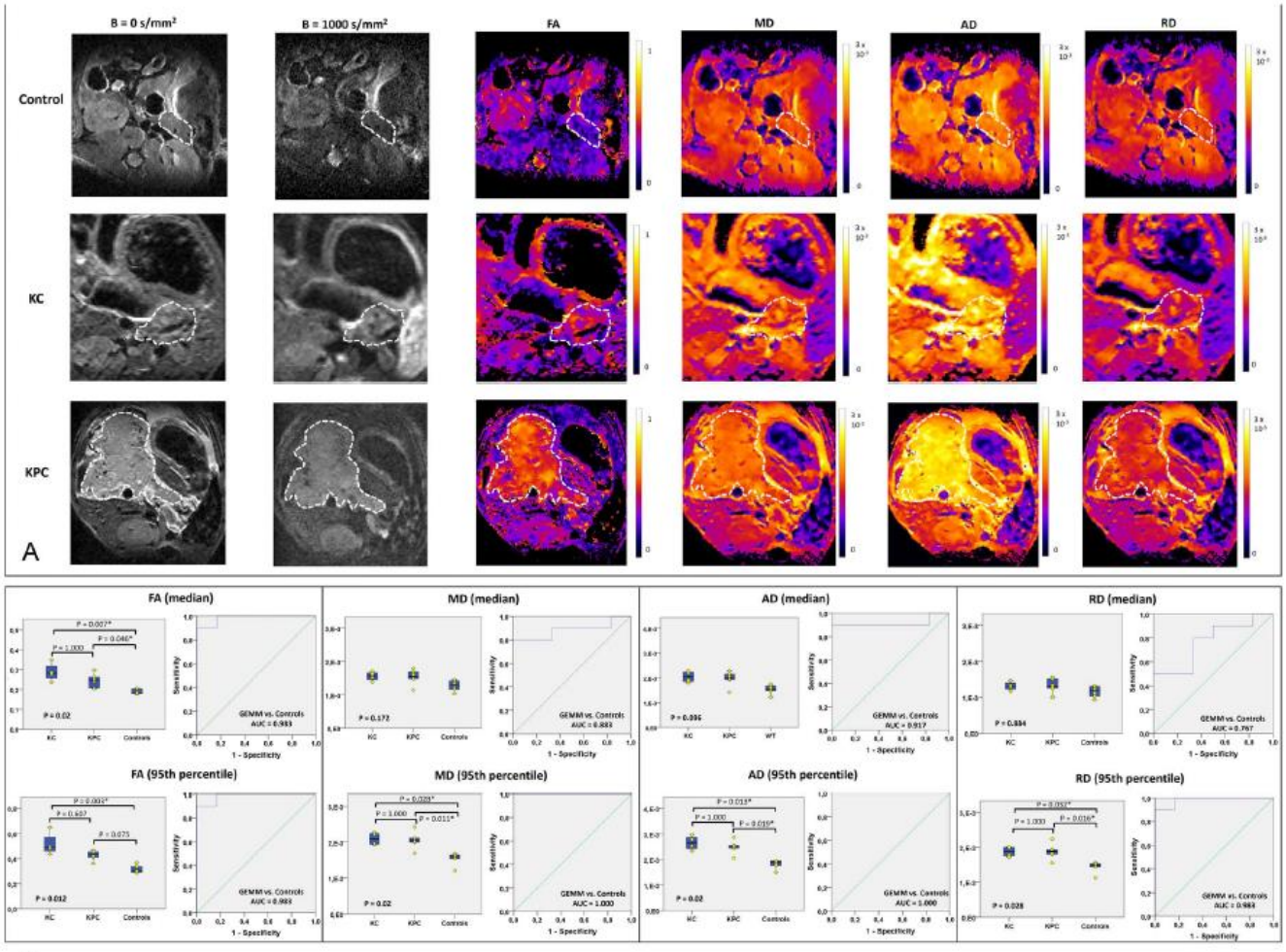


FIGURE 3. DWIs (averaged b = 0 and b = 1000 s/mm^2 images) and DTI maps (FA, MD, AD, RD) for representative KC, KPC, and healthy control mice. A, The maps produced with DTI showcase the differences between healthy controls, KC, and KPC mice. The KC presented here, with diffuse PanIN infiltration in the pancreatic parenchyma and no PDAC, has visually increased values in DTI derived maps, especially FA and AD. The KPC mouse is bearing a large PDAC, also with increased values in the same maps. In contrast, the healthy control mouse has a homogeneous pancreas with intermediate-low values in all maps. B, Quantitatively, the differences between groups of animals, including 10 GEMM (6 KPC and 4 KC) and 6 controls, provide a good discriminative ability of DTI-derived metrics. FA presents the best performance when using median values (AUC = 0.983); AD and MD present the best performance when using 95th percentile values (AUC = 1). MD, AD, RD expressed in mm^2/s.

© 2024 The Author(s). Published by Wolters Kluwer Health, Inc.

TABLE 4. In Vivo DTI With KC and KPC Mice—Presence of PDAC

PDAC	Present	Absent	P
No. animals	7	3	-
Models	KC: 1/4 KPC: 6/6	KC: 3/4 KPC: 0	0.033*
FA (median)	0.25	0.28	0.833
FA (95th percentile)	0.45	0.48	0.383
MD (median)	1.6E-3	1.5E-3	1.000
MD (95th percentile)	2.1E-3	2.0E-3	0.517
AD (median)	2.1E-3	1.9E-3	0.517
AD (95th percentile)	2.5E-3	2.5E-3	0.833
RD (median)	1.3E-3	1.3E-3	1.000
RD (95th percentile)	1.9E-3	1.8E-3	0.517

Continuous variables were expressed as medians.

Fisher exact test was used for comparing prevalence of PDAC in GEMM models.

Mann-Whitney *U* test was used for comparing GEMM with and without PDAC for each DTI metric.

*Statistically significant results.

Median FA obtained after pancreatic segmentation was significantly higher for both transgenic mice (n = 6 KPC, n = 4 KC) compared with controls (n = 6), with differences increasing and becoming significant also for MD, AD, and RD, when assessing the higher values observed in each group (ie, 95th percentile) (Fig. 3B). The discriminative performance of median DTI measurements obtained from the entire pancreas in each animal for differentiating GEMM from controls was high, ranging from 0.767 (95% confidence interval [CI]: 0.527–1.000) area under the curve (AUC) for RD, up to 0.983 (95% CI: 0.932–1.000) AUC for FA. The discriminative performance increased once more when assessing the parameters' 95th percentile, with AUC ranging from 0.983 (FA and RD, 95% CI: 0.932–1.000) to 1.000 (MD and AD, 95% CI: 1.000–1.000) (Fig. 3B). When comparing KC and KPC mice, the DTI metrics were similar between both groups of animals. Also, DTI metrics could not distinguish between GEMM with (n = 7) and without PDAC (n = 3) (Table 4).

MR Microscopy With DTI and T2* Characterizes Ex Vivo Pancreatic Abnormalities

To better understand the contrasts observed, we performed detailed MR microscopy and histology in pancreases harvested from KC mice (n = 12), KPC mice (n = 8), and healthy control mice (n = 5) (Supplemental Digital Content 3, Table with sample characteristics, http://links.lww.com/RLI/A980).

After alignment between MR microscopy and histology slides, enabling a direct comparison of MRI and histology, stark contrasts between DTI and T2* parameters in normal and abnormal tissue were observed (Fig. 4). High FA values are observed in areas of ADM, where PanIN lesions of variable degrees are found surrounded by fibrosis, as well as at the periphery of PDAC lesions. In contrast, areas of normal parenchyma demonstrate low FA values, allowing a clear distinction between different types of tissue. The MD, AD, RD, and ADC maps reveal high values in cystic and necrotic areas, most evident in AD maps, and intermediate/high AD values in fibrotic areas of ADM, PanIN, and PDAC. T2* maps present high values in the stroma of both PanIN and PDAC lesions. All the control pancreases show homogeneous FA, diffusivities, T2*, and ADC maps with lower values throughout the pancreatic parenchyma.

Quantitatively, as observed for in vivo DTI, DTI/T2* maps obtained from pancreas specimens allowed us to distinguish between GEMM and controls (Fig. 5; Supplemental Digital Content 4, Figure with all group comparisons, http://links.lww.com/RLI/A981). When comparing KPC and controls, median values were significantly different, with KPC presenting higher values for MD (+10.6%, $P = 0.004$), AD (+22%, $P = 0.001$), and RD (+7.7%, $P = 0.023$). When comparing KC and controls, only median AD was different (+14%, $P = 0.046$). The comparison of highest values in each specimen (95th percentile) enhanced the observed differences between GEMM and controls. For KPC versus controls, except for FA ($P = 0.128$), KPC presented higher MD (+41.2%, $P = 0.006$), AD (+45.4%, $P = 0.0018$), RD (+38.9%, $P = 0.004$), T2* (+69.6%, $P = 0.017$), and ADC (+43.2%, $P = 0.005$). For KC versus controls, KC presented higher FA (+186.7%, $P = 0.003$), MD (+38.2%, $P = 0.006$), AD (+47.5%, $P = 0.002$), RD (+35.7%, $P = 0.015$), T2* (+58.6%, $P = 0.010$), and ADC (+40.8%, $P = 0.006$). When comparing KC and KPC, no differences were observed for median or 95th percentile values; however, the lowest values (5th percentile) were lower in KC for MD (−15.8%, $P = 0.003$), AD (−14.4%, $P = 0.007$), and RD (−15.2%, $P = 0.005$). Variable median ADC for different diffusion directions in each animal further demonstrates diffusion anisotropy in the pancreas (Supplemental Digital Content 5, Figure with median ADC for all diffusion directions, http://links.lww.com/RLI/A982).

Histologically, ADM was present in all GEMM mice, most markedly in KC mice, as shown in Supplemental Digital Content 6 (Figure, representative segmented samples, http://links.lww.com/RLI/A983) and Table 5 (all samples). PDAC was mainly observed in KPC mice: 33.33% of KC and 87.5% of KPC mice. Both GEMM had PanIN lesions of grades 1 to 3, more marked in KC mice. Most mice had ≥70% of their pancreas affected: 75% of KC mice and 75% of KPC mice. The median lesion span in KC mice was 80.88% (IQR: 42.75) and in KPC mice was 91.45% (IQR: 36.62). Median adjusted score was 17 (IQR: 9) in KC mice and 26 (IQR: 1.75) in KPC mice.

DTI and T2* Correlate With Disease Burden and Severity

As seen in Figure 5, Supplemental Digital Content 7 (http://links.lww.com/RLI/A984), 8 (http://links.lww.com/RLI/A985) (Figures, lesion span and adjusted score correlation plots), and 9 (Table, lesion span and adjusted score correlation coefficients, http://links.lww.com/RLI/A980), DTI/T2* metrics correlate both with disease burden (lesion span) and severity (adjusted score), when using median and 95th percentile values. The highest correlation coefficients both for lesion span and for adjusted score were obtained with AD (median AD, $R = 0.789$; 95th percentile AD, $R = 0.729$; respectively). Other than FA and T2*, 5th percentile values of MRI metrics were not correlated with histological scores.

PanIN in the Human Pancreas Revealed by Ex Vivo DTI

Human pancreas samples (Supplemental Digital Content 10, Table with patient characteristics, http://links.lww.com/RLI/A980) presented relevant histological differences when compared with the GEMM counterparts: scattered foci of ADM, higher proportion of normal pancreatic parenchyma, and absence of PDAC (Fig. 6, Supplemental Digital Content 11, http://links.lww.com/RLI/A986). In 3 samples, parenchymal atrophy with fatty replacement was observed (Figs. 6B and C, Supplemental Digital Content 11B, http://links.lww.com/RLI/A986). After alignment between MR microscopy and histology, we observed clear contrasts between areas of ADM, PanIN, and surrounding normal pancreas. High FA, AD, and T2* values were observed in areas of ADM and surrounding PanIN lesions; contrast between lesions and surrounding parenchyma was evident in all maps. One pancreas sample with diffuse interstitial fibrosis, attributed to chronic pancreatitis, showed mid-high FA, AD, and T2* values irregularly scattered throughout the fibrotic tissue (Fig. 6C). Histologically, this diffuse interstitial fibrosis is haphazardly organized, whereas the periductal fibrosis forms a

© 2024 The Author(s). Published by Wolters Kluwer Health, Inc.

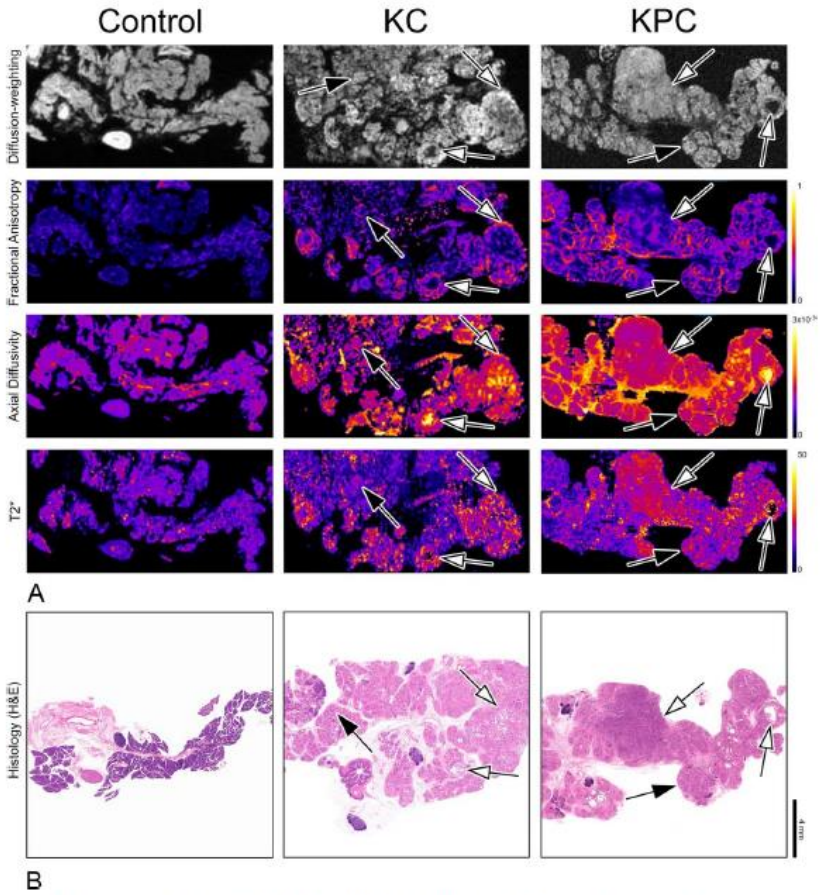


FIGURE 4. Comparison between MR microscopy and histology in GEMM. A, The healthy mouse pancreas is homogeneous, with low anisotropy, diffusivity, and T2* values; coil used: Cryoprobe. B, KC pancreas with extensive ADM and PanIN (black arrows), as well as PDAC (white arrows). Conventional diffusion weighting shows heterogeneous restricted diffusion. There are high anisotropy values in the periphery of areas with ADM, PanIN, and PDAC. High axial diffusivity is observed in cystic/necrotic areas, and intermediate diffusivity and high T2* values are seen in the lesions' stroma. Coil used: Cryoprobe. C, KPC pancreas with extensive PDAC (white arrows) and small areas of ADM and PanIN (black arrows). Conventional diffusion weighting is not helpful in delineating the pancreatic lesions. There are high anisotropy values in the periphery of PDAC and PanIN lesions; high diffusivity values in cystic/necrotic areas and regions with inflammatory infiltrates; and high T2* values in the lesions' stroma. Coil used: Micro5. AD is expressed in mm^2/s; T2* is expressed in milliseconds (ms).

sheath or cuff-like structure around ducts in areas of ADM, PanIN, and PDAC.

DISCUSSION

This study provides evidence establishing a potential role for DTI and T2* in characterizing PanIN and PDAC. We report that ex vivo and in vivo MRI detects PanIN-associated changes and PDAC, identifying potential mechanisms for the contrast and underscoring their translational relevance for imaging the human pancreas.

The process of carcinogenesis in PDAC follows a progressive development of PanIN, where genetic mutations and morphological changes are acquired until PDAC is finally established.[10,31] There is a recognized absence of noninvasive detection methods for PanIN, precluding research into PanIN biology, especially in humans.[7,32] Most current knowledge of PanIN was achieved with studies performed in GEMM.[9,31] Thus, the development of noninvasive detection methods can not only inform about PanIN biology and tumorigenesis, but also provide opportunities for early therapeutic interventions or close follow-up of patients, enabling PDAC diagnosis in resectable stages. Here, we leverage GEMM for DTI detection of PanIN, PDAC, and associated pancreatic changes, suggesting DTI/T2* as potential biomarkers for disease onset, staging, or monitoring. Our results also highlight the important variability between pancreatic structural changes in these models, probably caused by variable proportions of tumoral stroma, ductal structures, and inflammatory infiltrates, which should be accounted for in future studies.

The DTI and T2* maps provided more striking visual contrasts than conventional diffusion-weighted images, the method currently used in clinical practice. As observed by comparing MRI with histology, these contrasts appear to be derived from specific microstructural characteristics of the lesions: areas of anisotropy with high FA values corresponded to the peripheral zones of PanIN, ADM, and PDAC, where sheath/cuff-like periductal fibrosis is observed; areas of high diffusivities corresponded mostly to cystic and necrotic regions; areas of high T2* corresponded mostly to stromal components. Also, AD performed better than other metrics, including the clinical standard ADC, for lesion detection and correlated more closely with disease extent and severity. These results hint to differences in tissue microstructure

© 2024 The Author(s). Published by Wolters Kluwer Health, Inc.

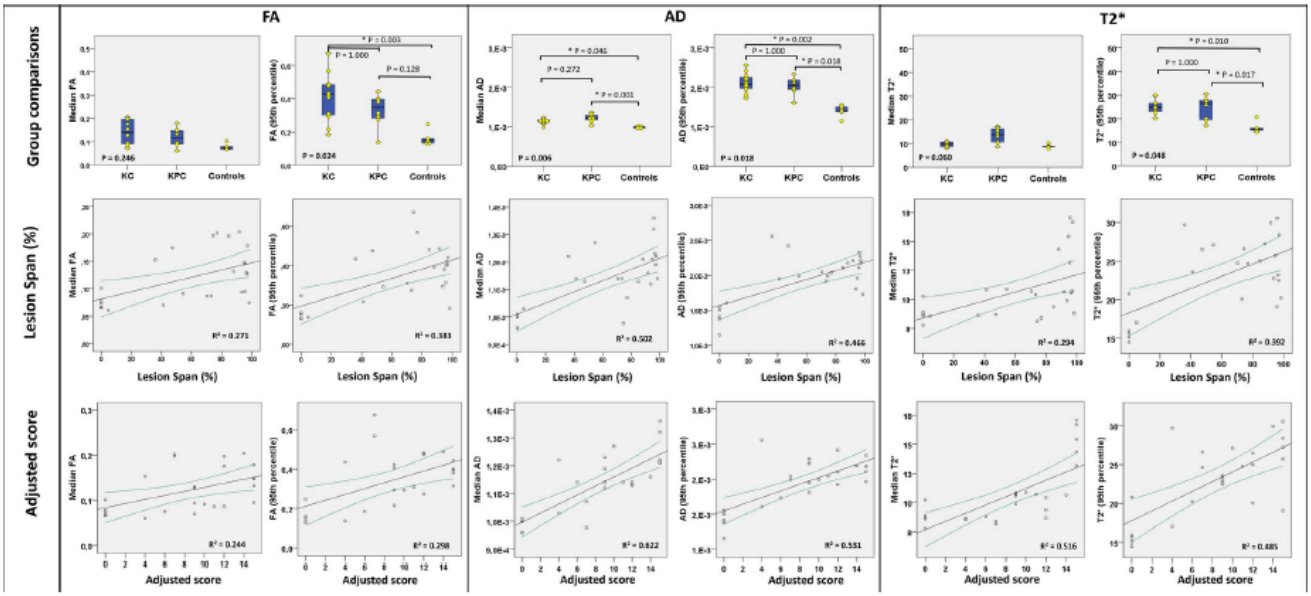


FIGURE 5. Group comparisons, lesion span, and adjusted score for DTI (FA and AD are shown) and T2* metrics. For group comparisons, the differences between GEMM and controls are highlighted when using the highest (95th percentile) values, where AD provided the largest differences. For lesion span correlation, the use of 95th percentile values improved the results, where AD was the most correlated metric. For adjusted score, both medians and the 95th percentile values showed significant correlations with disease burden and severity, but the 95th percentile values did not show an improvement when compared with median values. Again, AD provided the best performance (R^2 = 0.622, when using the median values). The group comparisons, lesion span, and adjusted score correlations for all MRI metrics can be found in Supplemental Digital Content 4, 7, and 8.

as the origin of the observed MRI contrasts and highlight the value of microstructural characterization through DTI, as previously described for other applications.[13,33,34]

PanIN remains an elusive lesion in humans. Noncommunicating pancreatic microcysts in magnetic resonance cholangiopancreatography were reported to predict the presence of PanIN in pancreatic specimens, with 61% accuracy.[7] Our findings show that DTI/T2* might be useful in this context, as the contrasts seen in human pancreas allowed a clear detection of PanIN. Regarding differentiation between degrees of PanIN and PDAC, we found a clear correlation between disease burden and severity and DTI/T2* metrics; however, the visual contrasts were mostly similar, both in vivo and ex vivo. This may question the specificity of DTI/T2* for visually differentiating low-grade from high-grade PanIN and PDAC, but further data are needed to address this question.

The presence of parenchymal atrophy with fatty replacement has been reported previously, as a finding associated with PanIN and early PDAC.[7,35,36] Our findings in human pancreas specimens corroborate these reports, with 3 out of 5 samples presenting fatty replacement. This was not observed on GEMM, however, as the animals' pancreases presented with increased size and parenchymal replacement by abnormal tissue. The presence of fatty tissue is not observed in our DTI/T2* data, as the acquisitions were performed with fat suppression, and no fat-sensitive pulse sequences were performed. The characterization of fatty replacement is an interesting point for future studies, especially if performed on the human pancreas.

DTI has been performed successfully for imaging the pancreas in clinical context.[16] However, its clinical role remains undetermined, both for PDAC detection/characterization and for characterizing other malignant lesions or nonmalignant pancreatic processes. Technical differences between MRI in basic research and clinical imaging are obvious, and pulse sequence adaptations with loss of resolution are expected due to hardware constraints in clinical scanners and time constraints when imaging patients. For PanIN detection, information loss with lower resolutions in 1.5 T and 3 T scanners might be overcome with the use of pulse sequences sensitive to microscopic anisotropy.[37] Future studies should investigate if DTI can be used in clinical context for PanIN detection and characterization, addressing the question of specificity for high- and low-grade PanIN and PDAC, as this issue is most

TABLE 5. Histological Analysis of KC, KPC, and Control Mice Used for MR Microscopy

Animal Model	Controls	KC	KPC
ADM	0%	100% (12/12)	100% (8/8)
Low-grade PanIN	0%	100% (12/12)	100% (8/8)
High-grade PanIN	0%	100% (12/12)	100% (8/8)
PDAC	0%	33.33% (4/12)	87.5% (11/12)
Lesion span (%)	0%	80.88 (IQR = 42.75)	91.45 (IQR = 36.62)
Adjusted score	0	17 (IQR = 9)	26 (IQR = 1.75)

Low-grade PanIN includes PanIN 1 and PanIN 2. Continuous variables expressed as medians and IQR.

© 2024 The Author(s). Published by Wolters Kluwer Health, Inc.

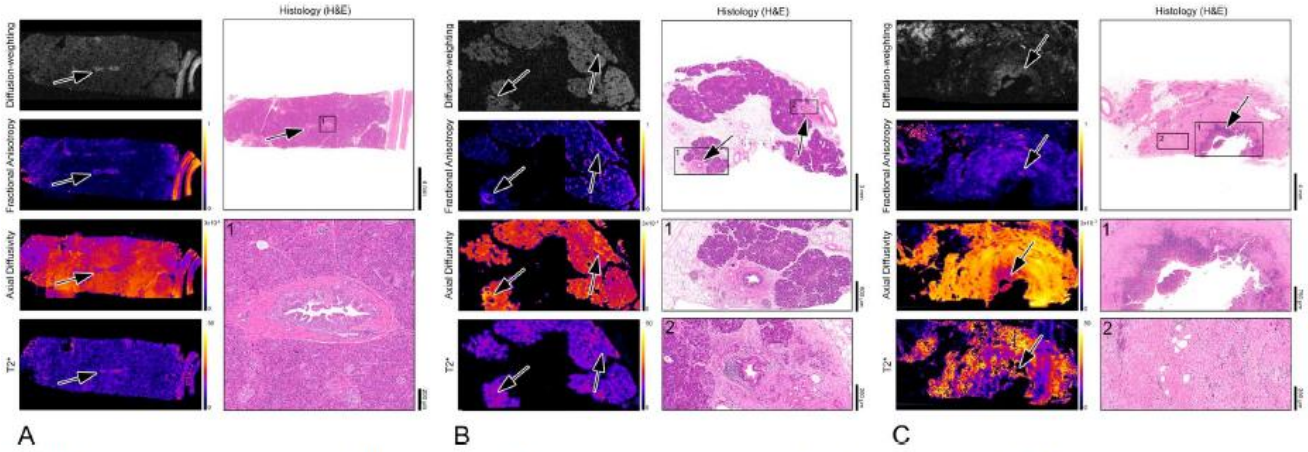


FIGURE 6. The contrasts observed with MR microscopy DTI in the human pancreas are similar to the ones seen in GEMM (2 remaining specimens are presented in Supplemental Digital Content 11). A, High anisotropy, high T2*, and low AD are seen in the periphery of a high-grade PanIN lesion, contrasting well with the surrounding normal pancreatic parenchyma (arrows). B, As observed previously in the KC/KPC mice, areas with ADM and low-grade PanIN have high anisotropy and AD values at their periphery, with high T2* values in the stroma (arrows). Large areas of fatty tissue are seen in the specimen. C, This specimen has extensive haphazardously deposited fibrotic deposition and fatty infiltration, consistent with chronic pancreatitis. There are low-grade PanIN with high anisotropy, intermediate AD, and T2* values (arrows), but the fibrosis has heterogeneous anisotropy, higher AD, and T2* values. Some areas of this specimen have irregular T2* values, probably due to fixation artifacts. AD is expressed in mm^2/s; T2* is expressed in milliseconds (ms).

relevant for implementing therapeutic interventions. Eventual combinations of DTI with other diagnostic tools could be used for increasing specificity, such as liquid biopsy and artificial intelligence.[38,39] Also, it would be interesting to investigate if DTI could be used in conjunction with 3D histological mapping, for detecting specific genomic profiles of PanIN and PDAC.[8] Multiparametric MRI could also be studied for characterizing premalignant lesions, harnessing information from different pulse sequences and including diffusion-based techniques like intravoxel incoherent motion, which have already demonstrated feasibility.[40–42]

We acknowledge some limitations of this research work. First, GEMM do not fully recapitulate morphological and biological features of human PanIN and PDAC, as PanIN lesions in the mouse are mostly present in the context of extensive ADM. Nevertheless, the observed image contrasts are useful for in vivo animal imaging, and large similarities with human pancreas samples were observed, suggesting relevance for human imaging. Second, the manual alignment between MRI and histology was suboptimal and could be considered a potential source of errors, as automatic registration was not viable due to the expected distortion and configurational changes during sample processing for histology. Third, the in vivo application developed here demonstrates the feasibility of the technique and its usefulness for differentiating GEMM from healthy controls but did not evaluate its role in determining different degrees of disease progression in vivo. Also, KC and KPC mice were observed in different age groups due to their different rates of disease progression. Future studies evaluating animals of the same transgenic line at different stages of disease progression should elucidate if DTI is useful for determining the stage of disease in similar age groups. Finally, although similarities of imaging contrasts were observed when imaging human pancreas samples, it remains to be determined if DTI can be successfully adapted to clinical scanners for imaging patients and maintain sensitivity toward these lesions. Our work provides exciting data in this regard and is encouraging for the development of clinical DTI applications for pancreatic imaging.

In conclusion, PanIN lesions were detected with DTI and T2* contrast in GEMM and human pancreas, suggesting high relevance as noninvasive biomarkers. This augurs well for characterizing PanIN progression and biology and associated pancreatic changes in both mice and humans.

ORCID ID

Noam Shemesh https://orcid.org/0000-0001-6681-5876

REFERENCES

1. Siegel RL, Miller KD, Fuchs HE, et al. Cancer statistics, 2022. *CA Cancer J Clin*. 2022;72:7–33.
2. Ducreux M, Cuhna AS, Caramella C, et al. Cancer of the pancreas: ESMO clinical practice guidelines for diagnosis, treatment and follow-up. *Ann Oncol*. 2015;26 (Suppl 5):v56–v68.
3. Campbell F, Smith RA, Whelan P, et al. Classification of R1 resections for pancreatic cancer: the prognostic relevance of tumour involvement within 1 mm of a resection margin. *Histopathology*. 2009;55:277–283.
4. Springfeld C, Ferrone CR, Katz MHG, et al. Neoadjuvant therapy for pancreatic cancer. *Nat Rev Clin Oncol*. 2023;20:318–337.
5. Ryan DP, Hong TS, Bardeesy N. Pancreatic adenocarcinoma. *N Engl J Med*. 2014;371:1039–1049.
6. Overbeek KA, Goggins MG, Dbouk M, et al. Timeline of development of pancreatic cancer and implications for successful early detection in high-risk individuals. *Gastroenterology*. 2022;162:772–785.e4.
7. Vullierme M-P, Menassa L, Couvelard A, et al. Non-branched microcysts of the pancreas on MR imaging of patients with pancreatic tumors who had pancreatectomy may predict the presence of pancreatic intraepithelial neoplasia (PanIN): a preliminary study. *Eur Radiol*. 2019;29:5731–5741.
8. Braxton AM, Kiemen AL, Grahn MP, et al. 3D genomic mapping reveals multifocality of human pancreatic precancers. *Nature*. 2024. Published online May 1, 2024:;629:679–687.
9. Alonso-Curbelo D, Ho YJ, Burdziak C, et al. A gene-environment-induced epigenetic program initiates tumorigenesis. *Nature*. 2021;590:642–648.
10. Storz P, Crawford HC. Carcinogenesis of pancreatic ductal adenocarcinoma. *Gastroenterology*. 2020;158:2072–2081.
11. Nilsson M, Englund E, Szczepankiewicz F, et al. Imaging brain tumour microstructure. *Neuroimage*. 2018;182:232–250.
12. Koh DM, Collins DJ. Diffusion-weighted MRI in the body: applications and challenges in oncology. *AJR Am J Roentgenol*. 2007;188:1622–1635.
13. Kiselev VG, Körzdörfer G, Gall P. Toward quantification: microstructure and magnetic resonance fingerprinting. *Invest Radiol*. 2021;56:1–9.
14. Fukukura Y, Kanki A. Quantitative magnetic resonance imaging for the pancreas. *Invest Radiol*. 2024;59:69–77.
15. Lanzman RS, Wittsack HJ. Diffusion tensor imaging in abdominal organs. *NMR Biomed*. 2017;30.
16. Nissan N, Golan T, Furman-Haran E, et al. Diffusion tensor magnetic resonance imaging of the pancreas. *PloS One*. 2014;9:e115783.

© 2024 The Author(s). Published by Wolters Kluwer Health, Inc.

17. Santiago I, Santinha J, Ianus A, et al. Susceptibility perturbation MRI maps tumor infiltration into mesorectal lymph nodes. *Cancer Res*. 2019;79:2435–2444.
18. Ianuş A, Santiago I, Galzerano A, et al. Higher-order diffusion MRI characterization of mesorectal lymph nodes in rectal cancer. *Magn Reson Med*. 2020;84:348–364.
19. Ariston Gabriel AN, Jiao Q, Yvette U, et al. Differences between KC and KPC pancreatic ductal adenocarcinoma mice models, in terms of their modeling biology and their clinical relevance. *Pancreatology*. 2020;20:79–88.
20. Bilreiro C, Fernandes FF, Andrade L, et al. Effective bowel motion reduction in mouse abdominal MRI using hyoscine butylbromide. *Magn Reson Med*. 2021;86:2146–2155.
21. Kellner E, Dhital B, Kiselev VG, et al. Gibbs-ringing artifact removal based on local subvoxel-shifts. *Magn Reson Med*. 2016;76:1574–1581.
22. Veraart J, Novikov DS, Christiaens D, et al. Denoising of diffusion MRI using random matrix theory. *Neuroimage*. 2016;142:394–406.
23. Veraart J, Sijbers J, Sunaert S, et al. Weighted linear least squares estimation of diffusion MRI parameters: strengths, limitations, and pitfalls. *Neuroimage*. 2013;81:335–346.
24. Harkins K, Does M. GitHub - remmi-toolbox/remmi-matlab: Matlab toolbox to reconstruct and process MRI data. Available at: https://github.com/remmi-toolbox/remmi-matlab. Accessed December 2, 2022.
25. Veite-Schmahl MJ, Rivers AC, Regan DP, et al. The Mouse Model of Pancreatic Cancer Atlas (MMPCA) for classification of pancreatic cancer lesions: a large histological investigation of the Ptf1aCre/+;LSL-KrasG12D/+ transgenic mouse model of pancreatic cancer. *PloS One*. 2017;12:e0187552.
26. Basturk O, Hong SM, Wood LD, et al. A revised classification system and recommendations from the Baltimore consensus meeting for neoplastic precursor lesions in the pancreas. *Am J Surg Pathol*. 2015;39:1730–1741.
27. Berman-Booty LD, Sargeant AM, Rosol TJ, et al. A review of the existing grading schemes and a proposal for a modified grading scheme for prostatic lesions in TRAMP mice. *Toxicol Pathol*. 2012;40:5–17.
28. Knoblaugh SE, Himmel LE. Keeping score: semiquantitative and quantitative scoring approaches to genetically engineered and xenograft mouse models of cancer. *Vet Pathol*. 2019;56:24–32.
29. Bankhead P, Loughrey MB, Fernández JA, et al. QuPath: open source software for digital pathology image analysis. *Sci Rep*. 2017;7:16878.
30. Andea A, Sarkar F, Adsay VN. Clinicopathological correlates of pancreatic intraepithelial neoplasia: a comparative analysis of 82 cases with and 152 cases without pancreatic ductal adenocarcinoma. *Mod Pathol*. 2003;16:996–1006.
31. Storz P. Acinar cell plasticity and development of pancreatic ductal adenocarcinoma. *Nat Rev Gastroenterol Hepatol*. 2017;14:296–304.
32. Wood LD, Canto MI, Jaffee EM, et al. Pancreatic cancer: pathogenesis, screening, diagnosis, and treatment. *Gastroenterology*. 2022;163:386–402.e1.
33. Alexander DC, Dyrby TB, Nilsson M, et al. Imaging brain microstructure with diffusion MRI: practicality and applications. *NMR Biomed*. 2019;32:e3841.
34. Gholizadeh N, Greer PB, Simpson J, et al. Characterization of prostate cancer using diffusion tensor imaging: a new perspective. *Eur J Radiol*. 2019;110:112–120.
35. Toshima F, Watanabe R, Inoue D, et al. Ct abnormalities of the pancreas associated with the subsequent diagnosis of clinical stage I pancreatic ductal adenocarcinoma more than 1 year later: a case-control study. *Am J Roentgenol*. 2021;217:1353–1364.
36. Sotozono H, Kanki A, Yasokawa K, et al. Value of 3-T MR imaging in intraductal papillary mucinous neoplasm with a concomitant invasive carcinoma. *Eur Radiol*. 2022;32:8276–8284.
37. Szczepankiewicz F, Lasič S, van Westen D, et al. Quantification of microscopic diffusion anisotropy disentangles effects of orientation dispersion from microstructure: applications in healthy volunteers and in brain tumors. *Neuroimage*. 2015;104:241–252.
38. Kenner B, Chari ST, Kelsen D, et al. Artificial intelligence and early detection of pancreatic cancer: 2020 summative review. *Pancreas*. 2021;50:251–279.
39. Heredia-Soto V, Rodríguez-Salas N, Feliu J. Liquid biopsy in pancreatic cancer: are we ready to apply it in the clinical practice? *Cancers (Basel)*. 2021;13.
40. Gurney-Champion OJ, Froeling M, Klaassen R, et al. Minimizing the acquisition time for intravoxel incoherent motion magnetic resonance imaging acquisitions in the liver and pancreas. *Invest Radiol*. 2016;51:211–220.
41. Concia M, Sprinkart AM, Penner A-H, et al. Diffusion-weighted magnetic resonance imaging of the pancreas: diagnostic benefit from an intravoxel incoherent motion model-based 3 b-value analysis. *Invest Radiol*. 2014;49:93–100.
42. Baskaya F, Lemainque T, Klinkhammer B, et al. Pathophysiologic mapping of chronic liver diseases with longitudinal multiparametric MRI in animal models. *Invest Radiol*. 2024;59:699–710.

© 2024 The Author(s). Published by Wolters Kluwer Health, Inc.

Supplemental Digital Content - Tables

Supplemental Digital Content 1, Table. Sample characteristics in *in vivo* DTI of KPC and control mice

Animal model	**Controls**	**KPC**	**KC**
Number of animals	6	6	4
Age (months-old)	3.0 (IQR = 0.44)	4.75 (IQR = 0.13)	9.25 (IQR = 1.88)
Animal weight (g)	28.5 (IQR = 6,6)	24.9 (IQR = 5.1)	24.8 (IQR = 8.3)
Animal Sex	1/6 females	4/6 females	2/4 females

Continuous variables expressed as medians and IQR.

Supplemental Digital Content 2, Table. Pancreatic lesion classification.

Classification System of Pancreatic Lesions [adapted from (23, 24)]	
Normal	Cuboidal to low-columnar epithelium with amphophilic cytoplasm
	Mucinous cytoplasm, nuclear crowding and atypia are not seen
Low grade	Flat epithelial lesions composed of tall columnar cells with basally located nuclei and abundant supranuclear mucin (previous PanIN 1A and 1B)
	Nuclei are small and round to oval in shape (previous PanIN 1A and 1B)
	Papillary, micropapillary or basally pseudostratified architecture (previous PanIN 1B)
	Mucinous epithelium may be flat but mostly papillary (previous PanIN 2)
	Nuclear abnormalities: loss of polarity, nuclear crowding, enlarged nuclei, pseudostratification, hyperchromatism (previous PanIN 2)
	Mitoses are rare and, when present, are not atypical (previous PanIN 2)
High grade	Papillary or micropapillary, may rarely be flat
	Cribiform
	Loss of polarity, dystrophic goblet cells (nuclei oriented toward the lumen and mucinous cytoplasm toward the basement membrane), anysocariosis, prominent nucleoli - *similar to carcinoma*
	Mitosis rare but maybe atypical
	Invasion through basement membrane absent - *difference from carcinoma*
PDAC	Marked cytonuclear abnormalities: clear malignant transformation
	Frequent mitosis, atypical
	Invasion through basement membrane
	Desmoplastic stroma

Supplemental Digital Content 3, Table. Sample characteristics in *ex vivo* MR Microscopy of KC, KPC and control mice

Animal model	**Controls**	**KC**	**KPC**
Number of animals	5	12	8
Age (months-old)	3.00 (IQR = 6.88)	8.88 (IQR = 1.25)	4.75 (IQR = 3.00)
Animal Sex	3/5 females	5/12 females	4/8 females

Continuous variables expressed as medians and IQR.

Supplemental Digital Content 9, Table. Pearson's correlation coefficients between MRI, Lesion Span and Adjusted Score

		Lesion Span	**Adjusted Score**
FA (median)	Pearson's R	0,520*	0,494*
	P	0,008	0,012
FA (95th percentile)	Pearson's R	0,619*	0,546*
	P	0,001	0,005
FA (5th percentile)	Pearson's R	0,445*	0,436*
	P	0,026	0,030
MD (median)	Pearson's R	0,525*	0,574*
	P	0,007	0,003
MD (95th percentile)	Pearson's R	0,615*	0,719*
	P	0,001	<0,001
MD (5th percentile)	Pearson's R	0,049	0,220
	P	0,816	0,291
AD (median)	Pearson's R	0,708*	0,789*
	P	<0,001	<0,001
AD (95th percentile)	Pearson's R	0,683*	0,729*
	P	<0,001	<0,001
AD (5th percentile)	Pearson's R	0,109	0,274
	P	0,605	0,184
RD (median)	Pearson's R	0,348	0,382
	P	0,088	0,059
RD (95th percentile)	Pearson's R	0,563*	0,690*
	P	0,003	<0,001

RD (5th percentile)	Pearson's R	-0,026	0,138
	P	0,903	0,511
T2* (median)	Pearson's R	0,542*	0,718*
	P	0,005	<0,001
T2* (95th percentile)	Pearson's R	0,626*	0,696*
	P	0,001	<0,001
T2* (5th percentile)	Pearson's R	0,337	0,488*
	P	0,100	0,013
ADC (median)	Pearson's R	0,493*	0,554*
	P	0,012	0,004
ADC (95th percentile)	Pearson's R	0,621*	0,722*
	P	0,001	<0,001
ADC (5th percentile)	Pearson's R	-0,032	0,082
	P	0,881	0,697

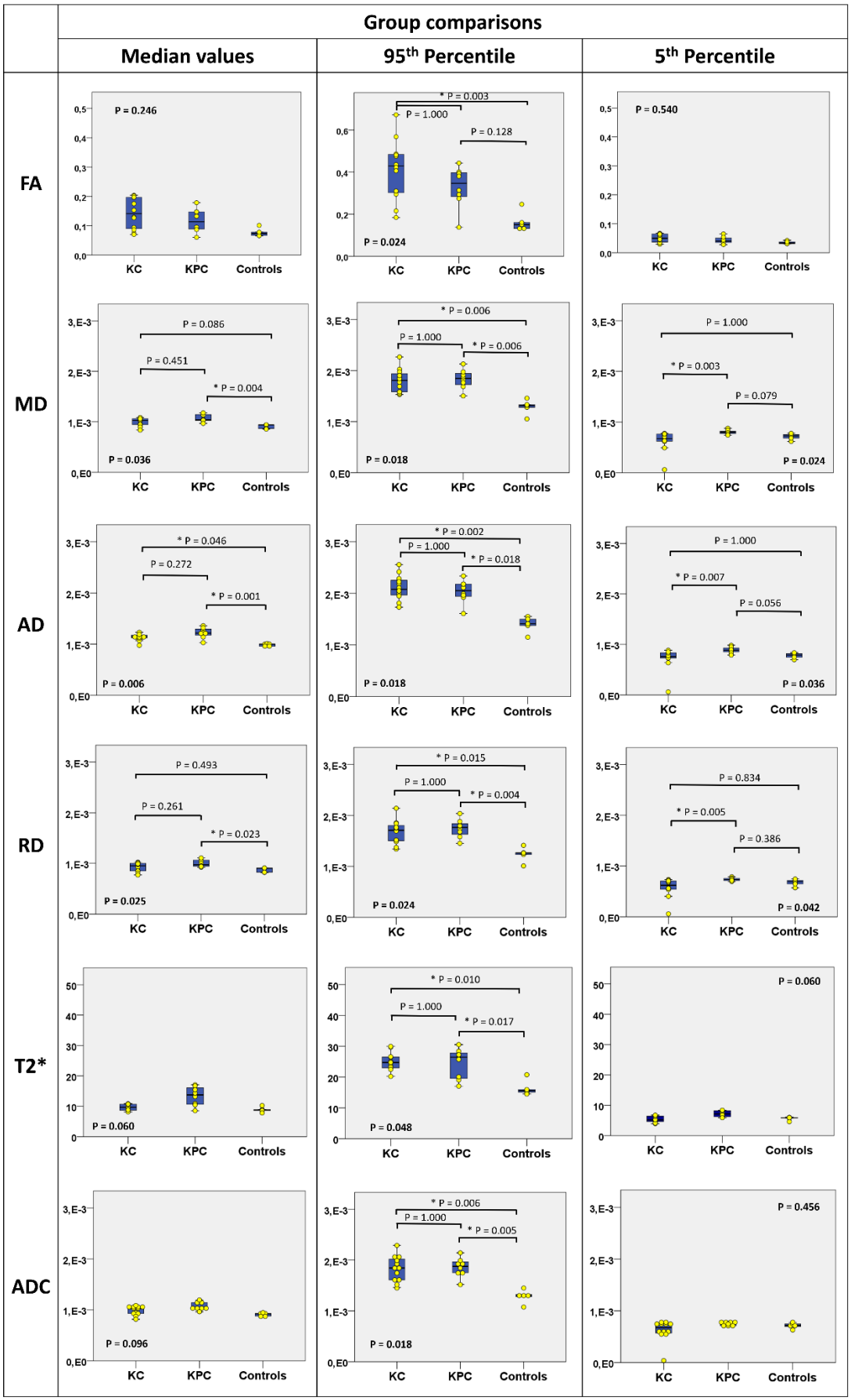
*denotes statistically significant values.

Supplemental Digital Content 10, Table. Patient characteristics for *ex vivo* MR Microscopy of pancreatic tissue leftovers after histopathological processing of resected pancreases.

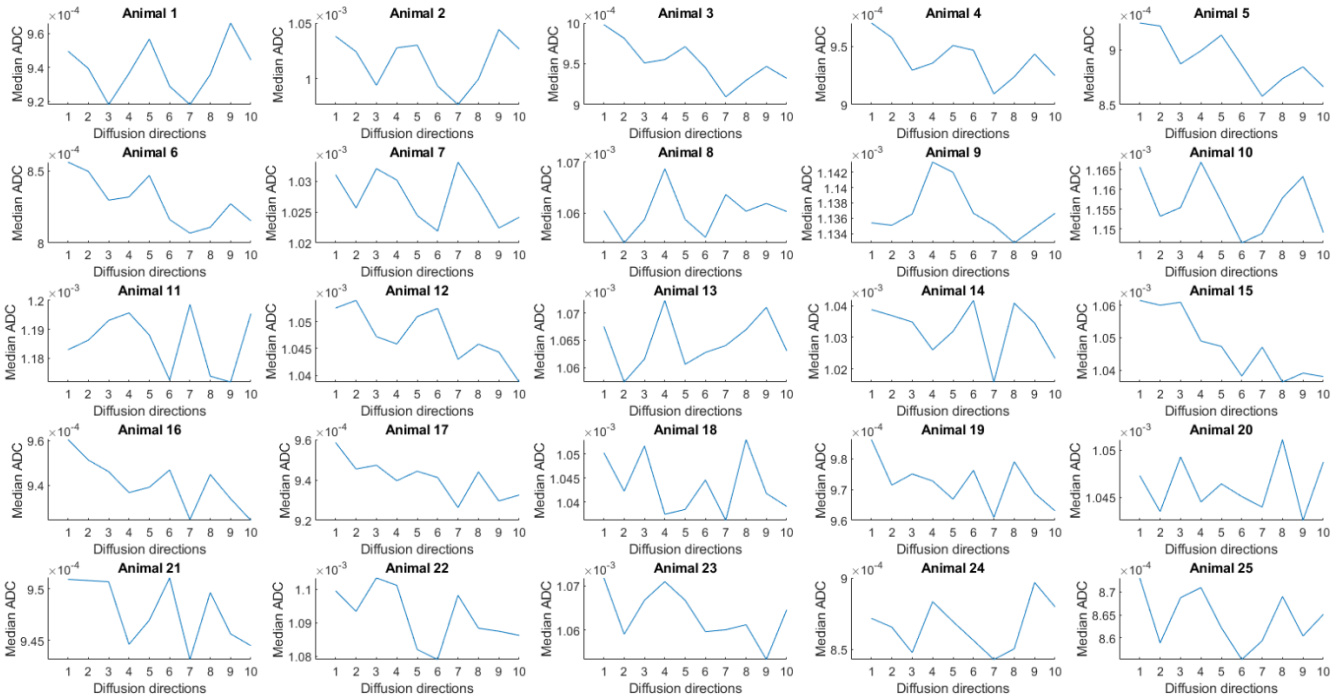
Patients	**Age**	**Sex**	**Neoadjuvant therapy**	**Surgery**	**TNM**	**Resection**
1	69	Male	FOLFIRINOX	Total pancreatectomy	ypT2 ypN0	R0
2	67	Male	FOLFIRINOX	Distal pancreatectomy, segmental colectomy, nephrectomy	ypT3 ypN1 ypM1	R1
3	64	Male	N/A	Total pancreatectomy	pT2 pN0	R1
4	71	Male	FOLFIRINOX	Cephalic pancreaticoduodenectomy	ypT2 ypN0	R0
5	53	Male	FOLFIRINOX, GEM-NAB	Total pancreatectomy	ypT2 ypN1	R0

Pathologically-defined TNM is presented.

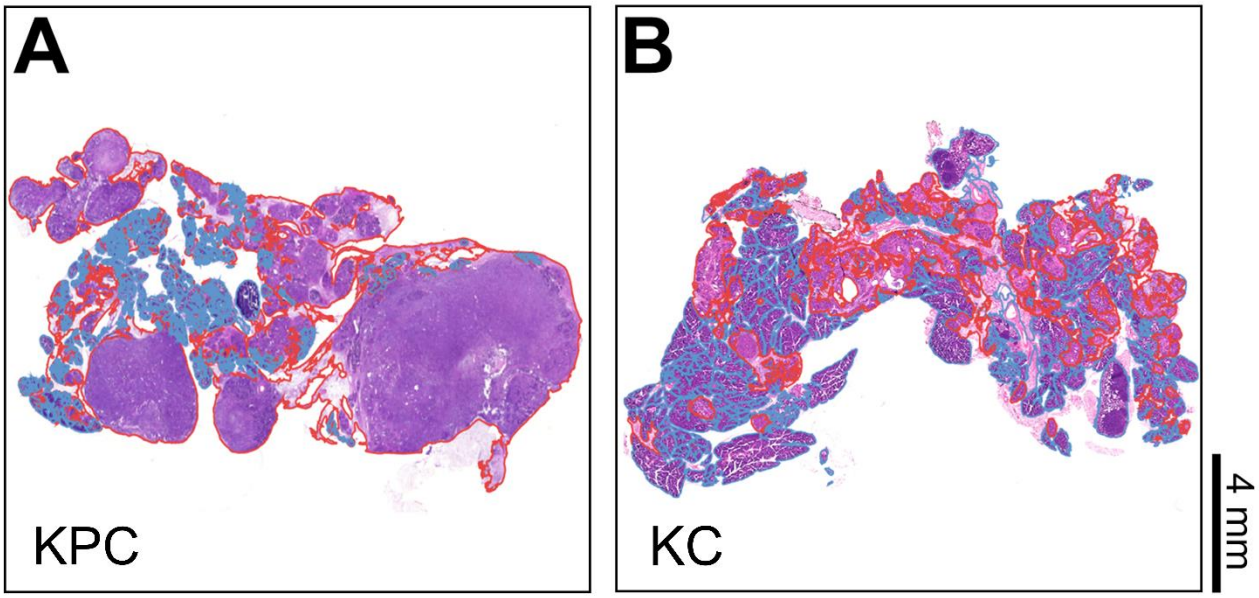
Supplemental Digital Content 4, Figure. Group comparisons for all DTI, T2* and ADC metrics.



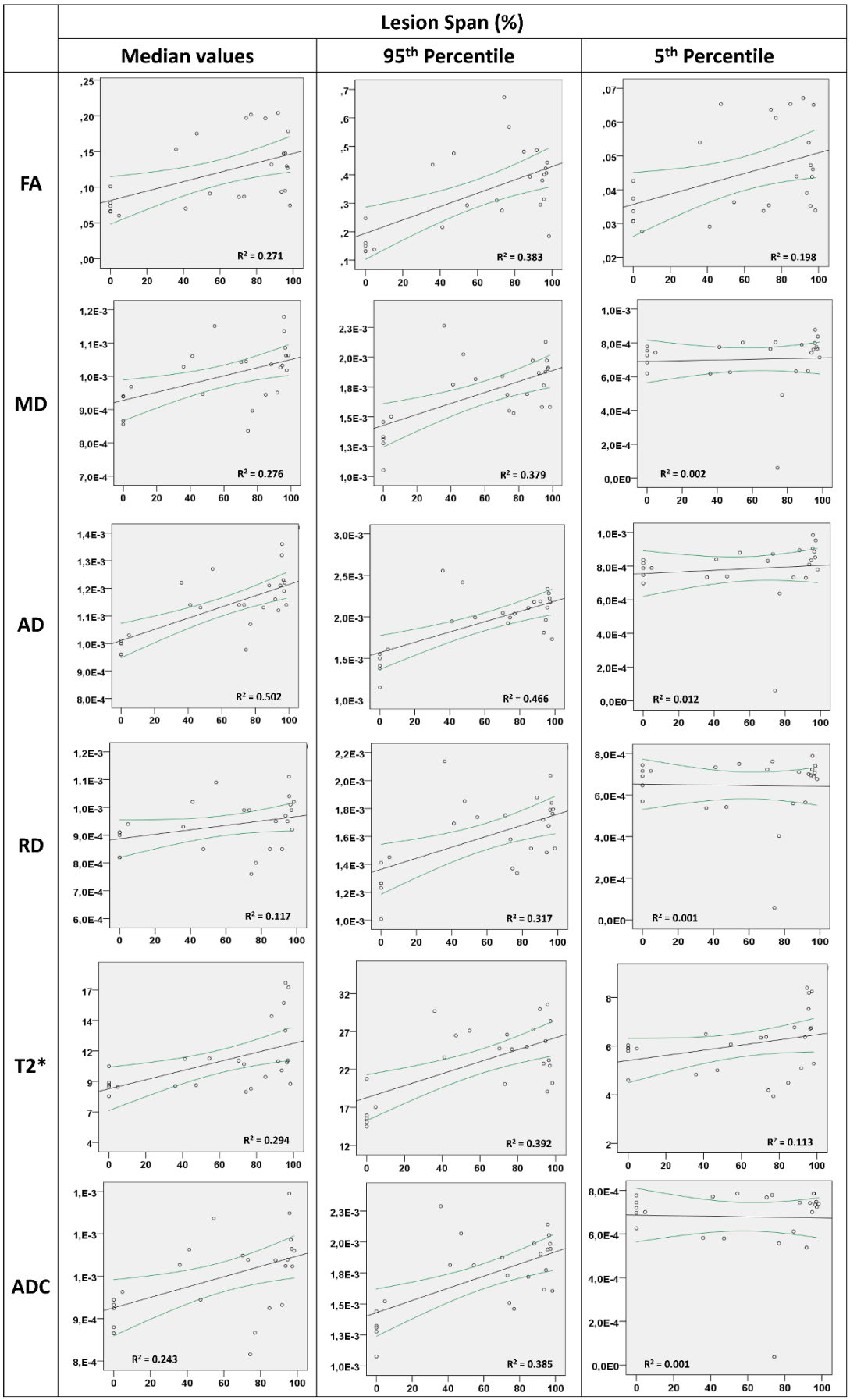
Supplemental Digital Content 5, Figure. Median ADC values for each diffusion direction in each animal. The observed ADC variability in each animal is consistent with diffusion anisotropy in the pancreas, as explored further with DTI.



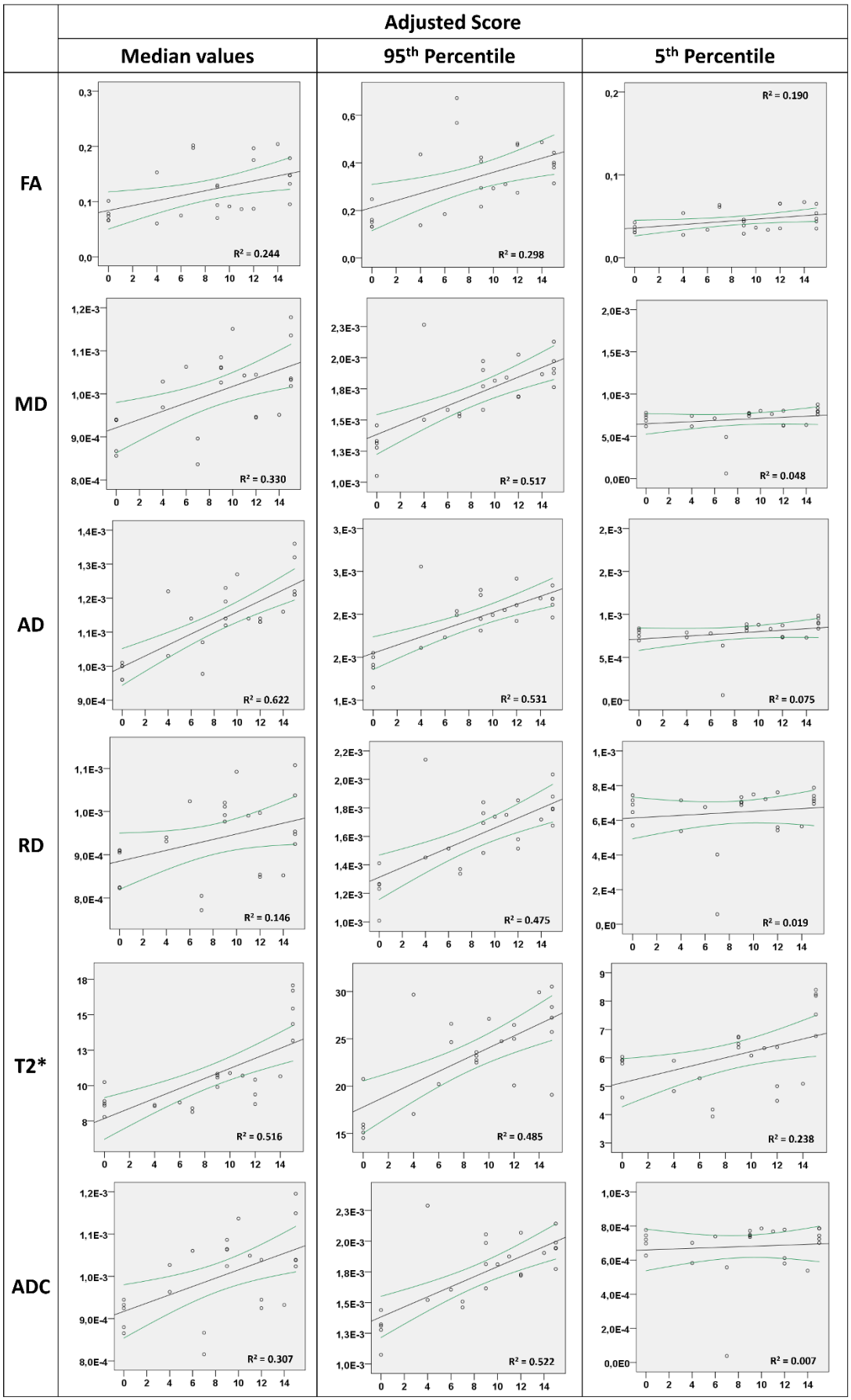
Supplemental Digital Content 6, Figure. Histological (H&E) segmentation and classification. Lesioned areas are segmented as red and normal pancreas as blue. A - KPC pancreatic specimen with extensive disease and PDAC tumors: 88% Lesion Span; 27 Adjusted Score. B - KC pancreatic specimen with limited disease and no PDAC: 36% Lesion Span; 14 Adjusted Score.



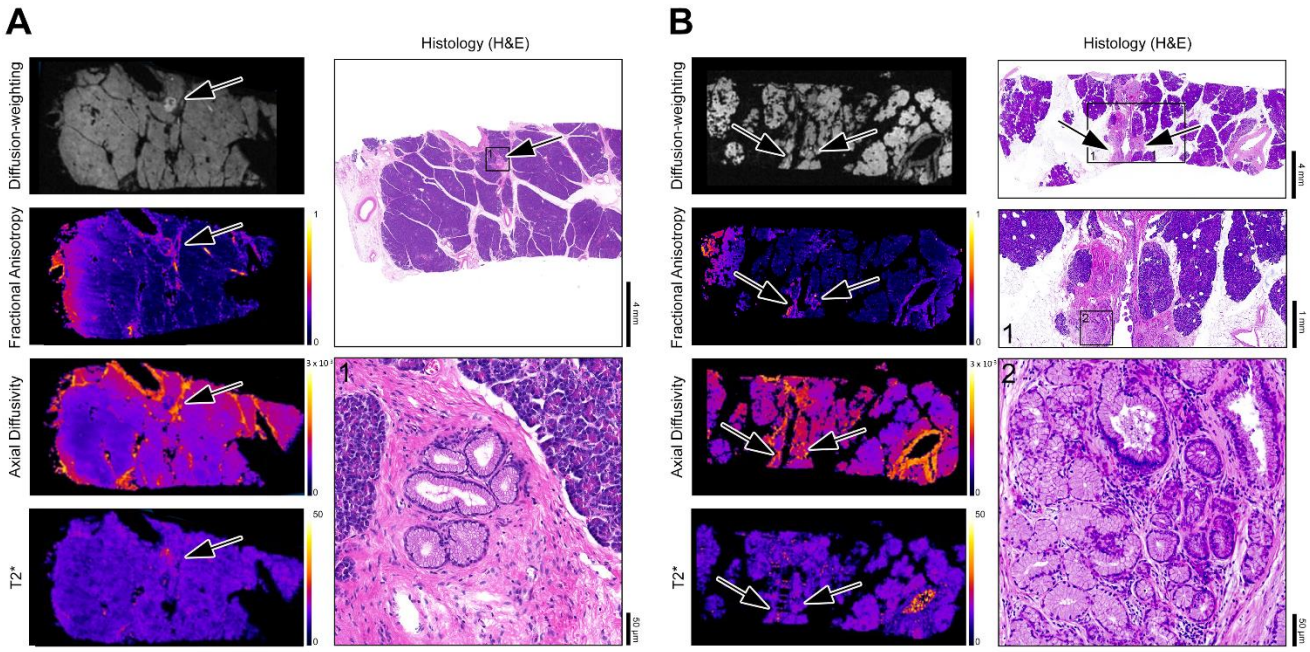
Supplemental Digital Content 7, Figure. Lesion Span correlation for all DTI, T2* and ADC metrics.



Supplemental Digital Content 8, Figure. Adjusted Score correlation for all DTI, T2* and ADC metrics.



Supplemental Digital Content 11, Figure. Two remaining Human pancreatic specimens. A - a small area with low-grade PanIN is histologically identified (arrows), showing restricted diffusion, high T2* values in its center, and high anisotropy, low AD in its periphery. B - areas with ADM and low-grade PanIN surrounding a large duct show high anisotropy and high AD at their periphery, with intermediate/high T2* in their center. In both specimens, large arteries with peri-vascular cuff-like fibrosis also demonstrate high anisotropy and high AD values at their periphery. Areas of fatty replacement are also observed. AD is expressed in mm^2/s; T2* is expressed in milliseconds (ms).



3.4. Diffusion Tensor Imaging and Diffusion Kurtosis Imaging of the Pancreas - Feasibility, Robustness and Protocol comparison in a Healthy population.

Bilreiro C, Andrade L, Henriques R, Loução N, Shemesh N, Matos C.

Accepted for publication in Abdominal Radiology on 10/03/2025.

Diffusion Tensor Imaging and Diffusion Kurtosis Imaging of the Pancreas - Feasibility, Robustness and Protocol comparison in a Healthy population

Carlos Bilreiro, MD[1,2,3], Luísa Andrade, MD[4], Rafael Henriques, PhD[2], Nuno Loução, MEng[2], Noam Shemesh, PhD[2], Celso Matos, MD[1,2].

[1]Radiology Department, Champalimaud Foundation, Portugal.
[2]Champalimaud Research, Champalimaud Foundation, Portugal.
[3]Nova Medical School, Portugal.
[4]Radiology Department, CUF Tejo Hospital, Portugal.

***Corresponding author:**
Carlos Bilreiro, Radiology Department, Champalimaud Foundation, Av. Brasilia 1400-038, Lisbon, Portugal
E-mail: carlos.bilreiro@fundacaochampalimaud.pt
Phone number: +351 210 480 048

Author e-mails:
Luísa Andrade: isa.c.andrade@hotmail.com
Rafael Henriques: rafael.henriques@neuro.fchampalimaud.org
Nuno Loução: nunoloucao@gmail.com
Noam Shemesh: noam.shemesh@neuro.fchampalimaud.org
Celso Matos: celso.matos@fundacaochampalimaud.pt

Funding: This work was supported by Champalimaud Foundation.

Diffusion Tensor Imaging and Diffusion Kurtosis Imaging of the Pancreas - Feasibility, Robustness and Protocol comparison in a Healthy population

Abstract

Purpose: This study aims to determine the feasibility, image quality, intra-subject repeatability and inter-reader variability of Diffusion tensor (DTI) and Diffusion kurtosis imaging (DKI) for pancreatic imaging using different protocols and report normative values in healthy individuals.

Methods: Single-institution prospective study performed on healthy volunteers in a clinical 3T scanner, using two different protocols (6/16 diffusion directions). Acquisitions were repeated twice to assess intra-subject repeatability. To assess inter-reader variability, Mean diffusivity (MD), Axial diffusivity (AD), Radial diffusivity (RD), Apparent diffusion coefficient (ADC) and Mean kurtosis (MK) values were extracted from segmented pancreas by two radiologists. A Likert scale was used by both readers to assess subjective image quality.

Results: Twelve healthy volunteers were recruited for each MRI protocol. The 6 diffusion directions protocol was shorter: 7 minutes vs. 14 minutes (corresponding to 4 minutes vs. 7.5 minutes for a DTI only reconstruction). No differences in image quality were found between protocols. Only MK maps showed implausible estimates, leading to the exclusion of median 16% and 17.7% pixels for the 6- and 16-direction protocols, respectively. Intra-subject repeatability was determined with negligible coefficients of repeatability for DTI; however, MK presented slightly higher values. Inter-reader agreement was excellent for all maps (ICC > 0.9).

Conclusions: DTI and DKI of the pancreas are feasible in clinical settings, with excellent inter-observer agreement and good image quality. Intra-subject repeatability is excellent for DTI, but some variability was observed with DKI. A 6-directions protocol may be preferred due to faster acquisition without quantitatively compromising estimates. MK inaccuracies prompt further research for improving artifact correction.

Keywords

Pancreas; Diffusion Tensor Imaging; Diffusion Kurtosis Imaging; Abdomen; Feasibility Studies; Healthy Volunteers.

Abbreviations

AD: axial diffusivity

ADC: apparent diffusion coefficient

CT: computerized tomography

DKI: diffusion kurtosis imaging

DTI: diffusion tensor imaging

DWI: diffusion weighted imaging

FA: fractional anisotropy

ICC: intraclass correlation coefficient

MD: mean diffusivity

MK: mean kurtosis

MRCP: magnetic resonance cholangiopancreatography

PDAC: pancreatic ductal adenocarcinoma

RD: radial diffusivity

SB-IPMN: side branch intraductal papillary mucinous neoplasia

SE-EPI: spin-echo echo planar imaging

SNR: signal to noise ratio

TSE: turbo spin-echo

Background

Technological advances in recent years have provided useful tools for pancreatic imaging, in both malignant and benign pathological processes. MRI with diffusion-weighted imaging (DWI) has high sensitivity for detecting liver metastases, neuroendocrine tumors, pancreatic ductal adenocarcinoma (PDAC), auto-immune pancreatitis, and can also help differentiate mass-forming pancreatitis from PDAC [109–113]. However, several issues remain poorly addressed by current pancreatic imaging, including characterization and risk stratification of side-branch intraductal papillary mucinous neoplasms (SB-IPMN), early detection of PDAC and precursor lesions, prognostication of patients with PDAC and neuroendocrine tumors, and assessing response after neoadjuvant therapy [22, 32, 61, 106, 114, 115].

DWI's correlation with cellular density is widely explored in pancreatic imaging with the use of Apparent Diffusion Coefficients (ADC) [116]. However, ADC is limited in capturing the full complexity of tissue microstructure, as it does not account for the directional dependence of diffusion, i.e. anisotropy. Diffusion-tensor imaging (DTI) is mostly used in neuroimaging applications, providing a rotationally invariant representation of the diffusion process and quantifying diffusion anisotropy [117]. Another aspect of the diffusion process not captured by ADC is the non-Gaussian behavior of diffusion, which has been associated with microstructural heterogeneity and can be quantified with Diffusion Kurtosis Imaging (DKI) [88, 89, 117]. Previous studies have tested DTI on patients with pancreatic cancer and acute pancreatitis, and DKI in patients with pancreatic cancer, providing encouraging data for these techniques as sources of non-invasive biomarkers [86, 87, 118]. Furthermore, a recent pre-clinical study reported DTI to have clear diagnostic potential for pancreatic pre-malignant lesions – pancreatic intraepithelial neoplasia [108]. However, DTI and DKI have technically demanding acquisitions (large number of diffusion directions, high b values), and optimal acquisition parameters for pancreatic DTI/DKI are still unclear. This entails lack of standardization in acquisition protocols and consequential variability in quantitative estimates across different studies, while also hindering the development of clinical applications [86, 87, 105, 118]. Additionally, DTI and DKI's clinical feasibility as a single acquisition, as well as their robustness in the clinical setting and image quality assessed by radiologists are still unknown.

Considering the potential of DTI and DKI for pancreatic imaging, the aim of this study is to determine the feasibility, robustness and inter-reader variability of these techniques for pancreatic imaging in a clinical setting. We compared different acquisition protocols with different number of diffusion directions and acquisition lengths, and described the expected findings in a healthy population, providing a clinically feasible short acquisition protocol and data on pancreatic DTI and DKI's image quality and robustness.

Methods

This single-institution prospective study with healthy volunteers received approval from Champalimaud Foundation Ethics Committee (project "DWI-P"), and each participant gave a fully informed consent before undergoing MRI.

Participants

Healthy volunteers were recruited from the Institution's staff and in an opportunistic way from visitors to the Institution.

Inclusion criteria were people aged 18 to 65 years-old, healthy, willing to participate and undergo MRI.

Volunteers with history of any pancreatic disease (acute or chronic pancreatitis, auto-immune pancreatitis, pancreatic exocrine insufficiency, Diabetes Mellitus, pancreatic tumors) were excluded from the study. Volunteers with contraindications for MRI, including claustrophobia or incompatible medical devices, were also excluded from the study.

MRI Acquisition

Each participant underwent MRI in a clinical 3T scanner (Ingenia®, Philips NV, The Netherlands) with a 16-channel phased-array body coil. Participants were instructed to fast for at least 4 hours before MRI.

The acquisition included a T2-weighted Turbo Spin-echo (TSE) in the axial plane, for pancreatic anatomical definition. For DTI and DKI, a 2D Spin-echo Echo-planar-imaging (SE-EPI) was acquired with 6 slices encompassing the entire pancreas, with the following b values: 0, 200, 1000 and 1700 s/mm^2 [100]. The complete parameter list is found in Table 1.

Two different diffusion direction protocols were tested: 16 and 6 evenly diffusion directions. The first protocol with 16 directions was aimed at providing a more robust representation of the diffusion tensor, while also providing redundant data for a more effective denoising, while sacrificing acquisition time length [77, 119, 120]. The second protocol with 6 directions provided a significantly faster acquisition, however with the minimum number of directions required for estimating the diffusion tensor, and with less redundant data for the denoising algorithm [77]. Scan lengths were recorded for comparison, as acquisition time was variable due to respiratory triggering.

Acquisitions were repeated twice in the same scanning session, in order to assess intra-subject repeatability.

Image processing

Datasets were analyzed using in-house developed code in MATLAB™ (MathWorks Inc., Natick, MA). Pre-processing included denoising based on Marchenko-Pastur principal component analysis (MP-PCA) and Gibbs unringing algorithms [120, 121].

DTI was fitted per voxel with a weighted-least-squares solution as described by Veraart, et al, using the acquired b values of 200 and 1000 s/mm^2 for removing perfusion-related effects [100, 122, 123]. This first calculation provides for each voxel a six-parameter tensor, from which three principal eigenvectors can be extracted, each with a corresponding eigenvalue. These eigenvalues (λ_1, λ_2, λ_3) numbered from largest to lowest, represent the three orthogonal diffusion coefficients in the diffusion frame of each voxel. From these diffusion coefficients, mean diffusivity (MD), axial diffusivity (AD), radial diffusivity (RD) and fractional anisotropy (FA) maps were produced, for each acquisition of each volunteer. MD was calculated as the average diffusion coefficient, as follows:

$$MD = \frac{\lambda_1 + \lambda_2 + \lambda_3}{3}$$

AD, the largest diffusion coefficient of each voxel was equal to λ_1. RD was calculated as the average of the two smaller diffusion coefficients:

$$RD = \frac{\lambda_2 + \lambda_3}{2}$$

FA, quantifying the amount of diffusion anisotropy in each voxel, was calculated as previously described[76]:

$$FA = \sqrt{{}^{3}/_{2}\left((\lambda_1 - \mathrm{MD})^2 + (\lambda_2 - \mathrm{MD})^2 + (\lambda_3 - \mathrm{MD})^2\right)/(\lambda_1^2 + \lambda_2^2 + \lambda_3^2)}$$

DKI was fitted to the directional averaged acquired data using b values of 200, 1000 and 1700 s/mm^2. The full details for DKI fitting in directional averaged signals are described in [91, 93], however, in short, mean signals for each b value are computed as the average from all directions before fitting. Then, the DKI model is fitted using a weighted linear least squares solution of the following expression:

$$MS(b) \approx S_0 e^{(-bMD + \frac{1}{6}b^2 MD^2 MK)}$$

Here, MS represents the directional averaged diffusion-weighted signal for each b value, S_0 the non-diffusion-weighted signal, MD is the mean diffusivity and MK the mean kurtosis. MK maps were then produced for analysis, for each acquisition for each volunteer.

ADC maps were produced for comparison as in standard clinical practice, using a monoexponential fit with b values of 200 and 1000 s/mm^2:

$$S(b) = S_0 e^{(-bADC)}$$

Where S represents the measured diffusion-weighted signal for a given direction. Only the first diffusion direction was used to calculate ADC, as in clinical practice, following the isotropic diffusion principle assumed by the conventional unidirectional model of DWI.

Image Analysis

Two abdominal radiologists, with 11 and 13 years of experience, delineated the entire pancreas in each slice using MATLAB™'s built-in segmentation tools, on b = 0 s/mm^2 images and supported by the T2-weighted images. The resulting Regions of interest (ROI) were then placed in the corresponding ADC, FA, MD, AD, RD and MK maps, for extracting quantitative data.

Measurements from each reader were compared to assess inter-reader variability. Measurements from each volunteer, regarding the two repeated acquisitions, were compared to assess intra-subject repeatability.

The results from each protocol (16 and 6 diffusion directions) were compared for each map. Besides median values and range comparisons, the 90th and 10th percentiles of the DTI, DKI and ADC maps were also extracted from each participant, in order to provide a more granular analysis of extreme measurements. Finally, a measurement of excluded voxels with implausible values due to artifactual results (i.e. negative diffusivity/kurtosis values, kurtosis values larger than 2.5, FA and diffusivity values larger than 1) was compared between each protocol for each map to assess if any of the protocols was more robust in terms of artifactual measurements. The > 2.5 cutoff for implausible positive MK estimates was selected on the basis of previous findings [88, 105, 118, 124, 125]. The preliminary MK estimations in our subjects also contributed to selecting this cutoff, as MK values > 2.5 were only rarely observed as outliers.

For subjective image quality assessment, each DTI and DKI map (FA, MD, AD, RD, MK and ADC) were classified by each reader using an adapted Likert scale from 1 (worst) to 5 (best), for the following parameters: anatomical delineation, image graininess, distortion artifacts, motion artifacts (Table 2). Ghost artifacts were also searched for but were not evident in our images, and were thus excluded from this analysis.

Statistical analysis

IBM SPSS® statistics v.24 was used for statistical analyses. The Kolmogorov-Smirnov was used to assess the normality of distribution of continuous variables, revealing not all tested variables had a normal distribution. We thus opted for non-parametric tests: Mann-Whitney's U test was used to compare groups of continuous and ordinal variables; Fisher's exact test was used for comparing categorical variables.

Bland-Altman analysis was used to assess intra-subject repeatability, and the coefficient of repeatability (r) was calculated according to [126, 127]:

$$r = 1.96 * \sqrt{\sum d^2 / n}$$

Where d is the difference between acquisitions and n the number of volunteers.

Intraclass correlation coefficient was used to assess inter-reader agreement for pancreatic quantification in each map, as follows: <0.5 considered poor, 0.5 to 0.75 considered moderate, 0.75 to 0.9 considered good, >0.90 considered excellent [128]. For subjective image quality comparisons, weighted Kappa was used to assess inter-reader agreement (quadratic form for weighting difference magnitude), and was classified as: less than chance (<0), slight (0.01 - 0.2), fair (0.21 – 0.4), moderate (0.41 – 0.6), substantial (0.61 – 0.8), almost perfect (>0.81) [129, 130].

$p < 0.05$ was considered significant.

Results

Scan length and image quality

Twelve healthy volunteers were included in each group of different MRI protocols (Table 3). Scan length was shorter for the 6 diffusion directions protocol: median 7 minutes for the full DTI and DKI acquisition (vs. 13 minutes for 16 directions), and 4 minutes for DTI only acquisition (vs. 7.5 minutes for 16 directions).

Qualitatively, both MRI protocols provided DTI and MK maps with good quality, comparable to the clinical standard ADC maps, as shown in Figure 1. The subjective evaluation of quality parameters revealed good to excellent anatomical delineation for MD, AD, RD and ADC maps, which was worse for FA and MK maps with mostly acceptable to good classifications (Table 4). Image graininess was classified as mild to not perceived for most MD, AD, RD and ACD maps, while it was more noticeable in FA and MK maps (not impactful to mild). Regarding distortion and motion artifacts, these were more frequently mild for all maps. There were no significant differences between diffusion direction protocols for the quality parameters assessed, with the sole exception of distortion artifacts for MD maps for reader 1 (mild for 6 diffusion directions and not perceived for 16 diffusion directions).

When assessing inter-reader agreement for image quality classification, weighted Kappa values revealed most often a substantial agreement (2/48 slight, 12/48 fair, 11/48 moderate, 17/48 substantial, 6/48 almost perfect) (Supplementary Table 1). Weighted Kappa values ranged between 0.11 (AD, Image graininess, 6 diffusion directions) and 1.00 (MD, Motion artifacts, 16 diffusion directions).

Regarding the quantification of implausible estimates, these were only relevant in MK maps, having excluded medians of 17.723% of pixels for the 16 diffusion directions protocol (ranging up to 45.3%) and 15.956% of pixels for 6 diffusion directions protocol (ranging up to 41.9%) ($p = 0.887$, Supplementary Table 2).

Figure 1 - DWI, DTI and DKI maps in two volunteers, for each MRI protocol (6 vs. 16 diffusion directions). Examples show both acquisitions for each volunteer. The pancreas is delimited in white in both volunteers, showing mostly homogeneous values in all maps, with a similar visual quality as the clinical standard ADC maps. MD, AD, RD and ADC maps are expressed in mm2/s.

Metric
B = 0 s/mm²
ADC
FA
MD
AD
RD
MK
16 Diffusion directions
6 Diffusion directions
Acquisition 1
Acquisition 2
Acquisition 1
Acquisition 2

Pancreatic DTI and DKI - quantitative analysis

The DTI (FA, MD, AD, RD), MK and ADC measurements extracted from the segmented whole pancreas from all volunteers can be found in Table 5. No differences in measurements were seen for both MRI protocols, except for FA: 0.231 for the 16 directions protocol and 0.276 for the 6 directions protocol ($p = 0.008$). The analysis of the 90th and 10th percentiles also revealed that differences in measurements are limited to FA, while all other DTI and DKI metrics provided similar results for both acquisition protocols.

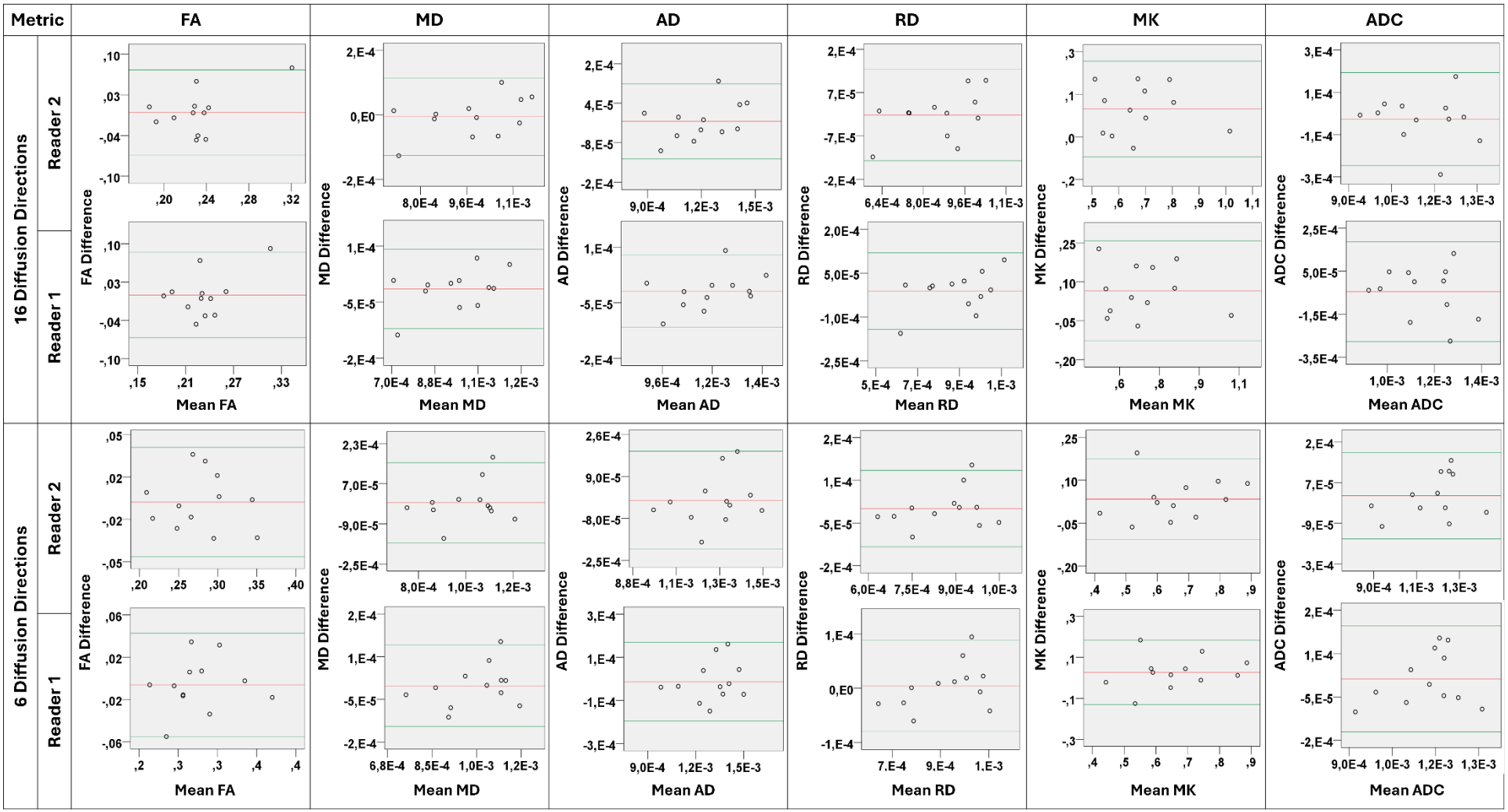
Supplementary Figures 1-4 show the individual subject boxplots for all diffusion measurements in the pancreas, for each acquisition protocol and for each reader. These showcase the consistency of distribution of measured pancreatic values in each map in a subject-by-subject basis, quite similar to the clinical standard ADC; however with MK measurements from some participants displaying large outlier numbers for both readers.

Repeatability and inter-reader agreement

When assessing intra-subject repeatability, Bland-Altman plots were used to demonstrate measurable differences between the first and second acquisitions for each volunteer and search for proportional bias (Figure 2). Differences in measurements for all maps fell within short 95% confidence intervals including zero, with only some rare and small-magnitude outliers, determining intra-subject repeatability and no proportional bias. The obtained coefficients of repeatability further determine robustness of DTI with small negligible values across metrics for both protocols (Table 6). However, higher coefficients of repeatability were obtained for MK, especially with the 16-directions protocol, reaching 0.445 (66.9% larger than the median) for the 16 directions and 0.228 (35.2% larger than the median) for the 6 directions protocols, respectively.

Inter-reader agreement for pancreatic DTI/DKI maps quantitative results after segmentation was excellent for every map and for both MRI protocols (intraclass correlation coefficients >0.9), as shown in Supplementary Table 3.

Figure 2 - Bland-Altman plots for all volunteers in each MRI protocol and for each reader. The quantitative differences between the first and second acquisition for each subject fall within short 95% confidence intervals (green lines) of their mean (red lines), including zero and presenting only rare and small-magnitude outliers, determining intra-subject repeatability.


Metric
FA
MD
AD
RD
MK
ADC
16 Diffusion Directions
6 Diffusion Directions
Reader 2
Reader 1
FA Difference
MD Difference
AD Difference
RD Difference
MK Difference
ADC Difference
Mean FA
Mean MD
Mean AD
Mean RD
Mean MK
Mean ADC

Discussion

This study demonstrates the feasibility, repeatability and inter-reader agreement of pancreatic DTI and DKI, while also providing the expected normal values of the respective maps when performed in the healthy pancreas and a subjective image quality analysis. The two MRI protocols compared showed no significant differences regarding image quality and repeatability, favoring the protocol with 6 diffusion directions due to shorter scan length. Slightly higher FA measurements may however be expected with the shorter protocol.

Nissan et al have previously demonstrated the feasibility of DTI of the pancreas in healthy volunteers and in patients with pancreatic cancer [86]. Our study further establishes the feasibility of DTI for the pancreas, including data on the intra- and inter-subject repeatability, inter-reader agreement, and different acquisition protocols. Furthermore, our subjective image quality analysis demonstrates DTI and DKI as comparable with the clinical standard ADC, with acceptable to excellent anatomical delineation, not impactful to mild image graininess and mostly mild distortion and motion artifacts.

Our results regarding ADC values are comparable with previous publications, some of which reported variability in ADC measurements with age and gender dependency [131, 132]. Our small sample of volunteers did not allow a comprehensive evaluation of possible age and gender differences influencing measurements in pancreatic DTI/DKI. Nevertheless, previous research did not report gender differences for pancreatic DTI [86].

The use of different numbers of diffusion directions for DTI has been studied in neuroimaging applications, and smaller numbers have been associated with inaccurate measurements, especially affecting FA [78, 133, 134]. This was also apparent in our study, where the 6-direction protocol provided higher FA values. Although the absolute difference was not large (0.231 for 16 directions and 0.276 for 6 directions), caution should still be employed when comparing FA values, especially if comparing measurements obtained from different gradient schemes. Other than FA, the remaining DTI and MK maps provided similar values for both direction protocols.

Nissan et al reported pancreatic FA values of 0.38 ± 0.06 in healthy volunteers, using 30 diffusion directions and a highest b value of 500 s/mm^2 [86]. Another study investigating DTI for characterizing acute pancreatitis reported FA values of 0.54 ± 0.12 in healthy volunteers, using 9 diffusion directions and highest b value of 500 s/mm^2 [87]. Our results show lower values for both acquisition protocols, using a highest b value of 1000 s/mm^2 (0.231 for 16 directions and 0.276 for 6 directions). Factors other than number of diffusion directions, such as signal-to-noise ratio (SNR), denoising techniques and choice of b value may account for disparities in FA measurements, with higher SNR and higher b values both contributing to lower FA estimations [135, 136].

Our results regarding AD measurements provided lower values when compared with a previous study: 1.203E-3 mm^2/s (IQR = 0.313E-3) and 1.343E-3 mm^2/s (IQR = 0.211E-3) mm^2/s respectively for each protocol, while previously reported values were 2.70E-3 ± 0.3E-3 mm^2/s (using b values of 0 and 500 s/mm^2) and 2.09E-3 ± 0.25E-3 mm^2/s (using b values

of 100 and 500 s/mm^2) [86]. The same study reported MD values of 2.04E-3 ± 0.28E-3 mm^2/s (using b values of 0 and 500 s/mm^2) and 1.44E-3 ± 0.16E-3 mm^2/s (using b values of 100 and 500 s/mm^2), while our results provided values of 0.987E-3 mm^2/s (IQR = 0.277E-3) and 1.064E-3 mm^2/s (IQR = 0.232E-3) respectively for each protocol. Although our measurements for AD and MD are lower, they are aligned with the conclusions of this study, where using a lower b value ≥100 s/mm^2 for removing perfusion effects provides lower estimations of diffusion coefficients. Our choice of higher b value also probably contributed to the lower diffusivity estimations [136]. These findings prompt caution when comparing diffusivity values between patients, as DTI parameters should be maintained as equal as possible to provide comparable estimates.

Noda et al evaluated pancreatic DKI in diabetic patients as a potential biomarker for HbA1C concentration levels, with a 3 diffusion directions protocol with b values of 0, 100, 500, 1000, 1500, and 2000 s/mm^2 [105]. They described a positive correlation between MK and HbA1C, and reported MK values of 0.60 ± 0.06 for patients with HbA1c < 5.7%, the group most comparable to our healthy volunteers. Despite differences in acquisition protocols, our results are just in line with these, with MK values of 0.663 (IQR = 0.214) and 0.647 (IQR = 0.228) respectively for each protocol. Granata et al assessed DKI in patients with pancreatic cancer for its diagnosis, with a maximum b value of 1000 s/mm^2 [118]. They reported kurtosis-corrected diffusion coefficient (D) as a valuable diagnostic measurement, but not MK. These results are encouraging for DKI as a way to get more accurate diffusivity estimates for pancreatic cancer diagnosis. While Granata et al did not show that MK has diagnostic value, future studies using higher b values (which are more adequate for DKI) might provide better results for MK [89].

Regarding scan length, the shorter 6-directions protocol may provide a valuable advantage for clinical imaging. Shorter acquisitions, besides being better tolerated by patients, are less affected by motion artefacts [137, 138]. Shorter scan lengths are also obviously desirable in any Radiology department allowing for higher throughputs.

When assessing the number of excluded voxels due to implausible values, DTI maps for both protocols were mostly unaffected. However, MK maps were clearly affected, with median 17.723% (16 directions protocol) and 15.956% (6 directions protocol) excluded pixels. Furthermore, high coefficients of repeatability obtained from MK measurements, especially with the 16-directions protocol (reaching 66.9% relative to its median value for one of the readers), indicate important variability in MK estimates. Kurtosis estimates are known to be more sensitive to image noise and artefacts than their diffusion counterparts, which could explain these results [92, 139]. Although denoising and artifact correction algorithms were used in pre-processing, and the MK estimation was performed with a robust signal-average technique, these results still advise caution when using DKI for pancreatic imaging [92, 93].

Possible causes for such inaccurate MK estimations might include physiological cardiovascular and bowel motion, and bowel gas artifacts, which were not directly addressed in our study and present relevant points for evaluation in future studies [107, 140, 141]. Other possible contributors to inaccurate MK estimations might be the parallel

acquisition induced artifacts, such as ghosting and low SNR, which were not obvious in our images [142]. However, due to the reduced field of view, areas outside the body where ghosting artifacts are more noticeable were not evaluated. Furthermore, methods for improving SNR, such as increasing slice thickness or signal averages may be used to improve MK estimations' accuracy, however at the cost of lower spatial resolution and lengthier acquisitions, respectively. In this study, we used a slice thickness of 3 mm to achieve higher spatial resolution and reduce partial volume effects. However, this decision resulted in lower SNR compared to a standard 5 mm thickness, which is a known trade-off [143]. The impact of slice thickness on SNR can be quantified theoretically: assuming all other imaging parameters remain constant (e.g., in-plane resolution, signal averages, receiver bandwidth, and diffusion directions), SNR is proportional to slice thickness. Therefore, increasing the slice thickness from 3 mm to 5 mm would lead to an expected SNR gain of 5/3. Applying uncertainty propagation to the DKI model, the standard deviation of MK estimates scales inversely with SNR [144]. This means that increasing the slice thickness from 3 mm to 5 mm would theoretically reduce the MK estimation error by a factor of 3/5, corresponding to a 40% reduction in the repeatability coefficient of MK estimation. These theoretical predictions provide a framework for generalizing our results to different slice thicknesses.

This study has limitations. First, the sample group of volunteers can be considered small, precluding analyses on possible gender and age differences. Second, our sample included mostly young and active people, which might not provide an optimal reference for subjects most often affected by pancreatic disease, later in life. Third, the volunteers' body-mass index was not registered, and could not be correlated with our results, as a possible source of bias. Fourth, as mentioned above, motion artifacts correction was not directly implemented in our study and presents an important point for improvement in future research. Fifth, our ADC computing method used the first direction of the DTI data, which differs from the current clinical standard trace of three orthogonal axes, and may entail diffusion anisotropy susceptibility. Finally, our pancreatic segmentation did not allow separate analyses on organ parts (head, body and tail), which have previously been described to have slightly decreasing diffusivities [86]. This remains an interesting point for further research.

In conclusion, DTI and DKI of the pancreas are feasible and repeatable techniques in a clinical 3T scanner, with excellent inter-observer agreement. However, issues with MK inaccuracies should be kept in mind, and further research might provide improvements by correcting sources of artifacts. A shorter protocol with 6 diffusion directions may be preferred, as it performs mostly similarly to a longer 16 directions protocol.

Table 1. MRI pulse sequence parameters.

Image acquisition	T2-weighted	DTI	DKI
Magnetic field strength	3 T	3 T	3 T
Pulse sequence	TSE	SE-EPI	SE-EPI
In-plane resolution (mm)	3 x 3	3 x 3	3 x 3
Slice thickness (mm)	3	3	3
Number of slices	30	6	6
Slice gap (mm)	3	10	10
TR	1207	2600	2600
TE	80	90	90
Signal averages	1	2 (b200), 4 (b1000)	2 (b200), 4 (b1000), 5 (b1700)
Acceleration factor	2	-	-
Partial-Fourier reduction factor	1	1.53	1.53
Fat-suppression	No	SPIR	SPIR
Parallel acquisition	SENSE (R = 2)	SENSE (R = 2)	SENSE (R = 2)
B values (s/mm^2)	-	200, 1000	200, 1000, 1700
Diffusion directions	-	6 / 16	6 / 16
Respiratory triggering	Yes	Yes	Yes

DTI: Diffusion Tensor Imaging; DKI: Diffusion Kurtosis Imaging; TE: Echo time; TR: Repetition time; R: parallel acquisition acceleration factor; TSE: Turbo spin-echo; SE-EPI: Spin-echo Echo-planar imaging; SENSE: Sensitivity Encoding; SPIR: Spectral Presaturation with Inversion recovery.

Table 2. Classification scale for subjective image quality assessment by two readers.

Quality parameters	**Classification scale**				
	1	2	3	4	5
Anatomical delineation	Poor	Suboptimal	Acceptable	Good	Excellent
Image graininess	Unreadable	Detrimental	Not impactful	Mild	Not perceived
Distortion artifacts	Unreadable	Detrimental	Not impactful	Mild	Not perceived
Motion artifacts	Unreadable	Detrimental	Not impactful	Mild	Not perceived

Image graininess and artifacts were classified according to their potential impact on diagnosis, if: rendering the images unreadable, detrimental to diagnosis, present but not impactful, mild, or not perceived.

Table 3. Volunteer and scanning characteristics.

	16 diffusion directions	**6 diffusion directions**	**P value**
Number of volunteers	12	12	-
Age (years)	35 (29-60)	37.5 (23-50)	0.443
Sex	8 Female / 4 Male	9 Female / 3 Male	1.000
Full scan length (min)	13 (12-26)	7 (6-10)	<0.001*
DTI only length (min)	7.5 (6-15)	4 (3-5)	<0.001*

Results displayed as medians and ranges (minimum-maximum). Mann-Whitney U test was used for comparisons between groups for continuous variables; Fisher's exact test used for categorical variables. *denotes statistically significant values.

Table 4. Subjective image quality assessment by two readers, protocol comparison.

DTI/DKI maps	Quality parameters	Reader 1			Reader 2		
		16 diffusion directions	6 diffusion directions	P	16 diffusion directions	6 diffusion directions	P
FA	**Anatomical delineation**	3.5 (2.0 – 5.0)	4.0 (2.5 – 5.0)	0.219	3.25 (2.0 – 5.0)	3.5 (2.0 – 5.0)	0.178
	Image graininess	3.00 (2.00 – 4.0)	4.00 (2.50 – 4.0)	0.178	3.75 (2.0 – 4.0)	4.0 (2.0 – 5.0)	0.242
	Distortion artifacts	4.25 (3.0 – 5.0)	3.5 (2.0 – 5.0)	0.198	3.75 (3.0 – 5.0)	3.5 (2.0 – 5.0)	0.755
	Motion artifacts	4.0 (3.0 – 5.0)	4.0 (3.00 – 5.0)	0.551	4.0 (2.5 – 5.0)	5.0 (3.0 – 5.0)	0.590
MD	**Anatomical delineation**	5.0 (4.0 – 5.0)	4.5 (3.0 – 5.0)	0.198	5.0 (4.0 – 5.0)	5.0 (3.0 – 5.0)	1.000
	Image graininess	5.0 (4.0 – 5.0)	5.0 (4.0 – 5.0)	0.713	5.0 (4.0 – 5.0)	5.0 (4.0 – 5.0)	0.478
	Distortion artifacts	5.0 (3.5 – 5.0)	4.0 (3.0 – 5.0)	0.01*	4.0 (3.5 – 5.0)	3.75 (3.0 – 5.0)	0.06
	Motion artifacts	4.5 (3.0 – 5.0)	4.0 (4.0 – 5.0)	0.443	4.5 (3.0 – 5.0)	4.25 (4.0 – 5.0)	0.887
AD	**Anatomical delineation**	5.0 (3.5 – 5.0)	4.0 (3.5 – 5.0)	0.068	5.0 (4.0 – 5.0)	5.0 (3.0 – 5.0)	0.932
	Image graininess	4.5 (3.5 – 4.5)	4.0 (3.0 – 5.0)	0.514	4.75 (3.5 – 5.0)	5.0 (4.0 – 5.0)	0.671
	Distortion artifacts	4.75 (4.0 – 5.0)	4.0 (3.0 – 5.0)	0.291	4.0 (3.0 – 5.0)	4.0 (3.0 – 5.0)	0.319
	Motion artifacts	4.0 (3.5 – 5.0)	4.75 (4.0 – 5.0)	0.114	4.0 (3.0 – 5.0)	4.5 (4.0 – 5.0)	0.590
RD	**Anatomical delineation**	5.0 (4.0 – 5.0)	4.0 (3.5 – 5.0)	0.078	5.0 (4.0 – 5.0)	5.0 (3.5 – 5.0)	0.713
	Image graininess	4.5 (4.0 – 5.0)	4.25 (4.0 – 5.0)	0.551	4.75 (3.0 – 5.0)	5.0 (3.0 – 5.0)	0.755

	Distortion artifacts	4.5 (4.0 – 5.0)	4.0 (3.0 – 5.0)	0.319	4.0 (3.0 – 5.0)	3.75 (3.0 – 5.0)	0.219
	Motion artifacts	4.0 (3.5 – 5.0)	4.75 (4.0 – 5.0)	0.291	4.5 (4.0 – 5.0)	4.25 (4.0 – 5.0)	0.843
MK	**Anatomical delineation**	3.5 (2.5 – 5.0)	3.75 (3.0 – 5.0)	0.887	4.0 (3.0 – 5.0)	3.5 (3.0 – 5.0)	0.198
	Image graininess	3.75 (3.0 – 4.0)	3.5 (3.0 – 4.5)	0.266	4.0 (3.0 – 5.0)	3.25 (3.0 – 4.5)	0.291
	Distortion artifacts	4.5 (3.0 – 5.0)	4.0 (3.0 – 5.0)	0.101	4.0 (3.0 – 5.0)	4.0 (3.0 – 5.0)	0.843
	Motion artifacts	4.0 (3.0 – 5.0)	4.0 (4.0 – 5.0)	0.443	4.0 (3.5 – 5.0)	4.25 (4.0 – 5.0)	0.478
ADC	**Anatomical delineation**	4.0 (3.0 – 5.0)	4.0 (3.0 – 5.0)	1.00	4.0 (3.5 – 5.0)	4.0 (3.0 – 5.0)	0.977
	Image graininess	4.0 (3.0 – 4.5)	4.0 (3.0 – 5.0)	0.843	4.0 (4.0 – 5.0)	4.5 (3.0 – 5.0)	0.347
	Distortion artifacts	4.0 (3.0 – 5.0)	4.0 (3.0 – 5.0)	0.887	4.0 (3.0– 5.0)	4.0 (3.0 – 4.5)	0.443
	Motion artifacts	4.0 (3.5 – 5.0)	4.5 (4.0 – 5.0)	0.143	4.0 (3.5 – 5.0)	5.0 (4.0 – 5.0)	0.068

Median values of classification for each reader for all acquisitions, with averaged repeated acquisitions per subject (12 classifications per reader for each diffusion directions protocol), are presented with minimum-maximum ranges. Mann-Whitney U test is used for comparisons. * Denotes statistically significant results.

Table 5. DTI, DKI and ADC pancreatic measurements obtained from protocols with 16 and 6 diffusion directions.

Metric	16 diffusion directions	6 diffusion directions	P value
FA (median)	0.231 (IQR = 0.025)	0.276 (IQR = 0.053)	0.008*
FA (90^{th} P)	0.351 (IQR = 0.060)	0.417 (IQR = 0.095)	0.017*
FA (10^{th} P)	0.134 (IQR = 0.017)	0.165 (IQR = 0.039)	0.006*
MD (median)	0.987 (IQR = 0.277)	1.064 (IQR = 0.232)	0.590
MD (90^{th} P)	1.157 (IQR = 0.313)	1.122 (IQR = 0.262)	0.590
MD (10^{th} P)	0.862 (IQR = 0.200)	0.871 (IQR = 0.224)	0.514
AD (median)	1.203 (IQR = 0.313)	1.343 (IQR = 0.211)	0.219
AD (90^{th} P)	1.407 (IQR = 0.367)	1.5909 (IQR = 0.200)	0.114
AD (10^{th} P)	1.040 (IQR = 0.269)	1.072 (IQR = 0.225)	0.378
RD (median)	0.892 (IQR = 0.250)	0.903 (IQR = 0.218)	0.932
RD (90^{th} P)	1.057 (IQR = 0.297)	1.080 (IQR = 0.252)	0.977
RD (10^{th} P)	0.739 (IQR = 0.183)	0.679 (IQR = 0.210)	0.843
MK (median)	0.663 (IQR = 0.214)	0.647 (IQR = 0.228)	0.843
MK (90^{th} P)	0.839 (IQR = 0.299)	0.822 (IQR = 0.236)	0.671
MK (10^{th} P)	0.338 (IQR = 0.197)	0.356 (IQR = 0.180)	1.000
ADC (median)	1.179 (IQR = 0.228)	1.191 (IQR = 0.152)	0.671
ADC (90^{th} P)	1.446 (IQR = 0.249)	1.430 (IQR = 0.097)	0.887
ADC (10^{th} P)	0.904 (IQR = 0.286)	0.962 (IQR = 0.232)	0.843

Results from pancreatic segmentation from one reader, averaged between two acquisitions for each volunteer. MD, AD, RD and ADC are expressed as $x10^{-3}$ mm^2/s to

facilitate comparisons. 90th P and 10th P represent 90th and 10th percentiles, respectively. Mann-Whitney U test was used for comparisons between groups. *denotes statistically significant values.

Table 6. Repeatability coefficients of DTI, DKI and DWI metrics for two readers, for both acquisition protocols, with corresponding proportion relative to the median values.

Metric	**16 Diffusion Directions**		**6 Diffusion Directions**	
	Reader 1	**Reader 2**	**Reader 1**	**Reader 2**
FA	0.012 (5.2%)	0.053 (23.0%)	0.015 (5.4%)	0.043 (16.2%)
MD	0.040 (4.1%)	0.098 (10.0%)	0.040 (3.8%)	0.018 (1.7%)
AD	0.105 (8.7%)	0.132 (11.1%)	0.046 (3.4%)	0.089 (6.6%)
RD	0.001 (0.1%)	0.083 (9.3%)	0.005 (0.6%)	0.045 (4.9%)
MK	0.326 (49.2%)	0.445 (66.9%)	0.228 (35.2%)	0.186 (28.8%)
ADC	0.180 (15.3%)	0.304 (26.0%)	0.1231 (10.3%)	0.083 (6.9%)

MD, AD RD and ADC are expressed as x10^{-3} mm^2/s to facilitate comparisons. The proportion of each coefficient related to its median value is expressed as percentage, to facilitate interpretation

Supplementary Table 1. Subjective image quality assessment by two readers, inter-reader reliability analysis.

DTI/DKI maps	Quality parameters	16 diffusion directions			6 diffusion directions		
		Reader 1	Reader 2	Weighted Kappa	Reader 1	Reader 2	Weighted Kappa
FA	**Anatomical delineation**	3.33 (2 – 5)	3.21 (2 – 5)	0.73 (0.57 – 0.88)	3.83 (2 - 5)	3.67 (2 – 5)	0.64 (0.39 – 0.89)
	Image graininess	3.13 (2 – 4)	3.21 (2 – 4)	0.61 (0.40 – 0.82)	3.46 (2 – 4)	3.71 (2 – 5)	0.65 (0.48 – 0.81)
	Distortion artifacts	4.17 (3 – 5)	3.75 (3 – 5)	0.67 (0.50 – 0.84)	3.71 (2 – 5)	3.63 (2 – 5)	0.90 (0.80 – 1.00)
	Motion artifacts	4.08 (3 – 5)	4.04 (2 – 5)	0.88 (0.86 – 1.00)	3.96 (3 – 5)	4.25 (3 – 5)	0.23 (-0.07 – 0.53)
MD	**Anatomical delineation**	4.79 (4 – 5)	4.79 (4 – 5)	0.50 (0.07 – 0.92)	4.50 (3 – 5)	4.67 (3 – 5)	0.80 (0.58 – 1.00)
	Image graininess	4.83 (4 – 5)	4.79 (4 – 5)	0.86 (0.60 – 1.00)	4.75 (4 – 5)	4.63 (4 - 5)	0.52 (0.17 – 0.88)
	Distortion artifacts	4.58 (3 – 5)	4.25 (3 – 5)	0.47 (0.17 – 0.78)	3.83 (3 – 5)	3.75 (3 – 5)	0.90 (0.76 – 1.00)
	Motion artifacts	4.42 (3 – 5)	4.42 (3 – 5)	1.00 (1.00 – 1.00)	4.25 (4 – 5)	4.42 (4 – 5)	0.46 (0.11 – 0.80)
AD	**Anatomical delineation**	4.67 (3 – 5)	4.71 (3 – 5)	0.79 (0.52 – 1.00)	4.21 (3 – 5)	4.63 (3 – 5)	0.15 (-0.08 – 0.37)
	Image graininess	4.17 (3 – 5)	4.58 (3 – 5)	0.40 (0.09 – 0.71)	4.04 (3 – 5)	4.67 (4 – 5)	0.11 (-0.14 – 0.36)
	Distortion artifacts	4.58 (4 – 5)	4.13 (4 – 5)	0.37 (0.17 – 0.57)	4.13 (3 – 5)	3.83 (3 – 5)	0.34 (-0.02 – 0.70)
	Motion artifacts	4.17 (3 – 5)	4.29 (3 – 5)	0.73 (0.50 – 0.96)	4.33 (4 – 5)	4.42 (4 – 5)	0.75 (0.50 – 1.00)
RD	**Anatomical delineation**	4.75 (4 – 5)	4.63 (4 – 5)	0.71 (0.42 – 1.00)	4.33 (3 – 5)	4.67 (3 – 5)	0.28 (-0.12 – 0.67)
	Image graininess	4.58 (4 – 5)	4.46 (3 – 5)	0.44 (0.17 – 0.72)	4.46 (3 - 5)	4.54 (3 – 5)	0.13 (-0.26 – 0.52)

	Distortion artifacts	4.50 (4 – 5)	4.13 (3 – 5)	0.44 (0.22 – 0.66)	4.13 (3 - 5)	3.79 (3 – 5)	0.28 (-0.09 – 0.65)
	Motion artifacts	4.54 (3 – 5)	4.42 (4 – 5)	0.56 (0.28 – 0.83)	4.33 (4 – 5)	4.42 (4 – 5)	0.43 (0.08 – 0-77)
MK	**Anatomical delineation**	3.67 (2 – 5)	4.08 (2 – 5)	0.63 (0.39 – 0.86)	3.63 (3 – 5)	3.71 (3 – 5)	0.74 (0.53 – 0.94)
	Image graininess	3.71 (3 – 5)	3.79 (3 – 5)	0.18 (-0.18 – 0.64)	3.50 (3 – 5)	3.50 (3 – 5)	0.89 (0.75 – 1.00)
	Distortion artifacts	4.38 (3 – 5)	3.96 (3 – 5)	0.52 (0.25 – 0.79)	3.88 (3 – 5)	3.88 (3 – 5)	0.40 (0.04 – 0.75)
	Motion artifacts	4.08 (3 – 5)	4.29 (3 – 5)	0.72 (0.52 – 0.92)	4.00 (4 – 5)	4.42 (4 – 5)	0.74 (0.48 – 1.00)
ADC	**Anatomical delineation**	4.08 (3 – 5)	4.04 (3 – 5)	0.67 (0.40 – 0.93)	4.08 (3 – 5)	4.21 (3 – 5)	0.59 (0.34 – 0.85)
	Image graininess	3.96 (3 – 5)	4.13 (4 – 5)	0.36 (-0.04 – 0.76)	3.96 (3 – 5)	4.38 (3 – 5)	0.27 (-0.07 – 0.62)
	Distortion artifacts	4.08 (3 – 5)	3.96 (3 – 5)	0.73 (0.45 – 1.00)	4.04 (3 – 5)	3.71 (3 – 5)	0.23 (-0.07 – 0.53)
	Motion artifacts	4.00 (3 – 5)	4.25 (3 – 5)	0.67 (0.34 – 0.99)	4.29 (4 – 5)	4.50 (4 – 5)	0.43 (0.11 – 0.76)

Average values of classification for each reader for all acquisitions, including repeated acquisitions per subject (24 classifications per reader for each diffusion directions protocol), are presented with minimum-maximum ranges. Weighted Kappa (quadratic) was used to assess inter-observer reliability and is presented with 95% confidence intervals.

Supplementary Table 2. Excluded artifactual voxels in DTI, DKI and ADC maps.

Metric	16 diffusion directions	6 diffusion directions	P value
FA	0.000%	0.000%	0.514
MD	0.000%	0.000%	0.514
AD	0.000%	0.000%	0.514
RD	0.000%	0.000%	0.514
MK	17.723% (IQR = 18.05)	15.956% (IQR = 9.042)	0.887
ADC	0.000%	0.000%	1.000

Excluded voxels are represented in percentages, with median values and IQR. Mann-Whitney U test was used for comparisons between groups.

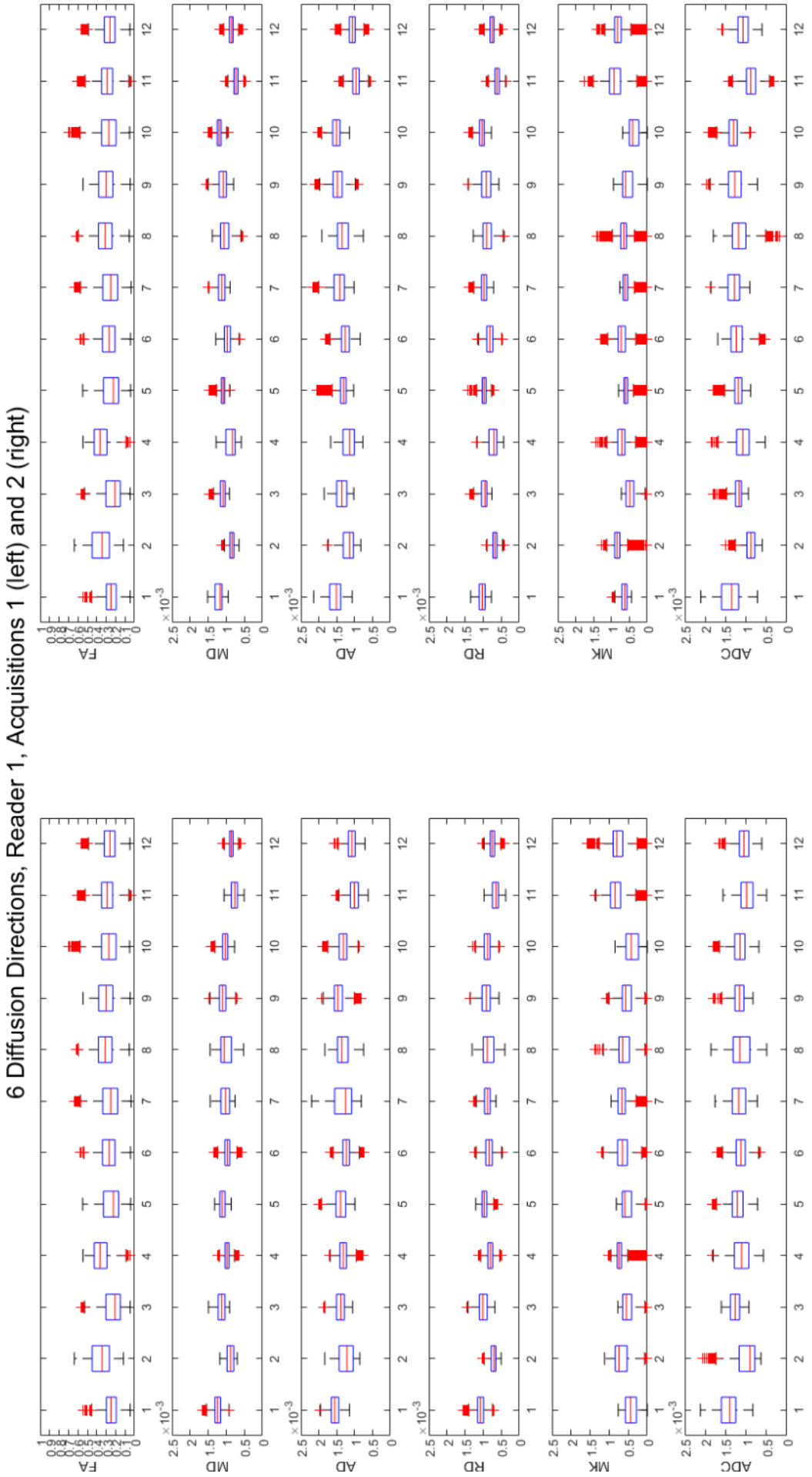
Supplementary Table 3. Intraclass correlation coefficients of DTI, DKI and DWI metrics for two readers, for both acquisition protocols.

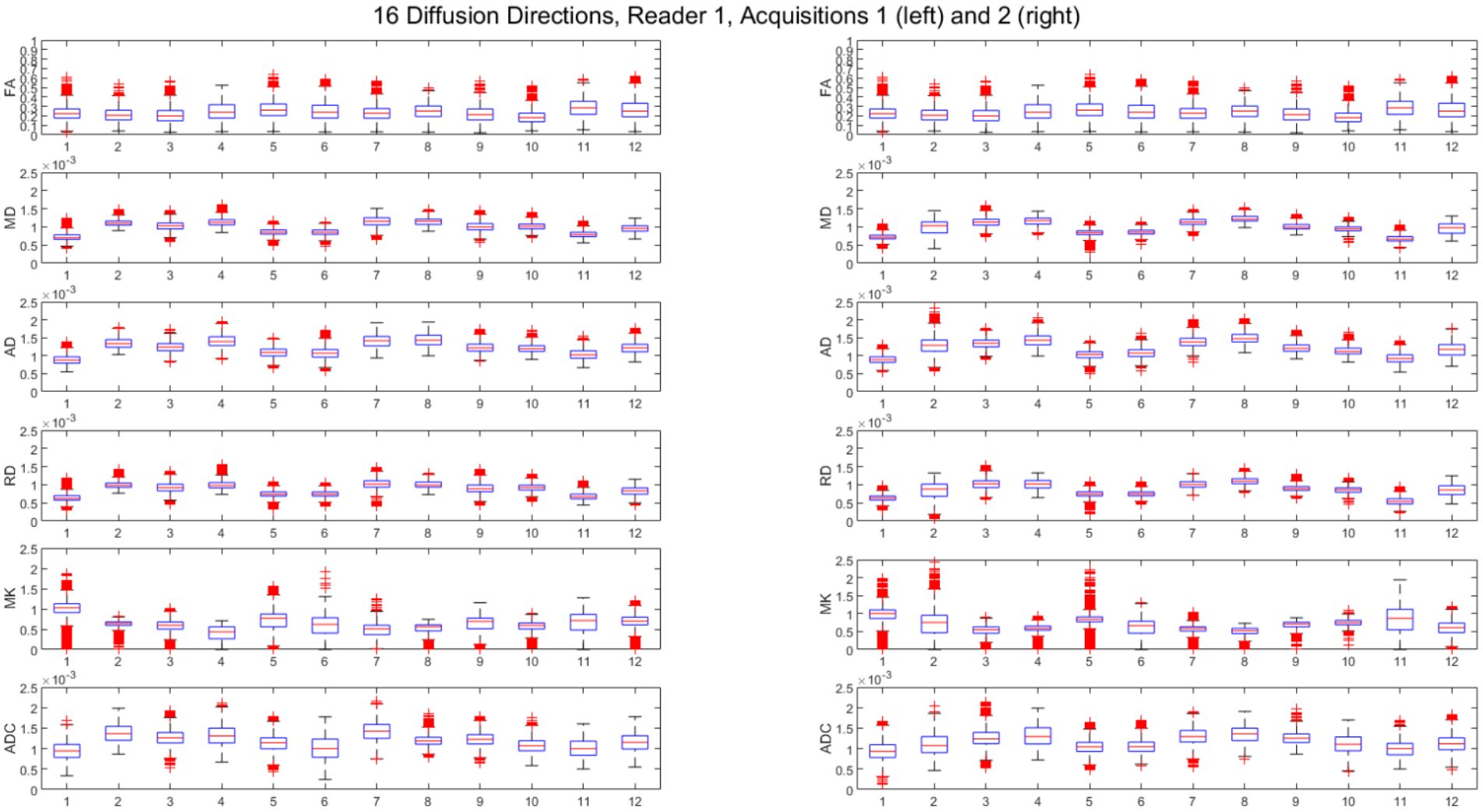
Metric	ICC	
	16 Diffusion Directions	**6 Diffusion Directions**
FA	0.967 (0.925-0.985)	0.910 (0.803-0.960)
MD	0.994 (0.986-0.997)	0.985 (0.965-0.993)
AD	0.995 (0.989-0.998)	0.969 (0.929-0.986)
RD	0.990 (0.977-0.996)	0.986 (0.968-0.994)
MK	0.992 (0.982-0.997)	0.984 (0.963-0.993)
ADC	0.971 (0.935-0.988)	0.962 (0.914-0.983)

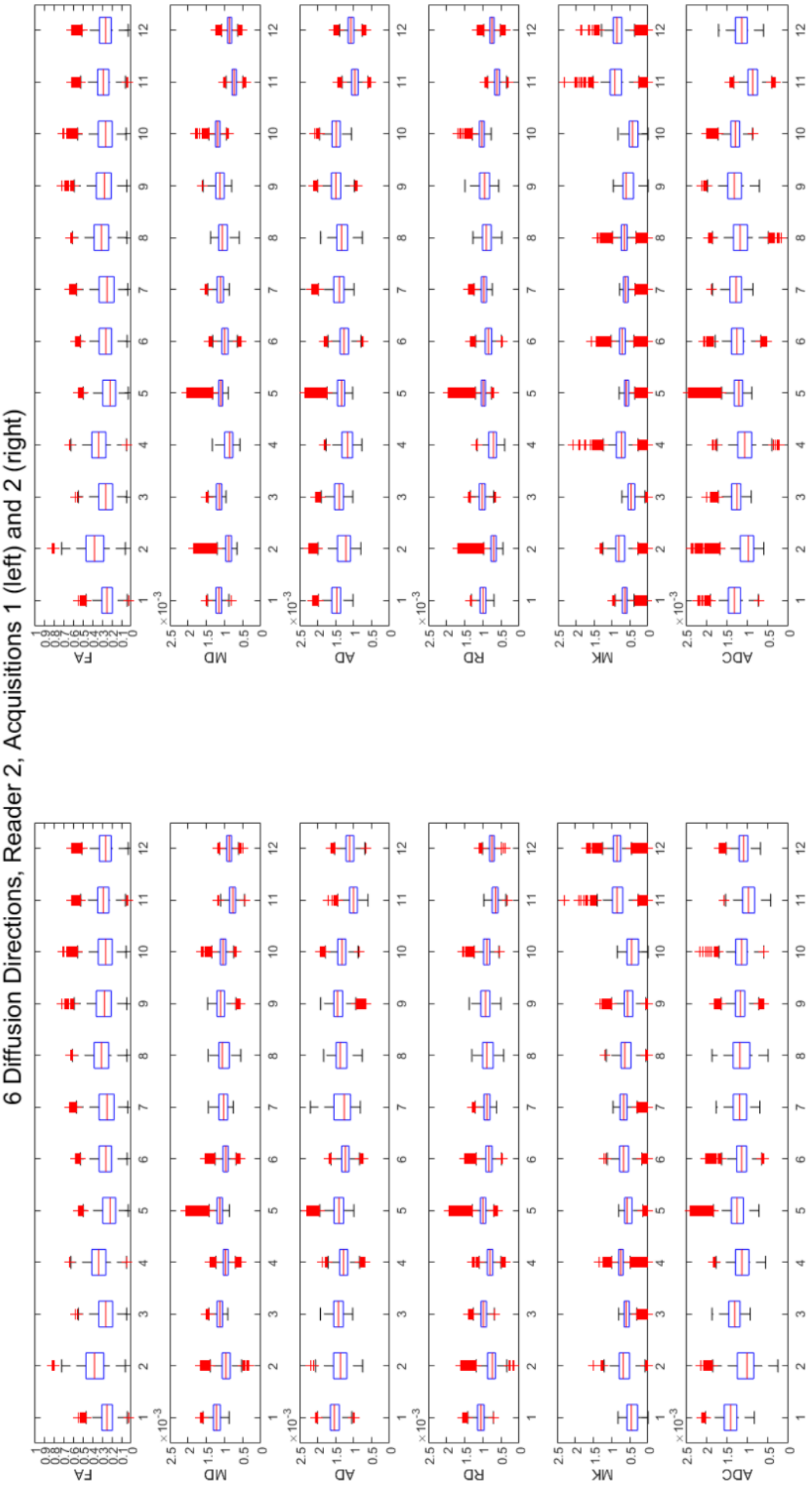
A two-way mixed model of single measures was used.

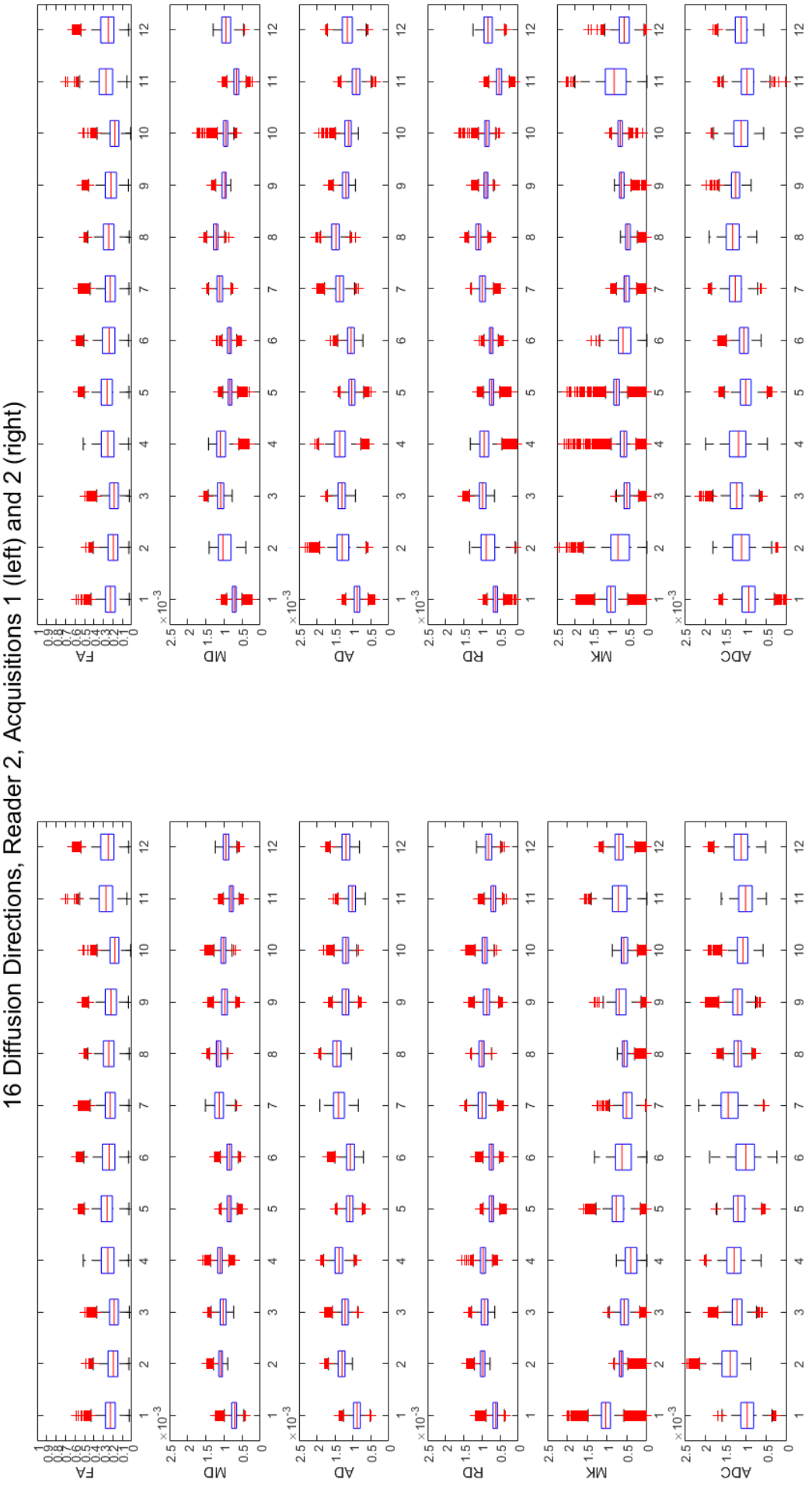
ICC is displayed with 95% confidence intervals. A p value of <0.001 was observed in all displayed results.

Supplementary Figure 1 - Boxplots for the 6 diffusion directions protocol as assessed by Reader 1, for each DTI, DKI and DWI metric (FA, MD, AD, RD, MK, ADC) for each volunteer.
Supplementary Figure 2 - Boxplots for the 16 diffusion directions protocol as assessed by Reader 1, for each DTI, DKI and DWI metric (FA, MD, AD, RD, MK, ADC) for each volunteer.
Supplementary Figure 3 - Boxplots for the 6 diffusion directions protocol as assessed by Reader 2, for each DTI, DKI and DWI metric (FA, MD, AD, RD, MK, ADC) for each volunteer.
Supplementary Figure 4 - Boxplots for the 16 diffusion directions protocol as assessed by Reader 2, for each DTI, DKI and DWI metric (FA, MD, AD, RD, MK, ADC) for each volunteer.


6 Diffusion Directions, Reader 1, Acquisitions 1 (left) and 2 (right)
FA
MD
AD
RD
MK
ADC


16 Diffusion Directions, Reader 1, Acquisitions 1 (left) and 2 (right)
FA
MD
AD
RD
MK
ADC
×10^-3


6 Diffusion Directions, Reader 2, Acquisitions 1 (left) and 2 (right)
FA
MD
AD
RD
MK
ADC


16 Diffusion Directions, Reader 2, Acquisitions 1 (left) and 2 (right)
FA
MD
AD
RD
MK
ADC

Chapter IV.

Discussion

Advanced diffusion-weighted imaging techniques are powerful instruments capable of extracting information on biological tissue microstructure, with potential clinical applications for pancreatic imaging. From clarifying conventional DWI's role in assessing response to neoadjuvant therapy for pancreatic cancer, to exploring DTI for the detection and characterization of pre-malignant lesions in the pancreas and determining optimal protocols for DTI and DKI of the pancreas, the works presented in this Thesis were ultimately aimed at developing imaging tools with potential for improving the dismal clinical scenario of pancreatic cancer.

4.1. The role of DWI in assessing response to neoadjuvant therapy in pancreatic cancer

Several studies have explored DWI with ADC values for assessing response to neoadjuvant therapy (NAT) in pancreatic cancer, however with conflicting results [145–153]. This systematic review and meta-analysis determined that DWI with ADC values for the assessment of response to NAT in pancreatic cancer may be useful, but its role is not yet fully clear due to heterogeneity and high risk for bias across studies. These limitations can be attributed to the reality of clinical practice, with difficulties in managing patients with pancreatic cancer, imperfect staging systems after NAT, and the evolution of NAT regimens and treatment recommendations in recent years [154, 155]. In the studies included, ADC values overlapped for responders and non-responders, however, a correlation between ADC values and histopathological response was reported in four studies. This hints to DWI having some sensitivity towards response to NAT, which is not fully captured by ADC measurements.

Technical issues affecting the reproducibility of ADC values were considered an important concern, with reported values varying widely between studies, both for responders and non-responders. This emphasizes the need for standardized and robust image acquisition protocols for reducing variability and artifacts [116, 140, 156–159]. Standardized image evaluation by radiologists through ROI placement is also recommended for reducing variability in data collection [160, 161].

Despite recent technological advances, response assessment after NAT in pancreatic cancer remains a challenge in clinical practice. The definition of response is relied upon

CA19-9 concentration values and traditional size criteria in imaging studies: increase in tumor size is suggestive of progressive disease, while stability or reduction in tumor size is considered a response [162–164]. This approach is suboptimal, however, as it may lead to unnecessary surgery being performed in cases of persistent locally advanced disease, or potentially resectable patients being excluded from surgery. Novel biomarkers are therefore needed, but conventional DWI appears to be insufficient [165–167]. Our systematic review and meta-analysis help establish DWI with ADC measurement as potentially useful, but current data is not enough to recommend its implementation in clinical practice.

Considering future perspectives, besides the implementation of standardized image acquisition and evaluation methods, the use of advanced diffusion-weighted techniques such as DTI and DKI might be relevant. Since simple ADC values appear to have some sensitivity to response to NAT, other more specific diffusion-based metrics may hypothetically provide more robust results.

4.2. A bowel motion reduction protocol enabling high-quality MRI of the mouse abdomen

In this study we have shown how hyoscine butylbromide (BUSC) is effective for bowel motion reduction in the mouse for an average duration of 40-45 min, best achieved when administering a single bolus of 5 mg/kg (high-dose BUSC protocol) in comparison to the 0.5 mg/kg dosage (low-dose BUSC protocol). The time interval from injection to start of bowel motion reduction was observed between 5.2 min and 13.1 min in the high-dose BUSC group.

Previous studies suggested little efficacy of BUSC as an antiperistaltic agent in mice, comparable to simply fasting, albeit without considerable amounts of supporting data [168, 169]. Our results revealed a different case, where BUSC is actually effective, and fasting is not effective at all. Both the subjective and objective motion quantification methods used in our study contributed to these conclusions. Glucagon might be an alternative to BUSC, although more expensive [170]. The intraperitoneal route of administration is a relevant factor to account for in future studies, as different routes of administration may produce different effects [171].

When testing the best performing protocol (high-dose BUSC) compared with no motion reduction, T2-weighted and Diffusion-weighted images showcased obvious improvements in image quality.

With this bowel motion reduction protocol established, advanced diffusion-weighted techniques (i.e., DTI) could now be used for imaging the mouse abdomen without significant artifacts.

4.3. Detecting pancreatic intraepithelial neoplasia with DTI

This work provides evidence establishing a potential role of DTI (and also T2*), in detecting and characterizing PanIN and PDAC. We present an *in vivo* application of DTI for pancreatic imaging in the mouse, MR Microscopy correlation with histology validating the observed image contrasts, and evidence for clinical translation potential in the human pancreas.

Considering a stepwise carcinogenesis of PDAC, akin to the well-established colon cancer tumorigenesis, a window of opportunity for early and preventive interventions has been recognized [172, 173]. Nevertheless, the absence of diagnostic tools for the most relevant lesions during carcinogenesis, i.e. PanIN, has rendered any intervention during this period impractical, and limited to other less relevant cystic lesions - IPMN and MCN [26, 174]. Moreover, much of what is currently know about PanIN was obtained with studies performed with GEMM [172, 175]. Hence, the development of non-invasive diagnostic tools can help further knowledge on PanIN and provide opportunities for preventive interventions. Our *in vivo* DTI experiments in mice describe an effective noninvasive method for PanIN detection, which may be used in future studies informing PanIN biology or testing novel therapies.

We found striking contrasts in DTI-derived maps, correlating with specific histological features: areas of diffusion anisotropy (high FA) corresponded to the peripheral zones of PanIN, ADM and PDAC, where sheath/cuff-like periductal fibrosis is observed; areas of high diffusivities corresponded mostly to cystic and necrotic regions; areas of high T2* corresponded mostly to stromal components. Regarding histologically defined disease burden and severity, AD provided the best correlations. Together, these findings underline the ability of DTI for providing metrics sensitive to tissue microstructure, as previously observed for other contexts [176–178].

DTI has been performed successfully for imaging the pancreas in clinical context, but its role in diagnosing or characterizing pathology remains mostly unexplored [86]. For PanIN detection in particular, technical constraints in clinical MRI will enforce significant adaptations, especially loss of image resolution. Pulse sequences sensitive to microscopic anisotropy may be used to overcome this limitation [179].

Regarding differentiation between low-grade PanIN, high-grade PanIN and PDAC, our results demonstrate a correlation between disease burden and severity, and DTI/T2* metrics. Nonetheless, visual contrasts were not strikingly differentiating for each lesion, which puts DTI's specificity for this matter into question. This is a clinically relevant point, which should be clarified in future studies. In this context, combining DTI with liquid biopsy or artificial intelligence may provide solutions for identifying high-risk lesions [180, 181].

4.4. DTI and DKI of the pancreas: feasibility, repeatability and inter-reader agreement in a clinical context

This study compares two protocols for DTI and DKI of the healthy pancreas in a clinical context, and demonstrates their feasibility, repeatability and inter-reader agreement. The two MRI protocols showed no relevant differences regarding image quality as determined by objective and subjective analysis, as well as intra-subject repeatability, as such, the protocol with 6 diffusion directions was favored due to shorter scan length.

The number of diffusion directions for DTI is relevant for estimating metrics accurately, especially affecting FA [78, 133, 134]. In line with previous findings, the 6-direction protocol provided slightly higher FA values, prompting caution when comparing FA values obtained from different gradient schemes. Diffusivities and MK maps provided similar values for both direction protocols. Other factors including signal-to-noise ratio (SNR), denoising techniques and choice of b value may account for disparities in FA measurements, which should also be taken into account in future studies [135, 136]. Regarding diffusivities (AD, MD, RD) estimation, the choice of lowest and highest b values influence estimations, and should be standardized when performing comparisons [86, 136].

DKI-derived MK maps were affected by implausible estimates, similar for both protocols, showing more variability in measurements when compared with DTI results. DKI is known for being more sensitive to noise and image artifacts than other diffusion-based techniques [92, 139]. Future studies should investigate methods for correcting cardiovascular and bowel motion, as well as bowel gas artifacts [107, 140, 141].

The shorter 6-directions protocol may provide a valuable advantage for clinical imaging. Shorter acquisitions, besides being better tolerated by patients, are less affected by motion artefacts [137, 138]. Shorter scan lengths are also obviously desirable in any Radiology department allowing for higher throughputs.

This study demonstrates how DTI (more so than DKI) can be confidently utilized for pancreatic imaging in clinical practice, with short acquisitions.

Chapter V.

Conclusions

1. Diffusion-weighted MRI might be useful for assessing response to neoadjuvant therapy in pancreatic cancer. However, further studies with robust data are needed to provide specific recommendations for clinical practice.

2. Buscopan® administration is advantageous for abdominal MRI in the mouse, endowing significant bowel motion reduction, starting 8.5 min after injection and lasting up to 45 min. Its use allows the acquisition of high-quality images of the mouse abdomen.

3. DTI is useful for detecting and characterizing PanIN *in vivo* in genetically engineered mice. MR Microscopy directly correlates with the underlying histological features of PanIN and PDAC, validating the microstructure probing abilities of DTI. DTI is also useful in the human pancreas for identifying PanIN, especially with AD and FA. These are encouraging findings for future clinical applications of pancreatic imaging.

4. DTI and DKI of the pancreas are feasible and repeatable techniques in a clinical 3T scanner, with excellent inter-observer agreement. MK inaccuracies prompt further research into artifacts correction. A shorter protocol with 6 diffusion directions may be preferred.

References

1. Bray Bsc F, Laversanne | Mathieu, Hyuna |, et al (2024) Global cancer statistics 2022: GLOBOCAN estimates of incidence and mortality worldwide for 36 cancers in 185 countries. CA Cancer J Clin 74:229–263. https://doi.org/10.3322/CAAC.21834

2. Siegel Mph RL, Giaquinto AN, Ahmedin |, et al (2024) Cancer statistics, 2024. CA Cancer J Clin 74:12–49. https://doi.org/10.3322/CAAC.21820

3. Haeberle L, Esposito I (2019) Pathology of pancreatic cancer. Transl Gastroenterol Hepatol 4:50. https://doi.org/10.21037/TGH.2019.06.02

4. Kleeff J, Korc M, Apte M, et al (2016) Pancreatic cancer. Nat Rev Dis Prim 2:. https://doi.org/10.1038/NRDP.2016.22

5. Bengtsson A, Andersson R, Ansari D (2020) The actual 5-year survivors of pancreatic ductal adenocarcinoma based on real-world data. Sci Reports 2020 101 10:1–9. https://doi.org/10.1038/s41598-020-73525-y

6. Campbell F, Smith RA, Whelan P, et al (2009) Classification of R1 resections for pancreatic cancer: the prognostic relevance of tumour involvement within 1 mm of a resection margin. Histopathology 55:277–283. https://doi.org/10.1111/J.1365-2559.2009.03376.X

7. Springfeld C, Ferrone CR, Katz MHG, et al (2023) Neoadjuvant therapy for pancreatic cancer. Nat Rev Clin Oncol 20:318–337. https://doi.org/10.1038/S41571-023-00746-1

8. Molina-Montes E, van Hoogstraten L, Gomez-Rubio P, et al (2020) Pancreatic Cancer Risk in Relation to Lifetime Smoking Patterns, Tobacco Type, and Dose-Response Relationships. Cancer Epidemiol Biomarkers Prev 29:1009–1018. https://doi.org/10.1158/1055-9965.EPI-19-1027

9. Wang YT, Gou YW, Jin WW, et al (2016) Association between alcohol intake and the risk of pancreatic cancer: a dose–response meta-analysis of cohort studies. BMC Cancer 16:212. https://doi.org/10.1186/S12885-016-2241-1

10. Yadav D, Lowenfels AB (2013) The Epidemiology of Pancreatitis and Pancreatic Cancer. Gastroenterology 144:1252. https://doi.org/10.1053/J.GASTRO.2013.01.068

11. Raimondi S, Lowenfels AB, Morselli-Labate AM, et al (2010) Pancreatic cancer in chronic pancreatitis; aetiology, incidence, and early detection. Best Pract Res Clin Gastroenterol 24:349–358. https://doi.org/10.1016/J.BPG.2010.02.007

12. Bosetti C, Rosato V, Li D, et al (2014) Diabetes, antidiabetic medications, and pancreatic cancer risk: an analysis from the International Pancreatic Cancer Case-Control Consortium. Ann Oncol 25:2065. https://doi.org/10.1093/ANNONC/MDU276

13. Eibl G, Rozengurt E (2017) KRAS, YAP, and obesity in pancreatic cancer: a signaling network with multiple loops. Semin Cancer Biol 54:50. https://doi.org/10.1016/J.SEMCANCER.2017.10.007

14. Turati F, Edefonti V, Bosetti C, et al (2013) Family history of cancer and the risk of cancer: a network of case–control studies. Ann Oncol 24:2651–2656. https://doi.org/10.1093/ANNONC/MDT280

15. Canto MI, Harinck F, Hruban RH, et al (2013) International Cancer of the Pancreas

Screening (CAPS) Consortium summit on the management of patients with increased risk for familial pancreatic cancer. Gut 62:339–347. https://doi.org/10.1136/GUTJNL-2012-303108

16. Bogdanski AM, Acedo P, Wallace MB, et al (2025) Recommendations, evidence and sustainability of screening for pancreatic cancer in high-risk individuals. Best Pract Res Clin Gastroenterol 101974. https://doi.org/10.1016/J.BPG.2025.101974

17. Blackford AL, Canto MI, Dbouk M, et al (2024) Pancreatic Cancer Surveillance and Survival of High-Risk Individuals. JAMA Oncol 10:1087–1096. https://doi.org/10.1001/JAMAONCOL.2024.1930

18. Klatte DCF, Boekestijn B, Onnekink AM, et al (2023) Surveillance for Pancreatic Cancer in High-Risk Individuals Leads to Improved Outcomes: A Propensity Score-Matched Analysis. Gastroenterology 164:1223-1231.e4. https://doi.org/10.1053/j.gastro.2023.02.032

19. Dbouk M, Katona BW, Brand RE, et al (2022) The Multicenter Cancer of Pancreas Screening Study: Impact on Stage and Survival. J Clin Oncol 40:. https://doi.org/10.1200/JCO.22.00298

20. Overbeek KA, Levink IJM, Koopmann BDM, et al (2022) Long-term yield of pancreatic cancer surveillance in high-risk individuals. Gut 71:1152–1160. https://doi.org/10.1136/GUTJNL-2020-323611

21. Maurer E, Lehman B, Matthäi E, et al (2024) Pancreatic cancer screening is effective in individuals at risk with predisposing germline gene variants, but not in gene variant-negative familial pancreatic cancer families. United Eur Gastroenterol J 12:1211–1221. https://doi.org/10.1002/UEG2.12631

22. Overbeek KA, Goggins MG, Dbouk M, et al (2022) Timeline of Development of Pancreatic Cancer and Implications for Successful Early Detection in High-Risk Individuals. Gastroenterology 162:772-785.e4. https://doi.org/10.1053/J.GASTRO.2021.10.014

23. Hruban RH, Maitra A, Kern SE, Goggins M (2007) Precursors to Pancreatic Cancer. Gastroenterol Clin North Am 36:831–849. https://doi.org/10.1016/J.GTC.2007.08.012

24. Brat DJ, Lillemoe KD, Yeo CJ, et al (1998) Progression of pancreatic intraductal neoplasias to infiltrating adenocarcinoma of the pancreas. Am J Surg Pathol 22:163–169. https://doi.org/10.1097/00000478-199802000-00003

25. Maitra A, Fukushima N, Takaori K, Hruban RH (2005) Precursors to invasive pancreatic cancer. Adv Anat Pathol 12:81–91. https://doi.org/10.1097/01.PAP.0000155055.14238.25

26. Vullierme M-PP, Menassa L, Couvelard A, et al (2019) Non-branched microcysts of the pancreas on MR imaging of patients with pancreatic tumors who had pancreatectomy may predict the presence of pancreatic intraepithelial neoplasia (PanIN): a preliminary study. Eur Radiol 29:5731–5741. https://doi.org/10.1007/s00330-019-06154-3

27. Basturk O, Esposito I, Fukushima N, et al (2021) Tumors of the pancreas. In: Gill A, Klimstra D, Lam A, Washington M (eds) WHO Classification of tumors, 5th ed. World Health Organization, pp 310–314

28. de la Fuente J, Chatterjee A, Lui J, et al (2023) Long-Term Outcomes and Risk of Pancreatic Cancer in Intraductal Papillary Mucinous Neoplasms. JAMA Netw Open 6:e2337799–e2337799. https://doi.org/10.1001/JAMANETWORKOPEN.2023.37799

29. Salvia R, Fernández-Del Castillo C, Bassi C, et al (2004) Main-Duct Intraductal Papillary Mucinous Neoplasms of the Pancreas: Clinical Predictors of Malignancy and Long-term Survival Following Resection. Ann Surg 239:678–687.

https://doi.org/10.1097/01.SLA.0000124386.54496.15

30. Muraki T, Jang KT, Reid MD, et al (2022) Pancreatic ductal adenocarcinomas associated with intraductal papillary mucinous neoplasms (IPMNs) versus pseudo-IPMNs: relative frequency, clinicopathologic characteristics and differential diagnosis. Mod Pathol 35:96–105. https://doi.org/10.1038/S41379-021-00902-X

31. Tanaka M, Chari S, Adsay V, et al (2006) International consensus guidelines for management of intraductal papillary mucinous neoplasms and mucinous cystic neoplasms of the pancreas. Pancreatology 6:17–32. https://doi.org/10.1159/000090023

32. Ohtsuka T, Fernandez-del Castillo C, Furukawa T, et al (2024) International evidence-based Kyoto guidelines for the management of intraductal papillary mucinous neoplasm of the pancreas. Pancreatology 24:255–270. https://doi.org/10.1016/J.PAN.2023.12.009

33. Valsangkar NP, Morales-Oyarvide V, Thayer SP, et al (2012) 851 resected cystic tumors of the pancreas: a 33-year experience at the Massachusetts General Hospital. Surgery 152:. https://doi.org/10.1016/J.SURG.2012.05.033

34. Pollini T, Marchegiani G, Facciorusso A, et al (2023) It is not necessary to resect all mucinous cystic neoplasms of the pancreas: current guidelines do not reflect the actual risk of malignancy. HPB 25:747–757. https://doi.org/10.1016/J.HPB.2023.03.001

35. Del Chiaro M, Besselink MG, Scholten L, et al (2018) European evidence-based guidelines on pancreatic cystic neoplasms. Gut 67:789–804. https://doi.org/10.1136/GUTJNL-2018-316027

36. Hruban RH, Adsay NV, Albores-Saavedra J, et al (2001) Pancreatic intraepithelial neoplasia: a new nomenclature and classification system for pancreatic duct lesions. Am J Surg Pathol 25:579–586. https://doi.org/10.1097/00000478-200105000-00003

37. Hruban RH, Takaori K, Klimstra DS, et al (2004) An illustrated consensus on the classification of pancreatic intraepithelial neoplasia and intraductal papillary mucinous neoplasms. 28:977–987. https://doi.org/10.1097/01.PAS.0000126675.59108.80

38. Detlefsen S, Sipos B, Feyerabend B, Klöppel G (2005) Pancreatic fibrosis associated with age and ductal papillary hyperplasia. Virchows Arch 447:800–805. https://doi.org/10.1007/S00428-005-0032-1

39. Brune K, Abe T, Canto M, et al (2006) Multifocal Neoplastic Precursor Lesions Associated With Lobular Atrophy of the Pancreas in Patients Having a Strong Family History of Pancreatic Cancer. Am J Surg Pathol 30:1067. https://doi.org/pas.0000213265.84725.0b

40. Basturk O, Hong SM, Wood LD, et al (2015) A Revised Classification System and Recommendations From the Baltimore Consensus Meeting for Neoplastic Precursor Lesions in the Pancreas. Am J Surg Pathol 39:1730–1741. https://doi.org/10.1097/PAS.0000000000000533

41. Andea A, Sarkar F, Adsay VN (2003) Clinicopathological correlates of pancreatic intraepithelial neoplasia: a comparative analysis of 82 cases with and 152 cases without pancreatic ductal adenocarcinoma. Mod Pathol 16:996–1006. https://doi.org/10.1097/01.MP.0000087422.24733.62

42. Yu DY, Yu YD, Kim WB, et al (2018) Clinical significance of pancreatic intraepithelial neoplasia in resectable pancreatic cancer on survivals. Ann Surg Treat Res 94:247–253. https://doi.org/10.4174/ASTR.2018.94.5.247

43. Konstantinidis IT, Vinuela EF, Tang LH, et al (2013) Incidentally discovered pancreatic intraepithelial neoplasia: What is its clinical significance? Ann Surg Oncol 20:3643–3647.

https://doi.org/10.1245/S10434-013-3042-2/METRICS

44. Matthaei H, Hong SM, Mayo SC, et al (2011) Presence of pancreatic intraepithelial neoplasia in the pancreatic transection margin does not influence outcome in patients with R0 resected pancreatic cancer. Ann Surg Oncol 18:3493–3499. https://doi.org/10.1245/S10434-011-1745-9

45. McCarthy DM, Brat DJ, Wilentz RE, et al (2001) Pancreatic intraepithelial neoplasia and infiltrating adenocarcinoma: Analysis of progression and recurrence by DPC4 immunohistochemical labeling. Hum Pathol 32:638–642. https://doi.org/10.1053/HUPA.2001.24991

46. Braxton AM, Kiemen AL, Grahn MP, et al (2024) 3D genomic mapping reveals multifocality of human pancreatic precancers. Nat 2024 1–9. https://doi.org/10.1038/s41586-024-07359-3

47. Hingorani SR, Petricoin EF, Maitra A, et al (2003) Preinvasive and invasive ductal pancreatic cancer and its early detection in the mouse. Cancer Cell 4:437–450. https://doi.org/10.1016/S1535-6108(03)00309-X

48. Shi C, Hong SM, Lim P, et al (2009) KRAS2 mutations in human pancreatic acinar-ductal metaplastic lesions are limited to those with PanIN: implications for the human pancreatic cancer cell of origin. Mol Cancer Res 7:230–236. https://doi.org/10.1158/1541-7786.MCR-08-0206

49. Hingorani SR, Wang L, Multani AS, et al (2005) Trp53R172H and KrasG12D cooperate to promote chromosomal instability and widely metastatic pancreatic ductal adenocarcinoma in mice. Cancer Cell 7:469–483. https://doi.org/10.1016/J.CCR.2005.04.023

50. Aguirre AJ, Bardeesy N, Sinha M, et al (2003) Activated Kras and Ink4a/Arf deficiency cooperate to produce metastatic pancreatic ductal adenocarcinoma. Genes Dev 17:3112–3126. https://doi.org/10.1101/GAD.1158703

51. Izeradjene K, Combs C, Best M, et al (2007) Kras(G12D) and Smad4/Dpc4 haploinsufficiency cooperate to induce mucinous cystic neoplasms and invasive adenocarcinoma of the pancreas. Cancer Cell 11:229–243. https://doi.org/10.1016/J.CCR.2007.01.017

52. Bardeesy N, Morgan J, Sinha M, et al (2002) Obligate roles for p16(Ink4a) and p19(Arf)-p53 in the suppression of murine pancreatic neoplasia. Mol Cell Biol 22:635–643. https://doi.org/10.1128/MCB.22.2.635-643.2002

53. Bardeesy N, Cheng KH, Berger JH, et al (2006) Smad4 is dispensable for normal pancreas development yet critical in progression and tumor biology of pancreas cancer. Genes Dev 20:3130–3146. https://doi.org/10.1101/GAD.1478706

54. Guerra C, Barbacid M (2013) Genetically engineered mouse models of pancreatic adenocarcinoma. Mol Oncol 7:232–47. https://doi.org/10.1016/j.molonc.2013.02.002

55. Ren B, Liu X, Suriawinata AA (2019) Pancreatic Ductal Adenocarcinoma and Its Precursor Lesions: Histopathology, Cytopathology, and Molecular Pathology. Am J Pathol 189:9–21. https://doi.org/10.1016/J.AJPATH.2018.10.004/ASSET/B5FDD24B-E501-4B7B-AF46-2C8C7C3EC440/MAIN.ASSETS/GR2.JPG

56. Hruban RH, Maitra A, Goggins M (2008) Update on Pancreatic Intraepithelial Neoplasia. Int J Clin Exp Pathol 1:306

57. Kopp JL, von Figura G, Mayes E, et al (2012) Identification of Sox9-Dependent Acinar-to-Ductal Reprogramming as the Principal Mechanism for Initiation of Pancreatic Ductal

Adenocarcinoma. Cancer Cell 22:737–750. https://doi.org/10.1016/J.CCR.2012.10.025/ATTACHMENT/C63CC906-21A8-4A21-B42E-516788FAF689/MMC1.PDF

58. Grimont A, Leach SD, Chandwani R (2021) Uncertain Beginnings: Acinar and Ductal Cell Plasticity in the Development of Pancreatic Cancer. Cell Mol Gastroenterol Hepatol 13:369. https://doi.org/10.1016/J.JCMGH.2021.07.014

59. Flowers BM, Xu H, Mulligan AS, et al (2021) Cell-of-origin influences pancreatic cancer subtype. Cancer Discov 11:660. https://doi.org/10.1158/2159-8290.CD-20-0633

60. Lee AYL, Dubois CL, Sarai K, et al (2019) Cell of origin affects tumour development and phenotype in pancreatic ductal adenocarcinoma. Gut 68:487–498. https://doi.org/10.1136/GUTJNL-2017-314426

61. Bilreiro C, Andrade L, Santiago I, et al (2024) Imaging of pancreatic ductal adenocarcinoma – An update for all stages of patient management. Eur J Radiol Open 12:. https://doi.org/10.1016/J.EJRO.2024.100553

62. Bilreiro C, Matos C (2021) Diffusion-weighted imaging of the pancreas. In: Matos C, Papanikolaou N (eds) Diffusion Weighted Imaging of the Hepatobiliary System. Springer, Cham

63. Brown R (1828) XXVII. A brief account of microscopical observations made in the months of June, July and August 1827, on the particles contained in the pollen of plants; and on the general existence of active molecules in organic and inorganic bodies. Philos Mag 4:161–173. https://doi.org/10.1080/14786442808674769

64. Langevin P (1908) Sur la théorie du mouvement brownien. C R Acad Sci 146:530–532

65. Einstein A (1905) Über die von der molekularkinetischen Theorie der Wärme geforderte Bewegung von in ruhenden Flüssigkeiten suspendierten Teilchen. Ann Phys 8:549–560

66. Purcell E, CARR H (1954) Effects of diffusion on free precession in nuclear magnetic resonance experiments. Phys Rev 94:630–638

67. Torrey HC (1956) Bloch Equations with Diffusion Terms. Phys Rev 104:563. https://doi.org/10.1103/PhysRev.104.563

68. Woessner DE (1961) Effects of Diffusion in Nuclear Magnetic Resonance Spin-Echo Experiments. J Chem Phys 34:2057–2061. https://doi.org/10.1063/1.1731821

69. Stejskal EO, Tanner JE (1965) Spin Diffusion Measurements: Spin Echoes in the Presence of a Time-Dependent Field Gradient. J Chem Phys 42:288–292. https://doi.org/10.1063/1.1695690

70. Koh DM, Collins DJ (2007) Diffusion-weighted MRI in the body: applications and challenges in oncology. AJR Am J Roentgenol 188:1622–1635. https://doi.org/10.2214/AJR.06.1403

71. Drake-Pérez M, Boto J, Fitsiori A, et al (2018) Clinical applications of diffusion weighted imaging in neuroradiology. Insights Imaging 9:535–547. https://doi.org/10.1007/S13244-018-0624-3/FIGURES/11

72. Kiselev VG (2021) Microstructure with diffusion MRI: what scale we are sensitive to? J Neurosci Methods 347:108910. https://doi.org/10.1016/J.JNEUMETH.2020.108910

73. Basser PJ (1995) Inferring microstructural features and the physiological state of tissues from diffusion-weighted images. NMR Biomed 8:333–344. https://doi.org/10.1002/NBM.1940080707

74. Novikov DS, Fieremans E, Jespersen SN, Kiselev VG (2019) Quantifying brain microstructure with diffusion MRI: Theory and parameter estimation. NMR Biomed 32:. https://doi.org/10.1002/NBM.3998

75. Basser PJ, Mattiello J, Lebihan D (1994) Estimation of the Effective Self-Diffusion Tensor from the NMR Spin Echo. J Magn Reson Ser B 103:247–254. https://doi.org/10.1006/JMRB.1994.1037

76. Le Bihan D, Mangin JF, Poupon C, et al (2001) Diffusion tensor imaging: Concepts and applications. J Magn Reson Imaging 13:534–546. https://doi.org/10.1002/JMRI.1076

77. Lebel C, Benner T, Beaulieu C (2012) Six is enough? Comparison of diffusion parameters measured using six or more diffusion-encoding gradient directions with deterministic tractography. Magn Reson Med 68:474–483. https://doi.org/10.1002/MRM.23254

78. Barrio-Arranz G, De Luis-García R, Tristán-Vega A, et al (2015) Impact of MR Acquisition Parameters on DTI Scalar Indexes: A Tractography Based Approach. PLoS One 10:. https://doi.org/10.1371/JOURNAL.PONE.0137905

79. Jeurissen B, Descoteaux M, Mori S, Leemans A (2019) Diffusion MRI fiber tractography of the brain. NMR Biomed 32:e3785. https://doi.org/10.1002/NBM.3785

80. Bäumer P, Pham M, Ruetters M, et al (2014) Peripheral Neuropathy: Detection with Diffusion-Tensor Imaging. https://doi.org/101148/radiol14132837 273:185–193. https://doi.org/10.1148/RADIOL.14132837

81. Metwalli NS, Benatar M, Nair G, et al (2010) Utility of axial and radial diffusivity from diffusion tensor MRI as markers of neurodegeneration in amyotrophic lateral sclerosis. Brain Res 1348:156–164. https://doi.org/10.1016/J.BRAINRES.2010.05.067

82. Kelly S, Jahanshad N, Zalesky A, et al (2017) Widespread white matter microstructural differences in schizophrenia across 4322 individuals: results from the ENIGMA Schizophrenia DTI Working Group. Mol Psychiatry 2018 235 23:1261–1269. https://doi.org/10.1038/mp.2017.170

83. Afzali M, Mueller L, Szczepankiewicz F, et al (2022) Quantification of Tissue Microstructure Using Tensor-Valued Diffusion Encoding: Brain and Body. Front Phys 10:809133. https://doi.org/10.3389/FPHY.2022.809133/BIBTEX

84. Chianca V, Albano D, Messina C, et al (2017) Diffusion tensor imaging in the musculoskeletal and peripheral nerve systems: from experimental to clinical applications. Eur Radiol Exp 1:1–8. https://doi.org/10.1186/S41747-017-0018-1/FIGURES/4

85. Lee Y, Kim H (2015) Assessment of diffusion tensor MR imaging (DTI) in liver fibrosis with minimal confounding effect of hepatic steatosis. Magn Reson Med 73:1602–1608. https://doi.org/10.1002/MRM.25253

86. Nissan N, Golan T, Furman-Haran E, et al (2014) Diffusion tensor magnetic resonance imaging of the pancreas. PLoS One 9:. https://doi.org/10.1371/JOURNAL.PONE.0115783

87. Li X, Zhuang L, Zhang X, et al (2016) Preliminary Study of MR Diffusion Tensor Imaging of Pancreas for the Diagnosis of Acute Pancreatitis. 11:e0160115. https://doi.org/10.1371/JOURNAL.PONE.0160115

88. Jensen JH, Helpern JA, Ramani A, et al (2005) Diffusional kurtosis imaging: The quantification of non-gaussian water diffusion by means of magnetic resonance imaging. Magn Reson Med 53:1432–1440. https://doi.org/10.1002/MRM.20508

89. Jensen JH, Helpern JA (2010) MRI quantification of non-Gaussian water diffusion by kurtosis analysis. NMR Biomed 23:698–710. https://doi.org/10.1002/NBM.1518

90. Steven AJ, Zhuo J, Melhem ER (2014) Diffusion kurtosis imaging: An emerging technique for evaluating the microstructural environment of the brain. Am J Roentgenol 202:. https://doi.org/10.2214/AJR.13.11365/ASSET/IMAGES/LARGE/01_13_11365_07_CMYK.JPEG

91. Henriques RN (2018) Advanced Methods for Diffusion MRI Data Analysis and their Application to the Healthy Ageing Brain. PhD Thesis, Univ Cambridge. https://doi.org/10.17863/CAM.29356

92. Henriques RN, Jespersen SN, Jones DK, Veraart J (2021) Toward more robust and reproducible diffusion kurtosis imaging. Magn Reson Med 86:1600. https://doi.org/10.1002/MRM.28730

93. Henriques RN, Correia MM, Marrale M, et al (2021) Diffusional Kurtosis Imaging in the Diffusion Imaging in Python Project. Front Hum Neurosci 15:675433. https://doi.org/10.3389/FNHUM.2021.675433/BIBTEX

94. Hui ES, Fieremans E, Jensen JH, et al (2012) Stroke assessment with diffusional kurtosis imaging. Stroke 43:2968–2973. https://doi.org/10.1161/STROKEAHA.112.657742

95. Raab P, Hattingen E, Franz K, et al (2010) Cerebral gliomas: diffusional kurtosis imaging analysis of microstructural differences. Radiology 254:876–881. https://doi.org/10.1148/RADIOL.09090819

96. Van Cauter S, Veraart J, Sijbers J, et al (2012) Gliomas: diffusion kurtosis MR imaging in grading. Radiology 263:492–501. https://doi.org/10.1148/RADIOL.12110927

97. Richter V, Nägele T, Erb G, et al (2024) Improved diagnostic confidence and tumor type prediction in adult-type diffuse glioma by multimodal imaging including DCE perfusion and diffusion kurtosis mapping – A standardized multicenter study. Eur J Radiol 171:111293. https://doi.org/10.1016/j.ejrad.2024.111293

98. Wang JJ, Lin WY, Lu CS, et al (2011) Parkinson disease: diagnostic utility of diffusion kurtosis imaging. Radiology 261:210–217. https://doi.org/10.1148/RADIOL.11102277

99. Falangola MF, Jensen JH, Tabesh A, et al (2013) Non-Gaussian diffusion MRI assessment of brain microstructure in mild cognitive impairment and Alzheimer's disease. Magn Reson Imaging 31:840–846. https://doi.org/10.1016/J.MRI.2013.02.008

100. Rosenkrantz AB, Padhani AR, Chenevert TL, et al (2015) Body diffusion kurtosis imaging: Basic principles, applications, and considerations for clinical practice. J Magn Reson Imaging 42:1190–1202. https://doi.org/10.1002/JMRI.24985

101. Tamada T, Prabhu V, Li J, et al (2017) Prostate cancer: Diffusion-weighted MR imaging for detection and assessment of aggressiveness-comparison between conventional and kurtosis models. Radiology 284:100–108. https://doi.org/10.1148/RADIOL.2017162321

102. Yuan J, Yeung DKW, Mok GSP, et al (2014) Non-Gaussian analysis of diffusion weighted imaging in head and neck at 3T: a pilot study in patients with nasopharyngeal carcinoma. PLoS One 9:. https://doi.org/10.1371/JOURNAL.PONE.0087024

103. Wu D, Li G, Zhang J, et al (2014) Characterization of breast tumors using diffusion kurtosis imaging (DKI). PLoS One 9:. https://doi.org/10.1371/JOURNAL.PONE.0113240

104. Goshima S, Kanematsu M, Noda Y, et al (2015) Diffusion kurtosis imaging to assess response to treatment in hypervascular hepatocellular carcinoma. AJR Am J Roentgenol 204:W543–W549. https://doi.org/10.2214/AJR.14.13235

105. Noda Y, Kanematsu M, Goshima S, et al (2016) Diffusion kurtosis imaging of the pancreas for the assessment of HbA1c levels. J Magn Reson Imaging 43:159–165. https://doi.org/10.1002/JMRI.24982

106. Bilreiro C, Andrade L, Marques RM, Matos C (2023) Diffusion-weighted imaging for determining response to neoadjuvant therapy in pancreatic cancer: a systematic review and meta-analysis. Eur Radiol. https://doi.org/10.1007/s00330-023-10381-0

107. Bilreiro C, Fernandes FF, Andrade L, et al (2021) Effective bowel motion reduction in mouse abdominal MRI using hyoscine butylbromide. Magn Reson Med 86:2146–2155. https://doi.org/10.1002/MRM.28824

108. Bilreiro C, Fernandes FF, Simões R V., et al (2024) Pancreatic Intraepithelial Neoplasia Revealed by Diffusion-Tensor MRI. Invest Radiol. https://doi.org/10.1097/RLI.0000000000001142

109. Altmayer S, Armelin LM, Pereira JS, et al (2024) MRI with DWI improves detection of liver metastasis and selection of surgical candidates with pancreatic cancer: a systematic review and meta-analysis. Eur Radiol 34:. https://doi.org/10.1007/S00330-023-10069-5

110. Brenner R, Metens T, Bali M, et al (2012) Pancreatic neuroendocrine tumor: added value of fusion of T2-weighted imaging and high b-value diffusion-weighted imaging for tumor detection. Eur J Radiol 81:. https://doi.org/10.1016/J.EJRAD.2012.01.032

111. Donati F, Casini C, Cervelli R, et al (2021) Diffusion-weighted MRI of solid pancreatic lesions: Comparison between reduced field-of-view and large field-of-view sequences. Eur J Radiol 143:109936. https://doi.org/10.1016/J.EJRAD.2021.109936

112. Choi SY, Kim SH, Kang TW, et al (2016) Differentiating mass-forming autoimmune pancreatitis from pancreatic ductal adenocarcinoma on the basis of contrast-enhanced MRI and DWI findings. Am J Roentgenol 206:291–300. https://doi.org/10.2214/AJR.15.14974/ASSET/IMAGES/LARGE/02_15_14974_05.JPEG

113. Wang ZH, Zhu L, Xue HD, Jin ZY (2024) Quantitative MR imaging biomarkers for distinguishing inflammatory pancreatic mass and pancreatic cancer—a systematic review and meta-analysis. Eur Radiol 34:6738–6750. https://doi.org/10.1007/S00330-024-10720-9/TABLES/3

114. Manfredi R, Bonatti M, Mantovani W, et al (2013) Non-hyperfunctioning neuroendocrine tumours of the pancreas: MR imaging appearance and correlation with their biological behaviour. Eur Radiol 23:3029–3039. https://doi.org/10.1007/S00330-013-2929-4

115. Lee L, Ito T, Jensen RT (2018) Imaging of pancreatic neuroendocrine tumors: recent advances, current status, and controversies. Expert Rev Anticancer Ther 18:837–860. https://doi.org/10.1080/14737140.2018.1496822

116. Barral M, Taouli B, Guiu B, et al (2015) Diffusion-weighted MR imaging of the pancreas: current status and recommendations. Radiology 274:45–63. https://doi.org/10.1148/radiol.14130778

117. Martinez-Heras E, Grussu F, Prados F, et al (2021) Diffusion-Weighted Imaging: Recent Advances and Applications. Semin Ultrasound, CT MRI 42:490–506. https://doi.org/10.1053/J.SULT.2021.07.006

118. Granata V, Fusco R, Sansone M, et al (2020) Magnetic resonance imaging in the assessment of pancreatic cancer with quantitative parameter extraction by means of dynamic contrast-enhanced magnetic resonance imaging, diffusion kurtosis imaging and intravoxel incoherent motion diffusion-weighted imaging. Therap Adv Gastroenterol 13:1756284819885052. https://doi.org/10.1177/1756284819885052

119. Ni H, Kavcic V, Zhu T, et al (2006) Effects of Number of Diffusion Gradient Directions on Derived Diffusion Tensor Imaging Indices in Human Brain. AJNR Am J Neuroradiol 27:1776

120. Veraart J, Novikov DS, Christiaens D, et al (2016) Denoising of diffusion MRI using random matrix theory. Neuroimage 142:394–406. https://doi.org/10.1016/J.NEUROIMAGE.2016.08.016

121. Kellner E, Dhital B, Kiselev VG, Reisert M (2016) Gibbs-ringing artifact removal based on local subvoxel-shifts. Magn Reson Med 76:1574–1581. https://doi.org/10.1002/MRM.26054

122. Veraart J, Sijbers J, Sunaert S, et al (2013) Weighted linear least squares estimation of diffusion MRI parameters: strengths, limitations, and pitfalls. Neuroimage 81:335–346. https://doi.org/10.1016/j.neuroimage.2013.05.028

123. Rydhög AS, Szczepankiewicz F, Wirestam R, et al (2017) Separating Blood and Water: Perfusion and Free Water Elimination from Diffusion MRI in the Human Brain. Neuroimage 156:423. https://doi.org/10.1016/J.NEUROIMAGE.2017.04.023

124. Henriques RN, Jespersen SN, Shemesh N (2019) Microscopic anisotropy misestimation in spherical-mean single diffusion encoding MRI. Magn Reson Med 81:3245–3261. https://doi.org/10.1002/MRM.27606

125. Wang X, Gao W, Li F, et al (2019) Diffusion kurtosis imaging as an imaging biomarker for predicting prognosis of the patients with high-grade gliomas. Magn Reson Imaging 63:131–136. https://doi.org/10.1016/J.MRI.2019.08.001

126. Bland JM, Altman DG (1999) Measuring agreement in method comparison studies. Stat Methods Med Res 8:135–160. https://doi.org/10.1177/096228029900800204

127. Sorace AG, Wu C, Barnes SL, et al (2018) Repeatability, Reproducibility, and Accuracy of Quantitative MRI of the Breast in the Community Radiology Setting. J Magn Reson Imaging 48:10.1002/jmri.26011. https://doi.org/10.1002/JMRI.26011

128. Koo TK, Li MY (2016) A Guideline of Selecting and Reporting Intraclass Correlation Coefficients for Reliability Research. J Chiropr Med 15:155. https://doi.org/10.1016/J.JCM.2016.02.012

129. Cohen J (1968) Weighted kappa: nominal scale agreement with provision for scaled disagreement or partial credit. Psychol Bull 70:213–220. https://doi.org/10.1037/H0026256

130. Landis JR, Koch GG (1977) The Measurement of Observer Agreement for Categorical Data. Biometrics 33:159. https://doi.org/10.2307/2529310

131. Lemke A, Laun FB, Klau M, et al (2009) Differentiation of pancreas carcinoma from healthy pancreatic tissue using multiple b-values: Comparison of apparent diffusion coefficient and intravoxel incoherent motion derived parameters. Invest Radiol 44:769–775. https://doi.org/10.1097/RLI.0B013E3181B62271

132. Herrmann J, Schoennagel BP, Roesch M, et al (2013) Diffusion-weighted imaging of the healthy pancreas: ADC values are age and gender dependent. 37:886–891. https://doi.org/10.1002/JMRI.23871

133. Kumpulainen V, Merisaari H, Copeland A, et al (2022) Effect of number of diffusion-encoding directions in diffusion metrics of 5-year-olds using tract-based spatial statistical analysis. Eur J Neurosci 56:4843. https://doi.org/10.1111/EJN.15785

134. Chen Y, Tymofiyeva O, Hess CP, Xu D (2015) Effects of rejecting diffusion directions on tensor-derived parameters. Neuroimage 109:160–170. https://doi.org/10.1016/J.NEUROIMAGE.2015.01.010

135. Farrell JAD, Landman BA, Jones CK, et al (2007) Effects of signal-to-noise ratio on the accuracy and reproducibility of diffusion tensor imaging-derived fractional anisotropy, mean diffusivity, and principal eigenvector measurements at 1.5 T. J Magn Reson Imaging

26:756–767. https://doi.org/10.1002/JMRI.21053

136. Crombé A, Nicolas R, Richard N, et al (2022) High B-value diffusion tensor imaging for early detection of hippocampal microstructural alteration in a mouse model of multiple sclerosis. Sci Reports 2022 121 12:1–15. https://doi.org/10.1038/s41598-022-15511-0

137. Zaitsev M, Maclaren J, Herbst M (2015) Motion Artefacts in MRI: a Complex Problem with Many Partial Solutions. J Magn Reson Imaging 42:887. https://doi.org/10.1002/JMRI.24850

138. Dogan BE, Scoggins ME, Son JB, et al (2018) American College of Radiology–Compliant Short Protocol Breast MRI for High-Risk Breast Cancer Screening: A Prospective Feasibility Study. Am J Roentgenol 210:214–221. https://doi.org/10.2214/AJR.17.18267/ASSET/IMAGES/LARGE/01_17_18267_03F.JPEG

139. Tabesh A, Jensen JH, Ardekani BA, Helpern JA (2011) Estimation of tensors and tensor-derived measures in diffusional kurtosis imaging. Magn Reson Med 65:823–836. https://doi.org/10.1002/MRM.22655

140. Geng R, Zhang Y, Starekova J, et al (2021) Characterization and Correction of Cardiovascular Motion Artifacts in Diffusion-Weighted Imaging of the Pancreas. Magn Reson Med 86:1956. https://doi.org/10.1002/MRM.28846

141. van Griethuysen JJM, Bus EM, Hauptmann M, et al (2018) Gas-induced susceptibility artefacts on diffusion-weighted MRI of the rectum at 1.5 T – Effect of applying a micro-enema to improve image quality. Eur J Radiol 99:131–137. https://doi.org/10.1016/j.ejrad.2017.12.020

142. Deshmane A, Gulani V, Griswold MA, Seiberlich N (2012) Parallel MR imaging. J Magn Reson Imaging 36:55–72. https://doi.org/10.1002/JMRI.23639

143. Edelstein WA, Glover GH, Hardy CJ, Redington RW (1986) The intrinsic signal-to-noise ratio in NMR imaging. Magn Reson Med 3:604–618. https://doi.org/10.1002/MRM.1910030413

144. Ku HH (1966) Notes on the use of propagation of error formulas. J Res Natl Bur Stand Sect C Eng Instrum 70C:263. https://doi.org/10.6028/jres.070c.025

145. Hussien N, Hussien RS, Saad DHA, et al (2022) The Role of MRI Pancreatic Protocol in Assessing Response to Neoadjuvant Therapy for Patients With Borderline Resectable Pancreatic Cancer. Front Oncol 11:. https://doi.org/10.3389/FONC.2021.796317

146. Okada KI, Hirono S, Kawai M, et al (2017) Value of apparent diffusion coefficient prior to neoadjuvant therapy is a predictor of histologic response in patients with borderline resectable pancreatic carcinoma. J Hepatobiliary Pancreat Sci 24:161–168. https://doi.org/10.1002/JHBP.430

147. Okada K ichi, Kawai M, Hirono S, et al (2020) Diffusion-weighted MRI predicts the histologic response for neoadjuvant therapy in patients with pancreatic cancer: a prospective study (DIFFERENT trial). Langenbeck's Arch Surg 405:23–33. https://doi.org/10.1007/S00423-020-01857-4

148. Bali MA, Pullini S, Metens T, et al (2018) Assessment of response to chemotherapy in pancreatic ductal adenocarcinoma: Comparison between diffusion-weighted MR quantitative parameters and RECIST. Eur J Radiol 104:49–57. https://doi.org/10.1016/J.EJRAD.2018.04.024

149. Kang JH, Lee SS, Kim JH, et al (2021) Multiparametric MRI for prediction of treatment response to neoadjuvant FOLFIRINOX therapy in borderline resectable or locally advanced pancreatic cancer. Eur Radiol 31:864–874. https://doi.org/10.1007/S00330-020-07134-8

150. Harder FN, Jungmann F, Kaissis GA, et al (2021) [18F]FDG PET/MRI enables early chemotherapy response prediction in pancreatic ductal adenocarcinoma. EJNMMI Res 11:. https://doi.org/10.1186/S13550-021-00808-4

151. Cuneo KC, Chenevert TL, Ben-Josef E, et al (2014) A pilot study of diffusion-weighted MRI in patients undergoing neoadjuvant chemoradiation for pancreatic cancer. Transl Oncol 7:644–649. https://doi.org/10.1016/J.TRANON.2014.07.005

152. Dalah E, Erickson B, Oshima K, et al (2018) Correlation of ADC With Pathological Treatment Response for Radiation Therapy of Pancreatic Cancer. Transl Oncol 11:391–398. https://doi.org/10.1016/J.TRANON.2018.01.018

153. Do RK, Reyngold M, Paudyal R, et al (2020) Diffusion-Weighted and Dynamic Contrast-Enhanced MRI Derived Imaging Metrics for Stereotactic Body Radiotherapy of Pancreatic Ductal Adenocarcinoma: Preliminary Findings. Tomogr (Ann Arbor, Mich) 6:261–271. https://doi.org/10.18383/J.TOM.2020.00015

154. Isaji S, Mizuno S, Windsor JA, et al (2018) International consensus on definition and criteria of borderline resectable pancreatic ductal adenocarcinoma 2017. Pancreatology 18:2–11. https://doi.org/10.1016/J.PAN.2017.11.011

155. Tempero MA, Malafa MP, Al-Hawary M, et al (2021) Pancreatic Adenocarcinoma, Version 2.2021, NCCN Clinical Practice Guidelines in Oncology. J Natl Compr Canc Netw 19:439–457. https://doi.org/10.6004/JNCCN.2021.0017

156. McTavish S, Van AT, Peeters JM, et al (2022) Gradient nonlinearity correction in liver DWI using motion-compensated diffusion encoding waveforms. Magn Reson Mater Physics, Biol Med 35:827–841. https://doi.org/10.1007/S10334-021-00981-6/FIGURES/8

157. Hu L, Zhou DW, Fu CX, et al (2021) Calculation of Apparent Diffusion Coefficients in Prostate Cancer Using Deep Learning Algorithms: A Pilot Study. Front Oncol 11:697721. https://doi.org/10.3389/FONC.2021.697721/BIBTEX

158. Sedlaczek OL, Kleesiek J, Gallagher FA, et al (2022) Quantification and reduction of cross-vendor variation in multicenter DWI MR imaging: results of the Cancer Core Europe imaging task force. Eur Radiol 32:8617–8628. https://doi.org/10.1007/S00330-022-08880-7/FIGURES/6

159. Virostko J, Craddock RC, Williams JM, et al (2021) Development of a standardized MRI protocol for pancreas assessment in humans. PLoS One 16:. https://doi.org/10.1371/JOURNAL.PONE.0256029

160. Ma C, Li J, Boukar MB, et al (2017) Optimized ROI size on ADC measurements of normal pancreas, pancreatic cancer and mass-forming chronic pancreatitis. Oncotarget 8:99085–99092. https://doi.org/10.18632/ONCOTARGET.18457

161. Ma C, Guo X, Liu L, et al (2017) Effect of region of interest size on ADC measurements in pancreatic adenocarcinoma. Cancer Imaging 17:1–7. https://doi.org/10.1186/S40644-017-0116-6/TABLES/5

162. Zins M, Matos C, Cassinotto C (2018) Pancreatic Adenocarcinoma Staging in the Era of Preoperative Chemotherapy and Radiation Therapy. Radiology 287:374–390. https://doi.org/10.1148/RADIOL.2018171670

163. Cassinotto C, Mouries A, Lafourcade JP, et al (2014) Locally advanced pancreatic adenocarcinoma: reassessment of response with CT after neoadjuvant chemotherapy and radiation therapy. Radiology 273:108–116. https://doi.org/10.1148/RADIOL.14132914

164. Strobel O, Neoptolemos J, Jäger D, Büchler MW (2019) Optimizing the outcomes of

pancreatic cancer surgery. Nat Rev Clin Oncol 16:11–26. https://doi.org/10.1038/S41571-018-0112-1

165. Zaharia C, Søreide K (2023) Call for better response evaluation after neoadjuvant therapy in pancreatic cancer. Br J Surg 110:294–296. https://doi.org/10.1093/BJS/ZNAC452

166. Xu J, Zhan H, Li F, et al (2021) Neoadjuvant therapy for pancreatic cancer: Limitations and advances of response assessment (Review). Oncol Rep 45:. https://doi.org/10.3892/OR.2021.7977

167. Soloff E V., Al-Hawary MM, Desser TS, et al (2022) Imaging Assessment of Pancreatic Cancer Resectability After Neoadjuvant Therapy: AJR Expert Panel Narrative Review. AJR Am J Roentgenol 218:570–581. https://doi.org/10.2214/AJR.21.26931

168. Grimm J, Potthast A, Wunder A, Moore A (2003) Magnetic resonance imaging of the pancreas and pancreatic tumors in a mouse orthotopic model of human cancer. Int J Cancer 106:806–811. https://doi.org/10.1002/ijc.11281

169. Partecke IL, Kaeding A, Sendler M, et al (2011) In vivo imaging of pancreatic tumours and liver metastases using 7 Tesla MRI in a murine orthotopic pancreatic cancer model and a liver metastases model. BMC Cancer 11:. https://doi.org/10.1186/1471-2407-11-40

170. Froehlich JM, Daenzer M, von Weymarn C, et al (2009) Aperistaltic effect of hyoscine N-butylbromide versus glucagon on the small bowel assessed by magnetic resonance imaging. Eur Radiol 19:1387–1393. https://doi.org/10.1007/s00330-008-1293-2

171. Gutzeit A, Binkert CA, Koh DM, et al (2012) Evaluation of the anti-peristaltic effect of glucagon and hyoscine on the small bowel: Comparison of intravenous and intramuscular drug administration. Eur Radiol 22:1186–1194. https://doi.org/10.1007/s00330-011-2366-1

172. Storz P (2017) Acinar cell plasticity and development of pancreatic ductal adenocarcinoma. Nat Rev Gastroenterol Hepatol 14:296–304. https://doi.org/10.1038/NRGASTRO.2017.12

173. Storz P, Crawford HC (2020) Carcinogenesis of Pancreatic Ductal Adenocarcinoma. Gastroenterology 158:2072–2081. https://doi.org/10.1053/J.GASTRO.2020.02.059

174. Wood LD, Canto MI, Jaffee EM, Simeone DM (2022) Pancreatic Cancer: Pathogenesis, Screening, Diagnosis, and Treatment. Gastroenterology 163:386-402.e1. https://doi.org/10.1053/J.GASTRO.2022.03.056

175. Alonso-Curbelo D, Ho YJ, Burdziak C, et al (2021) A gene-environment-induced epigenetic program initiates tumorigenesis. Nature 590:642–648. https://doi.org/10.1038/S41586-020-03147-X

176. Kiselev VG, Körzdörfer G, Gall P (2021) Toward Quantification: Microstructure and Magnetic Resonance Fingerprinting. Invest Radiol 56:1–9. https://doi.org/10.1097/RLI.0000000000000738

177. Alexander DC, Dyrby TB, Nilsson M, Zhang H (2019) Imaging brain microstructure with diffusion MRI: practicality and applications. NMR Biomed 32:e3841. https://doi.org/10.1002/NBM.3841

178. Gholizadeh N, Greer PB, Simpson J, et al (2019) Characterization of prostate cancer using diffusion tensor imaging: A new perspective. Eur J Radiol 110:112–120. https://doi.org/10.1016/J.EJRAD.2018.11.026

179. Szczepankiewicz F, Lasič S, van Westen D, et al (2015) Quantification of microscopic diffusion anisotropy disentangles effects of orientation dispersion from microstructure:

Applications in healthy volunteers and in brain tumors. Neuroimage 104:241–252. https://doi.org/10.1016/j.neuroimage.2014.09.057

180. Kenner B, Chari ST, Kelsen D, et al (2021) Artificial Intelligence and Early Detection of Pancreatic Cancer: 2020 Summative Review. Pancreas 50:251. https://doi.org/10.1097/MPA.0000000000001762

181. Heredia-Soto V, Rodríguez-Salas N, Feliu J (2021) Liquid Biopsy in Pancreatic Cancer: Are We Ready to Apply It in the Clinical Practice? Cancers (Basel) 13:. https://doi.org/10.3390/CANCERS13081986